MICROFLUIDIC GENERATION OF CANCER NANOMEDICINES

A Dissertation
Presented to
The Academic Faculty

by

Mohammad Mahdi Hasani-Sadrabadi

In Partial Fulfillment
of the Requirements for the Degree
Doctor of Philosophy in Bioengineering

Georgia Institute of Technology
December 2017

Copyright © 2017 by Mohammad Mahdi Hasani-Sadrabadi

MICROFLUIDIC GENERATION OF CANCER NANOMEDICINES

Approved by:

Dr. Karl I. Jacob, Advisor
School of Materials Science and Engineering
Georgia Institute of Technology

Dr. Mostafa A. El-Sayed
School of Chemistry & Biochemistry
Georgia Institute of Technology

Dr. Luke Brewster
School of Medicine
Emory University

Dr. Krishnendu Roy
Wallace H. Coulter Department of Biomedical Engineering *Georgia Institute of Technology*

Dr. J. Brandon Dixon
George Woodruff School of Mechanical Engineering
Georgia Institute of Technology

Date Approved: October 25, 2017

Dedicated to

My beautiful wife, Negin; If I had nothing in my life but you. I'd still have it ALL...

And to my parents, Mohammad Hossein and Farideh, whose unconditional love and prayers led to every success in my life...

ACKNOWLEDGEMENTS

Many people have contributed to my success in completing this dissertation. I was fortunate to have an outstanding committee. Prof. Karl Jacob has been a wonderful advisor and mentor, and I want to thank him for all of his helps and supports from the very first time that we talked about starting my PhD at Georgia Tech till now. He did everything to support me even before coming to Georgia Tech. He helped me professionally and personally. He gave me real freedom in terms of research subject as well as the number of projects that I could be involved in and so many more.

I would also like to convey my gratitude to my dissertation committee members: Prof. Luke Brewster, Prof. Mostafa A. El-Sayed, Prof. J. Brandon Dixon, and Prof. Krish Roy for being so cooperative and helpful. Their advice after the dissertation proposal and progress reports provided me with valuable ideas for the completion of the remaining work and filling the gaps. I am really grateful that I had the honor of having Prof. Mostafa El-Sayed, a legend in nanotechnology, as my mentor and had the privilege to use his valuable advises. Also benefiting from the valuable comments of Prof. Kirish Roy as a pioneer in cancer nanomedicine has been most helpful and encouraging for me and I highly appreciate it. The courses I took with Prof. Paul Russo, Prof. Andrés García, and Prof. Julia Babensee aided me a lot in formulating of my research. I would also like to thank Prof. Jeannette Yen and Prof. Sabir Khan, for their creative course, *Biologically Inspired Design*, and for giving me the permission to attend their instructive classes. I believe their courses helped me a lot in shaping the ideas for my research especially for Chapter 7. I would also like to thank Prof. Timothy Deming for permitting me to attend his class on Bioconjugate Chemistry.

This course has been really helpful through my experiments. In this sense, I also need to acknowledge my undergraduate mentors Prof. Hamid Modarres, Prof. Mahdi Rafizadeh, Prof. Homa Assempour and Prof. Seyed Reza Ghaffarian, and Prof. Nasser Mohammadi. In addition, I would like to thank Dr. Shahriar Hojjati Emami, Dr. Hamid Keshvari, Dr. Shahin Bonakdar, Prof. Mohammad Ali Shokrgozar and Prof. Hossein Baharvand that I have had the pleasure of working and engaging in research discussions.

I would also like to highly appreciate Prof. Paul Weiss (CNSI, UCLA) and his fantastic group for kindly accepting me and helping me a lot during the past 18 months. I would like to thank Dr. Alireza Moshaverinia (UCLA), Dr. Amir Sanati Nezhad (U Calgary), Dr. Morteza Mahmoudi (Harvard) and Dr. Lobat Tayebi (Marquette U) for being wonderful and supportive collaborators. I would also like to thank Prof. Philippe Renaud and his group at EPFL, for introducing me to, and ultimately grounding my work in, the world of microfluidics. I want to single out Dr. Arnaud Bertsch and Dr. Jules Van Dersarl for being such wonderful mentors and good friends.

I also need to thank my lovely aunt Dr. Roya Ameri, who was the first person who introduced me to polymer science and brought me to this era. I need to acknowledge, Dr. Homayoun Moaddel, who was the first person that taught me experimental work on polymer chemistry and physics. I had the honor of working with him for couple of years when no one else would trust a junior undergraduate. My best friend and colleague, Dr. Erfan Dashtimoghadam, was the main contributor to my success. I sincerely appreciate his encouragement and willingness to help me in numerous ways and his major contribution in my progress. I must also acknowledge friends and colleagues of mine Dr. Vahid Karimkhani, Mr. Mahdi Mohajeri, Dr. Nassir Mokarram, Dr. Hassan Pezeshgi, Dr.

Shahrouz Taranejoo, Dr. Payam Molla-Abbasi and Dr. Iman Shabani. They were truly influential and very supportive in encouraging me toward my advancement in the field. Dr. Ghasem Bahlakeh is another key collaborator and friend who contributed a lot especially in simulation parts of my research.

Last but not least, I would like to extend my thanks to my parents, Mohammad Hossein and Farideh, and my sisters, Zahra and Fatemeh, as well as my mother-in-law, Gity, for always being there for me. The continuous support, encouragement, and love from my family were most valuable for the successful completion of my doctorate degree and to God that made all of this possible.

Finally, I again want to express my thanks and love to my wife, Negin. She has made my life absolutely wonderful. I had to appreciate her patience and support on such an unpredictable journey that I have had.

TABLE OF CONTENTS

LIST OF TABLES

LIST OF FIGURES

hard NPs with and without UV irradiation (n = 5). (c) Quantitative tissue accumulation of NPs in tumor and other organs 48 h after tail vein injection of fluorescently-labeled NPs with and without UV irradiation. (d) Survival rates of tumor-bearing mice treated with different modularity of NPs. (e) In vivo vascular disruption in the subcutaneous matrigel model after treatment with targeted NPs with different formulations. The plugs were removed after the treatment and imaged by fluorescent microscopy. (f) Alteration in vessel morphology evaluated by measuring the RITC-Dextran leakage from the vasculatures. (g) Tumor tissue cross-section immunostained for TUNEL-positive cells. (h) Quantification of apoptosis by assessing the number of TUNE-positive cells. .....

SUMMARY

Cancer diagnosis and therapy are perhaps the most promising areas for nanotechnology in medicine, and are expected to soon have applications in the market. An ideal therapeutic agent should perform like a magic bullet to simultaneously target cancer cells and avoid healthy cells, therefore, increase the treatment efficiency and reduce side effects. The current research is mainly devoted to minimizing the negative impacts that anti-cancer drugs put on normal cells, and eventually propose a "smart drugs" as the ultimate goal. The goal of this dissertation was to develop a technological foundation for synthesis and evaluation of polymer-based cancer therapeutic. This was performed using a microfluidic platform for optimization, and characterization of resulted particles for controlled drug release within the tumor environment. This technique was first optimized to show the feasibility of making drug-nanoparticles (NPs) out of different synthetic and natural polymers with it. The biophysical properties of these particles were also investigated at nano-biointerface. The process was then adjusted to develop pH- responsive core-shell NPs enabling oral administration of hydrophobic cancer therapeutics. Precise coating over the NPs with a sacrificial pH-responsive layer prevented drug release in severe pH conditions of the gastrointestinal tract, while allowing the drug to be released in tumor proximity. This technique was also adjusted to fabricate complex NPs *via* controlled self-assembly of several components in a single step. Resulted particles can be used for theranostics applications or provide ultra-high drug loading capacity. Tuning the surface properties was also possible *via* this system and it was used to control immune-NPs and cancer cell-NPs interactions. To prolong blood circulation and enhance cell internalization,

feasibility of making one-dimensional nanocarriers by template-based self-assembly approach was also confirmed. These nanocarriers can serve as suitable candidates for combinatorial cancer therapy as they can load and deliver substantial amounts of drugs while allowing for hyperthermia effect thanks to their carbon nanotube core. Mechanical properties of nanocarriers can also influence a broad range of NPs' biological behaviors. Here, inspired by viruses, systematic investigation of the mechanobiological properties of NPs are done to determine the optimized range for *in vitro* and *in vivo* targeting. NPs with switchable mechanical properties are proposed capable of switching from soft to stiff state in the site of action and provide enhanced therapeutic efficiencies. Overall, we hope that this research provides broad information on how NP design can affect and control the efficacy of cancer nanomedicine. These findings point to the high potential of microfluidic platforms as engineering toolboxes that enable design of complex multifunctional nanomaterials via controlled bottom-up approach for various biomedical applications.

CHAPTER 1. OUTLINES

Nanomedicine has a wide range of possible applications, including disease prevention, diagnosis, monitoring, management, and treatment. Cancer diagnosis and therapy are perhaps the most promising areas for nanotechnology in medicine, and are expected to soon have applications in the market (1-3). Although there are many diverse problems in treating cancer, a magic bullet that can simultaneously target cancer cells and avoid healthy cells, therefore, increase the treatment efficiency and reduce side effects (4, 5), has long been the dream of cancer researchers (6). The current research is mainly devoted to minimize the negative impacts that anti-cancer drugs put on normal cells, and eventually propose a "smart drugs" as the ultimate goal (4). One of the most promising techniques is using engineered vehicles for drug transportation and targeting (7, 8). In an effort to reach this goal, targeted drug delivery systems (DDS) based on the polymeric nanoparticles are selected due to the unique opportunities that they offer as drug carriers (3, 7), although using the correct polymer is of great importance (7, 9, 10).

Nanoscale dimensions are known to have properties distinct from their bulk which creates additional opportunities for tuning material properties in this scale, and makes nanoparticles (NPs) great candidates to serve our means. Synthesizing polymeric NPs can be done using either top-down or bottom-up approaches. As bottom-up process involves the self-assembly of particles *via* intermolecular forces, it comes with this great opportunity to tailor the particle structure and properties (11). However, controlling a wide range of mechanical and chemical properties in this powerful technique can be really challenging (12).

Traditionally, drug loaded nanoparticles are formed with bulk self-assembly in the presence of the drug, which is then trapped in the formed particles (7, 13).

Rapid mixing, precise tunability, and reproducability independent of user talents are properties difficult to obtain through those traditional methods (14-17). Recently microfluidic approaches have made these properties more obtainable by introducing parameters such as flow ratio, mixing time, and microchip design (18, 19).

Fortunately, now we can create small and monodisperse nanoparticles (14, 20-22), by creating a narrowly defined mixing regime *via* hydrodynamic flow focusing (23, 24). This well-controlled mixing regime can be precisely adjusted with the microfluidic platform (primarily through flow ratio and velocity) and is crucial in creating monodisperse nanoparticles with tunable properties, including size, surface charge, compactness as well as drug encapsulation efficiency and release rate. As a demonstration of this, we detailed formation of various kinds of nanoparticles loaded with the anti-cancer drug Paclitaxel (PTX).

This project details an exciting innovation in nanoparticle formation for drug delivery: the ability to finely tune various physical and chemical properties of nanoparticles with microfluidic assembly and a study on how these nanoparticles can interact with cancer cells both *in vitro* and *in vivo*.

Furthermore, our system can be tuned to be water-based, and drive nanoparticle assembly with local changes in pH. This can avoid the use of organic solvent used by others, thus eliminate the biocompatibility issues raised by solvent residues.

Generally, NPs that are able to enter cells and release their therapeutic contents in close proximity to intracellular machineries can be of great value in the field of nanomedicine. Size and surface charge of these nanoparticulate systems strongly tune their nanobio-interactions. We demonstrated the ability to control the nanoparticle size and surface charge in a way that maximized cellular endocytosis in *Chapter 2*. In this chapter, the role of protein corona surrounding the NPs upon entering the blood plasma and before interacting with cells are also investigated. Moreover, considering NP's diffusion and sedimentation properties, we conducted our experiments for the cells in both upright and inverted configurations to show how disparities can vary depending on the concentration of NPs in the interaction zone.

The common chemotheraputic systems are normally administered by blood injection that may present significant dose of toxic drugs systemically. Our microfluidic approach can be adjusted to develop NPs for oral administration of cancer therapeutics. To this end, we developed a dual microfluidic platform for synthesis and coating of nanocarriers with highly pH-tunable core-shell structure as described in *Chapter 3*. Precise coating over NPs with a sacrificial pH-responsive layer prevents PTX release in severe pH conditions of the gastrointestinal tract, while allowing the drug to be released in tumor proximity. The release profile and cytotoxicity of the nanoparticles against various cell line were studied using sequential incubation in different pH conditions.

Furthermore, the proposed microfluidic-assisted synthesis of NPs can be adjusted to make more complex nanoparticles like "nano-in-nano" particles. In *Chapter 4*, we report a one-step approach for synthesis of finely tuned targeted hybrid NPs. A microfluidic platform was used to precisely control the nanoprecipitation of bisphosphonate-

functionalized copolymer, while co-encapsulating superparamagnetic iron oxide nanoparticles (SPIONs) and the anticancer drug at the same time. Designed NPs were tested to evaluate their affinity for hydroxyapatite (bone-like structure). *In vivo* experiments were also performed to check pharmacokinetic and biodistribution of these NPs such as tumor localization and suppression of a bone metastatic tumor.

Increasing the loading capacity of drug carrier and the efficiency of its targeting can significantly decrease the administered dosage of the drug. While traditional amphiphilic (co-)polymers cannot encapsulate substantial amounts of hydrophobic drugs, dendritic polymers like dendritic polyethylene (dPE) can be suitable candidates. In *Chapter 5*, we offered a microfluidic platform for synthesis of complex nanocapsules *via* controlled self-assembly of several components in a single step. The resultant nanocarriers can encapsulate large amounts of hydrophobic drugs while creating low complement activation as well as sustained release profile with high tunability.

Recently, scientists realized the importance of nanocarrier's shape on its blood circulation and cell internalization which adds more complexity to the designing elements of an ideal drug carrier (12). Such challenges become more prominent for hydrophobic anti-cancer drugs, which calls for multistep reactions for synthesis of engineered copolymers. On the other hand, combinatorial cancer therapies offer a great potential to increase the treatment efficiency and decrease the side effects. In *Chapter 6*, we tried to address this point by proposing a one-step microfluidic-assisted approach for controlled self-assembly of carbon nanotubes (CNT)-based hybrid nanostructures for combinatorial cancer therapy. The dendritic polyethylene nanoparticles (dPE), developed in Chapter 5, is used as a PTX loading materials. While CNTs fulfill the hyperthermia therapy, decorated

dPE nanoparticulate layer provides efficient loading of hydrophobic anticancer drugs. These nanostructures show high cellular uptakes, and sustainable release profiles with high tunability. Our proposed technique paves the way to design and fabricate complicated nanokits as fine-tuned drug delivery systems for targeted cancer therapy.

Mechanical properties of nanocarriers is an underrepresented factor that can affect a broad range of biological interactions of nanoparticles. However, there is no systematic study to investigate the mechanobiological properties of NPs while keeping all the other physical variants such as size and surface properties, constant. In *Chapter 7*, we tried to propose microfluidic-based engineering strategies for enhancing the efficacy of cancer nanotherapeutics by controlling their physicomechanical properties. At first, we aimed to optimize the required mechanical properties for effective *in vitro* and *in vivo* targeting of cancer cells in static and dynamic cultures. To achieve this goal and have a more realistic idea of the interactions around the tumor tissue, we developed a 3D tumor-on-chip (3DToC) device. Thanks to this platform we could provide dynamic and 3D cultures for tumor cells and were able to do real-time evaluations of the NPs-matrix interactions. Having these data collected, we then tried to optimize the required mechanical properties and accordingly design nanotherapeutics with prolonged blood circulation, enhanced tumor penetration tendency and apoptosis promoting capability. Eventually, to provide the needed trade-off for optimal mechanical properties, virus-mimicking nanoparticles capable of switching from soft-to-stiff state were proposed. Therefore, these particles could circulate the blood in their soft state while switching to their stiff mode upon arrival to target tissues so that they could express their highest penetration efficiency.

CHAPTER 2. UNDERSTANDING BIOPHYSICAL BEHAVIOURS OF MICROFLUIDIC-SYNTHESIZED NANOPARTICLES AT NANO-BIOINTERFACE[1]

Serious challenges in case of using unencapsulated oral drugs for cancer treatment are high potential for sequestration in the first few cell layers they come in contact with and binding to the interstitial ECM components. By encapsulating the drugs in nanoparticles (NPs) capable of entering the target cancer cells, drugs can be made safer until reaching their intracellular site of action and more effective once it reaches the site. Upon entering the bioenvironment, NPs establish a number of interactions with their surroundings based on their physicochemical properties. Here we demonstrate how the size-surface charge interplay of chitosan nanoparticles (NPs) affects the protein corona formation and endocytosis pathway in the HeLa cells at non-toxic concentrations. Generally, large NPs (102 and 161 nm) with low surface charge (+6.7 and +3.6 mV) exhibited weaker tendency for endocytosis in comparison with smaller ones (63 and 83 nm with 10 and 9.3 mV surface charge, respectively). This is mainly because the interactions of these NPs with the plasma membrane were too weak to release enough free energy required for cellular internalization. Furthermore, we tested the upright and inverted cell culture configurations to better understand the impact of the sedimentation and diffusion velocities of NPs on the resulting cellular uptake pattern in both serum free and serum containing culture medias. Considering the different particokinetics, the amount of

[1] *This work has been published by S. Soleimani, M.M. Hasani-Sadrabadi, F.S. Majedi, E. Dashtimoghadam, M. Tondar, K. I. Jacob, (2016) Colloids and Surfaces B: Biointerfaces 145, 802-811. Reproduced with permission from Elsevier.*

internalized NPs in upright and inverted positions differed in all cases by a factor of approximately three (for 161 nm particles), or less for smaller ones. Ultimately, our results offer a paradigm for analyzing the biobehavior of NPs under the precise control of their physicochemical characteristics.

2.1 Introduction

The effectiveness of nanomedicine in developing therapeutic systems with nanoscale components (e.g. nanoparticles – NPs) that can reach the pathologic sites depends on our ability to tailor such systems with a unique set of properties, including composition, structure, size, radius of curvature, shape and charge (*25*). Yet, very little is known about how these parameters influence the final biodistribution and pharmacokinetics of NPs (*26*).When the biological target for treatment is localized in the subcellular organelles, the plasma membrane plays a significant role because it acts as a bulwark that is only selectively permeable to small, uncharged molecules. To be effective, NPs must cross the plasma membrane to reach the action site of the drug, which requires careful design of NPs with specific properties that enables them to enter cells and reach their intracellular targets (*27*).

Despite the striking advances in nanoscience, relatively little is known about the interactions that occur during the cellular uptake. One of the most studied uptake mechanisms is endocytosis, an energy-dependent uptake process in which the cell membrane protrusions spread over NPs, forming vesicles known as endosomes that carry the engulfed NPs into the cellular interior (*28*). Different endocytic pathways in non-phagocytic cells (e.g. caveolae/clathrin mediated, caveolae/clathrin independent and

pinocytosis) have distinct components and mechanisms (*29*). Additionally, it has been reported that some NPs may slip directly through the plasma membrane of eukaryotic cells, which is similar to the processes exhibited by bacteria crossing the plasma membrane (*30*).

Clearly, cell type is an important parameter determining the internalization mechanism, but, the physicochemical properties of NPs are also key players of cellular uptake (*26, 31*). Particle size is an important parameter considering the space available in these endocytic compartments (*32*), but the interplay of different physicochemical characteristics may also play a decisive role.

Accumulation of NPs in pathologic sites can be adjusted both actively and passively (*33*). The passive homing mechanism of NPs in cancer is based on the enhanced permeability and retention effect (EPR) that allows a NP to penetrate into a tumor tissue due to the vascular hyperpermeability (380-780 nm in diameter pores) as well as the chance of taking long residence time within the cancerous hive due to the decreased, sluggish lymphatic drainage in the interstitial space (*34*). To take advantage of this phenomenon, the size of NPs needs to be optimized. Large NPs cannot pass through vascular fenestrations, or even if they could, they would not get far beyond the vessels to distribute throughout the whole tumor environment (*35*). In contrast, small NPs have the ability to penetrate deep into tumors. But, these particles can only remain there transiently(*36*, *37*). To establish a balance between an efficient distribution of NPs and a sufficiently long residence time, an optimum size is required for NPs (*33*).

In addition to the size, surface charge is another significant factor responsible for charge-charge interactions, which results in the formation of NP aggregations.

Sedimentation of NPs above cells, a factor that is often ignored, makes the final results less reliable and causes deviation from the *in vivo* conditions (*38*).

NPs with high surface energy will strongly interact with biomolecules in the bioenvironment; as a result NPs become surrounded by biomolecules, a masquerade called protein corona. This 'corona' lowers the metastable state energy of NPs. Thus, it seems logical that these NPs approach the cell surface as particles with a bio-corona (*39-41*). Hence, the coverage of NPs with a natural physiological coating layer can affect the cellular internalization patterns and NPs' final effects on cells' viability (*42, 43*).

Finally, in order to explore the effect of particle size on the NPs' bio-behavior, NPs with different sizes were selected for this study. To efficiently investigate the effect of size, the fundamental objective is to employ a fabrication procedure with high control over the NPs' size and monodispersity since even minute size changes may alter many non-specific interactions that occur at the cell–particle interface. To precisely fabricate the NPs, we employed a microfluidic technique taking advantage of a solvent free cross-junction device that can generate a narrow mixing regime via a hydrodynamically focused flow to form chemically and physically tuned monodisperse chitosan NPs (*17, 20, 44, 45*). This system lets us have a better understanding of the effects that key particle variables (size, chemical composition and surface charge) have on the cell entering mechanisms.

2.2 Materials and Methods:

2.2.1 Particle preparation:

The chitosan nanoparticles were fabricated according to a previously published protocol (*44*). To summarize it briefly, a solution of acetic acid (50 mL, 1% w/v; Sigma-Aldrich) containing one-gram chitosan (CS; M_n= 280 kg/mol, degree of deacetylation 83%, Fluka) was stirred for 12 h. The resulting solution was filtered with a 0.45-μm Nylon syringe filter. The solution pH was maintained at 5.5 by the drop-wise addition of sodium hydroxide (Sigma-Aldrich). 300 mg palmitic acid N-hydroxysuccinimide ester (Sigma–Aldrich) in absolute ethanol (Sigma-Aldrich) solution was added drop-wise to the chitosan solution at 98°C under reflux. The ethanol was allowed to dissolve and distribute homogeneously throughout the solution by stirring for 48 h. The solution temperature was then decreased to reach to the room temperature. Then, adding acetone under the pH of 9.0 precipitated chitosan in the solution. The resultant polymer precipitate was filtered twice, washed with an excess of acetone, and vacuum-dried at room temperature. The product was analyzed by 1 H NMR (Bruker 400 MHz) and the palmitoyl groups placement on chitosan chains was determined using the ninhydrin assay (*46*). The high molecular weight chitosan supplement (HMCS) was dissolved in aqueous acetic acid. Then, 0.5 mL acetic acid/acetate buffer (4 M, pH= 5.5) was added into 0.5 mL of the prepared solution. The test tubes were filled with 1 mL of ninhydrin reagent (Sigma–Aldrich) and placed in a boiling water bath for 20 min. The solutions were then cooled and their absorbance was read at 570 nm and compared with the unmodified chitosan solution, the control sample, and the acetic acid/acetate buffer, the blank sample (*47*).

The microfluidic device for the fabrication of nanoparticles consists of two inlets for water at a basic pH (pH 9.0) and one main inlet for the entrance of HMCS solution at an acidic pH (pH 4.5). The resulting outlet nanoparticle stream was collected in disposable

cuvettes (Eppendorf) and used for further analysis. A critical parameter in determining nanoparticle size is the mixing time, τ_{mix}, which can be estimated from the equation:

$$\tau_{mix} = \frac{W^2}{9D} \frac{1}{(1+\frac{1}{R})^2} \quad \text{(Eq. 2-1)}$$

where W is the main channel width (150 μm), D is the diffusion constant (10^{-9} m^2/s) and R is the ratio of the polymeric stream and basic water flow rates (R = 0.03–0.2).

For comparison with the microfluidic fabrication, bulk synthesized samples were also prepared as follows: the polymeric solutions were prepared by a constant stirred-dissolving of 2.5 mg/mL HMCS in 1% w/v acetic acid, and the nanoprecipitated HMCS molecules resulted at a pH of 7.4 by the drop-wise addition of 1M NaOH.

The fluorescently-labeled HMCS were synthesized based on the reaction between the fluorescein isothiocyanate (FITC) and the chitosan (*48*). The prepared FITC in methanol (2 mg/mL) was added gradually to the solution of 1% w/v acetic acid containing the HMCS. After 5 h of reaction in dark at room temperature, the FITC-labeled chitosan was precipitated in 0.2 M NaOH and separated from the unreacted FITC via a Sephadex G-50 column with 1/15 M phosphate buffer/0.2 M NaCl as an elution solvent. The fractions containing the labeled polymers were collected and dialyzed against deionized water using a 3 kDa molecular weight cut-off dialysis cartridge (Thermo Scientific, Rockford, IL). The process was continued for almost 4 days until no fluorescence was detected in the supernatant. The resulting sample was ultimately freeze-dried.

2.2.2 Particle size and surface charge analysis

Dynamic light scattering (DLS) and zeta potential measurements were performed using a Zetasizer (Zetasizer 3000HS, Malvern Instruments Ltd., Worcestershire, UK) in the backscattering mode at 173°C for the particles dispersed both in water and FBS at a concentration of 0.3 mg/ml. Three measurements were performed for each sample.

2.2.3 Turbidimetry

The measurement of transmittance of the nanoparticle suspensions was performed *via* the spectrophotometry method (Shimadzu UVmini-1240 UV-Vis spectrophotometer) at 25°C. Accordingly, the turbidity of suspensions (τ) was calculated based on the Beer-Lambert law:

$$\tau = -\frac{1}{L} ln\left(\frac{I}{I_0}\right) \qquad \text{(Eq. 2-2)}$$

where L, I, and I_0 are the thickness of the cell, the intensity of the light transmitted through the sample, and through the solvent, respectively. Measurements were done at the wavelength of 635 nm for at least three times.

2.2.4 Refractive index

A PTR 46 refractometer (Index Instruments, UK) was used to measure the refractive index of 1% v/v aqueous acetic acid solution which was obtained as n0 =1.332. The values of the refractive index increment (*dn*/*dc*) of the polymer solutions were determined through the asymmetric flow field-flow fractionation (AFFFF) method using AF2000 FOCUS system (Postnova Analytics, Landsberg, Germany). The dn/dc was measured at the wavelength of 635 nm.

2.2.5 In vitro cytotoxicity

The cytotoxicity tests were performed using an MTT colorimetric assay (*49*). The cytotoxicity of the nanoparticles was determined after 72 h incubation with the HeLa cells seeded in 100µl of the medium. The cells were left for 24 h to adhere to the plate. The HeLa cells were incubated with the NPs with concentrations varying from 10 to 1000 µg/ml at 37°C in a humidified 5% CO_2 atmosphere. After the incubation period, the negative control samples were prepared by adding the lysis solution to a few wells containing the cells only. The MTT assay solution was added to each well and remained for 3h to allow the MTT to diffuse through the medium and react with the cells. The optical density at 570 nm was measured using a Bio-Rad model 3550 microplate reader (Bio-Rad Laboratories).

Since the NPs had highly metastable surfaces, they might agglomerate and change their physical characteristics. As a result, the concentration of NPs on the cell surface was different from the initial bulk concentration. Considering the fact that toxicity, endocytosis and a collection of other factors are directly related to NPs' concentration, we preferred to minimize the effect of agglomeration by performing an inverted culture configuration. To do so, the cells were seeded on a coverslip and suspended in the medium (The cells faced the bottom of the wells). The rest of the experiment was the same as the upright position.

2.2.6 Uptake experiments

The HeLa cell line was used to investigate the uptake of the FITC-labeled HMCS NPs. The particles were incubated with the cells over a time period ranging from 0 to 5h (37°C, 5% CO_2). After incubating the cells with the particles, the cells were washed and trypsinized to detach from the plates. The resulting cells were centrifuged and suspended

in a 0.4% trypan blue solution in the Dulbecco's Phosphate Buffers Saline (DPBS) solution to quench the extracellular FITC fluorescence. The cells were centrifuged again and the dye solution was withdrawn. Then, the cell pellets were resuspended in DPBS. All of the samples were kept on ice until FACS analysis. Ultimately, the samples were analyzed by flow cytometry (CyAn ADP, Beckman Coulter, Inc) for the green and red fluorescence. The process was repeated for the cells positioned in an inverted configuration as described earlier.

2.2.7 Endocytosis blockage studies

The HeLa cells were seeded in a T-25 flask and treated with 0.1% NaN3 (Sigma-Aldrich) and 80 μM Dynasore (Sigma-Aldrich) in a serum-free MEM for 1 h before incubation of the nanoparticles at 37°C/5% CO_2. For the action of chlorpromazine, the cells were pre-incubated in a serum-free MEM containing 10 μg/ml chlorpromazine (ChemBridge) for 15 min at 37°C and 5% CO2. The medium was then replaced with a fresh media containing the inhibitors and particles. These cells were further incubated for 30 min at 37°C and 5% CO_2. The cells were washed with D-PBS and trypsinized and processed for the flow cytometry test. Moreover, to examine the contribution of macropinocytosis in the uptake cascade, the cells were incubated with a macropinocytosis inhibitor, 5-(N-ethyl-N-isopropyl) amirolide (EIPA), at the concentration of 100 μM for 30 min. Then, the cells were incubated with a fresh medium containing the nanoparticles. Then, the cells were washed after 1 h (*50*). The resulting cells were analyzed via FACS. To further explore the mechanism through which these nanoparticles entered the cells, we performed an internalization experiment at 4°C to block the active endocytosis cascade.

2.2.8 Incubation of Nanoparticles with the plasma:

Another experiment was also conducted with the particle–protein complexes. The particle suspensions were incubated with the fetal bovine serum (FBS). According to previous reports, 1h incubation time scale is enough to form a relatively stable protein corona on NPs' surface. After that, we selected 1 h for the formation of protein corona around nanoparticles. Then, the samples were centrifuged to pellet the particle–protein complexes and the pellets were resuspended in PBS, which were ready to be exposed to the cells. Note that in the medium that contained serum, the serum-to-particle surface ratio should be fixed to ensure the comparability between results (*51*).

2.2.9 Hemolysis of erythrocytes:

The sheep blood was collected in heparinized-tubes. The blood plasma was separated by centrifugation at 4500g for 5 min (Eppendorf Centrifuge 5804R, Eppendorf, Hamburg, Germany). The resultant pellet was washed three times with a cold 1.5×10^{-3} M phosphate-buffered saline (pH 7.4) (PBS) by centrifugation at 4500g for 5 min followed by resuspention in the same buffer. Afterwards, the nanoparticles were prepared in PBS buffer with concentrations of 50, 100, 200 and 500 μg/ml, mixed 1:1 with erythrocytes and incubated in a waterbath at 37°C for 60 min. After the centrifugation at 2400g for 5 min (Eppendorf mini spin, Eppendorf), the hemoglobin release was determined by the spectrophotometric analysis of the supernatant at 544 nm. The Dextran nanoparticles were used as negative control and the treated erythrocytes with PEI served as the positive control sample. Ultimately, the hemolysis percentage was calculated according to the below formulation:

$$\frac{(Absorption_{sample}-Blank_{sample})-(Absorption_{negative\ control}-Blank_{negative\ control})}{Absorption_{positive\ control}-Blank_{positive\ control}} \times 100\%$$

(Eq. 2-3)

2.3 Result and discussion

2.3.1 Nanoparticle fabrication

Due to the fact that NPs' size has remarkable impact on the nanobio interactions, it is crucial to choose a fabrication method that is successful in terms of monodispersity, stability, compactness and ordered composition over bulk and surface (*52*). To set up a system that can effectively control these properties, we need to account for inter and intra-molecular interactions as well as their strengths (*53*).

One of the easiest ways to control the electrostatic interactions is changing the pH spectrum, which affects the ionic strength of solutions and their impacts on NPs' assembly. We have previously designed a microfluidic system that arrests the NPs' growth when the electrostatic repulsion and hydrophobic attraction forces are balanced as a function of pH (*44*). In addition, convective forces and flow ratio play critical roles in giving the NPs' an ordered pattern both in bulk and the surface (*23, 44*).

Using the unique molecular mechanisms underlying this microfluidic system, the NPs were made from the assembly of cationic chitosan chains modified with the hydrophobic groups of N-palmitoyl with the degree of substitution of 18.2 ± 0.3 mol% (measured by the Ninhydrin assay). Four series of cationic NPs were fabricated: microfluidic fabricated nanoparticles (μF NPs) of 63, 83, and 102 nm as well as the bulk synthesized spheres of 161 nm.

The hydrodynamic diameter of synthesized nanoparticles at various flow ratios has been shown in Figure 2-1a. As can be seen, the time of mixing affect the size of the nanoparticles and size of the nanoparticles increases with increasing flow ratio. It should be noticed that over the whole flow ratio range the microfluidic generated nanoparticles were found to be smaller with narrower size distribution compared to the bulk synthesized nanoparticles. In fact, turbulence and convective mixing in the bulk method cause residence time distributions and consequently broader particle size distribution.

As can be seen in Figure 2-1a, Zeta potential of particles is decreasing with the size enlargement. Such an observation can be interpreted in terms of hydrophobic interactions among aliphatic moieties on chitosan chains. In other words, at low flow ratio and shorter mixing time, hydrophobically modified chains tend to form smaller and more compact nanoparticles formed owing to dominant intermolecular hydrophobic interactions rather than intramolecular interactions. In view of this, the lower flow ratio, the more unsubstituted amine groups are exposed on the surface and consequently the zeta potential increases (Figure 2-1a). As shown in Figure 2-1b, in the FBS media, more protein adsorption on the surface of particles with higher positive zeta potential results in particles

with higher negative zeta potential. Such an effect is more pronounced for the synthesized nanoparticles at lower flow ratios.

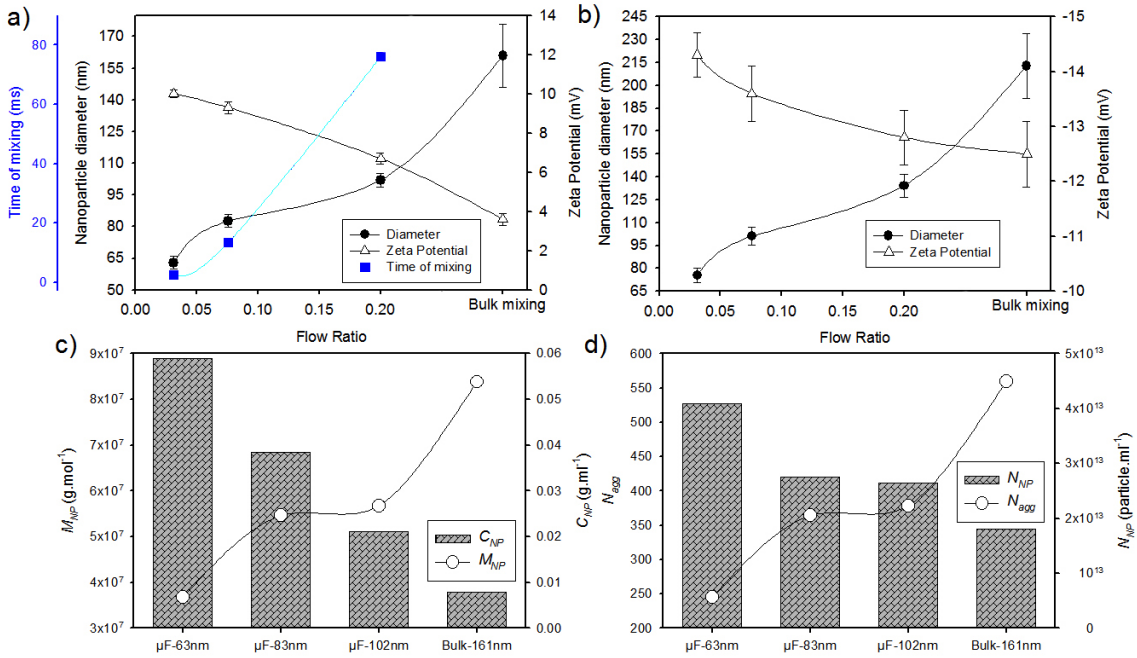

Figure 2-1 The effect of flow ratio on hydrodynamic diameter (Based on the DLS results) and zeta potential of the synthesized NPs in (a) the serum free and (b) 10% FBS containing culture media. The theoretical mixing time is also shown (a) as filled square in blue. (c) The calculated NPs' molecular weight (M_{NP}) and local polymer concentration (C_{NP}) inside the NPs as a function of size. (d) The aggregation number (N_{agg}) of the polymer chains in the corresponding NPs and concentration of NPs (N_{NP}) as a function of size. The lines are guide for the eyes.

The local polymer concentration inside the nanoparticles, c_{NP}, was calculated based on the Equation 2-4, which has been developed for spherical particles (*54*),

$$\tau = \frac{3\,c_t}{2c_{NP}\,R_h}\left(1 - \frac{2}{wc_{NP}}\left\{sin(wc_{NP}) - \frac{1}{wc_{NP}}[1 - cos(wc_{NP})]\right\}\right) \qquad \text{(Eq. 2-4)}$$

where c_t, τ, and R_h are the total polymer concentration, the turbidity of the particulate suspension, and the hydrodynamic radius of particles, respectively, and $w =$

$\frac{4\,\pi\,R_h(dn/dc)}{\lambda\,n_0}$ wherein λ is the wavelength of the turbidity measurements, n_0 is the refractive index of the solvent, and dn/dc is the refractive index increment of the polymer solution.

Generally, the hydrodynamic size of polymeric nanoparticles depends on the aggregation number of chains and their swelling state.

The results for c_{NP} calculated based on nanoparticles' size and their suspension turbidity has been shown in Figure 2-1c. As seen, the compactness of nanoparticles is increased with decreasing flow ratio. At shorter mixing time, higher probability of hydrophobic segments to form intermolecular association leads to formation of more compact nanoparticles. The estimation of compactness revealed that the bulk nanoparticles show lower value compared with the microfluidic nanoparticles synthesized even at the highest flow ratio of 0.2.

Having calculated the c_{NP}, the molecular weight of nanoparticles, M_{NP}, can be determined form Equation 2-5, wherein N_A is Avogadro's number,

$$M_{NP} = \frac{4}{3}\pi {R_h}^3 c_{NP} N_A \qquad \text{(Eq. 2-5)}$$

Accordingly, the number of polymer chains aggregated to form nanoparticles, N_{agg}, can be calculated from Equation 5, where M_n is number average molecular weight of polymer,

$$N_{agg} = \frac{M_{NP}}{M_n} \qquad \text{(Eq. 2-6)}$$

The results for aggregation number for nanoparticles synthesized at various flow ratios as well as bulk nanoparticles have been shown in Figure 2-1d. As can be seen, the number of aggregated chains rises with increasing time of mixing. Such observation suggests that at lower flow ratios and on the account of rapid mixing regime, chains have limited time to aggregate, which results in a lower number of kinetically assembled chains forming nanoparticles. The obtained results for compactness and aggregation number converge to indicate that at low flow ratio smaller and more compact nanoparticles composed of less number of aggregated chains are formed. In view of this, for bulk nanoparticles it could be inferred that the higher hydrodynamic size and lower compactness is due to the arrangement of hydrophobically modified chitosan chains to form intramolecular hydrophobic associations at longer time of mixing.

Although number of nanoparticles in suspension is always of great interest from a practical point of view, but due to measurement complexities is rarely reported. Based on the calculated values for compactness of the nanoparticles, the number density of the nanoparticles, *N*, can be obtained using Equation 2-7,

$$N = \frac{3\ c_t}{4 c_{NP} \pi\ {R_h}^3} \qquad \text{(Eq. 2-7)}$$

As shown in Figure 2-1d, the number density of nanoparticles decreases with increasing flow ratio, which well consistent with the aggregation number results.

2.3.2 Cellular viability

The high molecular weight cationic polyelectrolytes, such as chitosan, may induce an *in vitro* cytotoxicity owing to the possible plasma membrane disruption as a result of the ionic interactions between positively charged surfaces of NPs with the negatively charged membrane phospholipids (*55*). It is notable that regardless of charge density, size and shape, cationic particles are able to form holes in lipid bilayers, a phenomenon that can disrupt the balance between cells' interior and exterior ions and damage other important elements that are required for the maintenance of the membrane's integrity and the normal function of cells (*56*). The cytotoxicity of each NP group with concentrations varying from 10 to 1000 $\mu g.ml^{-1}$ was determined by the MTT cell viability assay. No obvious toxicity was detected, suggesting that these NPs were safe at the mentioned concentrations (Figure 2-2).

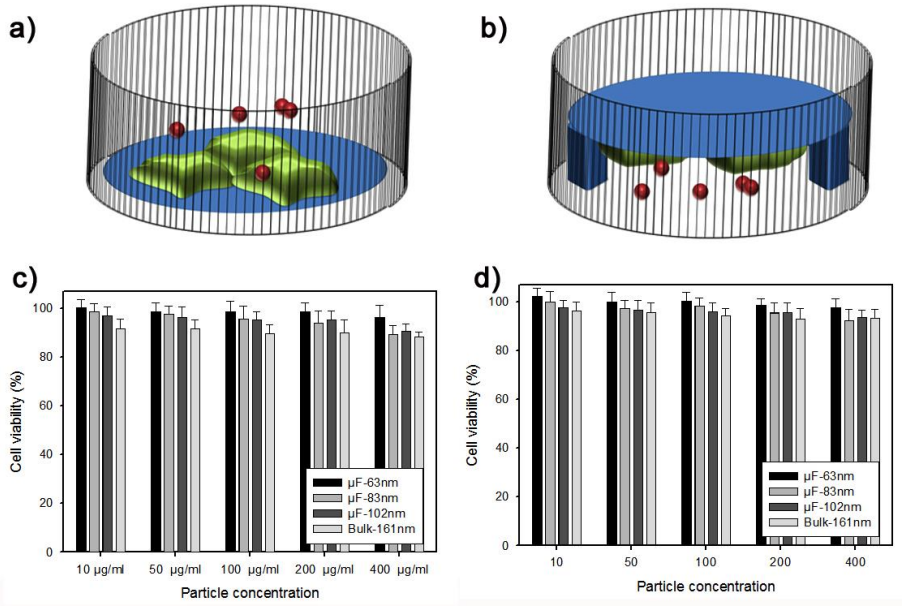

Figure 2-2 Since particles can sink down on the cell surface in an upright configuration, their nanotoxicity nature might change. (a,c) The cells in the upright configuration, which are assumed to experience higher NPs' concentrations. (b,d) The cells in an inverted cell configuration in which NPs' sedimentation occurs at the bottom of the well and results in the concentration reduction of NPs on the cell surface. The disparity between the viability rates for these two positions becomes larger when the sedimentation dominates the diffusion.

One of the kinetic features of NPs is their sedimentation behavior. It means that NPs gradually sink down on cells at the bottom of wells, creating concentration gradients in contact with cells. This growing concentration of NPs within the interaction zone increases the aggregation probability (*38*). Aggregation alters NPs' size, shape and density, leading to NPs' behavior transformations. Here an important question is that whether these aggregates affect cells differently in comparison with single particles.(*57*).

To understand how these aggregates, affect the cell viability, the MTT assay was performed for the invert cell configuration in which the nanoparticle aggregations settle down the bottom of the wells, not at the cell surface. The results show that even though the effects are small, they cannot be neglected, suggesting that the different nanotoxicity levels are due to the different sedimentation and diffusion rates of NPs (Figure 2-2).

2.3.3 Nanoparticles' endocytosis into cells

When NPs meet cells, they walk randomly to search for a suitable interaction site. Doing so, they face three different options depending on the nature of the local membrane and the NPs' ability to start a contact with that membrane: i) they can simply make contact and then move away in a manner that NPs land on the membrane, traverse through the membrane and detach in order to come back to their free diffusing state, ii) they can also touch membrane, adhere to that and stay there, iii) they would strongly attach to the membrane and enter cells (*26*).

Cell membrane re-conformation, parallel with NPs' curvature, costs a certain amount of energy. If some NPs were capable of forming stable bonds at the nanobio interface, which reduces the plasma membrane's Gibbs free energy, they can make the

membrane more prone to grow its contact zone with the NPs' surface, which further balances the resistive and driving forces (Figure 2-3) (*58*). If we assume that all of the driving forces act together to overcome the kinetic barrier, the inability of plasma membrane to reconfigure in a reasonable time scale, the surface chemistry and radius of curvature become the most important factors to consider when designing NPs. The surface chemistry is the first factor dictating the interaction of NPs with a wide variety of proteins, carbohydrates and lipids on the cell surface. The cellular uptake of NPs was measured in HeLa cells after 2 h of NP-cell incubation using CLSM (Figure 2-3, a-d) and FACS (Figure 2-3, g-h). The kinetics of NPs' uptake was also assessed using FACS (Figure 2-3, f). Note that trypan blue worked well for the quench of the FITC fluorescence of the NPs trapped in the extracellular matrix or those bound to the cell membrane but not internalized.

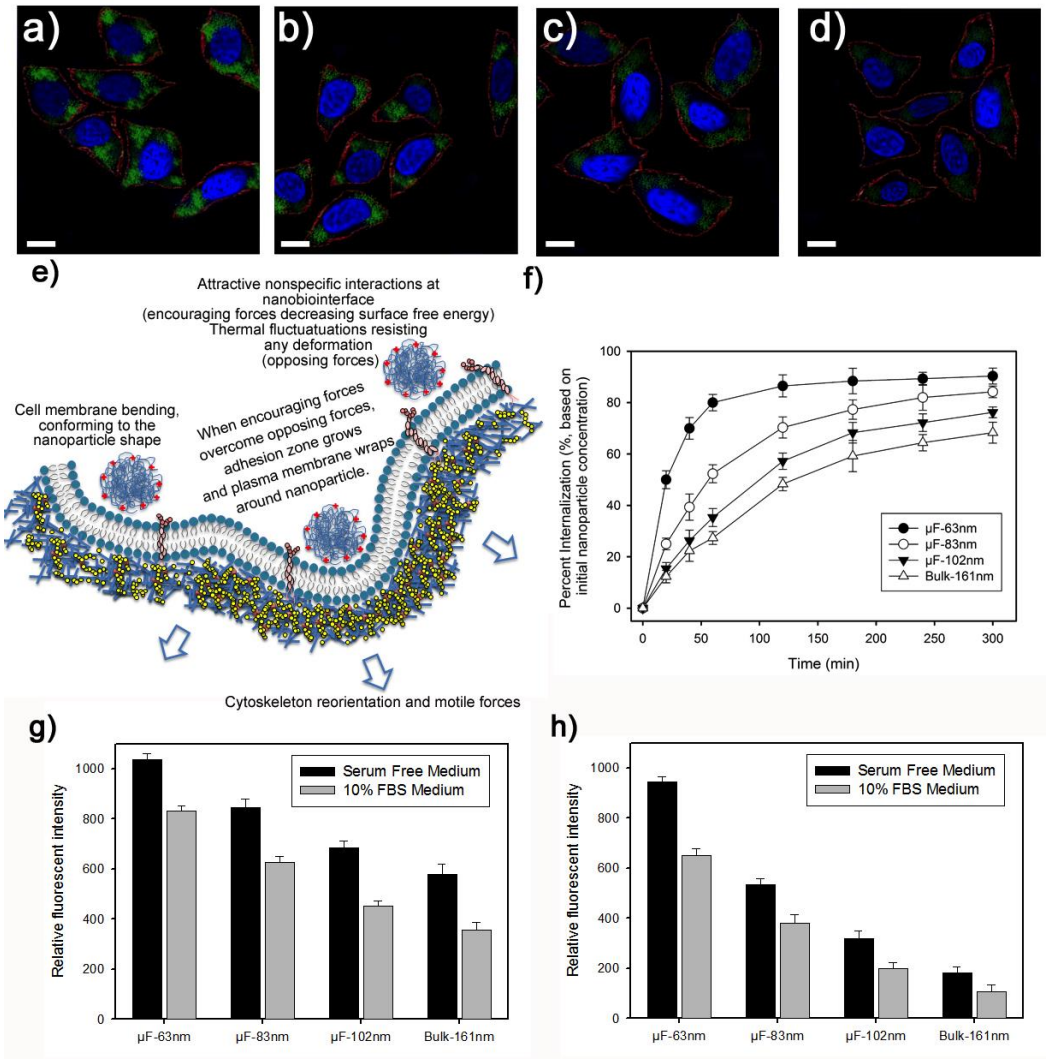

Figure 2-3 The confocal laser scanning microscopy (CLSM) images showing the cellular uptake of the FITC-labeled NPs, μF-63nm (a), μF-83nm (b), μF-102nm (c), and Bulk-161nm (d), after 2 h incubation with the HeLa cells. The cell nucleuses were stained with DAPI (blue). The green dots represent the internalized NPs and the red colors represent the cell membrane. The scale bar is 15 μm. (e) The schematic representation of NPs encountering a cell. Nanobio interactions are a set of specific and nonspecific interactions resulting in Gibbs free energy release. If this energy is large enough to resist the opposing forces (e.g. membrane reorganization process or thermal fluctuations), endocytosis will take place. f) The uptake kinetics of NPs incubated with the upright positioned cells in a serum-free medium. Initially, the NPs start to enter the hungry cells with a high endocytic capability. As the time passes by, the cells reach a saturation point, resulting in a steady state uptake pattern. (g-h) The cellular uptake of NPs incubated in a serum-free (black column) and in a 10% FBS containing culture (grey column) media in the upright (g) and inverted (h) configurations. The corona-coated NPs have a higher tendency for colony formation than the bare NPs. Obviously, the high tendency for settling down will supplement significantly less number of particles in contact with the cells in the inverted position, resulting in the salient uptake disparities in these two cell configurations.

The HeLa cells internalized all of the four groups of NPs, but their internalization kinetics was different. Indeed, less internalization took place for the larger NPs. As shown in Figure 2-3f, all of the NP groups had an increasing internalization rate at their initial stage of incubation. But as time passes by, they reach a plateau pattern, indicating that they reached a thermodynamically equilibrated state at which cells were almost saturated with the endocytosed particles. Since the probability of NPs' exocytosis was not surveyed, this plateau pattern can also be related to the balance between the endocytosed and exocytosed NPs.

In case of nonspecific interactions, NPs' surface charge has a decisive effect on guaranteeing the success or failure of the cellular internalization. For example, for larger NPs with a less surface charge density, weak unspecific interactions with the plasma membrane released less free energy than the amount that was required for the cell membrane reorientation, resulting in reduced cellular uptake.

For *in vitro* assessments, it is assumed that the Brownian motion creates a well-dispersed system in which the concentration is the same for the whole system. But, this assumption is implausible since the inevitable sedimentation phenomenon- settling down of the NPs at the bottom of the well- increases the NPs' concentration on the interaction zone. Depending on the sedimentation to diffusion ratio, this concentration gradient of NPs varies (*38*). For the traditional culture systems with upright configuration, NPs reach cell surface via both diffusion and gravitational sinking or sedimentation. But, when the cells are positioned in an inverted configuration, NPs' transportation takes place only via diffusion. It is obvious that in the upright configuration, the synergic effect of both sedimentation and diffusion results in a higher NPs' concentration in the interaction zone.

However, this concentration decreases when the effect of sedimentation is eliminated in an inverted configuration.

Since the cellular uptake of NPs depends directly on the interactions happening at the cell-particle contact zone (*59*), and considering that the number of particles in contact with the cell surface differs in the upright and inverted configurations, the NPs' internalization was also evaluated in the inverted position. Clearly, decreasing the number of NPs in contact with the cells resulted in the reduced internalization. This reduction was directly related to the diffusive and sedimentation behavior of NPs (Table 2-1).

NPs with high diffusivity can quickly move toward the cell surface before settling down. For these NPs, the difference in the cell uptake for the upright and inverted configurations was less than the uptake difference seen for NPs with a higher tendency for sedimentation rather than diffusion.

In static cell culture conditions, three processes control particles' motion: i) diffusion, ii) sedimentation and iii) advection (*60*). However, advection, which happens as a result of fluid motion, is not very important since culture media's disturbances and thermal fluctuations are too small to have a significant effect on particles' motion.

Table 2-1 ***The nanoparticles' sedimentation and diffusion behavior in the water and 10% FBS-containing culture medium.***

	in water			in 10%FBS containing culture medium		
Sample	Diffusion coefficient[1] $(m^2/s)\times10^{12}$	Drag coefficient[2] $(g/s)\times10^{10}$	Sedimentation coefficient[3] $(1/s)\times10^{11}$	Diffusion coefficient[1] $(m^2/s)\times10^{12}$	Drag coefficient[2] $(g/s)\times10^{10}$	Sedimentation coefficient[3] $(1/s)\times10^{11}$
µF-63nm	7.16	5.98	21.15	5.96	7.19	30.56
µF-83nm	5.44	7.86	15.64	4.45	6.92	23.43
µF-102nm	4.41	9.71	7.30	3.35	12.77	12.64
Bulk-161nm	2.79	15.33	2.58	2.11	20.26	4.50

[1] **Diffusion coefficient: $D=k_BT/6\pi\eta r$**; K_B: Boltzmann constant; T: absolute temperature; η: solution viscosity, r: hydrodynamic radius;

[2] **Drag coefficient: $f=k_BT/D$;**

[3] **Sedimentation coefficient: $S=m(\rho_{NP}-\rho_0)/f\rho_{NP}$**; m: mass of NPs; ρ_{NP}: NPs density; ρ_0: Density of the culture medium; $*\rho_{NP}=\varphi_{NP}(\rho_P-\rho_0)+\rho_0$; ρ_P: Density of the pure polymer; φ_{NP}: Volume fraction of polymer inside the particle

As shown in Figure 2-3f, the smaller NPs with higher potential for diffusion show a remarkably lower uptake difference in upright and invert configurations compared to the larger NPs. Note that for short heights of culture medium, NPs were in close proximity to cells whereas for longer heights only a limited number of NPs could reach cells. Thus, the culture medium volume was another important variable that had to be taken into account (*61*).

When NPs are exposed to biological fluids, they experience surface alterations, one of the most significant demonstrations of which is the formation of biomolecular corona. However, even in serum-free culture media, many proteins are adsorbed on the surface of NPs as a result of NPs' interaction with the cellular secreted metabolites such as cytokines.

To find out how these corona-coated particles affect the cellular uptake pattern, NPs were incubated with the cells in a 10% FBS containing culture medium for two hours. During this incubation, the NPs' surface charge dropped and approached that of the proteins and their hydrodynamic diameter became larger. Protein corona components present on the surface of NPs are of biological origin and some of them are able to start specific interactions with their complementary compartments expressed on the cell membrane. This protein masquerade, regardless of its ability to induce specific interactions, increases the size of NPs while reducing the adhesion power of NPs by eradicating the pristine metastable surface of NPs. Consequently, size enlargement beside lowered adhesion affinity of NPs for binding to cell membrane decreases the amount of cellular internalization (Figure 2-3f) (*59*). Since the surface charge of the particles incubated in the 10% FBS culture medium was not high enough to prevent their aggregation, it negatively influenced the system's stability. These aggregations had lower ability to enter cells.

The main factors affecting the aggregation of proteins are: i) hydrophobic complementarity, ii) electrostatic complementarity, and iii) shape complementarity (*62*). Generally speaking, the electrostatic complementarity is controlled by long-range ordered forces that bring complementary partners together to form specific chemical or physical bonds and associations (*63, 64*). In addition to electrostatic complementarity, hydrophobic mismatching and hydrophobic complementarity bonds have several roles in the processes of protein aggregation as well. Hydrophobic mismatching bonds are formed by the interactions between hydrophobic chains of proteins and lipids (*65*). They are structural, geometrical and curvature couplings with correct and incorrect binding modes. However, because of the high rate of the clustering process, misbinding is not hampered Even the

false complements can be stabilized over time since they will become trapped within the high-rate growing protein aggregations (*62*). As discussed above, protein-coated NPs have a variety of binding chances to form aggregations with high sedimentation coefficients (Table 2-1 and Figure 2-4a). Hence, it is expected that in comparison with the bare NPs, the corona-coated particles have higher uptake differences in the upward and inverted configurations (Figure 2-3, g-h).

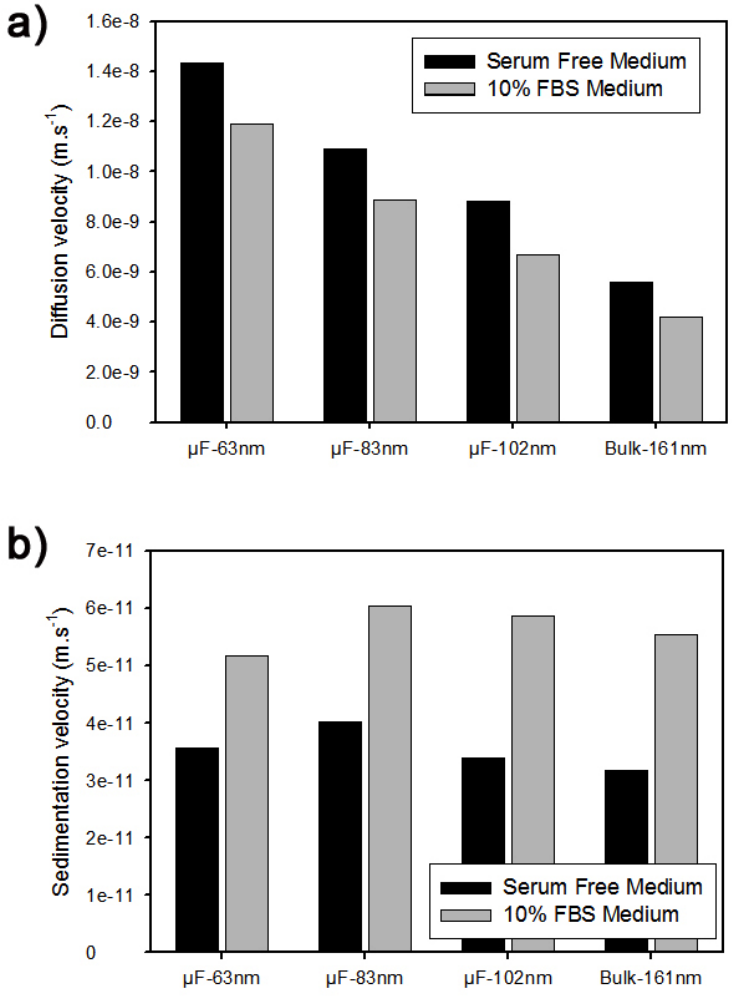

Figure 2-4 The diffusion[1] (a) and sedimentation[2] (b) velocities of the microfluidic and bulk synthesized nanoparticles in the protein free and 10% FBS media. [1]Diffusion velocity: $V_D=2D/x$; x: certain distance of travel (culture medium height); [2]sedimentation velocity: $V_s=2gr^2C_{NP}(\rho_P-\rho_0)/9\eta\rho_P$; g: gravitational acceleration, C_{NP}: NPs compactness.

To investigate the preferential internalization mechanisms of these NPs, the HeLa cells were treated with several pharmacological inhibitory agents, (*66, 67*) which blocked different endocytic pathways (Figure 2-5).

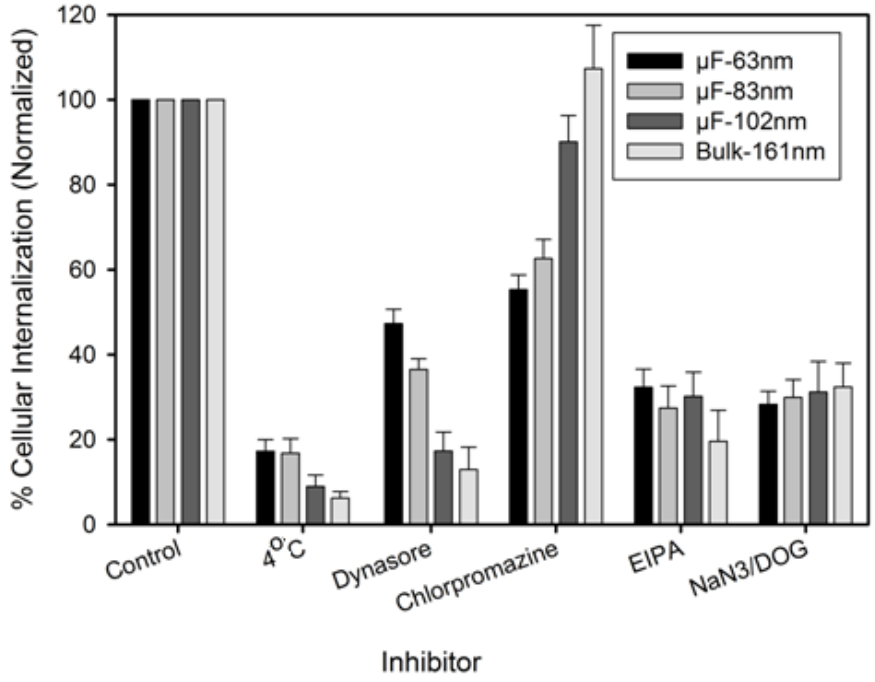

Figure 2-5 The uptake pattern of the NPs incubated with the cells treated with the pharmaceutical inhibitory agents.

To explore whether the endocytosis occurred actively (ATP driven) or passively (no cell machinery involvement during the internalization), the cells were pre-incubated with NaN3/2-deoxyglucose (NaN3/DOG) at 37°C to block the ATP synthesis by inhibiting the mitochondrial respiration (*31*). As a result, a noticeable decrease in the uptake was seen for all of the NP sizes emphasizing on the bold role of energy dependency. But some of the NPs were still localized in the cells even in the absence of ATP. This finding can be attributed to the presence of ATP and glucose in the serum-free medium. There is also the

likelihood of NPs' passive internalization. As NPs are absorbed on lipid bilayers, they locally reconstruct the plasma membrane, which enables NPs to diffuse or slip over lipid bilayers. NPs may prefer the microdomains of lipid bilayer called lipid rafts, where the liquid-ordered and liquid-disordered states of phospholipids coexist. These domains have more diffusion potential in comparison with other sites of the plasma membrane (*68*). All in all, NPs have shown different affinities for diffusion corresponding to their site of landing because different sites of the membrane show different viscosities with different diffusive states (*69, 70*).

To further study the NPs' diffusion via the plasma membrane, the internalization experiments were repeated again at 4°C where the active uptake is totally stopped (*31*). The uptake of NPs under this circumstance suggests that a small fraction of these NPs are able to directly slip through the cell membrane via diffusion. However, potential changes in the membrane fluidity and structure as a result of incubation at 4°C is unavoidable, which reduces the ability of the plasma membrane to bend. Since the passive internalization of the larger NPs requires higher degrees of local reconstruction in comparison with the smaller ones, the decreased flexibility of the cell membrane as a result of the 4°C incubation leads to a salient decrease of the larger NPs' uptake (6.2 ±1.5% for 161 nm and 9.0 ±2.7% for 102 nm particles) in comparison with the smaller particles (16.8 ±3.5 for 83 nm and 17.3 ±2.7 for 63 nm particles).

The ingestion of particles and fluids via endocytosis and micropinocytosis requires the formation of large endocytic vesicular compartments within cells by coordinated movements of the membranes and the actin cytoskeleton (*29*). Blocking the metabolic generation of protons during the actin polymerization can effectively impede the F-actin

polymerization. Na^+/H^+ exchangers exchange these protons with externally located Na^+ ions. Blocking this exchanging process results in an environmental acidification caused by H^+ accumulation, which stops further polymerization of the actin filaments. Amiloride and its family members, such as EIPA, are candidate inhibitory agents working on the basis of environment acidification by acting as general inhibitors of all the internalization pathways that are dependent upon the F-actin rearrangement. But this group of inhibitors can also cause cell-matrix dissociation, which is a serious side effect (*66*).

Micropinocytosis, the most occurring mechanism among the internalization pathways, attenuates as a result of actin polymerization blockage (*67*). Micropinocytosis is responsible for the internalization of large particles. But, if NPs' size becomes larger than the punctuate anchoring sites of the cytoskeleton, micropinocytosis will vanish because spreading of the cell lamellipodia around such particles will create local stresses, making the internalization process less functional (*71*). As a result of the actin polymerization blockage, the 161-nm particles experienced the largest decrease in internalization amount, 19.6 ±7.3% (Figure 2-5). The art of the cytoskeleton to bend the cell membrane in order to reorient it to particles' curvature, is one of the key steps in the endocytosis, which can be blocked by the F-actin polymerization obstruction. A certain amount of energy is required to make the cell membrane bend. For larger NPs, a greater amount of energy is required in order to reorganize the plasma membrane. As it was expected, the EIPA treatment reduced the NPs' internalization to 32.3 ±4.2, 27.4 ±5.2 and 30.2 ±5.7 for the 63, 83 and 102-nm particles, respectively (Figure 2-5).

One of the most studied mechanisms of endocytosis is clathrin-mediated pathway during which clathrin and other accessory proteins are clustered at the site of the coated pit

followed by the membrane bending around NPs. This bent region is connected to the flat region of the plasma membrane via a small neck that ultimately undergoes fission from the plasma membrane. This process is catalyzed by the ring-shaped assembly of the GTPase dynamin at the neck of the budding vesicle. The ruptured point is quickly healed completely (*29*). But, the clathrin endocytosis is not the only mechanism that benefits from the GTPase activity of dynamin. There is also another endocytic pathway based on the action of the wedge-shaped scaffolding proteins present on the plasma membrane. These proteins are called caveolins. They require the formation of dynamin helical structures to separate assembled vesicles, caveosomes, from the cell membrane (*69*).

To investigate the share of dynamin action in the uptake of NPs, the cells were treated with dynasore, which inhibits the GTPase activity of dynamin. In other words, dynasore can be considered as a chemical that inhibits the completion of both caveolae and clathrin- dependent endocytic pathways. Inhibiting the dynamin lets the cell membrane spread over the NPs with no splitting of the formed vesicles. As a result of the dynasore treatment, the NPs' internalization decreased to 47.3 ±3.4, 36.5 ±2.5, 17.3 ±4.5 and 12.9 ±5.3 for 63, 83, 102, and 161-nm particles, respectively. Moreover, we incubated the cells with a specific inhibitory agent of clathrin pathway to compare the results with those of the dynasore treatment to find out how the NPs' properties led them to prefer clathrin or caveolae mechanisms. As previously mentioned, the clathrin-mediated mechanism is one of the prominent pathways of uptake in which triskelion clathrin proteins act as key players of the scenario. The proportion of this mechanism in the uptake process is of great importance due to the presence of the dominant-negative proteins that specifically interfere with the clathrin-mediated endocytosis(*72*). This phenomenon is of particular interest since

our NPs are positively charged and it is expected that non-specific attraction forces can act as strong amplifiers of the cellular uptake.

To investigate the share of the clathrin pathway, the cells were pre-incubated with chlorpromazine, a cationic amphipathic molecule with a strong affinity for lipids (*73*). The resultant attraction force between chlorpromazine and lipids alters lipid fluidity within the plasma membrane. The physical state transformations of lipid constituent of the cell membrane can weaken the cell membrane ability to form invaginations. This inability leads to the clathrin-adaptin protein2 complex dissociation.

Although chlorpromazine acts specifically to block the clathrin-mediated pathway, the possible interactions of chlorpromazine with the cytoskeleton cargos or intracellular lipids may lead to undesired side effects, such as increasing the membrane's permeability. To avoid such negative outcomes, choosing the optimum concentration of chlorpromazine is of great importance.

55.3 ±3.4% of 63-nm particles were internalized after the pre-incubation of the cells with chlorpromazine. When the cells were treated with dynasore, 47.3 ±3.4 percent of these NPs were internalized. This result means that the 63-nm particles have a higher tendency to be internalized via the clathrin pathway in comparison with the caveolae pathway. This phenomenon can be due to the 63-nm NPs' higher cationic nature. Variable specific and non-specific adhesion strengths critically control the cellular uptake. This binding energy drives the process of membrane spreading over NPs, but the plasma membrane's bending rigidity and thermal fluctuations act against the deformation. If the encouraging forces are

large enough to overcome the opposing forces with respect to the free energy balance, the adhesion areas between cells and NPs grow and lead to a successful uptake (*58*).

For the 161 and 102-nm particles (107.3 ±10.2 and 90.1 ±6.2 respectively), a significant difference (Nearly 94 and 73% in the order that already mentioned) in the internalization amount in the dynasore and chlorpromazine treated cells was observed, showing the dominant maneuver of the caveolae-mediated internalization pathway.

It should be noted that a substantial number of accessory proteins take part in different routes of the endocytosis. The molecular compartments of some of these endocytic mechanisms may overlap. Accordingly, the inhibitory effects of the chemicals employed are not restricted to a defined internalization pathway.

2.3.4 EPR: The advanced state of NPs' extravasation art

Enhanced Permeation and Retention (EPR) effect is a crucial pharmacokinetic attribution of nanomedicine. Due to the derivation of tumor blood vessels from normal vessels present in healthy tissues, the normal neighboring vessels could affect some of the tumor blood vessels' properties, such as their cut off size, which varies with tumor type, growth location, and progression stage. For a single tumor, vessels' pore size distribution is highly heterogeneous, which should be carefully taken into consideration for designing nanomedicine tools. This pore size distribution also varies with orders of magnitude among different types of solid tumors from a few nanometers in the brain and pancreatic tumors to a few micrometers in some kinds of breast cancer (*74*).

There are several complications in the crosstalk between NPs and cells in tumor microenvironments. In addition to vessels' pores, the interstitial environment of tumors, mainly composed of the collagen and hyaluronan, have rough barriers with pore diameters ranging from a few to hundreds of nanometers. These barriers can cause steric hindrances on the way of NPs to central parts of the tumors (*75*, *76*). Thus, it is logical to consider NPs' size and diffusive behavior as a determinant factor in their interstitial trafficking.

For each nanoparticle size, there is an ideal pore size for which transvascular flux reaches its maximum level (*77*). As the size difference between NPs and vascular pores gets smaller, steric, hydrodynamic and electrostatic forces act more synergetic to either facilitate or hinder NPs' extravasation. In addition, the pressure gradient across vessels' walls acts as an encouraging parameter under these conditions. But, when the pores become larger in comparison with NPs, the dominant forces, which were described earlier, vanish. Likewise, the pressure gradient also disappears, leaving diffusion as the only mechanism of entrance (*77*).

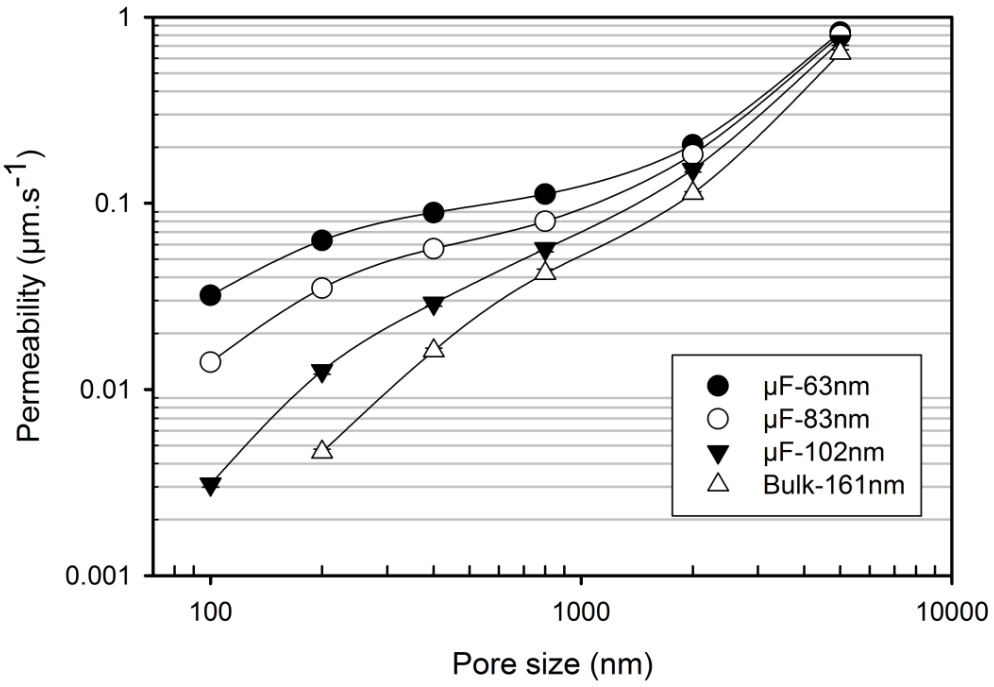

Figure 2-6 The NPs pass through the membranes with different pore sizes.

Thus, we can conclude that there must be an optimal ratio of nanoparticle size to vessel pore size where both diffusion and convection act synergetic for a successful extravasation process. For a definite nanoparticle size, there is an amount of surface charge density above which electrostatic forces are strong enough to dominate opposing forces, leading to an increased extravasation. But, if the vascular pore size becomes significantly smaller, steric and hydrodynamic forces become powerful barriers against which high surface charge cannot resist (*77*). It is noteworthy that there are two upper and lower extremes, above and below which, electrostatic forces do not have a key role in NPs' extravasation. These two extremes happen when the pore size is significantly smaller or larger than NPs' sizes. In order to simply study the extravasation behavior of our NPs, we used the 4-20% porous polycarbonate membranes with different pore sizes. As shown in Figure 2-6, when the membrane pore size is nearly equal to the size of NPs, the steric

hindrance results in a lower extravasation of the smaller NPs. when the pore size becomes larger than the NPs' size, the behavior of NPs becomes independent of the pore size in which all of the NPs show the same extravasation pattern.

2.3.5 Nanoparticles touching Red Blood Cells (RBCs)

The blood components are the first elements that NPs encounter when they are injected into the blood. To find out how wildly NPs act after they contact the blood elements, we studied erythrocytes' hemolysis when they were incubated with the NPs. We chose PEI as positive control since free PEI results in the necrotic cell death due to its ability to damage erythrocytes' membrane integrity at the very first stage of contact. Dextran was selected as negative control due to its reputation for blood compatibility.

The toxicity magnitude of NPs depends on their concentration and their time of incubation with cells. Fischer et al. demonstrated the cationic charge density as a key parameter directly affecting the magnitude of cell damage (*43*). Accordingly, higher surface charges resulted in higher degrees of hemolysis. In addition, concentration increment also led to more intense cellular damages. The 63-nm particles had the highest potential for the erythrocytes damage, but their offensive effects, even at high concentrations (e.g. 500 μm), was less than 11.5%, indicating that these NPs are safe for injection (Figure 2-7).

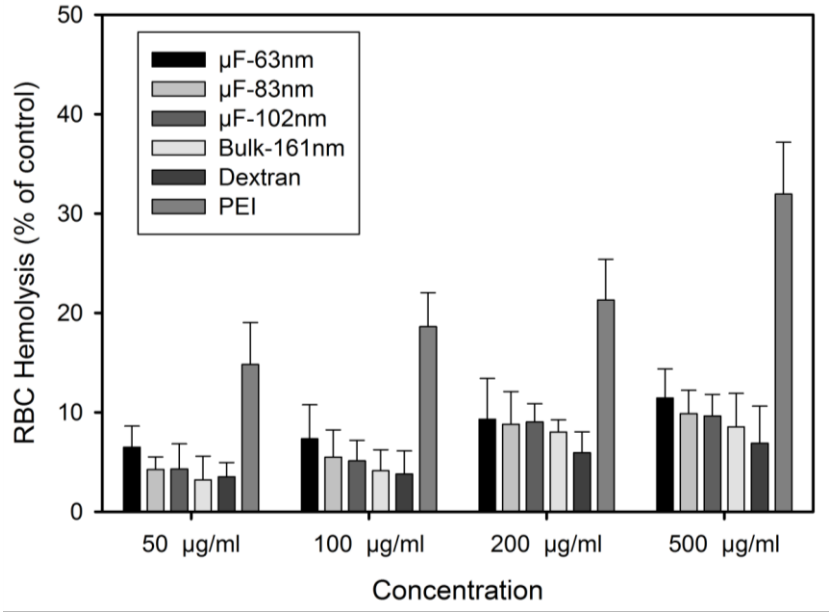

Figure 2-7 The NPs incubated with the RBCs. The higher concentrations and higher charge densities of NPs increased the damages to the RBCs.

2.4 Conclusions

Generally, NPs that are able to enter cells and release their therapeutic contents in close proximity to intracellular machineries have a bright future in the field of nanomedicine. Size and surface charge of these nanoparticulate systems strongly tune their nanobio interactions. In the current study, we evaluated the role of NPs' size-surface charge interplay in dictating their cellular internalization. Furthermore, the role of biomolecular corona surrounding the NPs upon entering the biological fluids was also investigated. To date, almost all of the cellular studies on NPs have been carried out with cells positioned in the upright configuration, which may add errors to final results, depending on the NPs diffusion to sedimentation ratio. We conducted our experiments for the cells in both the upright and inverted configurations to show how disparities can vary depending on the concentration of NPs in the interaction zone. Altogether, these results are expected to

provide a paradigm for explicating the nanobio interactions happening when NPs face cells and other complicated biological components.

CHAPTER 3. MICROFLUIDIC MANIPULATION OF CORE/SHELL NANOPARTICLES FOR ORAL DELIVERY OF CHEMOTHERAPEUTICS: A NEW TREATMENT APPROACH FOR COLORECTAL CANCER [2]

Conventional chemotherapy systems are normally administered by injection that may introduce significant concentrations of toxic drugs systemically. To address that we demonstrate an efficient tumor targeting nanoparticulate drug delivery system, designed as oral administration for cancer therapy. For the first time, a dual microfluidic platform has been employed to synthesize nanocarriers with highly pH-tunable core-shell structure. These nanocarriers consist of a fine-tuned self-assembled polymeric core precisely coated with a sacrificial pH-responsive layer fabricated via a microfluidic device with two discrete mixing steps. The sacrificial shell protects the core layer with drugs, which encapsulated in the core layer, and prevents their release in severe pH conditions of the gastrointestinal tract, while allowing for drug release in the proximity of a tumor. Quantum and molecular dynamic simulations were performed to investigate molecular interactions governing behavior of the core-shell system. The release profile and cytotoxicity of the nanoparticles (loaded with paclitaxel, PTX) against Caco-2 cell line were studied using sequential incubation in different pH conditions. The obtained results revealed a PTX release profile highly dependent on environmental pH. This microfluidic approach is a new way for efficient chemotherapeutic delivery systems to deliver more potent therapeutics to the

[2] *This work has been published by M.M. Hasani‐Sadrabadi, S. Taranejoo, E. Dashtimoghadam, G. Bahlakeh, F.S. Majedi, J.J. Van Dersarl, M. Janmaleki, F. Sharifi, A. Bertsch, K. Hourigan, L. Tayebi, P. Renaud, K. I. Jacob (2016) Advanced Materials 28 (21), 4134-4141. Reproduced by permission of Wiley-VCH.*

target site. Such advancements in oral administration routes promise ‘chemotherapy at home’ for future cancer care.

3.1 Introduction

Colon cancer is one of the most prevalent cancers today that is affecting people at an increasing rate. Currently, the lifetime risk of developing colon cancer runs at 5-6%.(*78, 79*) Considering the growing rate of colorectal cancer, considerable scientific effort has been applied to find effective therapeutic approaches.(*80-82*) During the conventional route of chemotherapy, influencing of non-tumor cells and hence involving normal tissues/organs are unavoidable. Due to these side effects, the contribution of cytotoxic chemotherapy in cancer survival is limited. Nanoparticulate drug delivery systems make the chemotherapeutic approaches more selective with less off-target toxicity. A central challenge in nanomedicine is fine design of nanoparticles for their desired physicochemical properties in a reproducible manner. A significant part of this research has been focused on developing smart targeting drug delivery systems, to both minimize side effects and increase drug efficacy.(*83-86*) Oral drug delivery is an important administration pathway as it improves patient compliance and is self-administrable, which allows for more regular dosing schedules at a lower cost. Oral chemotherapeutics can also lead to lower toxicity and improved efficacy.(*87-90*) Due to the pH variations in the gastrointestinal tract during oral drug administration,(*91-93*) employing pH sensitive polymers as carriers can result in more specific chemotherapeutic delivery for cancer therapy.(*91-99*) Polymers and copolymers such as methacrylic acid (MAA) and methylacrylate (MA) or ethylacrylate (EA) are typical pH responsive polymeric materials employed in the preparation of extended release oral administered drugs for cancer therapy.(*98, 100, 101*) These copolymers are insoluble at low pH but dissolve at high pH, triggering the encapsulated drugs or inner core to be released.(*101*) Despite recent advances in chemotherapeutic delivery systems for colon cancer, most researches have focused on conventional bulk

mixing, which results in polydisperse nanoparticles (NPs).(*99, 102, 103*) However, attaining more precise drug release profiles requires a reproducible approach to fabricate finely-tuned nanocarriers with a narrow size distribution and predetermined properties. We have recently introduced a microfluidic technique to synthesize monodisperse chitosan based NPs for cancer therapy applications.(*99, 103*) Compared to bulk mixing producer, microfluidic systems can synthesize the nanoparticles in a well-controlled, reproducible and high-throughput manner. Moreover, microfluidic systems, by mixing dissimilar materials (with distinct functional groups) at varying ratios, provide a solution for the challenge of finding right formulation for delivering therapeutic agents to specific sites in the body.

Chitosan derivatives are widely used in drug delivery applications due to their outstanding biological characteristics.(*104*) Here we employ a hydrophobically modified chitosan derivative, N-palmitoyl chitosan, to improve the loading of hydrophobic anticancer drugs.(*20*) Moreover, N-palmitoyl chitosan chains allow for NPs to be shaped via self-assembly, avoiding problems related to the removal of chemical crosslinking agents.(*23, 99, 105*) Microfluidic platforms, benefiting from a controlled mixing regime, provide adjustable drug encapsulation efficiency and release rate from self-assembled hydrophobically modified chitosan (HMCS).(*52, 99, 103*) In this study, we used microfluidic techniques to design well-controlled monodisperse HMCS NPs coated by a pH-responsive layer (Eudragit FS 30D) with an adjustable thickness. The NPs behavior was assessed as they were exposed to variant pH conditions that simulate the digestive tract environment. Quantum mechanics (QM) and classical molecular dynamics (MD) simulations were also performed to investigate the molecular interactions governing the behavior of the chitosan-Eudragit layered system.

3.2 Experimental

3.2.1 Materials

Chitosan with a deacetylation degree of 84% was purchased from Pronova Biopolymers. Size-exclusion chromatography measurements revealed a weight-average molecular weight (M_w) of 400 kg.mol^{-1} and a polydispersity index (M_w/M_n) of ~2.7. The hydrophobic modification of chitosan was accomplished through the reaction of amino groups on the biopolymer chains with a palmitic acid N-hydroxysuccinimide ester (Sigma–Aldrich) in absolute ethanol. The substitution of C_{15} aliphatic groups on the chitosan backbone was confirmed by ^{1}H NMR spectroscopy (Bruker 400 MHz). The details of the modification procedure and characterization methods have been described elsewhere**.**(*99*) Eudragit (FS 30D), a pH sensitive derivative of PMMA, was purchased from Evonik Industries.

Ninhydrin assay was employed to determine the substitution degree of the hydrophobically modified chitosan (HMCS) samples.(*99*) In brief, a solution was prepared through adding 0.5 mL of 4 M acetic acid/acetate buffer (pH= 5.5) into the same volume of an aqueous acetic acid solution of HMCS. Adding 1 mL of ninhydrin reagent (Sigma-Aldrich), the test tubes were incubated in a boiling water bath for 20 min, followed by cooling the solutions at ambient temperature. Absorbance intensity was assessed at 570 nm using Shimadzu UV mini-1240 UV-vis spectrophotometer while employing unmodified chitosan solution and the acetic acid/acetate buffer solution as the control and blank samples, respectively. According to this assay method, value of 18.2 ± 0.3 mol% was obtained as the degrees of hydrophobic substitution for HMCS.

3.2.2 Microfluidic device fabrication

Microfluidic chips were fabricated at the EPFL Center for Micronanotechnology (CMi)with PDMS (Sylgard 184, Dow Corning, Switzerland) *via* soft lithography method. Silicon wafers spin-coated with SU-8 photocurable epoxy to a thickness of 60 μm on the

normal 4 inch silicon wafer and then baked. Conventional photolithography is used to fabricate master that contains patterned relief structures on the surface in the clean room.

The surface of molds was modified using trimethylethoxy silane (Sigma) as self-assembled monolayer to prevent PDMS sticking. PDMS resin and its curing agent (10:1), poured over the patterned master mold, degassed in desiccators, and baked in the oven. After curing, PDMS was removed from the wafer and the holes were punched. The PDMS was then bonded to a glass slide after oxygen plasma activation (100 mW, 1 min; Diener electronic GmbH). Each of microfluidic devices consists of three inlets and one outlet. Fluorescent flows were used to determine the range of stable flow rates.

3.2.3 Synthesis of HMCS nanoparticles

The PDMS microfluidic device (μR1) had two inlets for basic water (pH of 9) as precipitation agent, one for the aqueous solution of HMCS with the pH of 5.5, and one outlet. The water stream was split into two, in order to achieve two lateral water streams at the same flow rate. The mixing channel was 150 μm wide, 60 μm high and 1 cm long.

For bulk synthesis of nanoparticles, polymeric solutions were prepared by dissolving HMCS (2.5 $mg.mL^{-1}$) in acetic acid solution (1% w/v) under constant stirring. The precipitation of HMCS molecules and formation of the nanoparticles were performed by dropwise addition of 1M NaOH to adjust the pH to 7.4. For drug loaded nanoparticles, Paclitaxel (Sigma-Aldrich) was dissolved in acidic water (pH 4.5) and mixed with the polymeric solution. The preparation of nanoparticles was performed as described above.

3.2.4 Coating HMCS nanoparticles with Eudragit

The Tesla micromixer (μR2) consists of two inlets for Eudragit FS 30D (0.2 wt%) in ethanol/ deionized water solution as coating polymer, one for the aqueous solution of HMCS nanoparticles at 1 $mg.mL^{-1}$, all at the constant pH of 6.5, and one outlet.

3.2.5 Characterization of nanoparticles

The size and size distribution of the prepared NPs at pH 7.4 were investigated using dynamic light scattering (Zetasizer 3000HS, Malvern Instruments Ltd., Worcestershire, UK). To characterize the shape and size of the prepared NPs, transmission electron microscopy (TEM; CM200-FEG-Philips) was employed. First, dilute suspensions of the NPs samples were deposited onto the Cu grid with a carbon film, and the instrument was operating at 100 kV accelerating voltage. ImageJ software was employed to analyze the obtained images.

To study the effect of pH and immersion time on the structure and size of the NPs, 2 mg of NPs were immersed in 1 ml of PBS media when applying sequential change in buffer pH (4, 7.4, and 5.5) in consecutive time intervals (0-5, 5-12, and 12-30 h, respectively). At predetermined time intervals, samples were collected and measured using dynamic light scattering as stated before.

The core-shell nanoparticles were washed and then suspended in the simulated gastric fluid (SGF). SGF was prepared by dissolving 2 g sodium chloride and 3.2 g purified pepsin in 7 ml of hydrochloric acid and diluted with water to 1000 ml. The pH of the test solution was 1.2 (*106*). The size of nanoparticles was measured as a function of time using DLS. By changing the media after washing of nanoparticles, the hydrodynamic diameter of nanoparticles were measured in the simulated intestinal fluid (SIF). SIF was prepared by dissolving 68.05 g potassium dihydrogen phosphate (KH_2PO_4) and 8.96 g sodium hydroxide in 10 L water. The pH of this solution was 6.8 (*106*). The size of nanogels was determined in their equilibrium swelling state by DLS method.

3.2.6 Cell uptake, CLSM and Fluorescence activated cell sorting (FACS) studies

The cellular uptake of FITC-labeled nanoparticles (f-NP) was measured using Fluorescence activated flow cytometry (FACS) on a CyAn^{TM} ADP Analyzer (Beckman Coulter, Inc). For the FACS analysis, human epithelial colorectal adenocarcinoma (Caco-2) cells (10^6 cells) were dispersed into Eppendorf tubes. The NPs pre-processed in different pH separately before being added to the cells for the internalization experiments. Then, f-HMCS NPs were added at concentration of 100 $\mu g.mL^{-1}$, except for the unstained negative control, and the cells were incubated for 2 h in normal medium in a standard tissue culture incubator (37°C in a 5% CO_2). The cells were then washed using ice-cold PBS containing 10% FBS, and transferred into FACS tubes. All samples were kept on ice until FACS analysis.(*99*) The same experiments also performed on human cervical carcinoma epithelial (HeLa) and MCF-7 (Michigan Cancer Foundation-7) breast cancer cell lines.

For microscopy, 10^5 cells per well were seeded on round glass cover-slips in 12-well plates. Once reaching 80% confluency, the growth media was aspirated and 400μL of f-NPs in PBS was added to each well, at concentrations of 0.2 μM. Cells were then incubated for 2 h at 37°C and 5% CO_2 at different pH levels. Then, samples were washed five times with PBS and fixed them with 3% paraformaldehyde solution, cell nuclei were stained with DAPI (0.2 μM). Fluorescent microscopy measurements were performed using a ZEISS LSM700 UP2 (Jena, Germany) confocal laser scanning microscope (CLSM).

3.2.7 Cell proliferation assay

Effect of different NP concentrations on the cell proliferation was evaluated by MTT assay. In brief, Caco-2 and MEF cells were cultured on standard 96-well plate at a density of 10^4 cells per well. After incubating for 24 h, the culture medium was replaced by fresh medium containing specific concentrations of uncoated and coated NPs (50-800 mg/ml) and

incubated for 72 h. Then, tetrazolium salt (M2128, Sigma) was added for an additional 4 h. Thereafter, formazan crystals were dissolved in Dimethyl sulfoxide (Sigma) while shaking for 20 min. Absorbance at 570 nm was measured by utilizing a standard microplate reader.

3.2.8 Drug encapsulation and in vitro *release*

In vitro drug release from PTX-loaded NPs was studied using a dialysis cassette (3500 MWCO, Thermo Scientific) immersed in PBS. Briefly, 1 ml of PTX-loaded NPs suspension in phosphate buffered saline (1 $mg.ml^{-1}$) PH 7.4 was introduced into the dialysis cassette, then gently shaken and incubated at a temperature of 37°C. A Sequential pH change (4, 7.4, and 5.5) in PBS medium was applied. The pH of PBS medium was kept constant at 4 in the first 72 h, then was increased to 7.4 for simulating human intestinal fluid in the next 72 h interval, and finally reached to 5.5 and remained without any further change for the third similar time interval. Samples were periodically removed and studied using high-performance liquid chromatography (HPLC). 2 ml mixture of sample and acetonitrile in a same portion was assessed. Separation procedure was done at a constant flow rate of 1 $ml.min^{-1}$, followed by PTX detection at a wavelength of 230 nm. In this study, a reverse phase C_{18} column and a mixture of acetonitrile:water (60:40 v/v) were employed as the stationary and mobile phases, respectively.

To eliminate the sampling effect during release tests, drug concentration was corrected according to following equation (*99*):

$$C_n^{\,l} = C_n[V_T/(V_T-V_S)](C_{n-1}^{\,l}/C_{n-1}) \qquad \text{(Eq. 3-1)}$$

where $C_n^{\,l}$ is the corrected concentration of the n^{th} sample, C_n is the measured concentration of PTX in the n^{th} sample, C_{n-1} the measured concentration of the $(n-1)^{th}$ sample, V_T is the volume of receiver fluid, and V_S represents volume of the drawn sample (1 mL).

3.2.9 Statistical analysis

For statistical analysis SigmaPlot software (version 11.0) was used. Data are presented as mean values ± SD. Comparison of two groups was performed by unpaired or paired t-test, while comparison of more than two groups was performed using ANOVA. Differences were considered significant at $p < 0.05$.

3.2.10 Fluidic Modeling

In this simulation, two dimensional modeling of a Tesla micromixer with ten individual mixer units is carried out using COMSOL Multiphysics 4.2. Continuity and Navier-Stokes equations along with Convection-Diffusion equation are solved using finite element method for this geometry. Equations of continuity and momentum for steady state and an incompressible fluid as follows:

$$\nabla.\vec{u} = 0 \qquad \text{(Eq. 3-2)}$$

$$\rho\vec{u}.\nabla\vec{u} = -\nabla p + \mu\nabla^2\vec{u} \qquad \text{(Eq. 3-3)}$$

where $\vec{u}$ is fluid flow velocity, ρ is fluid density, μ is fluid dynamic viscosity and p is pressure. In this study, all fluid properties are assumed to be equal to those of water, i.e. density of 1000 kg/ m^3, and a viscosity of 0.001 Pa- s.

The micromixer has three inlets and one outlet. The inlet boundary condition is defined as:

$$\vec{u} = U_0 \cdot \vec{n} \qquad \text{(Eq. 3-4)}$$

where U_0 is the free stream velocity which is assumed to be 9.26 10^{-4} and 0.003704 m/s for main and both sheath flows, respectively. Outlet boundary condition is set to be at the atmospheric pressure. It is assumed that no slip boundary condition is applied on the remaining walls. The mass transport equation is

$$\frac{\partial C}{\partial t} + \nabla.\vec{N} = 0 \qquad \text{(Eq. 3-5)}$$

where $\vec{N}$ is the flux vector defined as:

$$\vec{N} = -D\vec{\nabla}C + C\vec{u} \qquad \text{(Eq. 3-6)}$$

In the above equation, D denotes diffusivity and C is concentration. Also, the inlet boundary condition for concentration is approximated by a concentration of one in both sheath flow and the diluents with a concentration of zero in the main flow inlet.

Tesla mixer uses Coanda effect in order to bend fluid stream lines and increase mixing effects. As flow enters the micromixer, part of it deflects toward the side narrow channel due to Coanda effect. The remaining part of fluid flows through the curved- section until these two sub-flows join and integrate again. Then this recombined flow again experiences another Coanda effect and this separation and mixing continues until the flow reaches the outlet.

3.2.11 Computational details

In order to fundamental understanding of Eudragit coated chitosan constituting core-shell nanoparticles at molecular level, first principle quantum mechanics (QM) and molecular dynamics (MD) simulations were carried out to explore their molecular interactions governing behavior of Eudragit-chitosan layered system.

3.2.12 First principle simulations

First principle QM simulation methods were applied for three molecular systems including Eudragit, chitosan, and Eudragit-chitosan cluster. QM simulations were specifically utilized to assess the intermolecular interaction energy between Eudragit and chitosan, which determine their affinity to each other. The interaction energy ($\Delta E_{binding}$) between Eudragit and chitosan was computed by using the following equation:

$$\Delta E_{binding} = (E_{Eudragit\text{-}chitoasn} - (E_{Eudragit} + E_{Chitosan}) \quad \text{(Eq. 3-7)}$$

where, $E_{Eudragit\text{-}chitoasn}$ is the electronic energy of molecular system consisting of Eudragit and chitosan polymers, and $E_{Eudragit}$ and $E_{Chitoasn}$ represent electronic energy of molecules Eudragit and chitosan, respectively.

Molecular structures for Eudragit and chitosan polymers are shown in Figure 3-1. It is known from Eudragit chemical structure that the ratio of ester groups to carboxyl groups (i.e., the *x* plus *y* to *z* ratio) is 10:1. Due to the highly expensive computational time of QM calculations, only one monomeric unit of Eudragit and chitosan was chosen for QM evaluations involving Eudragit, chitosan and Eudragit-chitosan cluster model. In particular, because of such time-consuming QM computations, it was difficult for the case of Eudragit monomer to preserve the mentioned 10:1 ester groups to carboxyl groups ratio at electronic-structure calculation scale. Consequently, for Eudragit structure, QM examinations were executed on Eudragit monomer containing only single unit of methyl acrylate, methyl methacrylate and methacrylic acid.

For QM modeling studies, geometries of all structures including Eudragit, chitosan, as well as the Eudragit-chitosan cluster model were initially optimized by means of Hartree-Fock (HF) theory employing 6-31G** basis set.(*107*) Then, the optimized structures so obtained were further optimized by density functional theory (DFT) (*108, 109*) using B3LYP hybrid

functional (*110, 111*), first with 6-31G** basis set and then with larger basis set of 6-311G**.(*112*) These successive QM calculations were performed to attain fully optimized structures. The electronic energies corresponding to final optimized structures were used to determine interaction (binding) energy between Eudragit and chitosan. All QM computations were carried out by means of Gaussian 09 software package.(*113*)

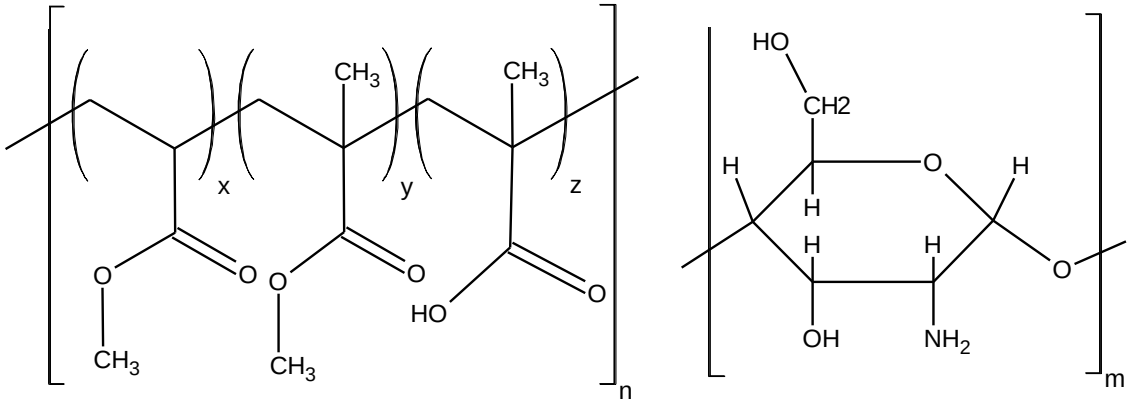

Figure 3-1 Chemical structures of (a) Eudragit, and (b) chitosan polymers.

3.2.13 MD simulations

In order to examine the structural characteristics of Eudragit and chitosan in Eudragit-chitosan layered system, for which Eudragit layer interacts with chitosan layer, MD simulations were conducted on a three-dimensional (3D) cell consisting of Eudragit and chitosan chains. First, polymeric chains of chitosan and Eudragit both with polymerization degree of 50 (i.e., the values of *n* and *m* in Figure 3-1) were constructed. The constructed polymers were subjected to energy minimization for 5000 steps using Smart minimizer algorithm available in Materials Studio software.(*114*) Then, with using minimum energy Eudragit and chitosan polymers, corresponding 3D simulation cells were created. Subsequently, the Eudragit and chitosan simulation cells were utilized in order to create another 3D simulation cell representing a simulation cell consisting of Eudragit and chitosan layers with chitosan as lower layer, and Eudragit chain located at a distance of at

least 10 Å above the chitosan layer. The 10 Å initial interlayer distance was chosen to eliminate dependency of the final structure form MD simulation upon its initial structure. Moreover, to reduce the interactions between Eudragit and chitosan layers to only one side, and thereby removing periodic boundary conditions (PBC) in z direction, vacuum distances were placed below chitosan layer and above Eudragit layer, as shown in Figure 3-2.

The constructed layered cell was first optimized by means of Smart minimizer algorithm for 5000 steps, and then subjected to NVT MD simulations of 750 ps at temperature of 300 K. MD simulations were carried out by use of COMPASS force field (*115*, *116*), an ab initio based force field that have been successfully applied in earlier MD studies of polymeric materials. Non-bonded electrostatic and van der Waals (vdW) interactions were truncated at cutoff distance of 9.5 Å, and long-range electrostatic interactions were calculated using Ewald summation method. Newton equation of motion was integrated *via* velocity Verlet procedure by using 1 fs as time step.(*117*) Andersen thermostat was employed to control temperature at desired level. All MD simulations were done using Materials Studio software.(*114*)

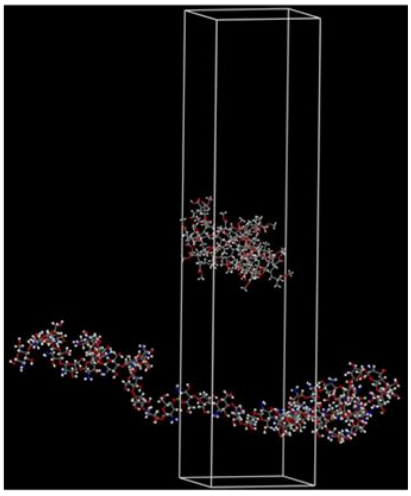

Figure 3-2 Eudragit-chitosan layered 3D cell used for MD simulation. All atoms of Eudragit and chitosan polymers are in Line, and Ball & Stick style, respectively. The color code is: carbon in gray, oxygen in red, nitrogen in blue, and hydrogen in white.

3.3 Results and Discussion

Schematic representations of the microfluidic platforms are shown in Figure 3-3a. The nanoparticle cores are created in the first microreactor, where hydrodynamically focused flow precisely controls the mixing time of the two solutions (HMCS and water), creating monodispersed nanoparticles with precisely controlled properties. These particles are then coated in a Tesla micromixer, where they are sealed with a Eudragit (pH-sensitive PMMA derivative) shell. The micromixer inputs (flow ratios) determine the reactor conditions, and thus the nanocapsule properties. The effect these inputs have on the nanocapsule Zeta potential, Eudragit shell thickness, and overall NP size and morphology is shown in Figure 3-3c. The design of the Tesla micromixer was finalized using COMSOL Multiphysics software to investigate the flow/concentration profiles. Using two-dimensional modeling of ten individual mixer units the continuity and constitutive Navier-Stokes equations along with convection-diffusion equation were solved using finite element method for various geometries. The inlet boundary condition is approximated by the sheath flow and core flow concentrations and flow rates. Tesla mixers use the Coanda effect to bend fluid stream lines and increase the mixing effects. As flow enters the micromixer, part of it deflects toward the side narrow channel due to the Coanda effect, while the remaining fluid flows through the curved- section until these two sub-flows merge. This recombined flow then experiences the Coanda effect again, and this separation and mixing continues until the flow reaches the outlet. The concentration distribution for this Tesla micromixer is shown in Figure 3-3 (b-i). For this flow condition, full mixing is obtained after passing two cell-pairs. The velocity stream lines are shown in Figure 3-3 (b-iii).

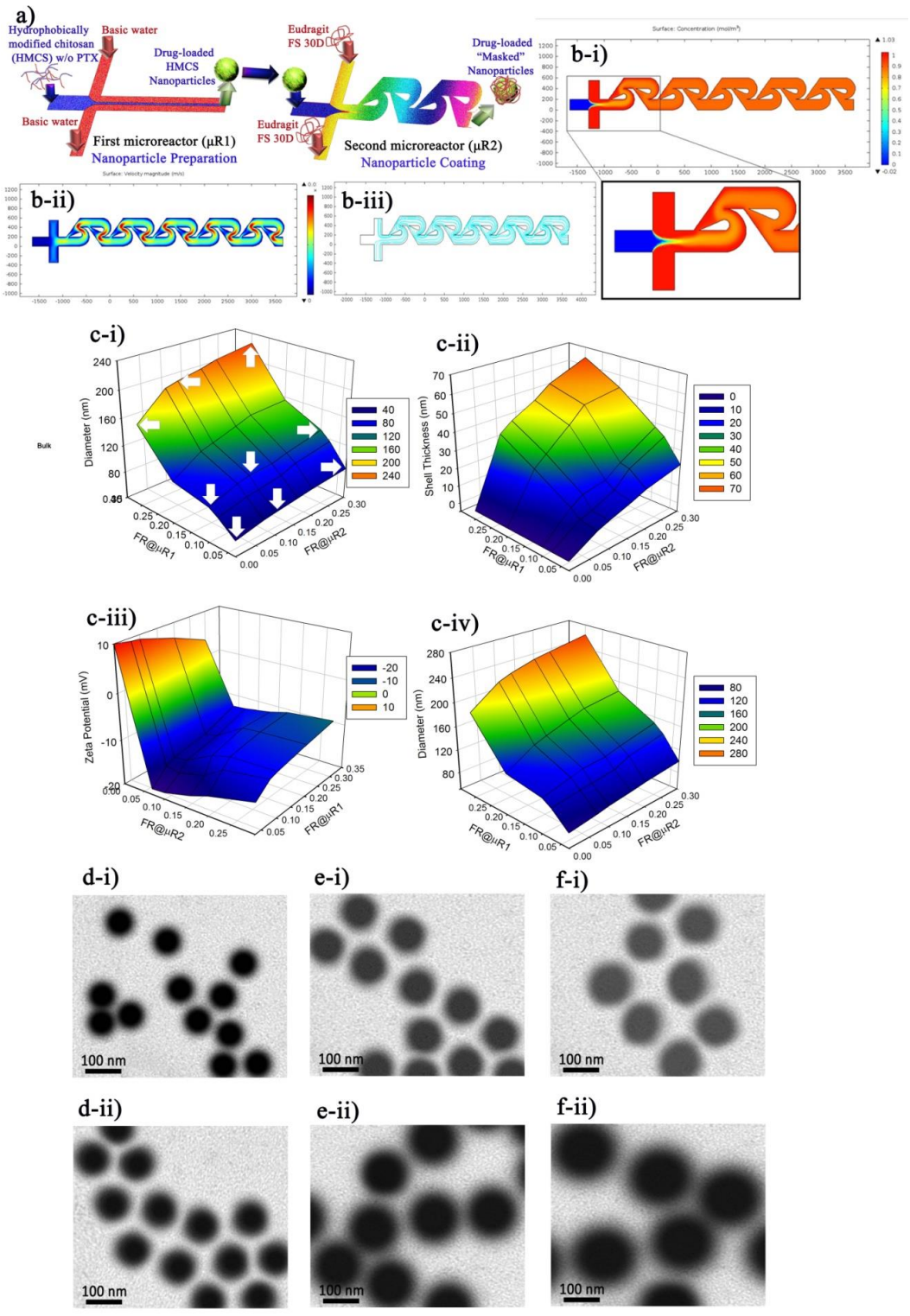

Figure 3-3 (a) A schematic representation of the dual microfluidic platform used to synthesis tunable core-shell nanoparticles: a cross-junction microfluidic device used to control formation of chitosan based NPs from polymer core flow, which hydrodynamically focused with sheath flows of water at basic pH (μR1), and a Tesla micromixer to make Eudragit FS

30D coated onto NPs (μR2). (b) COMSOL simulation results on concentration distributions (b-i), velocity distributions (b-ii), and velocity streamlines (b-iii) for the Tesla micromixer. (c) 3D plots of NPs' experimental characteristics, which were adjusted via the parameters of μR1 and μR2. (c-i) NPs' diameter without paclitaxel (PTX), (c-ii) shell thickness, (c-iii) Zeta potential, (b-iv) diameter with PTX. The white arrows represent the positions of NP samples selected for further experiments. (d-e) Transmission electron microscopy (TEM) images of uncoated (i) and masked (ii) HMCS NPs; (d-i) μR1:0.03, no coating, (d-ii) μR1:0.03, μR2: 0.10, (e-i) μR1:0.10, no coating, (e-ii) μR1:0.10, μR2: 0.10, (f-i) R1: Bulk, no coating, (f-ii) R1: Bulk, μR2: 0.10.

Increasing the flow ratio (volumetric ratio of sheath flow to main flow from 0.03-0. in the microreactors caused a strong increase in total NP diameter for both neat and PTX-loaded particles (Figure 3-3c-i and 1c-iv). Figure 3-3 (c-ii) shows the shell thickness for the coated NPs increases with increasing flow ratio. For instance, by increasing the flow ratio in the Tesla micromixer (μR2) from 0.07 to 0.3 while keeping the flow ratio constant for the first micromixer (0.03)), the average shell thickness increased from 8 nm to more than 22 nm. A more complex trend in Zeta potential variation was observed. As shown in Figure 3-3 (c-iii), the highest Zeta potential value (+10 mv) occurred for the NPs synthesized at the lowest flow ratio in reactor 2 (0.07). This is consistent with the shell thickness results. The Eudragit supportive layer and HMCS core have negative and positive charges, respectively. Hence, decreasing the shell thickness, as a direct consequence of decreasing the flow ratio in micromixer 2, resulted in NPs with a higher net positive charge, and an increased Zeta potential.

Employing the microfluidic process is a significant improvement over the traditional bulk mixing procedures, and results in NPs with smaller diameter for both uncoated and masked NPs at all flow ratios. A broad distribution of residence times in the turbulent regime and variations of local pH at bulk mixing condition are considered the main reasons for such non-uniformity in bulk NPs.(*103, 105*) The first microreactor establishes a well-controlled hydrodynamically focused mixing region with short and narrowly distributed residence times, defined by the input flow rates and ratios, which generates smaller NPs with uniform diameter and microstructure.(*99, 103, 105*) In the first micromixer (cross-junction), the pH

increases through diffusion of the basic water into the aqueous polymer stream, which leads to HMCS amine group deprotonation and aggregation of the macromolecules. A narrow distribution of residence times provided by on-chip diffusion mixing gives the opportunity for the polymer chains to benefit from similar reaction times.(*99*) Solution pH controls the balance between electrostatic repulsion and hydrophobic attraction forces, so the time scale associated with the pH rearrangement determines the self-assembly timescale, which is short in the microfluidic device and thus generates small and uniform NPs (Figure 3-3 (d-i)).(*99*)

In microreactor 2, bulk mixing and laminar flow are the predominant routes of mass transfer, where reactions mainly occur in the microscale rather than the molecular scale. This resulted in more non-uniformity in shell thickness and morphology of the masked NPs. The very slow kinetic diffusion of Eudragit chains prevents the '*t*' microreactor design used to create the NP cores from being used to coat the NPs.(*118*) This limitation leads to the design of the Tesla mircoreactor with alteration in shape, residence time and thus the predominant route of mass transfer. Still, the NPs coated with Eudragit in the microreactor were more uniformly coated than those coated via bulk mixing.

In order to better understand the molecular interactions in the Eudragit-chitosan core-shell NPs, molecular dynamics (MD) simulations were conducted on a three-dimensional (3D) cell consisting of Eudragit and chitosan chains by use of COMPASS force field. Equilibration of the simulated structures was first checked by monitoring time evolution of the potential energy as well as temperature of the cell (Figure 3-4).] As shown, the total potential energy and temperature fluctuate slightly around an average value, which indicates an equilibrium condition has been achieved.

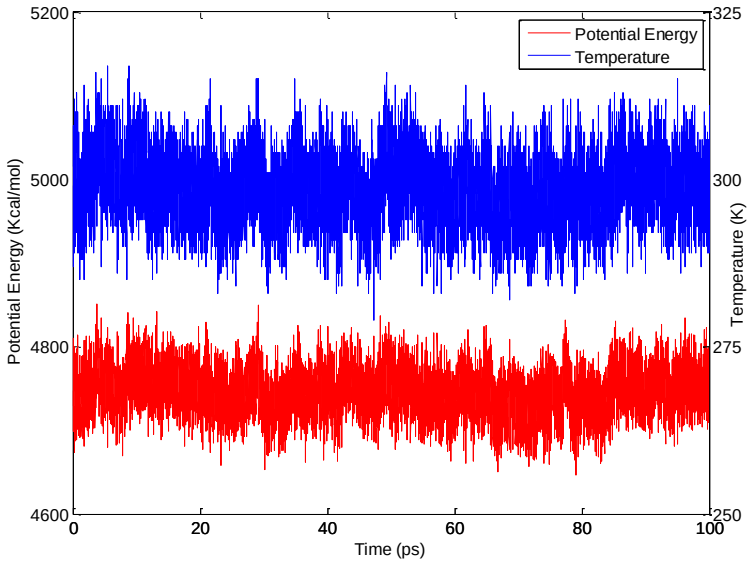

Figure 3-4 Total potential energy and temperature variation against simulation time during last 100 ps NVT MD simulation.

The final structure from the last 100 ps NVT (moles (N), volume (V) and temperature (T) are conserved) MD simulation of layered Eudragit-chitosan cell is shown in Figure 3-5 (a). To make a better comparison, the initial layered structures used for MD simulation are also shown. It is obvious that in comparison with the initial 3D cell the distance between Eudragit and chitosan layers in the equilibrated cell became closer. Such an observation is attributed to the strong affinity of Eudragit and chitosan chains, as confirmed quantitatively by the binding energy value, and the strong intermolecular hydrogen bonding interactions between Eudragit and chitosan. Figure 3-5 (a) shows both the initial and final structures with periodic boundary conditions, which clearly demonstrates the tendency of Eudragit and chitosan chains to interface tightly.

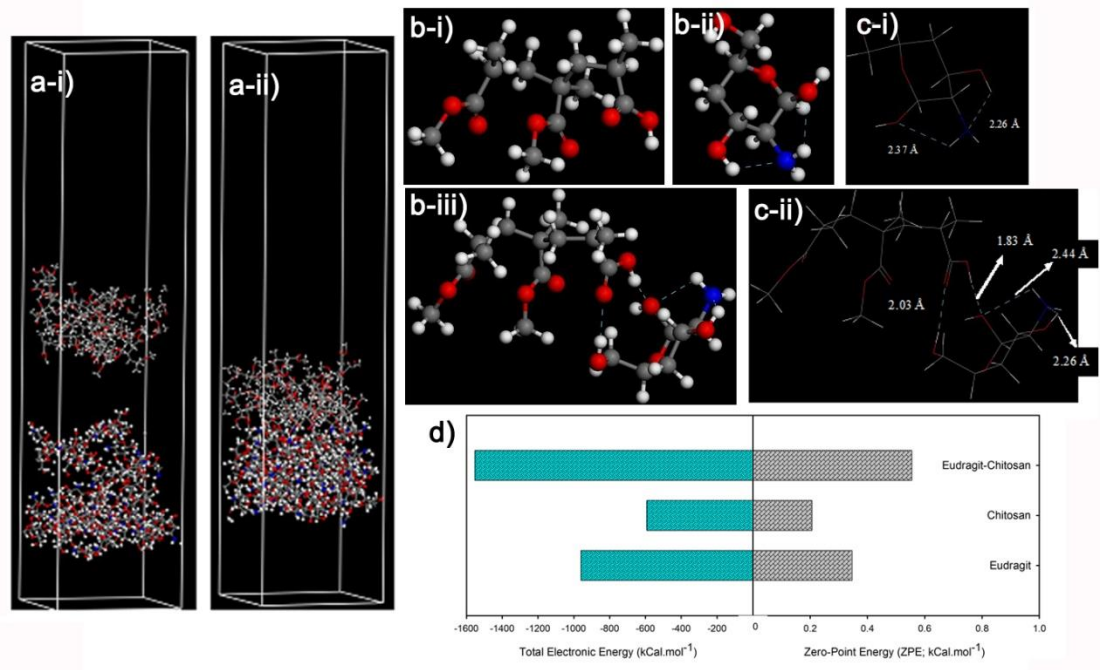

Figure 3-5 (a) Eudragit-chitosan layered structure (a-i) initial structure and (a-ii) after 600 ps NVT MD simulations. Polymer chains are shown inside the simulation cell with periodic boundary conditions; All atoms of Eudragit and chitosan polymers are in Line, and Ball & Stick style, respectively. (b) B3LYP/6-311G optimized model structure of (b-i) Eudragit, (b-ii) chitosan and (b-iii) Eudragit-chitosan cluster. Hydrogen bonding interactions are shown as dashed line; All atoms are in Ball and Stick model. (c) Hydrogen bond length in B3LYP/6-311G** optimized model structure of (c-i) chitosan, and (c-ii) Eudragit-chitosan cluster. Hydrogen bonding interactions are shown as dashed lines. All atoms are in Line style. The color code for all items is: carbon in gray, oxygen in red, nitrogen in blue, and hydrogen in white. (d) Total electronic energy (Hartrees) and ZPE (Hartrees) (kCal.mol^{-1}) for B3LYP/6-311G** optimized Eudragit, chitosan and Eudragit-chitosan cluster structures.**

First principle quantum mechanics (QM) simulations were applied for the three molecular systems including Eudragit, chitosan, and Eudragit-chitosan clusters. QM simulations were specifically utilized to assess the intermolecular interaction energy between Eudragit and chitosan, which allows us to determine their affinity to each other. Figure 3-5 (b) shows the final energy-minimized model structures for Eudragit, chitosan as well as Eudragit-chitosan, resulted from B3LYP/6-311G** level of theory. We find that the optimized monomer structure of Eudragit is not able to form any intramolecular hydrogen bonds, while chitosan can form intramolecular hydrogen bonds between amine ($–NH_2$) and hydroxyl (–OH) groups. In the simulation, hydrogen bonds are assumed when two

hydrogen donor and hydrogen acceptor atoms satisfy the following geometrical conditions: (1) the distance between a hydrogen donor atom and hydrogen acceptor atom is less than 2.5 Å, and (2) the hydrogen donor-hydrogen-hydrogen acceptor angle is greater than 90°. For the single chitosan structure, the nitrogen atom in the amine groups act as both hydrogen donor and hydrogen acceptors, while the oxygen atom in one of hydroxyl groups directly attached to the chitosan backbone act as a hydrogen donor in hydrogen bond formation, and the oxygen atoms in the other hydroxyl group directly bonded to the polymer backbone appears as hydrogen acceptor atoms.

In the case of Eudragit-chitosan cluster model, two intermolecular hydrogen bonding interactions are formed between Eudragit and chitosan units, in which oxygen atoms in the Eudragit carboxylic group act as hydrogen bond donor and acceptor atoms, and hydroxyl group attached to the backbone *via* methyl group and hydroxyl group directly attached to the backbone act as hydrogen donor and acceptor atoms, respectively. These types of interactions show that Eudragit polymers are able to interact via their methacrylic acid groups with chitosan. The intramolecular hydrogen bonds formed in chitosan only structures and in of Eudragit-chitosan clusters are the same.

In order to gain further insights into the interaction between Eudragit and chitosan, length of the hydrogen bonding interactions was examined (Figure 3-5 (c)). The depicted hydrogen bond lengths clearly indicate that intramolecular hydrogen bond length in chitosan and also in chitosan interacting with Eudragit is almost the same, which signifies that interaction of chitosan with Eudragit does not influence the strength of intramolecular hydrogen bonding interactions within chitosan. However, as the intermolecular hydrogen bond length in Figure 3-5 (c-ii) exhibits, the length of the Eudragit-chitosan hydrogen bonds is shorter than that of intramolecular hydrogen bonds within chitosan, which demonstrates the strong binding affinity between Eudragit and chitosan chains. The findings of the QM and MD simulation results are consistent with each other.

Total electronic energy and zero-point energy (ZPE) corrected total electronic energy of the final B3LYP/6-311G** optimized Eudragit, chitosan, and Eudragit-chitosan structures are shown in Figure 3-5 (d). From these total energy levels the interaction energy (ΔE) values for the Eudragit-chitosan cluster model were calculated to be -11.23 kCal.mol^{-1} ($\Delta E_{electronic}$) and -9.60 kCal.mol^{-1} (ΔE_{ZPE}). We observed that the interaction energies are negative, which is indicative of the fact that Eudragit and chitosan chains tend to be located in the vicinity of each other and interact together. The Eudragit-chitosan affinity is associated with their intermolecular interactions, especially the hydrogen bonding displayed in Figure 3-5 (b).

Figure 3-6 shows the hydrodynamic diameter of synthesized core-shell NPs over time at in various pH conditions. The pH alterations were intended to somewhat mimic the digestive tract. In the gastrointestinal tract, the intraluminal pH increases from highly acidic medium (pH 1-2 which increases to 4 during digestion) in the stomach to about pH 7.4 in the terminal ileum of the small intestine. This change is followed by a pH drops to 5.7 in the caecum (Colon).(*119*) It is worth noting that no significant differences were found in the gastrointestinal pH levels between normal subjects and people suffering from colorectal carcinoma.(*120*)

Generally, the size of NPs depends on the number of polymer chains as well as their swelling state. It has been shown that swelling state is highly affected by the compactness of self-assembled NPs, which can be controlled by changing the flow ratio on microfluidic platforms.(*105*) The probability of hydrophobic side chains competing with intramolecular interactions is highly influenced by the mixing time, where it has been shown that longer mixing time results in less compact NPs.(*105*) As is shown in Figure 3-6, NPs synthesized at lower flow ratios in µR1 (t-shape microreactor) show higher stability, which is due to their more compact structure. In comparison with microfluidic NPs, less compact bulk synthesized NPs show less resistance to chemical and physiological alterations, leading to

more swelling when exposed to pH alteration. Increasing the pH to 7.4 is associated with an initial NP swelling, and is followed by a significant decrease in the size of the NPs. Early stage increase in diameter of the NPs can be interpreted as the swelling of the Eudragit layer in the solubilizing pH medium. Subsequently, gradual dissolution of the Eudragit layer in the neutral medium leads to a drop in the size of the NPs. It should be noticed that the observed differences in the size of the NPs are related to their different compactness. After removal of the Eudragit layer, the next change in pH from 7.4 to 5.5 results in a significant increase in the size of NPs. Swelling of the NPs in this stage is due to the electrostatic repulsion of the highly protonated HCMS chains, which ends in dissolution of the swollen NPs (Figure 3-6). Bulk synthesized NPs coated at FR of 0.1 were found to show the most significant and rapid size alterations The overall diameter changes of the NPs were less significant over the first pH transition (pH 4 to 7.4) compared to the second transition (pH 7.4 to 5.5). This effect was more pronounced for the microfluidic NPs, which disclose the ability of microfluidic synthesis method to produce dense and compact NPs.(*105*) Over the second pH transition, the removal of the shell layer cause their size to change significantly.

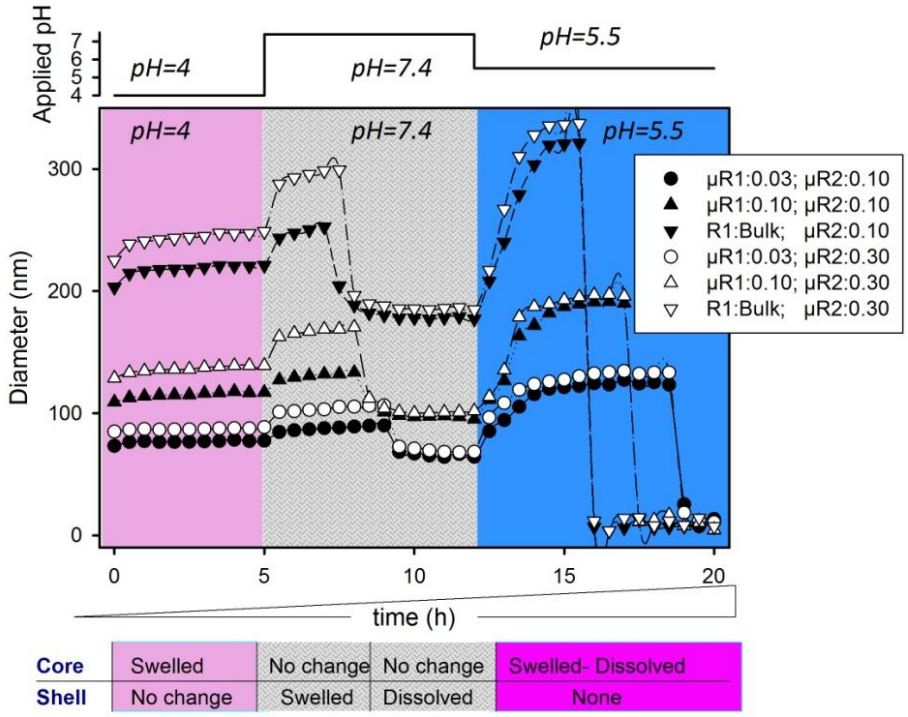

Figure 3-6 pH/time dependency of hydrodynamic diameter for different types of Eudragit coated NPs.

The dynamic size of microfluidic core-shell nanoparticles formed at μR1:0.03, μR2: 0.10 in the simulated gastric (SGF) and intestinal fluids (SIF) also investigated and shown in Figure 3-7.

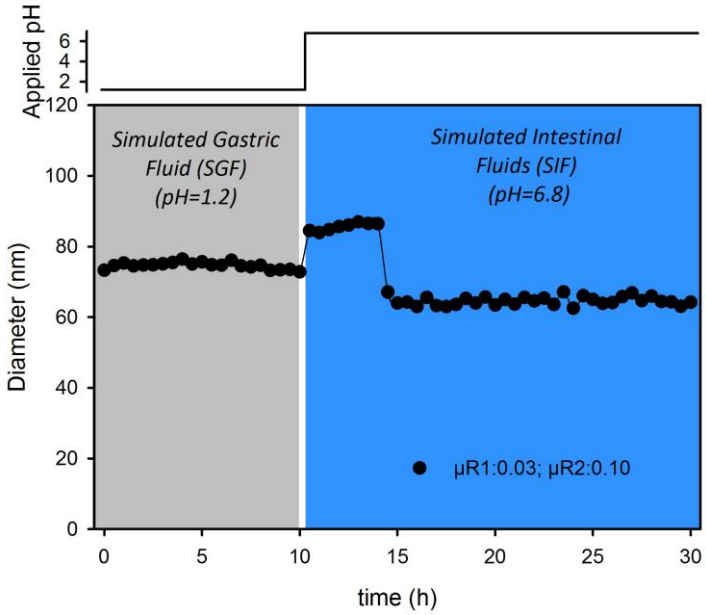

Figure 3-7 The dynamic size of microfluidic core-shell nanoparticles formed at μR1:0.03, μR2: 0.10 in the simulated gastric (SGF) and intestinal fluids (SIF).

Stability of core-shell nanoparticles (μR1:0.03, μR2: 0.10) after incubation for 120 h in the gastric simulated (pH=4) and intestinal simulated (pH=7.4) conditions are examined (Figure 3-8).

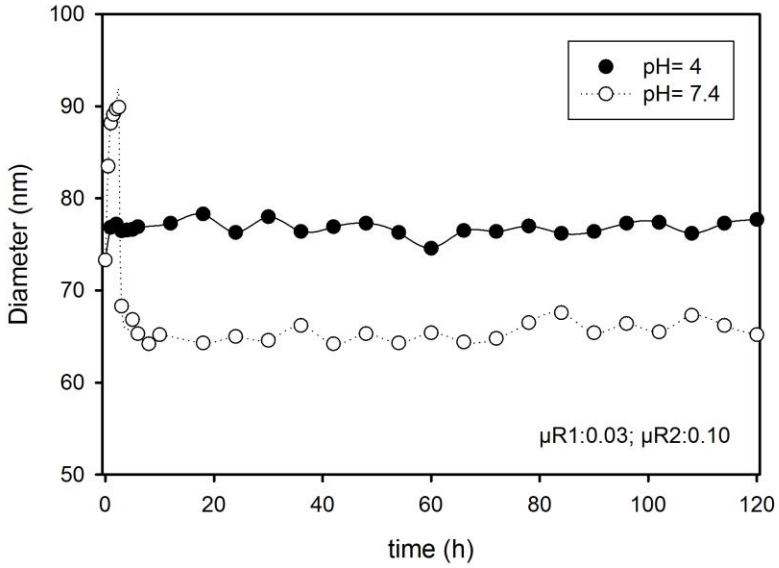

Figure 3-8 Stability of core-shell nanoparticles (μR1:0.03, μR2: 0.10) after incubation for 120 h in the gastric simulated (pH=4) and intestinal simulated (pH=7.4) conditions. The shell (Eudragit) dissolved after incubation at neutral pH (pH=7.4) in about 30 min and subsequently we have bare chitosan NPs.

Here, we also tried to show the applicability of this approach for other charged polymers. As shown in Figure 3-9, we coated chitosan-based bulk- and microfluidic-synthesized NPs by Alginate (as a representative charged natural polymer) in addition to Eudragit (as a representative charged synthetic polymer). We also made PEI/DNA nanoplexes and coated them with Alginate and Eudragit using the same microfluidic platform.

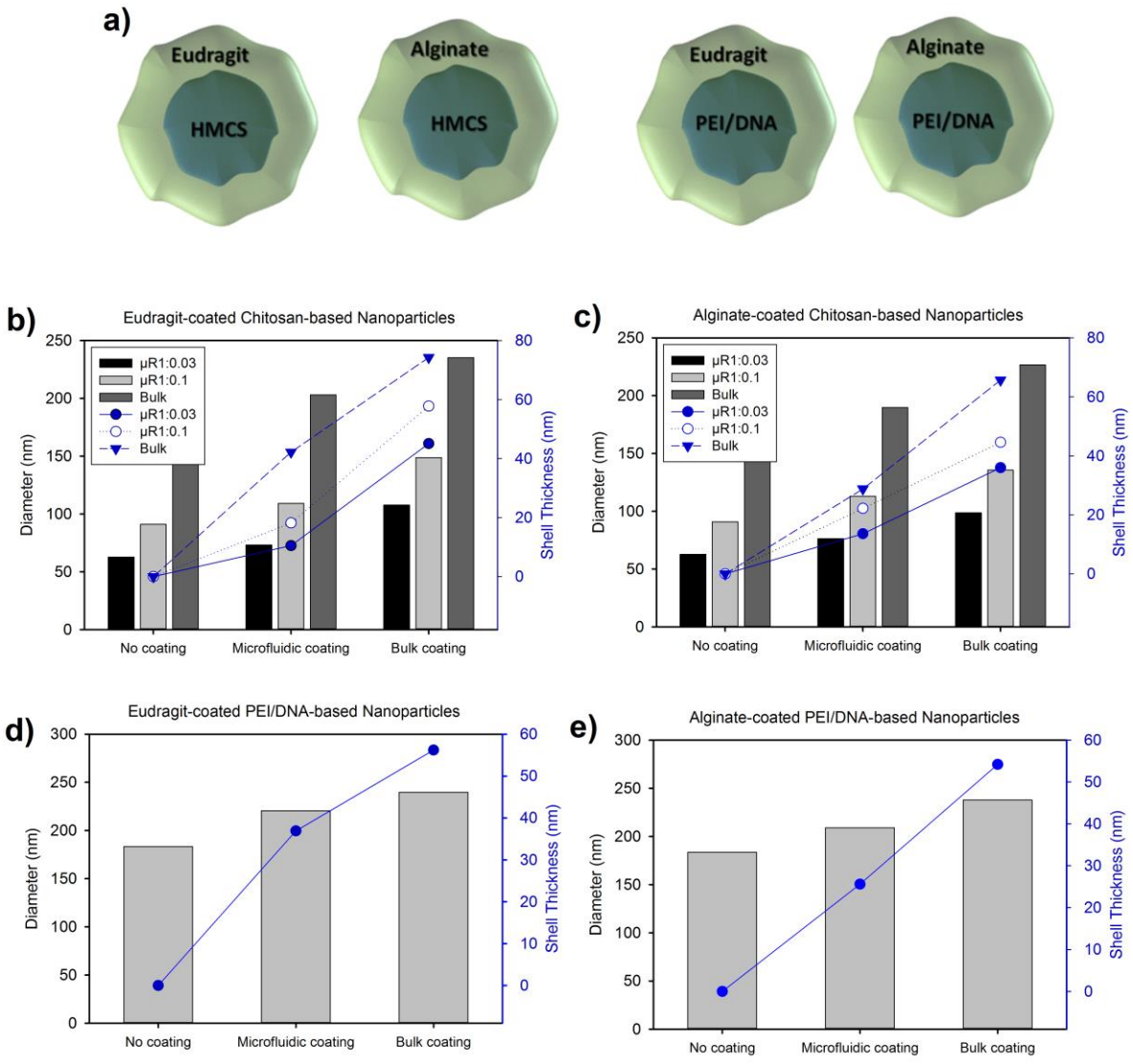

Figure 3-9 The proof-of-concept results of applicability of proposed coating technique for other charged macromolecules. Here we tested our approach in four different systems (a). Eudragit (b) and Alginate (c) coating of chitosan-based nanoparticles using both of microfluidic and bulk coating methods. Chitosan nanoparticles were synthesized using both of bulk mixing and microfluidic assisted synthesizing methods. The Eudragit (d) and Alginate (f) coating of positively charged PEI/DNA-based nanocomplex also examined. The flow ratio of 0.10 is used for all of microfluidic assisted coating experiments

Figure 3-10a shows the *in vitro* release profiles of different synthesized paclitaxel (PTX) loaded NPs over the sequential changes in pH (4, 7.4, and 5.5) at 37 °C. The relatively rapid initial drug release from uncoated NPs (both microfluidic and bulk synthesized particles), more than 30% in the first 24 h, has been typically reported for PTX-loaded

chitosan-based NPs at low pH medium.(*121, 122*) In the self-assembled NPs, drug molecules may have been partially loaded in the outer layers of particles, specifically in the case of bulk synthesized NPs, resulting in their accelerated release. Core-shell NPs which were prepared on the dual microfluidic platforms, have more developed release profiles, limited burst release at low pH, followed by more sustained release profiles at the next successive pH levels (7.4 and 5.5).

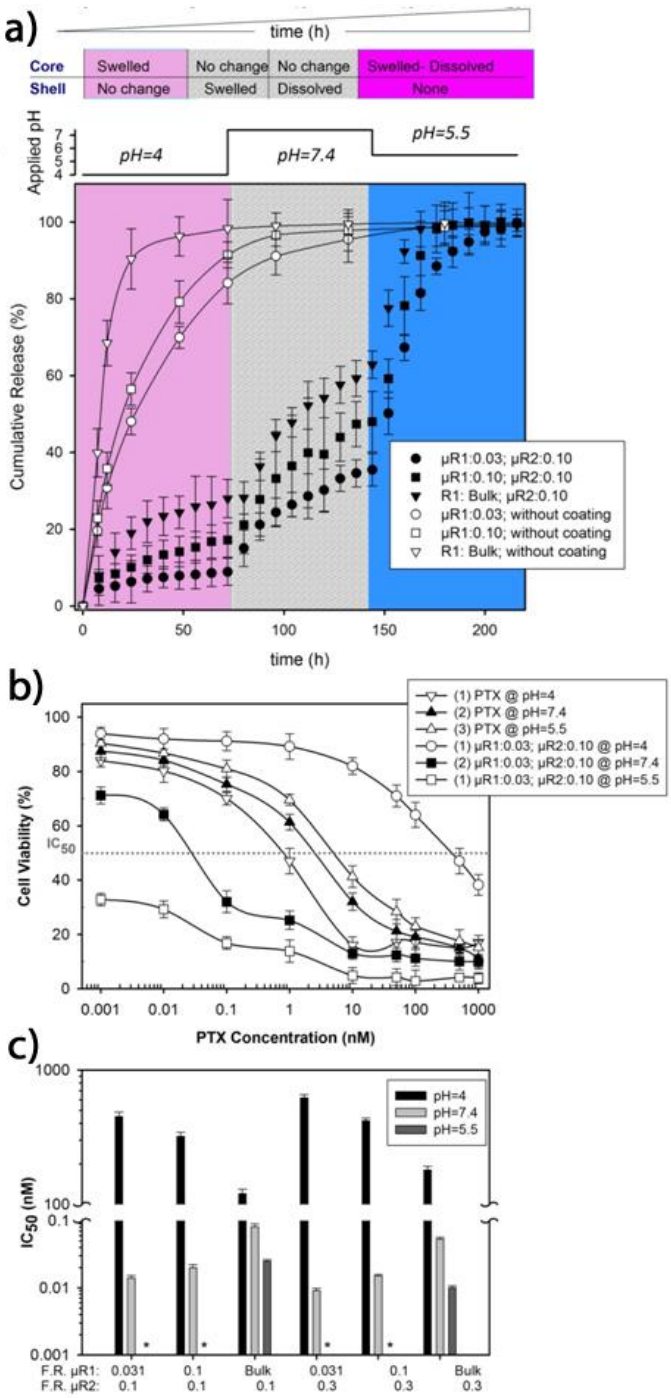

Figure 3-10 Cumulative in vitro release of PTX from uncoated (empty symbols) as well as coated (filled symbols) chitosan-based NPs after sequential change in pH (4, 7.4, and 5.5) at 37 °C (Mean ± SD, n = 3 independent experiments). (b) Cell viability of Caco-2 cells after 72 h exposure to free PTX as well as PTX loaded NPs as a function of pH at 37°C. (c) IC_{50} values for different types of uncoated/coated NPs after sequential incubation at different pH. Lower IC_{50} value indicate more potent therapeutic agent. * indicate IC_{50} < 0.001. Results presented as mean value ± SD, n = 3 independent experiments.

As previously stated, using microfluidics provides the possibility to synthesis more compact and smaller NPs in comparison with bulk synthesized particles. Hence, the slower release rate of the microfluidic prepared NPs is due to their relatively more compact microstructure.(*105*) Coating the NPs with Eudragit, as shown in Figure 3-10a, strongly affected the release profile. The pH-sensitive Eudragit outer layer, which is insoluble in low pH environment, hinders PTX diffusion to the surface of the NPs in early stage of release and reduces burst release in the acidic medium. In the case of uncoated NPs, the major part of the encapsulated PTX is released in the first stage (acidic pH), an effect which is more pronounced for the bulk synthesized NPs. Obviously, the release rate of the microfluidic NPs accelerated after increasing pH from 4 to 7.4, which is in contrast of the decreased release rate of the uncoated NPs after a similar pH Transition. This trend is attributed to the dissolution and higher swelling ratio of Eudragit layer at neutral pH in comparison with acidic pH. Such pH-responsive release behavior has been reported by some researchers.(*123, 124*)

Practically, coating the NPs with pH-sensitive layer gives them the ability to bypass the acidity of gastric fluid without releasing considerable amounts of the loaded drug.(*124*) After dissolution of the supportive layer at higher pH, modified chitosan core forms a gel like insoluble structure, hence the rate of drug release is controlled.(*125*) Interestingly, a further acceleration of release rate was observed for the microfluidic NPs after decreasing pH from 7.4 to 5.5. Over the last release stage, protonation of amino groups on chitosan chains causes swelling of NPs, which ultimately results in an increased rate of PTX release.(*126*)

The effect of unloaded NPs at different concentrations (50-800 $\mu g.ml^{-1}$) on the viability of two kinds of cells (Caco-2 and MEF) after 72 h using the MTT assay is presented in Figure 3-11. These results are the average of a series of three different experiments. All types of

NPs have shown cell viability levels of more than 90% after 72 h, indicating low toxicity of the coated and uncoated chitosan nanocarriers.

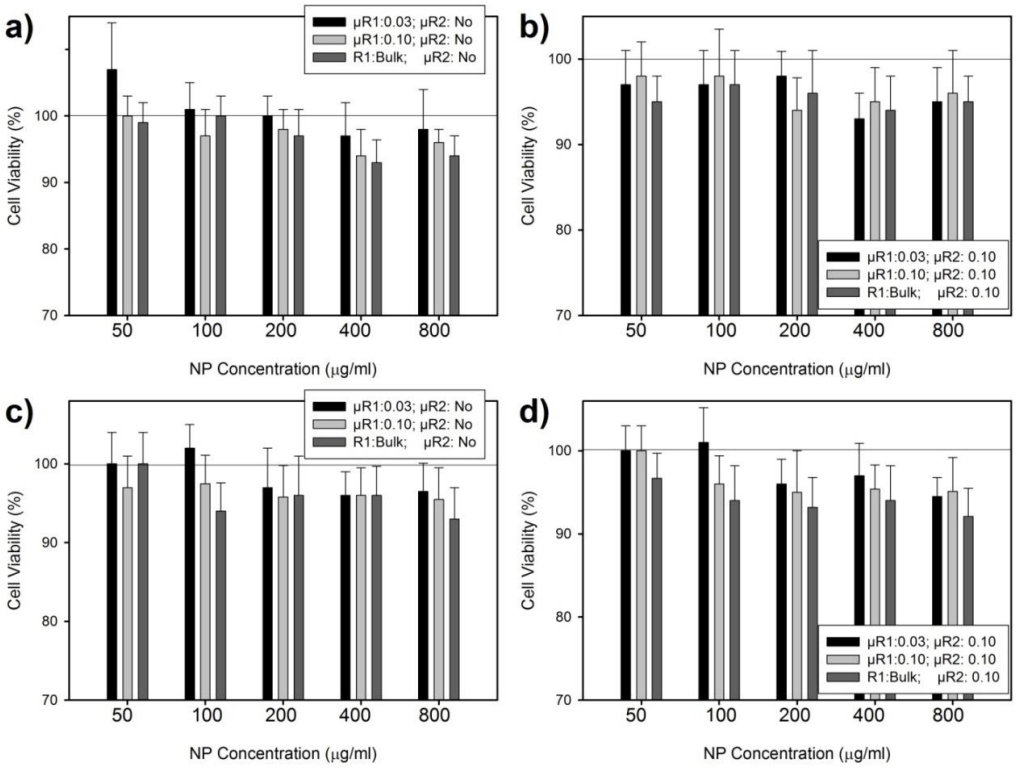

Figure 3-11 Cell viability of Caco-2 (a, b) and MEF (c, d) cells after 72 h exposed to the (a, c) uncoated and, (b, d) coated unloaded chitosan NPs at different concentration and 37°C, (Mean ± SD, n = 3 independent experiments).

Cell viability and IC_{50} results for different types of the synthesized NPs are presented in Figure 3-10. Figure 3-10b displays the viability of Caco-2 cells after 72 h exposure to different concentrations of the PTX loaded NPs as a function of pH at 37°C. Increasing PTX concentration caused a sharp drop in cell viability.(*127*, *128*) It is also found that pH of the medium plays a leading role in the toxicity of PTX loaded NPs. Sequential incubation at different pH caused a significant decrease in the Caco-2 cell viability. As stated above, sequential incubations at pH 7.4 and 5.5 leads to dissolution of the outer layer and swelling of inner core respectively, which resulted in increased release of the drug. There is also a clear relationship between the amount of released PTX and the IC50 value. Amoozgar *et*

al. reported incubation of the cells at pH 6.2 with PTX loaded NPs, coated with a layer of chitosan, caused a significant dose-dependent reduction of the value of cell viability. This trend was comparable of moderate decrease in viability of the cells incubated with the PTX-loaded NPs at pH 7.4.(*129*) Such pH-dependent cytotoxicity has been reported elsewhere even for neat chitosan-based NPs. Loh *et al.* reported Caco-2 cellular uptake of chitosan NPs in pH 6.0 results in lower cell viability than at pH 7.4.(*130*)

Figure 3-10c illustrates the IC_{50} trend, which shows the effective PTX concentration required for a 50% decrease in cell viability. Results show that for all the PTX-loaded NPs IC_{50} decreased when applying the pH sequence. This finding implies3enhanced efficiency of the PTX loaded NPs in the sequential incubation at different pH values (4, 7.4, and 5.5). Interestingly, the viability of cells incubated with unloaded NPs varies little with NP properties (flow ratio), again emphasizing the pH-dependency of IC_{50} on the drug delivery efficacy of microfluidic NPs synthesized at lower flow ratios.

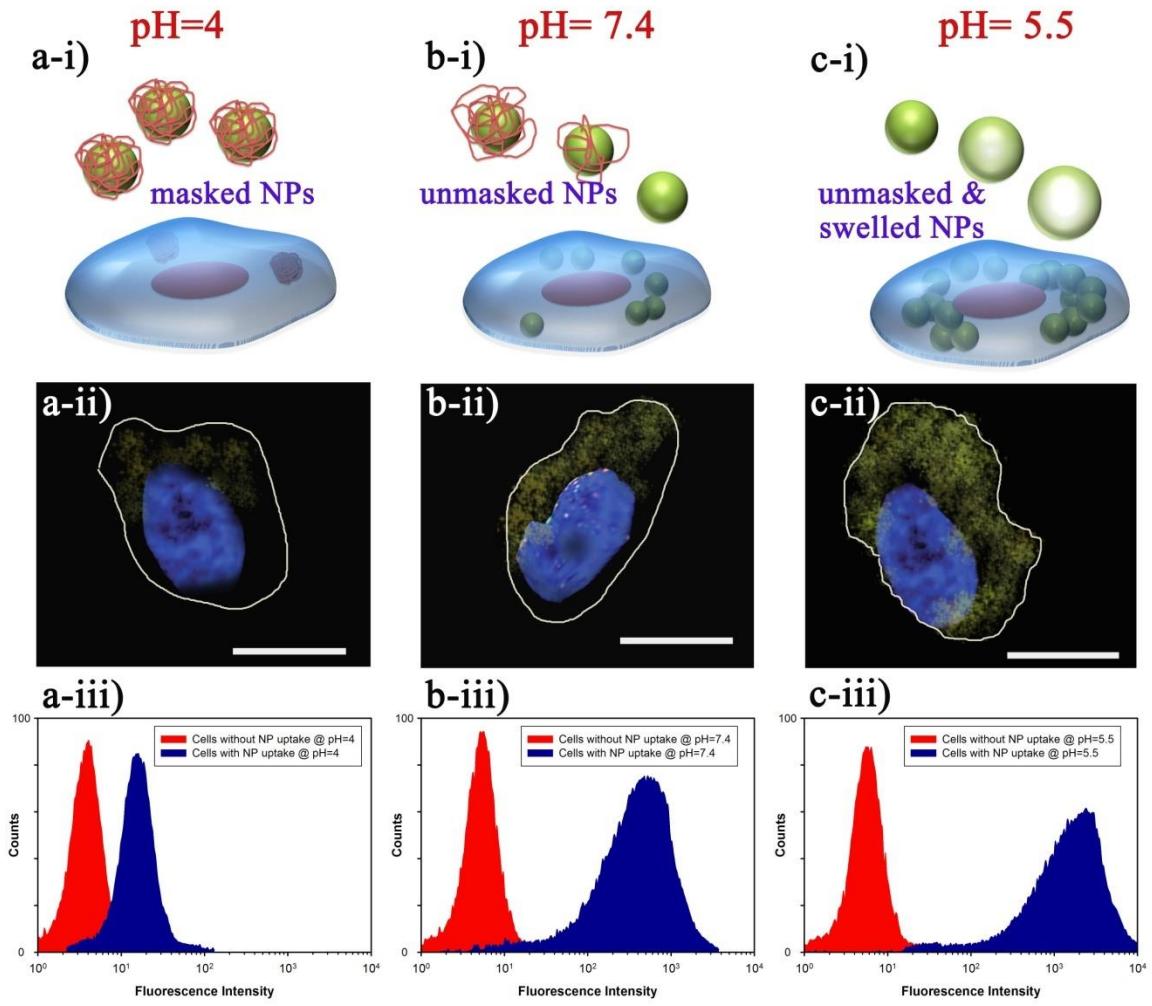

Figure 3-12 (i) Schematic representation of facilitated cellular uptake of NPs after unmasking upon incubation at different pH. (ii) Confocal laser scanning microscopy (CLSM) images showing cellular uptake of FITC-labeled HMCS NPs after 2h incubation with Caco-2 cells after changing the medium pH. Cell nucleus stained with DAPI (blue fluorescence), the green dots represent internalized NPs. Scale bar is 15 µm. (iii) Fluorescence activated cell sorting (FACS) results of facilitated cellular uptake after unmasking of NPs at different pH.

As shown in Figure 3-12, changing the pH from 4 to 7.4 and then 5.5, results in unmasking of HMCS NPs and facilitated cellular uptake of NPs. It seems masked NPs with anionic surfaces have less interaction with the negatively charged cell membrane, which leads to lower transfection efficiency. It was previously reported that surface charge affects cellular uptake of chitosan-based NPs.(*131*)

Changing the pH to 7.4 is combined with the dissolution of Eudragit layer and a higher degree of cellular accessibility for unmasked HCMS NPs. Although removing the Eudragit shell generates more cellular transfection, a greater amount of cellular uptake is observed with protonation of amino groups of chitosan as a result of changing the pH from 7.4 to 5.5.(*126, 132, 133*) Due to this charge, as shown in Figure 3-3 (c-iv), chitosan NPs are often endocytosed by the cells.(*99, 134*) The cell uptake trend is quantitatively reported in Figure 3-12 (iii). The ratio of the florescence intensity for cells with and without NP uptake shows the NPs uptake efficiency, and increased with altering the pH to 7.4 and then 5.5. The cellular uptake is positively correlated with the surface charge in the NPs. Normally transfection efficiency of chitosan is higher for culture medium with lower pH value due to a higher degree of chitosan protonation.(*121, 131*)

Cellular uptake nanoparticles as a function of applied pH is evaluated in other cancerous cell lines (MCF-7 and HeLa cells) and the results are presented in Figure 3-13 and the same trends are seen in the other cell lines as well. To investigate the effects of presence of serum proteins on NPs-cells interactions, cellular uptake of prepared coated and uncoated NPs is measured in serum-based culture (10% FBS containing medium) in three different cell lines (Figure 3-13) as a function of pH and after 2 h of incubation.

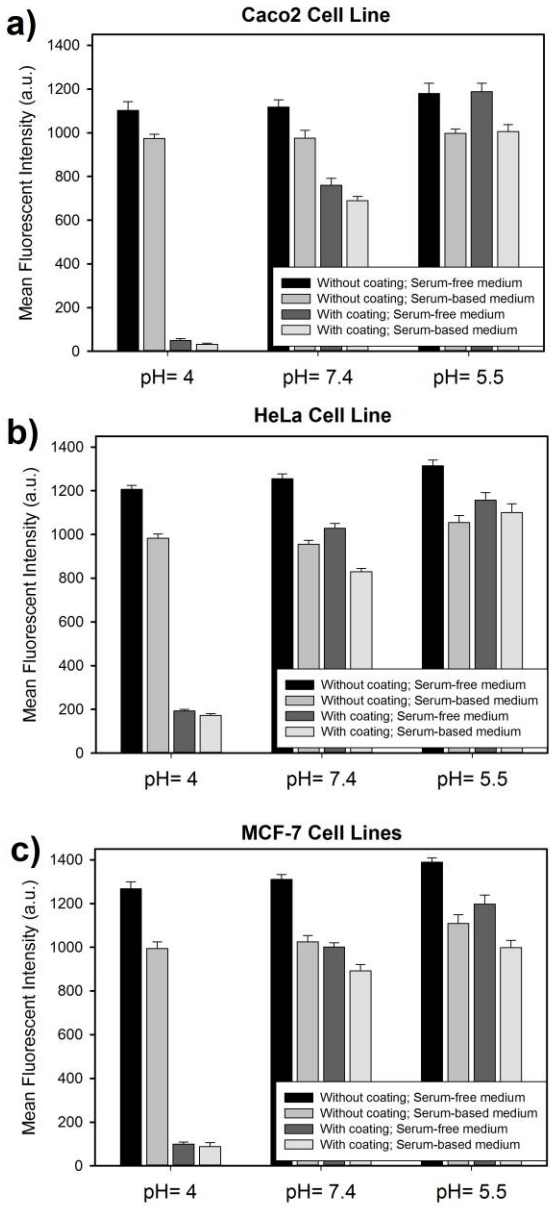

Figure 3-13 Cellular uptake of FITC-labeled nanoparticles as a function of applied pH in Caco2 (a), HeLa (b), and MCF-7 (c) cell lines. The effects of pH-sensitive coating as well as presence of serum-based media (10% FBS containing culture) investigated by measuring fluorescent intensity of cultured cells after 2 h of incubation with nanoparticles at 37°C using flow cytometry. The pH value of media changed subsequently from 4 (gastric mimic pH) to 7.4 (intestinal mimic pH), and from 7.4 to 5.5 (tumor local pH). Values indicate mean ± standard deviation from triplet independent measurements.

3.4 Conclusion

Nanoparticle systems, due to their unique features as drug carriers, have attracted a great deal of interest in colon cancer chemotherapy. For the first time, we employed a dual microfluidic procedure to attain highly tunable core-shell drug carriers with customized and reproducible characteristics adjusted for targeted colon cancer therapy. Self-assembled hydrophobically modified chitosan nanoparticles (NPs) were produced in a cross-junction microfluidic device and finely coated with a pH- sensitive copolymer (Eudragit) through a Tesla micromixer. Quantum mechanics (QM) and classical molecular dynamics (MD) simulations indicate a good level of molecular interactions between the layered nanostructures. NPs fabricated and coated via microfluidics showed increased cellular uptake during pH changes compared to those prepared with bulk mixing. MTT assays and *in-vitro* results showed coating the NPs with a pH-sensitive Eudragit layer gives the NPs the ability to bypass the acidic gastric fluid without releasing the majority of the loaded anticancer drug. Considering the pH-sensitive characteristics of the microfluidic NPs, such a highly tunable drug delivery system enabling physiological-stimuli release is a potential route to develop efficient targeting colon chemotherapeutic agents.

CHAPTER 4. ON-CHIP SYNTHESIS OF FINE-TUNED BONE-SEEKING HYBRID NANOPARTICLES[3]

Reproducibility of physicochemical properties of multifunctional nanoparticles has been always their major challenge for various for therapeutic and diagnostic applications. Commonly nanoparticles are produced as rather heterogeneous mixtures with a subsequent range of functional properties. Here we report an one-step approach for synthesis of finely tuned targeting hybrid nanoparticles (HNPs). A microfluidic platform was used to precisely control the nano-precipitation of bisphosphonate-conjugated poly(D,L-lactide-co-glycolide) chains, while co-encapsulating superparamagnetic iron oxide nanoparticles (SPIONs) and the anticancer drug. The size of the nanoparticles was found to increase with rising mixing times, whereas smaller and more compact HNPs, were obtained at the rapid mixing regimen. Furthermore, drug encapsulation studies revealed significantly higher loading (73-80%) efficiencies for the microfluidic technique compared to the conventional bulk synthesis techniques (50%), and a sustained release profile was achieved with the microfluidic synthesized HNPs. The HNPs were shown to have a strong affinity for hydroxyapatite, as demonstrated *in vitro* bone binding assay, which was further supported by molecular dynamics simulations. *In vivo* proof of concept results verified the prolonged circulation of targeted microfluidic HNPs. Biodistribution as well as non-invasive bioimaging experiments showed higher tumor localization and suppression of targeted HNPs to the bone metastatic tumor compared with controls. The hybrid bone-targeting nanoparticles fabricated with fine, reproducible precision can be considered as promising nanoplatforms for various theragnostic applications.

[3] *This work has been published in part by M.M. Hasani-Sadrabadi, E. Dashtimoghadam, G. Bahlakeh, F.S. Majedi, H. Keshvari, J.J. Van Dersarl, A. Bertsch, A. Panahifar, P. Renaud, L. Tayebi, M. Mahmoudi, K. I. Jacob (2015) Nanomedicine 10 (23), 3431-3449.*

4.1 Introduction

Finding the optimal treatment for bone cancers, osteoporosis, osteoarthritis, and other bone diseases has long been a matter of great interest for health care providers (*135, 136*). Particular emphasis has been centered on the development of personalized treatments for bone cancers, in order to both improve the efficacy of drugs and reduce the side effects associated with chemotherapy. Many bone tumors are linked to some form of excessive local bone resorption (*i.e.,* osteolytic tumors) or formation (*i.e.,* sclerotic tumors), distinguishable by their unique appearance on radiography and uptake of radioactive tracer on bone scintigraphy (*137, 138*). Osteosarcoma is the most common primary bone malignancy and an aggressive osteoblastic form of bone cancer, which is characterized by its rapid osteoblastic activity, followed by sclerosis of the affected regions (*139*). The ^{99m}Tc-MDP (^{99m}Tc-methylene diphosphonate) scan from patients with osteosarcoma is accompanied by significant homogeneous accumulation of the radioactive bisphosphonate (BP) tracer in the primary tumor as well as in the metastatic sites (*140*). These distinctive patterns in bone cancers could be used to design a bone-seeking platform carrying anti-cancer drugs for more efficient drug delivery (*141-143*). Nanoparticles (NPs) have unique properties that make them good candidates for this purpose. This type of approach, centered around smart and active targeting, may result in a considerable decrease in side effects of chemotherapy drugs, and more efficient destruction of tumor cells (*144, 145*).

Inorganic NPs can be tracked *in vivo* with many imaging modalities, as their high electron density structures and/or their magnetic properties make them good contrast agents (*83, 146-148*). Among the different types of magnetic particles, superparamagnetic iron oxide NPs (SPIONs) are recognized as one of the most promising materials for biomedical applications such as image guided drug delivery and cancer treatment (*149-151*). SPIONs can use active targeting by conjugating targeting ligands, and also be directed towards tumors by using a weak external magnetic field (*152*). Moreover, magnetic fluid

hyperthermia using magnetic liposomes has been shown to successfully reduce the volume of osteosarcoma tumor in animal models (*153*).

The aim of this work is to develop a single-step microfluidic assisted route to reproducibly synthesize finely tuned multifunctional bone-seeking hybrid NPs (HNPs), with the potential for future applications in treatment and imaging of bone cancers (*i.e.*, theragnosis). In recent years, microfluidics has emerged as a distinctive approach for the synthesis of a variety of well-defined nano-/microstructures, while using only small amounts of reagents (*14, 15, 20, 23, 99, 154-156*).

Here, we demonstrate the microfluidic design of multifunctional targeting nanocarriers capable of concurrent diagnostic imaging, delivery of chemotherapy drugs, and hyperthermia treatment. HNPs consisting of poly(lactic-co-glycolic acid) (PLGA) chains were conjugated with bisphosphonate molecules as the bone-targeting moiety, and were subsequently loaded with Paclitaxel (PTX), as a model anti-cancer drug, and SPIONs as a magnetic resonance imaging (MRI) contrast agent.

Special attention was placed on characterizing nanoprecipitation of the PLGA chains in terms of size, number of aggregated polymeric chains and compactness of the synthesized HNPs, as well as their drug loading efficiency. Size, polydispersity, and drug release patterns are governed through mixing time during particle formation, and was tightly controlled using the hydrodynamic flow focusing technique in a microfluidic platform. In order to assess behavior of PLGA chains in the vicinity of hydroxyapatite (HA) crystals, all-atom molecular dynamics (MD) simulations were conducted to explore the effects associated with the conjugated BP functional groups onto the polymer chains.

4.2 Materials and Methods

4.2.1 Materials

Acid terminated poly(D,L-lactide-co-glycolide) (PLGA; lactide:glycolide 50:50; M_n= 31,500 g.mol^{-1}; M_w= 48,000 g.mol^{-1}; M_w/M_n= 1.52 (GPC); inherent viscosity: 0.53 dL.g^{-1}) was acquired from Sigma-Aldrich (Resomer RG 504H). The refractive index increment (dn/dc) of the polymer solution was measured to be 0.05 mL.g^{-1} using asymmetric flow field-flow fractionation (AFFFF) method.

Acid terminated PLGA (PLGA-COOH) chains were functionalized as reported elsewhere (*157, 158*). In brief, 65 mg of lyophilized bisphosphonate (sodium Alendronate, Sigma) was dissolved in 1 ml dimethylsulphoxide (DMSO, Sigma) and subsequently added to 7.8 gr of acid terminated PLGA (PLGA-COOH), which was previously activated using 1-Ethyl-3-(3-dimethylaminopropyl) carbodiimide (EDC, Sigma)/ N-hydroxysuccinamide (NHS, Sigma); dissolved in 4 ml of equivalent mixture of DMSO and dichloromethane (DCM, Sigma) at 2°C and stirred for 2 h. The mixture was then gradually heated up to the room temperatures and stirred for 10 h. Afterwards, the reaction solution was dialyzed (Spectra/Por CE dialysis tubing, 500-1000 MWCO, Spectrum Labs) 3 times against 1 L of deionized water for 24 h. Finally, the dialyzed conjugated polymer was lyophilized and kept in freezer until use.

Superparamagnetic iron oxide NPs (SPIONs) were synthesized by alkaline co-precipitation of ferric and ferrous chlorides in aqueous solution as reported before (*159*). Solutions of $FeCl_3.6H_2O$ (0.086M) and $FeCl_2.4H_2O$ (0.043M) were mixed and precipitated with concentrated ammonia while stirring vigorously. The immediately formed black precipitate was washed several times with ultra-pure water until the pH decreased from 10.0 to 7.0. The precipitate was collected and refluxed in a mixture of 0.8M nitric acid and 0.21M aqueous $Fe(NO_3)_3.9H_2O$ for 1 h. During this step, the initial black slurry turned brown and formation of nitric oxide was observed. The system was allowed to cool down to room temperature, the remaining liquid was discarded, and 100 ml of ultra-pure water was added to the slurry to re-disperse the precipitate. The brown suspension was dialyzed for 2 days

against 0.01M nitric acid, and stored at 4°C. During this final synthesis step, the Fe_3O_4 mostly oxidized to Fe_2O_3.

4.2.2 Device Fabrication

Microfluidic devices were fabricated with poly(dimethylsiloxane) (PDMS, Sylgard 184, Dow Corning, Switzerland) *via* soft lithography technique. Silicon wafers spin-coated with SU-8 50 photocurable epoxy (Microchem, Inc.) to a thickness of 60 μm and baked. Lithography, development and annealing (at 150°C) procedures were performed at the EPFL Center for Micronanotechnology (CMi) to obtain negative master mold on the normal 4 inch silicon wafer. The surface of molds was modified using a self-assembled monolayer (SAM) of trimethylethoxy silane (Sigma) by vapor exposure for 40 min to prevent PDMS sticking. PDMS monomers and curing agent (10:1), poured over the mold, degassed in desiccators for 30 min, and cured in the oven (Memmert) at 80°C for 1 h. After curing, PDMS was removed from the mold and required holes were punched using a 150 μm diameter punch. The PDMS was then bonded to a glass slide using O_2 plasma (100 mW, 1 min; Diener electronic GmbH). The PDMS-based microfluidic device consists of two inlets for water, one for the polymer/SPIONs/drug solution in THF, and one outlet. The water flow was split into two streams at the flow focusing cross-junction. The mixing channel was 120 μm wide, 50 μm high and 1 cm long. Aqueous solution of Fluorescein sodium (Sigma) and water were used to determine the range of stable flow rates (data not shown).

4.2.3 Synthesizing of (hybrid) nanoparticles

For the bulk synthesis of (hybrid) NPs (HNPs), PLGA/PLGA-BP solution in THF (5 $mg.mL^{-1}$) was prepared (with-/out SPIONs) under stirred condition. The nanoprecipitation

and formation of the HNPs was performed by drop-wise addition of this solution to 25 mL of water while stirring.

For the drug-loaded HNPs, Paclitaxel (PTX, Sigma-Aldrich) was dissolved in THF and mixed with the polymeric (PLGA/PLGA-BP) solution. HNPs were then synthesized according the same procedure described above.

For the microfluidic synthesis of NPs, PLGA/PLGA-BP solution in THF (5 $mg.mL^{-1}$) was prepared under stirred conditions and then introduced into chip as the core flow using syringe pumps (Harvard Apparatus, PHD2000; HA200I model). The water streams, as the non-solvent, were introduced to the chip as lateral flows. To vary the degree of flow focusing, the flow ratios (FRs) of the polymer solution and water streams were adjusted using micropumps.

For the drug-loaded HNPs, PTX was dissolved in THF at initial loading of 10 wt% (0.5 $mg.mL^{-1}$) and mixed with the polymer (PLGA/PLGA-BP) solution. Microfluidics-assisted synthesis of HNPs was performed according to the same procedure as described above.

4.2.4 Characterization

Transmission electron microscopy (TEM; CM200-FEG-Philips) were used to characterize the synthesized NPs. A dilute suspension of NPs was prepared and deposited onto the Cu grid with a carbon film. The morphology and size of the particles were characterized via diffraction (amplitude) contrast and (for crystalline materials) through high-resolution (phase contrast) imaging. The TEM was equipped with a LaB6 source operating at 100 kV accelerating voltage. The images were analyzed using ImageJ software (version 1.44p) with at least 20 different images.

Dynamic light scattering (DLS) and zeta potential measurements were performed using a Zetasizer (Zetasizer 3000HS, Malvern Instruments Ltd., Worcestershire, UK) in backscattering mode at 173° for the diluted suspensions in water.

Transmittance of the prepared samples was measured at room temperature (20°C) with a Shimadzu UV mini 1240 UV/visible spectrophotometer at the wavelength of 550 nm. Turbidity (τ) was calculated from the transmittance based on the Beer-Lambert law (*160*):

$$\tau = -\frac{1}{L}\, ln\left(\frac{I_t}{I_0}\right) \qquad (\text{Eq. } 4-1)$$

Where, L is the length of light path in the sample cell (1.0 cm quartz cuvette), I_t is the intensity of the light transmitted through the sample, and I_0 is the intensity of the light transmitted through the solvent (*i.e.*, deionized water). Measurements were repeated at least three times and mean values were reported.

The magnetic properties of NPs were evaluated using a vibrating sample magnetometer (VSM, ADE 4HF) at room temperature.

To determine the *in vitro* drug release profile, lyophilized PTX-loaded HNPs (1 mg) were dispersed in 1 mL of phosphate buffered saline (1X PBS, pH 7.4). The solutions were placed into a dialysis cartridge (3500 Da, Thermo Scientific, Rockford, IL) and immersed in 1 L PBS while gently shaken in a 37°C water bath. At predetermined time intervals, aliquots of the buffered solutions were collected for analysis, and an equivalent volume of fresh PBS was added to the water bath.

The PTX concentration was measured with the high-performance liquid chromatography (HPLC) by mixing the 1 mL sample with 1 mL of acetonitrile. A reverse phase C18 column was used as the stationary phase and the mobile phase was consisted of acetonitrile/water (60:40 vol/vol). Separation was carried out at a flow rate of 1 $mL.min^{-1}$ and PTX was

detected at the wavelength of 230 nm. This method was evaluated over a linear range of 1–100 μg.mL^{-1}. In this range, the percent deviation from theoretical value was found to be less than 5% and the coefficients of linearity remain greater than 0.96 using clean PTX standards. The PTX concentration in the solution was corrected to eliminate the sampling effects according to following equation (*99*):

$$C_n^l = C_n[V_T/(V_T-V_S)](C_{n-1}^l/C_{n-1}) \quad \text{(Eq. 4-2)}$$

Where, C_n^l is the corrected concentration of the n^{th} sample, C_n is the measured concentration of PTX in the n^{th} sample, C_{n-1} the measured concentration of the $(n-1)^{th}$ sample, V_T is the volume of receiver fluid, and V_S represents the volume of sample drawn (1 mL).

lyophilized PTX-loaded nanoparticles (1 mg) were dissolved in THF and the PTX concentrations were measured using a same HPLC protocol as mentioned before. The drug loading content and loading efficiency were determined by applying the following equations:

PTX Loading content = (weight of the loaded PTX/weight of the NPs)×100 (Eq. 4-3)

PTX Loading efficiency = (amount of PTX in the NPs /initial amount of the PTX)×100

(Eq. 4-4)

Relative activities of PTX were evaluated by measuring the maximum rate of tubulin polymerization relative to the standard samples. The stability of PTX in the free and encapsulated states was investigated by measuring their activities using the tubulin protein assay after storage at temperatures of 25°C and 37°C over two weeks in 96-well plates according to previously reported protocols (*161*). In brief, at defined time intervals of 1 day, NPs were separated using centrifugation and re-dispersed in water at pH 4.5 to extract

the PTX from the NPs. The PTX was then separated using HPLC to perform a tubulin protein assay. PTX at defined concentrations in the 1-10 µM range was reacted with 50 µl of tubulin protein solution (general tubulin buffer, tubulin glycerol buffer, 1 mM GTP) and the reaction was followed by measuring the increase in apparent absorption at 350 nm over 1 h at 37°C using an ELISA plate reader (Safire II, Tecan AG, Mannedorf, CH).

10 ml of blood was acquired from mice and 2% w/v RBC solution was obtained. In brief, the blood was first centrifuged at 5000 rpm at 4°C for 10 min. The supernatant was then removed, and the erythrocytes were re-suspended with ice-cold PBS (pH = 7.4), followed by repeated centrifugation. This procedure was repeated four times to ensure removal of released hemoglobin. Finally, cells were resuspended in ice-cold PBS to provide RBC solution (2% w/v). The nanoparticles and Polyethylenimine (PEI) as reference polymer was also prepared at serial concentrations of 100, 200, 400, and 1000 $\mu g.ml^{-1}$ with PBS (pH = 7.4). Then, 2 ml of the nanoparticle suspensions were added to centrifuge tubes containing 2 ml of the 2% w/v RBC solution and incubated at 37 °C for 1 h. Subsequently, the samples were centrifuged for 10 min at 2000 rpm, and 200 µl aliquots of the supernatants were transferred to 96-well plates. Absorbance of the released hemoglobin was measured at wavelength of 545 nm using a microplate reader.

To evaluate the binding capacity of the synthesized bone-targeting and unconjugated NPs to bone, hydroxyapatite binding assay was carried out in vitro, using the PLGA-FITC as a fluorescence marker (*162*). Briefly, FITC-labeled NPs were dispersed in PBS (1X, pH 7.4) at concentration of 2.5 $mg.ml^{-1}$ (pH 7.4) and incubated with 200 mg of hydroxyapatite powder (HA, Sigma-Aldrich) in a final volume of 10 ml. The incubated samples were centrifuged at 5000 rpm for 5 min and 2 ml of supernatant solution was collected at the times of 0, 5, 15, 30, 45, and 60 min. The fluorescence intensity of supernatant was assayed to detect unbind nanoparticles using spectrofluorophotometer (RF-5301PC, Shimadzu, Kyoto, Japan) at excitation wavelength of 496 nm. As positive controls, both PLGA-

SPION-BP/ PLGA-SPION nanoparticles were incubated at the same condition without HA powder. The HA binding efficiency (in percent) was estimated as mean value of at least three independent experiments. One drop of the precipitated HA powders on a glass slide was imaged using fluorescent microscope to visually show the binding of FITC-labeled NPs.

For pharmacokinetics (blood circulation) studies, nine female BALB/c mice (18–21 g) were randomly divided into three groups for the three different kinds of NPs. All mice were fed with commercial diet and water *ad libitum* and were on alternating 12 h light/dark cycles. All three groups were injected *via* tail vein at the same dose of 2 mg per kg of mice's body weight. Blood samples were drawn from the retro-orbital sinus at different times of 0 min, 30 min, 1 h, 2 h, 5 h, 10 h, 18 h, 30 h, 48 h, 65 h, and 72 h into heparinized tube and then samples were centrifuged for 15 min. The plasma was separated and stored at −20 ^{o}C in dark before analysis. The plasma concentration of NPs defined based on fluorescence intensity of FITC groups using BioTek Microplate Reader (Winooski, VT). The normalized plasma concentrations of applied NPs are shown as a function of time. The data were fitted to a two-compartment model, from which the fast and slow half-lives characterizing the NPs formulations were extracted.

Luciferase- positive MDA-MB-231 breast cancer cell line were plated at 40% confluency and cultured for 24 h. The cells were then trypsinized, washed, and resuspended in DMEM at 10^7 cells.ml^{-1} and kept on ice before injection. Female BALB/c mice were given an intratibial injection of the luciferase positive breast cancer cell line (0.1 ml). The mice were anesthetized with mixture of Xylazine and Ketamine before injection. After a week of tumor inoculation, mice were randomized in four different groups (i) PBS only (control sample), (ii) non-targeted NPs (microfluidic NPs), (iii) targeted bulk-synthesized NPs (bulk NP-BP), and (iv) targeted microfluidic-synthesized NPs (microfluidic NP-BP). At the next day of tumor inoculation (day 1) and day 30, animals were injected with 0.1 ml of

D-luciferin (10 $mg.ml^{-1}$) in PBS, and after 10 min, imaged under anesthesia with 2.5% isofluorane by bioluminescence imaging using the Xenogen bioluminescence imaging system (Xenogen Corp., Hopkinton, MA). At experimental endpoints, luciferin-injected animals were sacrificed based on institutional animal care and use guidelines. Luminescence is expressed as photons/sec/ROI (region of interest) minus background luminescence. The change in bioluminescence signal over time considered as an indicative of tumor size in this study. For biodistribution studies, after scarifying of mice (day 30 after treatment), selected organs were dissected and placed inside the imaging system. Mice autofluorescence and background signals were eliminated.

Apoptosis cells were identified through a TUNEL assay (In Situ Cell Detection Assay kit; Roche) according to the manufacturer's protocol. Images were captured by fluorescence microscope.

The results are statistically analyzed using unpaired t-tests. For all tests the statistical significance is set at $p < 0.05$. $p < 0.01$ is considered as statistically very significant.

2.5. Computational Details

Molecular Models of PLGA and PLGA-BP

PLGA molecules are copolymers of poly lactic acid (PLA) and poly glycolic acid (PGA). For MD simulations, block PLGA copolymers consisting of PLA and PGA both with degree of polymerization of 30 was first constructed, as shown in Supplementary Figure 4-1a. Subsequently, for the case of PLGA-BP copolymer, which are terminated by BP, the BP was covalently bonded from its amino group ($-NH_2$) to one end of PLGA having free carboxylic acid group. After construction, molecular structure of both PLGA and PLGA-BP polymers were optimized by means of Smart minimizer algorithm. Then, two three-dimensional (3D) cubic amorphous cells, containing only one PLGA and PLGA-BP

polymeric materials, were created at a density of 1 g.cm^{-3} by making use of Amorphous Cell module implemented in Materials Studio software (*114*). These 3D simulation cells were initially optimized for 2000 energy minimization steps, and then equilibrated by MD simulations carried under NVT ensemble for 100 ps at 300 K. The resulting optimized PLGA and PLGA-BP molecules from MD simulations were placed on top of different HA surfaces for subsequent simulations.

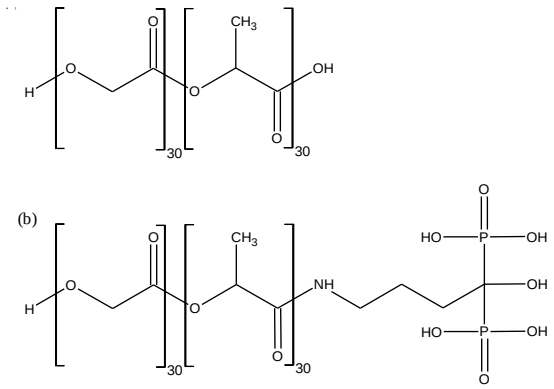

Figure 4-1 Chemical structure of (a) poly lactic-co-glycolic acid (PLGA), and (b) poly lactic-co-glycolic acid covalently bonded with bisphosphonate (PLGA-BP) used for MD simulations.

2.5.1. HA surfaces

HA materials have crystallographic structure with chemical formula of ($Ca_{10}(PO_4)_6(OH)_2$), hexagonal *$P6_3/m$* space group, as well as unit cell parameters of a=b=9.424 Å, c=6.879 Å and ά=β=90°, γ=120° (*163*). In order to cover potential interfacial interactions of HA with PLGA (and PLGA-BP), three different HA crystallographic surfaces including (100), (110) as well as (001) were selected for current MD simulation analyses, as these are the most commonly studied HA surfaces in experiments (*164, 165*). These surfaces were built by cleaving HA unit cell along the corresponding HA surface with a surface thickness value of around 13 Å. Surface area of all HA surfaces were increased in both directions so as to ensure appropriate surface interactions with neighboring PLGA and PLGA-BP molecules.

The constructed surfaces were then converted to 3D periodic cells by applying a vacuum space of thickness 150 Å above the surface. The use of this vacuum space above HA surface interacting with polymers together with certain surface thickness of 13 Å is to restrict PLGA and PLGA-BP intermolecular interactions to only one side of HA surfaces. Energy-minimized PLGA and PLGA-BP were then laid on top of as-built HA surfaces at a location more than at least 12 Å apart from the upper surface of HA, as studied for various HA surfaces.

4.2.5 MD simulations

MD simulations of PLGA and PLGA-BP equilibration phase, and simulation of PLGA and PLGA-BP positioned on top of different HA surfaces (i.e., HA-PLGA and HA-PLGA-BP) were performed by using COMPASS (condensed-phase optimized molecular potentials for atomistic simulation studies) force field (*115, 116*). Partial atomic charges for HA surfaces were assigned as follow: hydroxyl hydrogen atoms, +0.6; hydroxyl oxygen atoms, -1.6; oxygen atoms in PO_4, -1.4; phosphorus atoms, +2.6; calcium atoms, +2, which were taken from reference (*166*). Similar to MD simulation of 3D cells for PLGA and PLGA-BP, all HA-PLGA and HA-PLGA-BP simulation systems were first optimized by running 2000-step minimization. This was followed by a 1-ns MD simulation under NVT ensemble conditions at 300 K.

All atomistic MD simulations were carried out using Discover module of Materials Studio software (*114*). Non-bonded van der Waals (vdW) and electrostatic interactions were taken into account using Ewald summation method. Velocity Verlet integration algorithm was used to solve Newton's equation of motion with a time step of 1 fs (*117*). Andersen thermostat was used to control the temperature during NVT dynamics simulations. Periodic boundary conditions (PBC) were imposed in all three directions. In the case of HA-PLGA

and HA-PLGA-BP, positions of all atoms in HA surface were kept fixed during MD simulations.

The final structure attained at the end of 1-ns NVT MD simulation of all HA-PLGA as well as HA-PLGA-BP simulation systems were used to determine the interaction (binding) energy of PLGA and PLGA-BP with different HA surfaces. Interaction energy was calculated according to the following equation:

$$\Delta E_{binding} = E_{HA\text{-}PLGA\text{-}BP} - (E_{HA} + E_{PLGA/PLGA\text{-}BP}) \quad \text{(Eq. 4-5)}$$

Where, $E_{PLGA/PLGA\text{-}BP}$ represents potential energy of entire simulation system (that is, HA-PLGA or HA-PLGA-BP) in which all atoms constituting HA surfaces have been kept constrained, E_{HA} is potential energy of unconstrained HA surfaces without PLGA or PLGA-BP, and $E_{PLGA/PLGA\text{-}BP}$ indicates potential energy of PLGA or PLGA-BP without HA surfaces.

The increased PLGA interaction energy with HA surfaces upon its BP-modification is as a result of stronger interfacial interactions, for instance, strong electrostatic interactions with uppermost calcium atoms, which is probably the strongest for HA (110) according to higher concentration of calcium atoms on its top surface shown, and hydrogen bonding interactions. Here, the intermolecular hydrogen bonding interactions between BP terminal groups in PLGA-BP with surface oxygen atoms in PO_4 units as well as hydroxyl oxygen and hydrogen atoms in HA surfaces are investigated. To further analysis of intermolecular interactions between surfaces of HA and PLGA (and PLGA-BP) polymeric materials, which are crucial for enhanced interactions of HA-PLGA-BP as compared to HA-PLGA systems, radial distribution function (also called pair correlation function) were evaluated for different atomic pairs. For a pair of atoms consisting of A and *B*, RDF $g_{A\text{-}B}(r)$, which indicates the probability distribution of *B* atoms around reference *A* atoms, is defined as follows:

$$g_{A-B}(r) = \frac{\left(\frac{n_B}{4\pi r^2 \Delta r}\right)}{\left(\frac{N_B}{V}\right)} \qquad \text{(Eq. 4-6)}$$

Where n_B is the number of *B* atoms located around reference *A* atoms inside a spherical shell with thickness Δr, N_B is the total number of *B* atoms and *V* is the cell volume.

4.3 Results and Discussion

Controlled nanoprecipitation of PLGA and PLGA-BP into NPs was achieved using a polydimethylsiloxane (PDMS)-based cross-junction microfluidic device consisting of perpendicular channels, which provides a hydrodynamically focused Tetrahydrofuran (THF) polymeric solution in in a stream of water, as shown in Figure 4-2a. The lateral streams of water act as a non-solvent for PLGA/PLGA-BP, and forms NPs during lateral diffusion of water molecules (molecular mixing). The microfluidic core flow was previously studied by using Fluorescein solution as the core flow, and monitoring flow stability with a fluorescent microscope to determine the range of flow rates that create a stable mixing interface. In microfluidic based synthesis, nanoparticle properties are greatly affected by the mixing time (τ_{mix}, residence time in the microreactor), which can be adjusted by varying the flow rate of polymer solution to water. Therefore, the flow ratios (FR) were adjusted from 0.03 to 0.2 (*167*), the fluidically stable range previously determined by the fluorescent flow experiment. This FR range resulted in τ_{mix} to vary from 2.5 to 75 ms (Figure 4-2b).

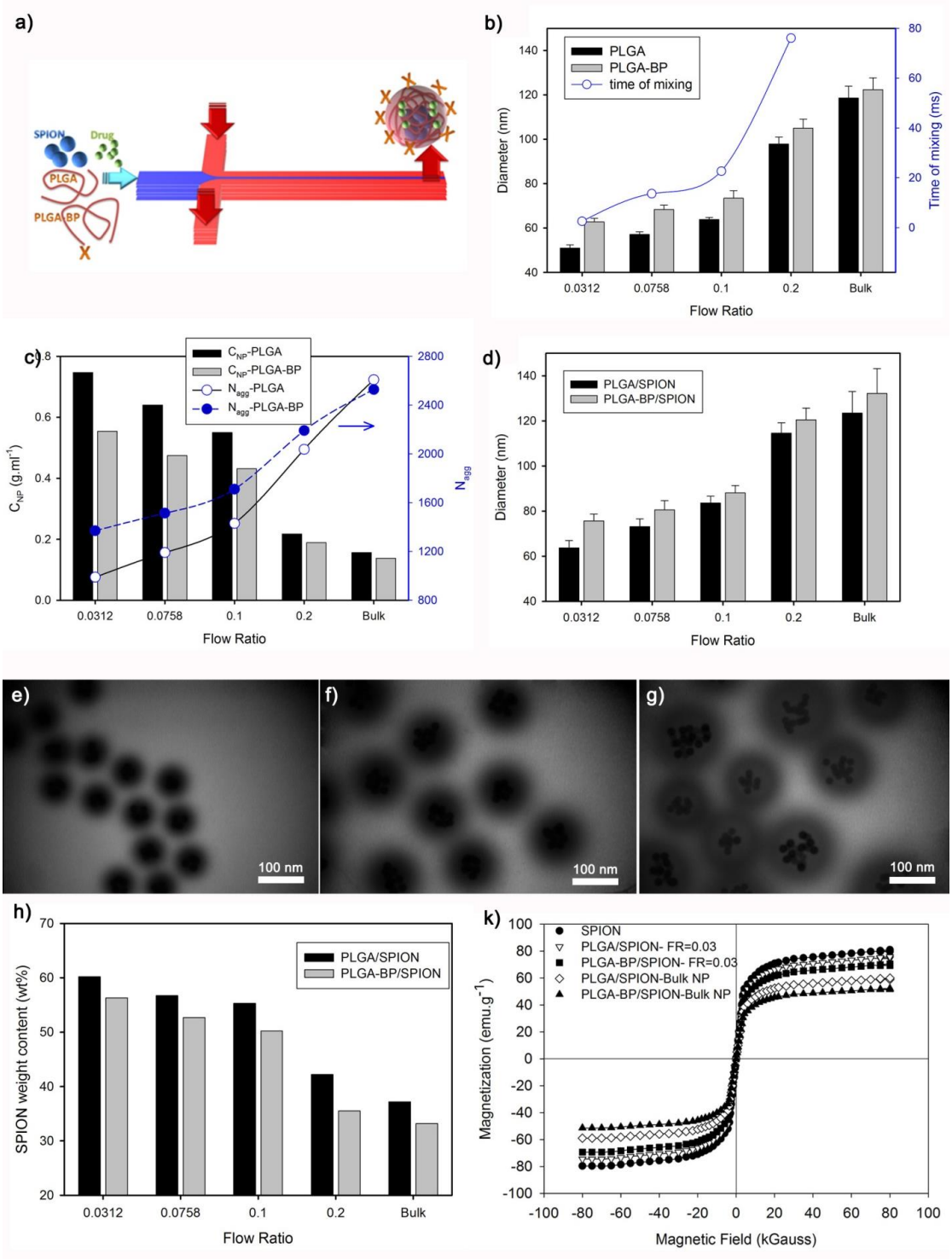

Figure 4-2 The physical characteristics of microfluidic synthesized nanoparticles. (a) Schematic representation of the cross-junction microfluidic device used for controlled formation of PLGA based (magnetic/targeted) NPs. (b) The hydrodynamic diameter of the microfluidic/bulk synthesized nanoparticles. The mixing time for each flow ratio (FR; the ratio of flow rate of polymer solution to water flow) was calculated and shown as open circles.

(c) Local polymer concentration (C_{NP}) inside the PLGA/PLGA-BP nanoparticles as a function of the flow ratio. Aggregation numbers (N_{agg}) of the PLGA/PLGA-BP chains in the corresponding nanoparticles as a function of flow ratio. The lines are only as a guide. (d) The hydrodynamic diameter of the SPIONs-loaded synthesized hybrid nanoparticles based on PLGA and PLGA-BP using the microfluidic platform or the bulk synthesis method. (e-g) TEM images of the magnetic hybrid nanoparticles; PLGA-BP/SPIONs: FR=0.03 (e), PLGA-BP/SPIONs: FR=0.1 (f), PLGA-BP/SPION: bulk (g). (h) The iron weight content of the loaded SPIONs into PLGA/PLGA-BP nanoparticles at four different flow ratios in comparison with those formed via the bulk mixing method. (k) Magnetic hysteresis for the microfluidic/bulk synthesized SPIONs-loaded PLGA/PLGA-BP nanoparticles in comparison with the bare SPIONs.

In this article, we compared the formation of NPs composed of pure PLGA with those formed from co-precipitation of PLGA:PLGA-BP chains. NMR analysis showed the conjugation yield of PLGA-BP to be 41 mol%. We designed the final product to have 20 mol% BP (*i.e.*, PLGA-BP), thus 50:50 composition of PLGA: PLGA-BP was used in the NPs synthesis.

Compared with bulk mixing methods, it has been shown that microfluidic synthesis locks NPs kinetically in a rapid mixing regimen that leads to the formation of smaller NPs with a higher degree of monodispersity (*14, 168*). Dynamic light scattering (DLS) results showed that longer mixing time leads to the larger NPs for both PLGA and PLGA/PLGA-BP NPs (Figure 4-2b). The hydrodynamic size of bisphosphonate-PLGA NPs was found to be larger than unmodified PLGA NPs. This difference was more pronounced at lower FRs where an approximate size difference of 23% was observed between the compounds at a 0.03 FR. The Zeta potentials of the resultant NPs are shown in Figure 4-3.

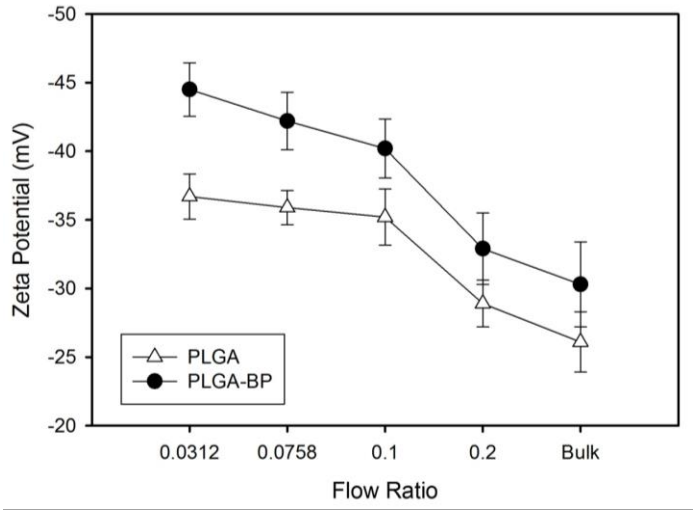

Figure 4-3 Zeta potential values for PLGA and PLGA-BP nanoparticles that are formed at different flow ratios as well as bulk synthesized nanoparticles.

Generally, the hydrodynamic size of colloidal polymeric NPs depends on the polymer contents and their swelling state, which are driven by the competing intra/intermolecular interactions during the mixing process. In order to quantify the polymer concentration of the NPs, we employed a recently developed method for estimating the local polymer concentration inside the spherical NPs (*45, 160*). Using this approach, valuable information on the PLGA NPs can be obtained based on their size (Figure 4-2b) and the turbidity of their suspension (Table 4-1). Local polymer concentration in NPs, C_{NP}, was calculated based on Eq.5 (*45, 160*),

$$\tau = \frac{3\,c_t}{2c_{NP}\,R_h}\left(1 - \frac{2}{wc_{NP}}\left\{sin(wc_{NP}) - \frac{1}{wc_{NP}}[1 - cos(wc_{NP})]\right\}\right) \qquad \text{(Eq. 4-7)}$$

where τ, C_t, and R_h are respectively turbidity of the NPs suspension, total polymer concentration in the suspension, and hydrodynamic radius of the NPs, $w = \frac{4\,\pi\,R_h(dn/dc)}{\lambda\,n_0}$, where λ, n_0, and *dn/dc* are the wavelength for the turbidity measurements, the refractive index of the solvent, and the refractive index increment of the polymer in the measurement,

respectively. It is worth noting that this method was developed for spherical particles with low polydispersity index (PDI), and the narrow size distribution of our microfluidic synthesized NPs (PDI<0.13) meets this requirement.

Table 4-1 The turbidity and calculated physical characteristics of the synthesized NPs at different FRs.

PLGA Nanoparticles

F.R.	turbidity	Cnp (g/ml)	Nagg	N (particles/ml)
0.031	0.903	0.7468	989	4.83E+14
0.075	0.841	0.6399	1191	4.01E+14
0.1	0.824	0.55	1430	3.34E+14
0.2	0.513	0.2175	2037	2.35E+14
Bulk Mixing	0.438	0.1562	2608	1.83E+14

PLGA-BP Nanoparticles

F.R.	turbidity	Cnp (g/ml)	Nagg	N (particles/ml)
0.031	0.989	0.5542	1370	3.49E+14
0.075	0.9466	0.4743	1514	3.16E+14
0.1	0.907	0.4316	1710	2.80E+14
0.2	0.5512	0.189	2191	2.18E+14
Bulk Mixing	0.4794	0.1377	2528	1.89E+14

The C_{NP} values calculated using Eq.5 at various flow ratios are reported in Figure 4-2c. The results show that smaller, but more compact; NPs are formed at lower flow ratios. The higher polymer concentration inside the unconjugated PLGA NPs can be attributed to the repulsive forces of the phosphonate groups of the PLGA-BP chains. However, the difference in the compactness (C_{NP}) of these groups was found to be less pronounced at higher flow ratios. The compactness of the bulk-synthesized NPs, despite their much higher PDI, also estimated based on the Eq.5. The data in Figure 4-2 indicate that the

hydrodynamic flow focusing approach can tune the compactness of the polymeric NPs precisely, resulting in NPs with different properties customized for different applications.

As shown in Figure 4-2 (b-c), the size of the NPs increased while their compactness (C_{NP}) decreased with increasing the mixing time. This could be due to either swelling and/or increased number of aggregated chains to form PLGA NPs. To differentiate between the two, the aggregation number of polymer chains (N_{agg}) must be calculated. Having determined C_{NP}, the molecular weight of NPs (denoted as M_{NP}) can be calculated as:

$$M_{NP} = \frac{4}{3}\pi {R_h}^3 C_{NP} N_A \qquad \text{(Eq. 4-8)}$$

where N_A is Avogadro's number.

Accordingly, the aggregation number of polymer chains forming NPs, N_{agg}, can be determined from Eq.7,

$$N_{agg} = \frac{M_{NP}}{M_n} \qquad \text{(Eq. 4-9)}$$

where M_n is the average molecular weight of the participating polymers.

Upon microfluidic mixing, rapid nanoprecipitation of polymer chains leads to the formation of the NPs. As shown in Figure 4-2c, N_{agg} rises with increasing flow ratio. At the lower flow ratios, mixing time is shorter than the time required for aggregation, $\tau_{mix} < \tau_{agg}$; hence, a lower number of polymeric chains are kinetically locked inside the NPs. Therefore, the increase in the hydrodynamic radius of NPs was as a result of increased number of aggregated chains that are loosely packed at the higher flow ratios. This phenomenon was more pronounced in the case of PLGA-BP chains. In this view, adjustable microfluidic mixing has enabled varying mixing times in order to optimize the precipitation

of the PLGA chains. The volume number density of NPs (the number of particles per unit volume of the suspension) is one of the important properties of nanoparticulate systems, but is rarely reported due to experimental difficulties, despite its practical importance. Using the known C_{NP} values already determined, the number density of the particles, N, could be estimated based on the following equation (we assume volume filling),

$$N = \frac{3\ c_t}{4 c_{NP} \pi\ {R_h}^3} \qquad \text{(Eq. 4-10)}$$

It was found that the number density of synthesized NPs increases with decreasing the flow ratio (*i.e.*, time of mixing) (Table 4-1).

Many researchers are using microfluidic platforms to design finely tuned NPs (*14, 15, 20, 23, 99, 154-156*). For example, Valencia *et al.* developed a microfluidic rapid mixing system to produce lipid-polymer-quantum dot hybrid NPs (*169*). In a recent study, complex nanocapsules composed of dendritic polyethylene NPs as anticancer drug nanocarriers was reported (*156*). Here we demonstrate the capability of a microfluidic approach to synthesize magnetic hybrid NPs (HNPs). By introducing superparamagnetic iron oxide NPs (SPIONs) into the microfluidic core flow, the SPIONs are entrapped inside the polymeric chains during polymeric nanoparticle formation. The average hydrodynamic diameter of the synthesized SPIONs by our co-precipitation method was 11±4 nm. The same flow ratios as the previous PLGA/PLGA-BP experiments were also used to synthesize SPIONs-loaded NPs. As shown in the Figure 4-2d, the size of loaded NPs was found to increase in the range of 4-25% for PLGA and 8-21% for the PLGA-BP-based HNPs. TEM images of the SPIONs-PLGA-BP HNPs at the flow ratios of 0.03 (48±5 nm), 0.1 (67±16 nm), as well as the bulk synthesized (111±21 nm) HNPs are presented in the Figure 4-2 (e-g), respectively. All HNPs were spherical. The entrapped solid SPIONs are recognizable from their higher density on the TEM images. More rapid mixing regimens

resulted in a higher number of SPIONs being encapsulated inside the HNPs (Table 4-2) in both PLGA and PLGA/PLGA-BP systems. This phenomenon could be due to the narrower flow focusing region at the lower flow ratios (the rapid mixing regime) that more quickly facilitates the solvent exchange process and can result in faster precipitation of PLGA (PLGA-BP) chains in a more confined volume, which increases the probability of SPION entrapment. The iron content of the HNPs was measured by ICP-OES (Inductively Coupled Plasma – Optical Emission Spectrometry) after digestion with HCl (Figure 4-2h). As illustrated, the efficiency of SPION entrapment was highly affected by the mixing time. In the more rapid mixing regimens, the weight content of SPIONs was in the range of 55-60% for PLGA HNPs and 50-56% for the PLGA-BP HNPs.

Table 4-2 Calculated numbers of SPION particles that can be trapped in the synthesized nanoparticles (NPs) at different FRs.

PLGA Nanoparticles

F.R.	Radius (nm)	Volume of each NP (mL)	Polymer Weight of each NP (mL)	Weight of SPION NPs inside HNPs (g)	Number of SPION in final HNPs (particles)	Volume fraction (vol. %)
0.031	25.48	6.93E-17	5.17E-17	3.12E-17	9	9.37
0.075	28.54	9.74E-17	6.23E-17	3.53E-17	11	7.56
0.1	31.9	1.36E-16	7.48E-17	4.14E-17	12	6.34
0.2	48.9	4.9E-16	1.07E-16	4.50E-17	13	1.91
Bulk Mixing	59.3	8.73E-16	1.36E-16	5.08E-17	15	1.21

PLGA-BP Nanoparticles

F.R.	Radius (nm)	Volume of each NP (mL)	Polymer Weight of each NP (mL)	Weight of SPION NPs inside HNPs (g)	Number of SPION in final HNPs (particles)	Volume fraction (vol. %)
0.031	31.37	1.29E-16	7.17E-17	4.03E-17	12	6.50
0.075	34.16	1.67E-16	7.92E-17	4.17E-17	12	5.21
0.1	36.71	2.07E-16	8.94E-17	4.49E-17	13	4.51
0.2	52.51	6.06E-16	1.15E-16	4.07E-17	12	1.40
Bulk Mixing	61.2	9.6E-16	1.32E-16	4.39E-17	13	0.95

The hysteresis loop for various HNPs at room temperature is shown in Figure 4-2k. The absence of remanence and coercivity confirmed the superparamagnetic properties of the SPION-loaded HNPs. The magnetic saturations for the microfluidic synthesized HNPs at FR 0.03 were approximately 66 and 60 emu.g^{-1} for the PLGA/SPIONs and PLGA-BP/SPIONs, respectively. These values are 94% and 86% of the magnetic saturation of the pristine SPIONs (≈70 emu.g^{-1}). The bulk synthesis resulted in lower saturation values of 51 and 44 emu.g^{-1} for the PLGA/SPIONs and PLGA-BP/SPIONs, respectively. These results were expected since a larger number of SPIONs were encapsulated in the HNPs with microfluidics. Moreover, the more compact nature of the NPs assembled via microfluidics brings the magnetic particles closer to each other and subsequently alters the magnetic character of the HNPs.

The colloidal stability of the hybrid NPs were also studied by measuring their hydrodynamic size as a function of time at 4 and 25ºC. No significant change was observed in the size of the HNPs over one month.The partial amphiphilic nature of PLGA chains allows for the encapsulation of both hydrophilic and hydrophobic compounds. In addition to encapsulation of magnetic NPs in the PLGA/PLGA-BP NPs, we further aimed to load Paclitaxel (PTX), a potent hydrophobic anticancer drug, inside the HNPs to further develop them as multifunctional HNPs. Surprisingly, after encapsulation of PTX into the HNPs, the size of NPs was decreased by approximately 10% (Figure 4-4a). This phenomenon could potentially be due to the overall increase in the hydrophobicity of the PLGA mixture in the presence of PTX molecules, which provides more effective PLGA chain association (*14*). Loading efficiency, with the initial drug content of 10 wt%, was evaluated and plotted as a function of flow ratio in Figure 4-4b. Simultaneous injection of drug/polymer mixtures is an effective route to encapsulate hydrophobic drugs with nanoprecipitation. As previously reported, using controlled nanoprecipitation with microfluidics enables remarkably higher drug loading compared to conventional bulk mixing methods (*99*).

Figure 4-4b shows the loading efficiency of PTX in PLGA-BP HNPs was in the range of 73-80% in the rapid mixing regimen, and dropped to 50-58% with longer mixing. A similar trend was also observed for the non-conjugated PLGA NPs (Figure 4-4b). In should be noted that the presence of SPION does not (<5%) alter the encapsulation efficiency of PTX.

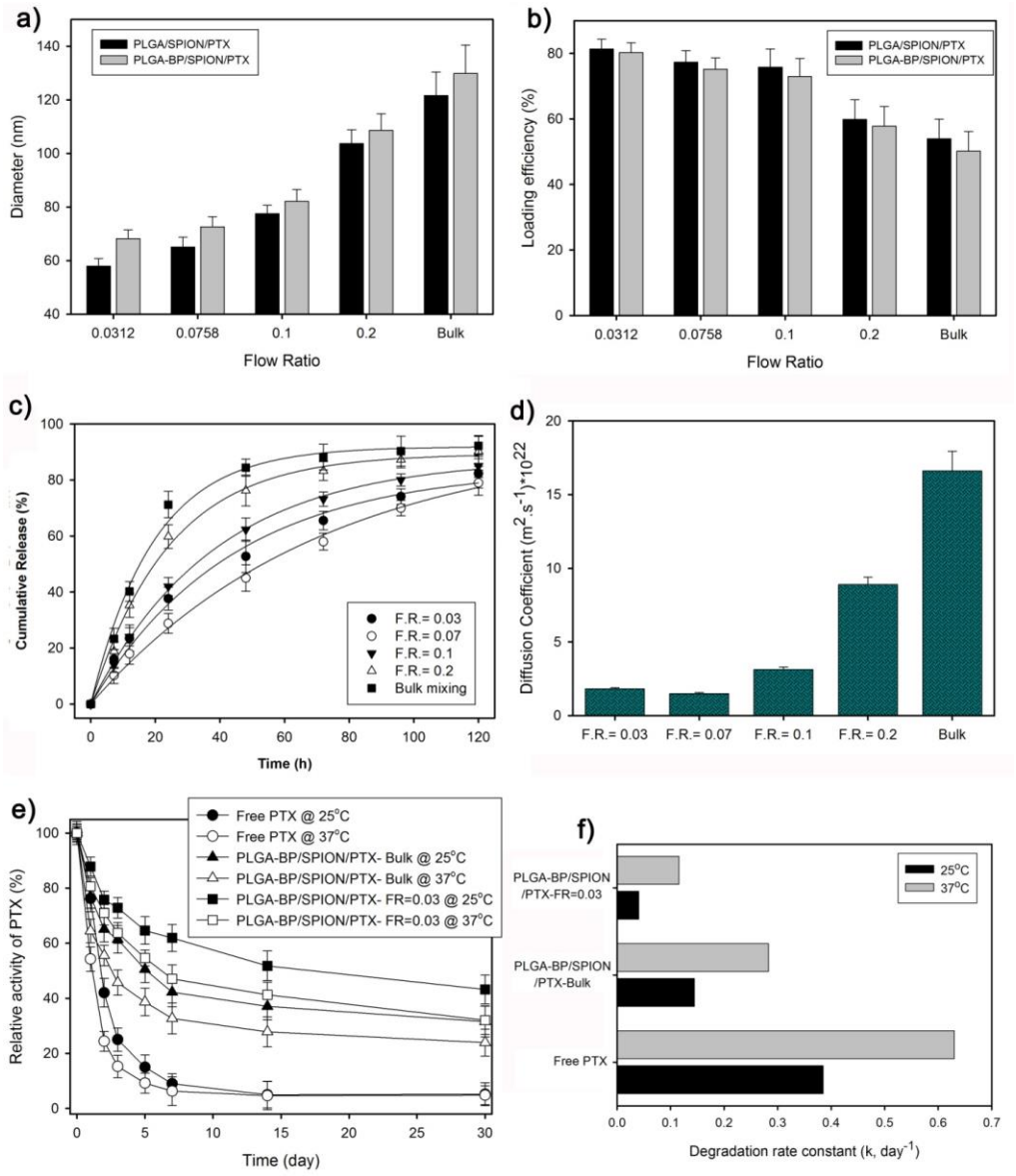

Figure 4-4 Various features of paclitaxel (PTX) loaded microfluidic synthesized hybrid nanoparticles. (a) The hydrodynamic diameter of PTX-loaded microfluidic/bulk synthesized nanoparticles based on PLGA and its BP-conjugated equivalent. (b) PTX loading efficiency as a function of the flow ratio in comparison with the nanoparticles synthesized *via* the bulk mixing method at an initial drug content of 10 wt%. (Mean ± SD, n = 5 independent experiments). (c) Cumulative *in vitro* release profiles of PTX from PLGA-BP/SPIONs-PTX

HNPs synthesized from various methods at pH 7.4 and at 37°C. (Mean ± SD, n = 3 independent experiments). (d) PTX diffusion coefficients from HNPs as a function of the mixing time. (e) Relative activity (%) of PTX at 25°C and 37°C for free drug and drug loaded microfluidic/bulk synthesized hybrid nanoparticles evaluated *via* the tubulin polymerization assay. (f) The PTX degradation rate constant (*k*) for the various drug loaded HNPs at 25°C and 37°C.

The *in vitro* drug release profile of the synthesized PLGA-BP/SPION NPs in PBS (Phosphate Buffered Saline, pH= 7.4) at 37 °C is shown in Figure 4-4c. The patterns exhibited a relatively sustained release over 5 days. As shown, the microfluidically synthesized HNPs showed slower release patterns, which could be attributed to their more compact nanostructures (Figure 4-2c). The required time to release half of the loaded drug ($t_{50\%}$) from the bulk synthesized HNPs was about 15.5 h, whereas this time was 39, 53.4, 32.7, and 20.1 h for HNPs formed at the flow ratios of 0.03, 0.075, 0.1 and 0.2, respectively. The slower release was associated with the higher compactness of the microfluidic synthesized HNPs. Furthermore, the diffusion coefficient of drug molecules from the HNPs was calculated (*156*) using Eq.9 and reported in Figure 4-4d.

$$\frac{M_t}{M\infty} = 6\left(\frac{D}{\pi R}\right)^{1/2} \qquad \text{(Eq. 4-11)}$$

Where M_t/M_∞ represents the fraction of released PTX at time *t*, *D* is the diffusion coefficient of the drug molecules and *R* is the hydrodynamic radius of HNPs. The results imply that compactness of the HNPs is the key factor in defining the release behavior. As expected, more compact HNPs showed significantly lower diffusion coefficients of 1.8×10^{-22}, 1.5×10^{-22}, and 3.1×10^{-22} $m^2.s^{-1}$, at the flow ratios of 0.03, 0.07, and 0.1, respectively. The NPs formed at the 0.2 flow ratio, as well as with bulk mixing (slow mixing regimen), showed larger diffusion coefficients of 8.9×10^{-22}, and 16.6×10^{-22} $m^2.s^{-1}$, respectively.

The efficiency of drug encapsulation and the drug release characteristics are important parameters in designing nanocarriers. However, it is equally important to assess the activity of the encapsulated drug. We used the tubulin polymerization assay at two different

temperatures, 25 and 37°C, for this purpose. Although the stability of PTX generally decreases at higher temperatures, this trend was less pronounced for drugs encapsulated in the microfluidic HNPs (Figure 4-4e). The time required for degradation of 50% of the initial PTX activity was found to be 413 and 144 h at 25 and 37°C for microfluidic HNPs at flow ratio of 0.03 (as an optimum sample due to its smaller size and sustained release properties), compared to 115 and 59 h for the bulk synthesized HNPs. The degradation half-life of the free PTX was also measured as 43 h at 25°C and 26 h and 37°C. As is depicted in Figure 4-4e, drug degradation is generally considered to be a first order process described by $ln(a/a_0) = kt$, where a is the activity of drug at time t, a_0 is the initial drug activity, and k is the degradation rate constant which can be calculated at the half-life of drug ($t_{1/2}$). As exhibited in Figure 4-4f, the degradation rate constant (k) for the PTX-encapsulated microfluidic synthesized HNPs is much smaller than the bulk synthesized HNPs and free PTX at both 25 and 37°C. Such improved PTX stability promises prolonged drug activity *in vivo*. Compact HNPs-PTX hampered diffusion of water molecules and protected the drug from epimerization and degradation (*99*).

Surface functionalizations of NPs are often necessary to impart specific capabilities for *in vivo* applications. The ideal NPs should prevent immune system recognition and red blood cell (RBC) hemolysis. It has been shown that negatively charged surface groups can protect NPs against such unfavorable events (*170*). A study of RBC hemolysis by HNPs at concentrations of 50, 100, 200, and 500 $\mu g.ml^{-1}$ compared to polyethylenimine (PEI), as a positive control, are shown in Figure 4-5. All HNPs showed low levels of RBC hemolysis even at higher concentrations, with no significant statistical difference among the samples.

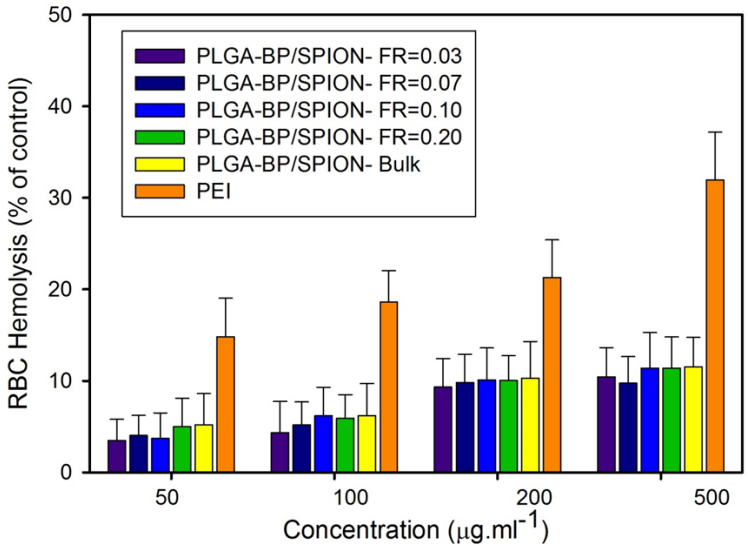

Figure 4-5 Hemolysis assay of PLGA-BP/SPION nanoparticles that are formed at different flow ratios as well as bulk synthesized nanoparticles in comparision with PEI as an control sample. Data are presented as the average value ± standard deviation (n> 3).

Due to their small size, NPs can reach their targets by passing through intercellular tight-junctions and diffuse with enhanced permeation and retention (EPR) (*171, 172*). Therefore, particles in the size range of 50-200 nm can passively target their sites of action (*168*). Introducing a targeting moiety to NPs can further enhance their targeting efficiency. In primary or metastasized bone cancers, bone tissue is often exposed at lysis sites (*157, 162*). Here we have introduced bisphosphonate (BP) molecules to the hybrid NPs as a bone targeting moiety to foster active targeting of bone tumors. BPs exhibit strong affinity to the exposed bone surfaces (*142, 157, 158, 162, 173, 174*) mainly because their phosphonate groups act as 'bone hooks,' although hydroxyl and nitrogen groups can also contribute through hydrogen binding to the hydroxyapatite (HA) structure (*175, 176*). The attachment of microfluidically synthesized BP-conjugated NPs at the surface of HA microcrystals was visually studied by using PLGA-FITC as a fluorescent marker. The molar ratio between PLGA/PLGA-FITC was calibrated for each sample independently, so that fluorescent intensity corresponds to nanoparticle concentration, not size. Figure 4-6a shows that NPs bind to HA surfaces after 30 min of incubation. The loosely bound particles were washed

away before fluorescence imaging. The fluorescence intensity of HNPs synthesized in the lower flow ratios (*i.e.*, rapidly mixed regimen) was found to be higher compared to the other NPs.

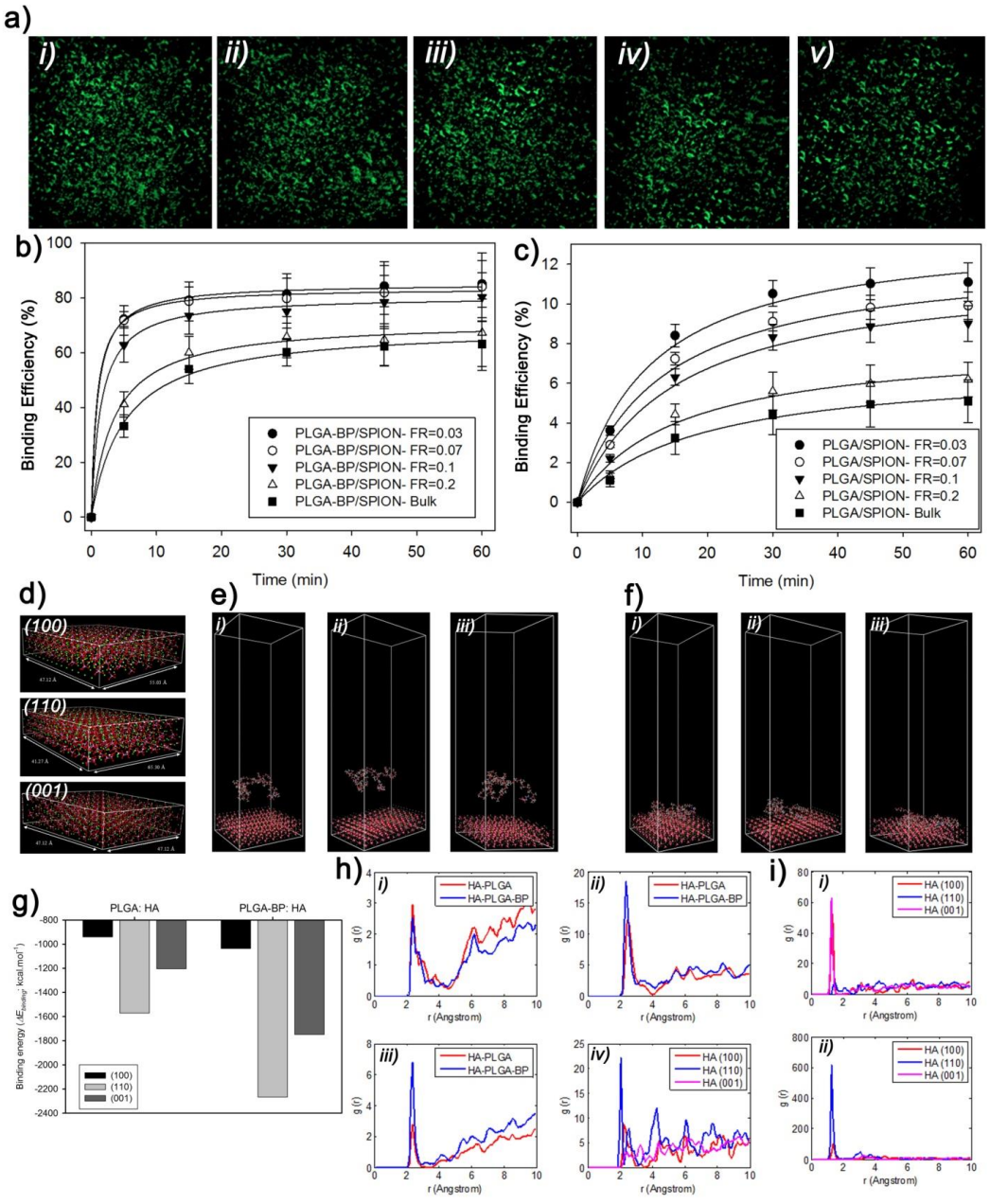

Figure 4-6 The binding affinity of HNPs to the bone minerals. (a) Fluorescent images of FITC-labeled BP-conjugated HNPs, which are formed via a microfluidic platform at different flow ratios of 0.03 (i), 0.07 (ii), 0.1 (iii), 0.2 (iv), compared with the bulk synthesized particles (v) at the surface of HA after 30 min of incubations and washing. (b) Binding kinetics of various

types of BP-conjugated and (c) non-conjugated FITC-labeled HNPs to the HA. The HNPs were incubated with HA microcrystals for 5, 10, 30, 45, and 60 min. (Mean ± SD, n= 3 independent experiments). (d) The structure of HA (100), (110), and (001) surfaces in the Ball & Stick style. The height (thickness) of all surfaces is approximately 13 Å. The color code is: oxygen atoms in red, hydrogen atoms in white, calcium atoms in green, and phosphorus atoms in purple. (e) Initial structures of (i) HA (100)-PLGA-BP, (ii) HA (110)-PLGA-BP, and (iii) HA (001)-PLGA-BP. All atoms are shown in line style. (f) Final equilibrated structures of (i) HA (100)-PLGA-BP, (ii) HA (110)-PLGA-BP, and (iii) HA (001)-PLGA-BP, obtained at the end of 1-ns NVT MD simulation. All atoms are shown in line style. (g) Binding energy (kcal.mol^{-1}) of PLGA and PLGA-BP polymers to different HA surfaces. (h) RDFs of oxygen atom double bonded to carbon in PLGA or PLGA-BP with calcium ions in (i) HA (100), (ii) HA (110), and (iii) HA (001) surfaces; (iv) RDFs of oxygen atoms in PLGA-BP with calcium ions for different HA surfaces. (i) RDFs of hydroxyl hydrogen atoms in BP bonded to PLGA with (i) oxygen atoms in PO_4 units and (ii) hydroxyl oxygen atoms in HA surfaces for different HA surfaces.

To estimate the binding capacity of the PLGA-SPIONs-BP NPs to bone tissue, a HA binding assay was employed *in vitro*. The binding efficiency of the PLGA-SPIONs and PLGA-SPIONs-BP to HA is shown in Figure 4-6 (b,c). Non-targeting PLGA-SPIONs showed low binding efficiency, in the range of 5-11%, whereas the targeting NPs (PLGA-SPIONs-BP) exhibited considerably higher binding to the HA (63-85%). Moreover, the microfluidics synthesized NPs showed higher binding to HA compared with the bulk synthesized particles. More than 73% of the targeting HNPs were bound to the HA after 15 min. These results suggest successful targeting of bone tumors with the HNPs.

In order to obtain an in-depth understanding of PLGA polymer behavior in the vicinity of the HA crystals, all-atom molecular dynamics (MD) simulations under two different simulation conditions, with and without BP, were performed. In order to explore the interfacial interactions between HA crystals and PLGA or PLGA-, the three most common HA crystallographic surfaces, (100), (110), and (001), were studied Figure 4-6d (*164, 165*).

These surfaces were built by cleaving the HA unit cell along the corresponding HA surface with a surface thickness of 13 Å. The surface area of all HA surfaces was increased in both directions to ensure appropriate surface interactions with neighboring PLGA and PLGA-BP molecules. The constructed surfaces were then converted to 3D periodic cells by

applying a vacuum space with a vertical distance of 150 Å above the surface. Energy-minimized PLGA and PLGA-BP were then positioned on the top of as-built HA surfaces at a location at least 12 Å from the upper surface of HA (cf. Figure 4-6e) for PLGA-BP and Figure 4-7a for PLGA at various surfaces).

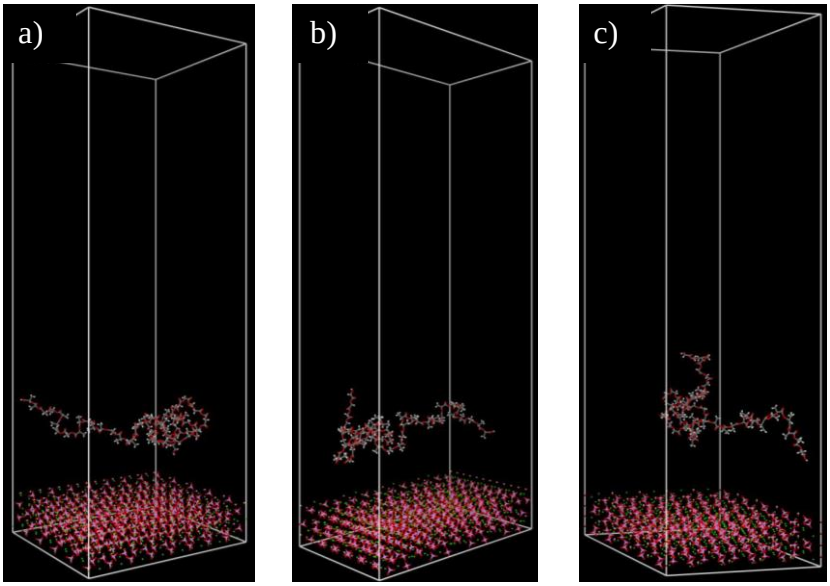

Figure 4-7 Initial structures of (a) HA (100)-PLGA, (b) HA (110)-PLGA, and (c) HA (001)-PLGA. All atoms were shown in Line style.

Final equilibrated structures for MD simulations of PLGA and PLGA-BP above HA (100), HA (110), and HA (001) are shown in Figure 4-8 and Figure 4-6f, respectively. It was observed that PLGA/PLGA-BP molecules approached all three studied HA crystallographic surfaces. This type of strong localization of polymeric chains in the vicinity of different HA surfaces is indicative of strong intermolecular interactions. Consequently, it can be concluded that PLGA-BP has strong HA surface attachment ability. This affinity mostly originates from interactions with surface atoms in the HA.

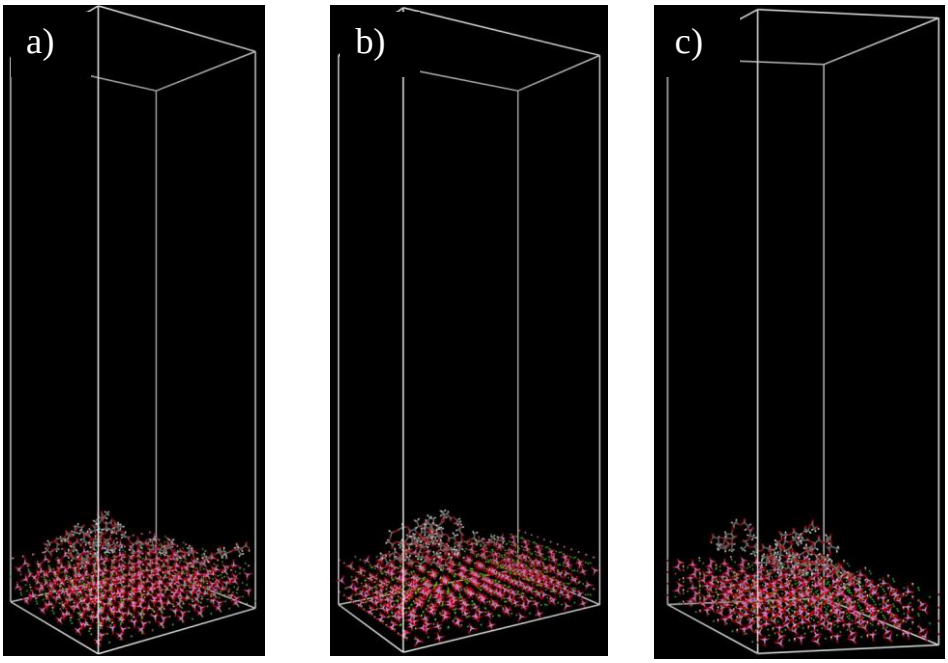

Figure 4-8 Final equilibrated structures of (a) HA (100)-PLGA, (b) HA (110)-PLGA, and (c) HA (001)-PLGA, obtained at the end of 1-ns NVT MD simulation. All atoms were shown in Line style.

In order to quantitatively assess the association of PLGA and PLGA-BP polymers to different HA surfaces, binding energies of simulated 3D cells were calculated, and presented in Figure 4-6g for all studied HA surfaces. Simulations show that for all HA surfaces interacting with PLGA or PLGA-BP, the binding energies were negative, which corroborate that both compounds tend to be close to HA surfaces. Moreover, the presence of BP end groups leads to a significant increase in the absolute value of interaction energy. The simulations show that HA (110) and HA (001) surfaces are most favored for PLGA-BP interactions.

The strong electrostatic interactions of bisphosphonate molecules with the uppermost calcium atoms is the main reason for the highest binding energy being at the HA (110) surface. Figure 4-9 displays that phosphonate terminal groups in PLGA-BP are able to form hydrogen bonds with surface oxygen atoms in $-PO_4$ units as well as hydroxyl oxygen and hydrogen atoms on HA surfaces. Radial distribution functions (RDFs; also called pair

correlation function) were evaluated for different atomic pairs as a further analysis of the intermolecular interactions.

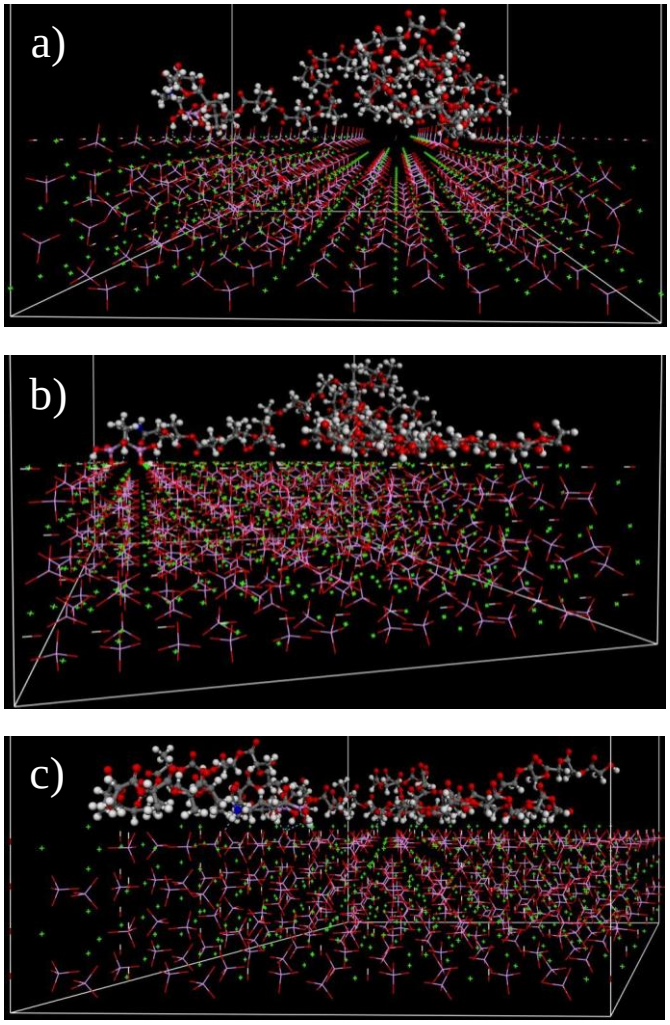

Figure 4-9 Iintermolecular hydrogen bonding interactions between BP bonded to PLGA and (a) HA (100), (b) HA (110), and (c) HA (001). Hydrogen bonds were shown as dash line. All PLGA-BP atoms are in Ball & Stick model.

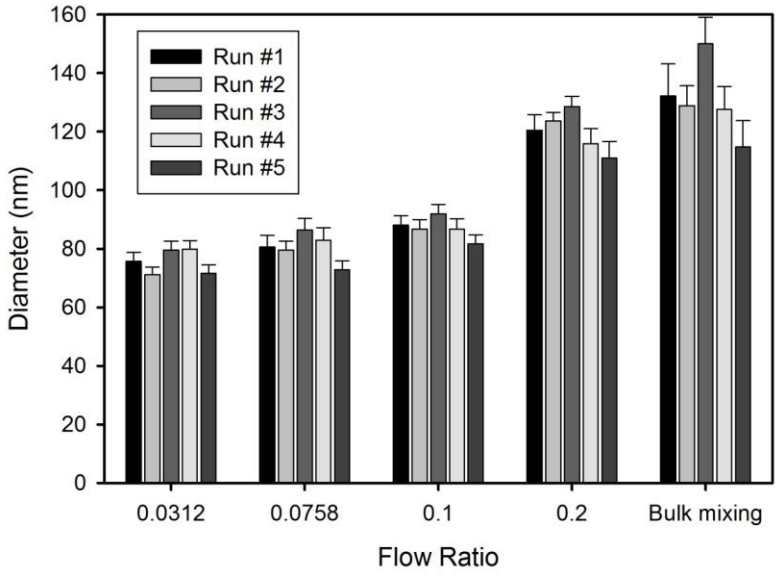

Figure 4-10 Reproduction of PLGA-BP/SPION nanoparticle at five different independent experiments with reproduced microfluidic microchannels.

Figure 4-6h, presents the RDF results between oxygen atoms double bonded to carbon atoms in both PLGA and PLGA-BP NPs, with respect to calcium ions in HA surfaces. The appearance of the first intensified peak in these RDFs implies that both PLGA and PLGA-BP polymers have strong interactions with HA surfaces. Moreover, except for the RDFs for the HA (100) surface, the peak height in RDFs corresponding to HA:PLGA-BP is greater than that of HA:PLGA, which further suggests that modifying PLGA polymers with BP molecules increases the interactions with HA surfaces. In the case of HA (100) surfaces, RDFs of oxygen atoms with calcium atoms in PLGA and PLGA-BP do not show significant difference, which is in agreement with the corresponding binding energies provided in Figure 4-6g.

It is clear that all RDFs demonstrate a first sharp peak, especially for HA (110) surfaces, indicative of powerful BP interactions with HA surfaces. The BP hydrogen bonding interaction with HA surfaces is also examined by evaluating the RDFs for hydroxyl hydrogen atoms in BP with regards to oxygen atoms in PO_4 and hydroxyl oxygen atoms in

various HA surfaces. As seen in Figure 4-6i, the appearance of the first sharp peak confirms the strong BP interaction with HA surfaces by the formation of intermolecular hydrogen bonds. The position of sharp peaks is observed at distances less than 2.5 Å, which is the required hydrogen acceptor atom-hydrogen atom distance for the formation of hydrogen bonds. These simulation results are in agreement with our experimental findings, and confirm that the conjugation of BPs onto PLGA chains significantly improves their affinity to HA surfaces.

To evaluate the functionality of designed NPs *in vivo*, FITC-labeled nanoparticles were administered through the tail vein in BALB/c mice. Pharmacokinetics of the microfluidic- and bulk-synthesized NPs was first investigated in the absence of PTX drug. Figure 4-11a displays the blood circulation profile of NPs based on the fluorescence recovery of FITC-labeled NPs following systemic administration of NPs. Based on a two-compartment model (fitted curves) the targeted microfluidic-synthesized nanocarriers are found to be a stable and long-circulating system that provide enhanced delivery of loaded therapeutics compared with either non-targeted NPs or targeted bulk-synthesized particles.

The biodistribution studies were performed by monitoring and quantitative measurements of fluorescence-labeled NPs distributed in mice tissues. As shown in Figure 4-11b, synthesized NPs showed mostly localization in the liver, kidney, and tumor and relatively low accumulation in the lung, heart, and spleen. There was no significant difference between the targeted and non-targeted NPs was observed for their lung, heart, and spleen localization (Figure 4-11b).

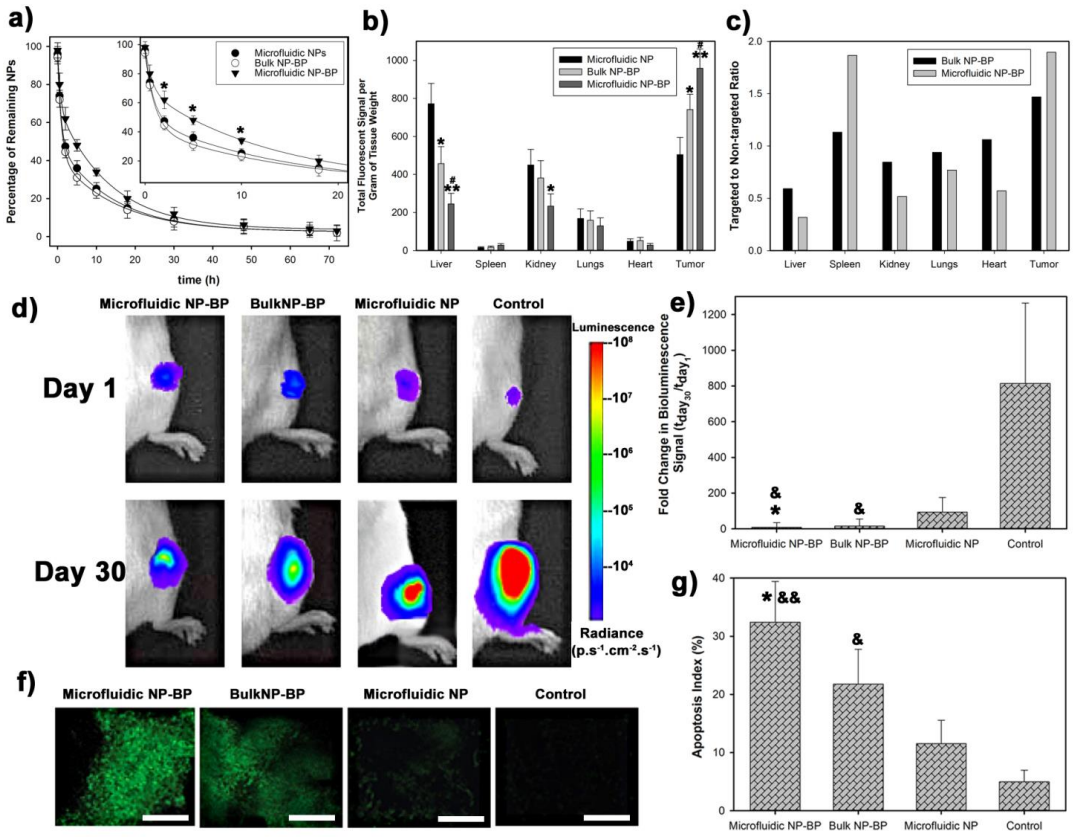

Figure 4-11 ***In vivo*** **efficacy evaluation of nanoparticles. (a) Pharmacokinetic data represent percentage of remaining NPs at several time points after intravenous injection of NPs to BALB/c mice. Data includes background subtraction of blood auto-fluorescence. Two-compartment model is fitted to determine the NPs' half-lives. (b) Quantification of fluorescence signal of FITC-labeled NPs (total fluorescence signal per tissue weight) in order to determine the effects of targeting on biodistribution profiles of NPs in liver, spleen, kidneys, lung, heart, and tumor and ratio of tissue accommodation for targeted microfluidic and bulk NPs in comparison with non-targeted microfluidic NPs (c). (d) Bioluminescence images of mice after injection of luciferase positive human breast cancer cells (MDA-MB-231) in tibia of BALB/c mice at day 1 and day 30. Color scale shows the bioluminescence intensity and the change in photon flux upon treatments with various types of PTX-loaded NPs. NPs are systematically administrated at the same dose of 0.5 mg per kg of mouse's body weight, after seven days of tumor implantation. The PBS based treatment is used as a control. The color scale indicates luminescence intensity in radiance (photons/sec/cm^2/steradian). (e) The fold change in bioluminescence intensity of tumor-bearing mice upon treatment with targeted and non-targeted PTX-loaded NPs at day 30 based on the quantification of bioluminescence images. (f) Histological sections of bone metastasis tumors at tibia sites are stained using the TUNEL kit and detected by immunofluorescence microscopy. The green fluorescence signals indicate induction of apoptosis upon different treatments which is quantified in (g). The presented data are expressed as average ± SD. The results are statistically analyzed using unpaired t-tests. For all tests the statistical significance was set at $p < 0.05$. $p < 0.01$ is considered as statistically very significant. *$p < 0.05$ and **$p < 0.01$ between targeted (either microfluidic or bulk synthesized) NPs and non-targeted microfluidic NPs. $^{\#}p < 0.05$ between**

targeted microfluidic synthesized NPs and targeted bulk synthesized NPs. $^{\&}p < 0.05$ and $^{\&\&}p < 0.01$ between all types of NP-based treatments and control (PBS treatment) samples.

Although accumulation in liver is a common challenge for nanoparticulate delivery systems (*177*), but the obtained results here promises use of BP molecules at the surface of NPs can considerably lower their liver accumulation compared with non-conjugated NPs. The relative change in total fluorescent signal per tissue weight of targeted NPs over corresponding non-targeted particles in different tissues are shown in Figure 4-11c. The results showed 1.5- and 1.9-fold increase in normalized fluorescence signal of targeted NPs over non-targeted particles at the tumor site for bulk- and microfluidic-synthesized NPs, respectively (Figure 4-11c). The targeting-dependent biodistribution profile of FITC-labeled NPs in the bone metastasis highlights the role of BP groups as targeting moieties, in agreement with reported data elsewhere (*174, 177, 178*).

An intratibial model of bone metastasis was developed to evaluate the anti-tumor efficacy of prepared NPs. Bioluminescence images of mice after injection of luciferase positive human breast cancer cells (MDA-MB-231) in tibia of BALB/c mice at day 1 and day 30 were monitored to estimate tumor volume after treatment with various NPs (Figure 4-11d). The targeted NPs (microfluidic NP-BP and Bulk NP-BP) containing equivalent amount of PTX drugs showed significant decrease in the rate of tumor growth implanted into the tibia of mice (p-value < 0.05) in comparison with PBS treated animals. The tumor growth suppression in the case of treatment with targeted microfluidic NPs was significantly (p-value < 0.05) higher than non-targeted microfluidic NPs (Figure 4-11e). Mice treated with free PTX (1 $mg.kg^{-1}$) showed a slight decrease in rate of tumor growth as compared with NPs-treated groups. Here also TUNEL apoptosis assay was performed on tumor sections to test whether the tumor suppression with NPs treatment is related to induce apoptosis in treated tumor. As shown in Figure 4-11f, the apoptosis level was enhanced after treatment

with targeted NPs, whereas the highest number of apoptotic cells can be found in tumor treatment with targeted microfluidic NPs (Figure 4-11g).

The presented results suggest that the developed nanoparticle mediated drug delivery to bone by BP-conjugation significantly increase the therapeutic outcome, which could be further increased by applying magnetic fields to add the hyperthermia effects as well.

4.4 Conclusion

Bone-targeting anti-cancer hybrid nanoparticles (HNPs) were developed through an one-step incorporation of active agents superparamagnetic iron oxide NPs (SPIONs) and paclitaxel (PTX) into nanoprecipitated poly(D,L-lactide-co-glycolide) (PLGA) chains. Using microfluidic chips we were able to precisely tune size, compactness, and polydispersity of HNPs. The demonstrated microfluidic method is distinctive as it provides control over nanoprecipitation of polymeric chains while encapsulating diagnostic and therapeutic compounds inside the HNPs *in situ*. PLGA chains were functionalized with bisphosphonate (BP) molecules as hydroxyapatite targeting moieties to impart bone-seeking capacity to the designed HNPs. It was found that at lower flow ratios (*i.e.*, shorter mixing times), less number of polymer chains contribute to form smaller and more compact NPs. Drug encapsulation and release profile studies revealed higher loading efficiency (>75%), a suppressed drug degradation rate, as well as more sustained release patterns for the microfluidic synthesized HNPs compared with those prepared with bulk mixing. The HNPs conjugated with BPs showed significantly higher bone binding affinity, which was confirmed by a HA binding assay. Furthermore, molecular interactions between PLGA-BP chains and three HA crystallographic surfaces, simulated with computational molecular dynamics, validated the significantly improved tendency of the conjugated polymer chains to bind to HA surfaces. Based on pharmacokinetic results, targeted microfluidic HNPs showed higher blood circulation half-life compared to other NPs. Owing to smaller size

and BP surface functional groups, the developed HNPs provide improved biodistribution through the body and higher accommodation in tumor tissue compared with either non-targeting or bulk-synthesized particles. *In vivo* studies verified the prolonged circulation of targeted microfluidic HNPs and non-invasive bioluminescence imaging showed higher level of tumor suppression in the case of bone metastatic tumor treatment with targeted microfluidic HNPs. The presented results converge to suggest the developed microfluidic fabrication method as a reproducible (Figure 4-10) and versatile approach to synthesize tailored multifunctional NPs for personalized theragnostics including chemotherapy, magnetic resonance imaging and hyperthermia treatment.

CHAPTER 5. MICROFLUIDIC-ASSISTED SELF-ASSEMBLY OF COMPLEX DENDRITIC POLYETHYLENE DRUG DELIVERY NANOCAPSULES[4]

Microfluidic platform for the synthesis of complex nanocapsules is presented via a controlled self-assembly. The monodisperse nanocapsules in the range of 50–200 nm consist of a dendritic polyethylene core and a Pluronic copolymer shell. The resultant nanocarriers encapsulate large amount of hydrophobic anticancer drug like paclitaxel while providing a low complement activation as well as sustained release profile with high tunability.

5.1 Introduction

Particles with nanoscale dimensions have long been known to have properties distinct from their bulk counterparts. This opportunity to alter and tune material properties has made nanoparticles (NPs) a popular research area. Synthesizing polymer NPs is possible using either top-down or bottom-up processing. As bottom-up processing involves the self-assembly of particles via intermolecular forces, it offers the greatest opportunities to tailor the particle structure and properties.(*11*) However, this technique is both powerful and unruly, as it comes with the price of being challenging to control.

Nanomedicine has a wide range of possible applications, including disease prevention, diagnosis, monitoring, management, and treatment. Cancer diagnosis and therapy are perhaps the most promising areas for nanotechnology in medicine, and are expected to soon have applications in the market.(*1-3*) Although there are many diverse problems in

[4]*This work has been published by M.M. Hasani‐Sadrabadi, V. Karimkhani, F.S. Majedi, J.J. Van Dersarl, E. Dashtimoghadam, F. Afshar-Taromi, H. Mirzadeh, A. Bertsch, K. I. Jacob, P. Renaud, F. J. Stadler, I. Kim, (2014) Advanced Materials 26 (19), 3118-3123. Reproduced by permission of Wiley- VCH.*

treating cancer, a magic bullet that can simultaneously target cancer cells and avoid healthy cells, therefore, increasing treatment efficiency and reducing side effects,(*4, 5*) has long been the dream of cancer researchers. One of the most promising techniques is using engineered vehicles for drug transportation and targeting.(*7, 8*) Polymer NPs are promising candidates for the delivery vehicle, although using the correct polymer is of great importance.(*7, 9, 10*)

Dendritic polymers have been widely used as vehicles for the prevention, diagnosis, and treatment of various types of cancer.(*179*) These polymers have increased the efficiency of drug delivery, but they come with concerns over nanotoxicity.(*1*) Due to their high functionality, dendrimers have a very high tendency to bind to amphiphilic lipids, heavy metal ions, bile acids, vitamins, proteins, and nucleic acids, which can cause serious side effects to the body. For example, dendritic polymers have been established to damage cell membranes through lipid binding, and affect oxygen delivery and peroxide metabolism by complexing with iron and zinc ions.(*1*) Due to their complex and costly syntheses, advancing dendritic polymers to human trials has been limited thus far.(*1, 179*) Recently, dendritic polyethylene (dPE) NPs have demonstrated their usefulness across various aspects of materials science(*180-183*) due to their unique and interesting properties. dPE consists of highly branched polyethylene (PE) that is completely hydrophobic, but unlike its linear counterparts, dPE is soluble in common organic solvents and, furthermore, can be easily synthesized using a one-pot recipe.

We have chosen to focus on dPE as the polymer for NP drug delivery due to its biocompatibility, hyperbranched architecture, and size, which is on the order of 30 nm and allows us to make self-assembled NPs in the range of 50–200 nm, an ideal size for drug delivery.(*171*) Moreover, many studies have shown that hyperbranched polymers have higher encapsulation efficiencies than their linear counterparts.(*184*) Most importantly,

dPE is completely hydrophobic, which makes it an excellent carrier for anticancer drugs, which are almost entirely hydrophobic.

Current dPE synthesis methods typically utilize multistep cascade chemical reactions to create large, well defined, and monodisperse NPs.(*185*) To ensure the solubility of highly hydrophobic dPEs in the blood and other aqueous environments in the body, researchers have successfully applied cascade (homo- and co-) polymerization(*186*) reactions or "grafting-to" methods.(*187*) Although these techniques facilitate the creation of elegant and complex dPE structures for drug delivery and bioconjugation,(*188, 189*) the necessary process is very tedious, requires tremendous effort to make these systems, and is accompanied by sacrificing catalytic activity. To address these complications, we developed microfluidic chips that use guided self-assembly to produce monodisperse PEGylated hydrophobic-hydrophilic core-shell structures of dPEs with triblock copolymers. Consequently, through microfluidic assembly, we can avoid multistep and complex chemical reactions, and we have better control over the NP properties.

5.2 Experimental Section:

5.2.1 Materials

All reactions were performed under a purified nitrogen atmosphere using standard glove box and Schlenk techniques. Polymerization grade ethylene (SK, Korea) was purified by passing it through columns containing Fisher RIDOX^{TM} catalyst and 5 Å/13X molecular sieves. Organic solvents were purified by standard procedures and stored over molecular sieves (4 Å). All other reagents used in this study were purchased from Sigma-Aldrich and used without further purification.

The Pd-diimine catalyst used in this study, [(ArN=C(Me)–(Me)C=NAr) Pd (CH_3)(N≡CMe)] SbF_6 (Ar=2,6-$(iPr)_2C_6H_3$) (**1**), was synthesized following a procedure

reported in literature,[S1] which is briefly described as follows. In a round-bottom flask, 30 mmol of 2,6-diisopropyl-aniline, 15 mmol of butane-2,3-dione, and a catalytic amount of formic acid are added to 50 mL of methanol. After 24 h, the medium is filtered, and the yellow solid was washed 3 times with 25 mL of cold methanol and dried *in vacuo*. Under an inert atmosphere, 1.5 mmol of (COD)PdClMe and 1.5 mmol of diimine ligand are dissolved in diethyl ether. The reaction is run for 24 h at room temperature. The formed air-stable orange precipitate is recovered by filtration, then washed 3 times with 25 mL of diethyl ether and dried *in vacuo* (yield 93.7%). To synthesize the final catalyst, 1 mmol of $AgSbF_6$ was added to an acetonitrile solution of [(ArN=C(Me)–(Me)C=NAr)Pd(CH_3)(Cl) (1 mmol in 50 mL of acetonitrile) at room temperature, resulting in the immediate precipitation of AgCl. This mixture was then stirred overnight. AgCl was removed via filtration, and the solvent was evaporated. The solid was dissolved in dichloromethane. Pentane was subsequently added to precipitate the product. The resulting solid was filtered, washed 3 times with 25 mL of pentane and dried *in vacuo* (yield>95%). Ethylene polymerization was performed in a 250 mL oven dried round-bottom flask equipped with a magnetic stirrer and an external thermometer. High dilution techniques were adopted to reduce the monomer mass transport effect. After adding the palladium(II) catalyst (100 μmol, 80.3 mg), the reactor was charged with dried dichloromethane (80 mL) by using a syringe and immersed in a constant temperature bath previously set to the desired temperature. The most reproducible reaction temperature for multiple runs was 35 °C. When the reactor was equilibrated with the bath temperature, polymerization was initiated by introducing ethylene into the reactor after removing nitrogen gas under vacuum (polymerization carried out in atmospheric pressure). After 24 h, the flow of ethylene was stopped and the polymerization mixture was concentrated in vacuum. For the removal of residual catalysts, the remaining mixture was dissolved in petroleum ether and passed through a column of silica gel and neutral alumina to obtain a colorless solution. The

solvent was removed and the viscous oily PE was dried for 24 h under vacuum at 70 °C (8.7 gr).

For checking ligand purity, analytical thin layer chromatography was conducted using Merck 0.25 mm silica gel 60F precoated aluminum plates with a fluorescent indicator, UV254. 1H-NMR and 13C-NMR spectra were recorded on a Varian Gemini-2000 (400 MHz, 100 MHz) spectrometer. All chemical shifts were reported in parts per million (ppm) relative to residual $CDCl_3$ (δ 7.24) for ^{1}H-NMR and $CDCl_3$ (δ 77.00) for ^{13}C-NMR. The branching numbers for PE were determined by ^{1}H-NMR and ^{13}C-NMR spectroscopy (Figure 5-1). For ^{1}H-NMR, branching was determined by using the ratio of methyl groups to the overall number of carbons and was reported as branches per thousand carbons.

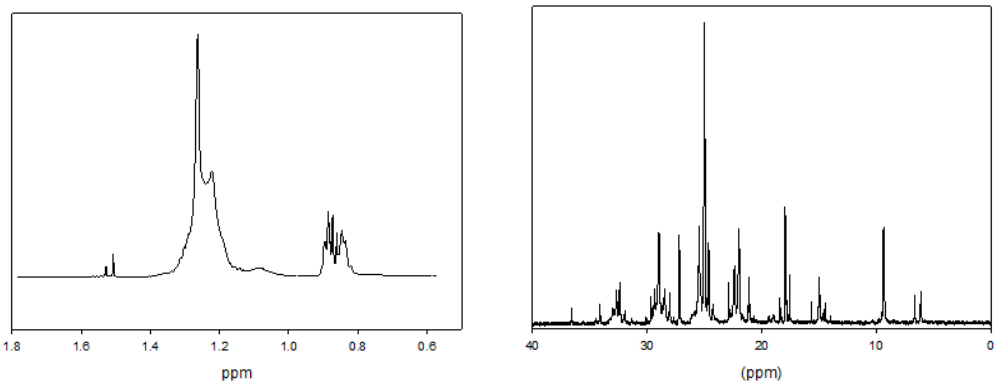

Figure 5-1 ^{1}H-NMR (left) and ^{13}C-NMR (right) spectra for the determination of branching numbers for PE.

For the SEC analysis, two mixed bed columns (Polymer Labs., PLgel Mixed-C, 300 mm × 7.5 mm) were used at a column temperature of 40 °C. SEC chromatograms were produced using multi-angle laser light scattering (MALLS, Wyatt, TREOS) at a wavelength of 670 nm, a refractive index detector (Shodex, RI-101), and a Viscotek differential viscometer using THF (Samchun, HPLC grade) at an eluent flow rate of 0.8 mL/min. Polymer samples for the SEC analysis were dissolved in THF at a concentration of ca. 5.0 mg/mL and an

injection volume of 100 μL. Average values of the refractive index increment (dn/dc) 0.073 mL/g were used in determining molar mass.

Thermal analysis of dPE was carried out with a differential scanning calorimeter (DSC 1, Mettler Toledo) at a 10 °C/min heating rate under nitrogen atmosphere. The results of the second scan were reported to eliminate the difference in sample history. Typically, the samples were heated to 50 °C (1st heating scan), kept at 50 °C for 5 minutes, cooled to -100 °C at 10 °C/min, and then heated again to 25 °C at 10 °C/min (2nd heating scan). Maximal melting peak temperature and enthalpy of fusion of the melt-crystallized states were determined using the second heating scan. The inflection point for the heat flow as a function of temperature was taken as the glass transition temperature. The crystallinity, χ, was calculated from enthalpy of fusion by the following equation:

$$\chi = (\Delta H_f / \Delta H_f^*) \times 100 \qquad \text{(Eq. 5-1)}$$

using the value $\Delta H_f^* = 290$ J/g for 100%-crystalline polyethylene.

Rheological measurements were performed on a Malvern Kinexus Pro using a Peltier Temperature Controller and a 20 mm/2° cone/plate geometry. The rheological properties were determined by dynamic mechanical measurements in the frequency range of $\omega = 100 \ldots 0.1\ s^{-1}$ with a shear strain of $\gamma_0 < 10\%$, which is in the linear-viscoelastic range for polymer melts. The tests were conducted at temperatures *T* between -10 °C and 80 °C. dPE has an almost Newtonian behavior that is obvious from the independence of viscosity to frequency $|\eta^*(\omega)|$, which indicates the absence of sizable amounts of entanglements.

5.2.2 Fabrication of microfluidic devices

Microfluidic devices were fabricated with poly(dimethylsiloxane) (PDMS) using a standard micromolding process. To make the master molds, silicon wafers were spin-coated with SU-8 50 photocurable epoxy (Microchem, Inc.) to a thickness of 60 μm.

Baking, lithography, and development procedures were performed at the EPFL Center for Micronanotechnology (CMi) to obtain negative microchannels on the wafer. The wafers were annealed at 150 °C to eliminate surface cracks in the SU-8. After performing the thermal annealing, the surfaces of the resultant molds were coated with a self-assembled monolayer (SAM) of trimethylethoxy silane (Sigma) by vapor exposure for 40 min. The SAM prevents sticking of the PDMS to the mold. PDMS (Sylgard 184, Dow Corning) monomer and curing agent were mixed with a weight ratio of 10:1, pored over the mold, degassed in desiccators, and cured in an oven (Memmert) at 80 °C for 1 h. After curing, PDMS was removed from the mold and in-/outlet holes were punched using a 150 μm diameter punch. The PDMS was then bonded to a glass slide using oxygen plasma (100 mW, 1 min; Diener electronic GmbH). The PDMS-based microfluidic device had two inlets for neutral pH water, one for the Pluronic/dPE solution in THF, and one outlet. The water stream was split into two in order to achieve two water streams at the flow focusing cross-junction. The mixing channel was 150 μm wide, 60 μm high and 1 cm long.

5.2.3 Fabrication of nanocapsules

For the bulk synthesis of nanocapsules (NCs), dPE/Pluronic solution in THF was prepared under stirred conditions. The nanoprecipitation and formation of the NCs was performed by drop-wise addition of this solution to water under vigorous stirring. For the drug-loaded NCs, paclitaxel (PTX, Sigma-Aldrich) was dissolved in THF and mixed with the polymeric (dPE and Pluronic® F-127) solution. The preparation of the NCs used the same procedure detailed in the previous paragraph.

For the microfluidic synthesis of nanocapsules (NCs), dPE/Pluronic solution in THF was prepared under stirred conditions and then introduced into microchip as a main flow. The water streams act as a nonsolvent, and drives self-assembly during lateral stream mixing. To vary the degree of focusing, and consequently the mixing time, the flow ratio between

the polymer and water streams can be easily adjusted using Syringe Pumps (Harvard Apparatus, PHD2000; HA200I model).

For the drug-loaded NCs, paclitaxel (PTX, Sigma-Aldrich) was dissolved in THF at four different initial loading of 5, 10, 15, and 20 wt% mixed with the polymeric (dPE and Pluronic® F-127) solution. The preparation of the NCs used the same procedure detailed in the previous paragraph. As a control samples, mixture of Pluronic F127 and PTX (at initial loading weight of 10 wt%) was used without presence of dPE at constant flow ratio of 0.076.

5.2.4 Characterization of naocapsules

Atomic force microscopy (AFM; Bruker's Dimension FastScan) and transmission electron microscopy (TEM; CM200-FEG-Philips) were used to characterize the morphology of the NCs. A dilute suspension of NCs was prepared and deposited onto the Cu grid with a carbon film. The shape and size of the particles were characterized via diffraction (amplitude) contrast and (for crystalline materials) through high-resolution (phase contrast) imaging. The TEM used a LaB6 source operating at 100 kV accelerating voltage. The images were characterized using ImageJ software with at least 20 different measurements.

Dynamic light scattering (DLS) and zeta potential measurements were performed using a Zetasizer (Zetasizer 3000HS, Malvern Instruments Ltd., Worcestershire, UK) in backscattering mode at 173° for water diluted systems.

Transmittance of the prepared samples was measured at room temperature (20 °C) with a Shimadzu UV mini 1240 UV/visible spectrophotometer with a wavelength of 550 nm. Turbidity (τ) was calculated from the transmittance using the Beer-Lambert law:

$$\tau = -\frac{1}{L}\, ln\left(\frac{I_t}{I_0}\right) \qquad (\text{Eq. } 5-2)$$

where L is the length of light path in the sample cell (1.0 cm quartz cuvette), I_t is the intensity of the light transmitted through the sample, and I_0 is the intensity of the light transmitted through the solvent (deionized water). Measurements were performed at least three times with the mean values.

As described elsewhere, measuring of C3 and C3b migration through crossed electrophoresis proved C3 cleavage as a consequent of complement activation. Human serum was obtained from healthy donors, and stored at -80°C before use. Then diluted NCs in human serum at 1/4 in VBS^{2+} (veronal-buffered saline containing 0.15mM calcium and 0.5mM magnesium ions) were incubated for 1 h at 37°C with mild stirring. Afterward, 5 µl of each sample was subjected to isoelectric focusing on agarose gel. Subsequently, second-dimension electrophoresis was done on Gelbond® films (Cambrex Bio Science, Rockland) in agarose gel containing a polyclonal antibody to human C3, to recognize both C3 and C3b (Complement C3 antiserum raised in goat; Sigma-Aldrich). Finally, the film was stained with Coomassie blue (Sigma). A semiquantitative estimation of the proportion of native and cleaved C3 was done through the relative sizes of immunoprecipitation peaks, and the ratio between the height of peaks of C3 and C3b was calculated (C3/C3b ratio).

Poly(methyl methacrylate) (PMMA) (M_W = 120 kDa; Sigma-Aldrich) nanoparticles, which were used as positive control,[S7] were prepared using the same microfluidic technique. In brief, PMMA was first dissolved in THF and then the solution introduced to the designed PDMS microchannels as the core flow. It was then hydrodynamically focused between the lateral water streams. Afterward, PMMA nanoparticles were dialyzed against distilled water using Spectrpor® membrane 50 kDa for 48 h.

To determine the *in vitro* drug release profile, lyophilized PTX-loaded NCs (1 mg) were dispersed in 1 mL of phosphate buffered saline (1X PBS, pH 7.4). The solutions were placed into a 3 kDa molecular weight cut-off dialysis cartridge (Thermo Scientific,

Rockford, IL). The cartridge was immersed in 1 L PBS and gently shaken in a 37 °C water bath. At predetermined intervals, buffered solutions were collected and replaced with an equivalent volume of fresh PBS.

The PTX concentration was measured with high-performance liquid chromatography (HPLC) by mixing the 1 mL sample with 1 mL of acetonitrile. A reverse phase C18 column was used as the stationary phase and the mobile phase was consisted of acetonitrile/water (60:40 vol/vol). Separation was carried out at a flow rate of 1 $mL \cdot min^{-1}$ and PTX was detected at a wavelength of 230 nm. This method was evaluated over a linear range of 1–100 $\mu g \cdot mL^{-1}$. In this range, the percent deviation from theoretical value was found to be less than 5% and the coefficients of linearity remain greater than 0.96 using clean PTX standards.

The PTX concentration in the solution was corrected for sampling effects according to following equation: [S8]

$$C_n^{\,l} = C_n[V_T/(V_T-V_S)](C_{n-1}^{\,l}/C_{n-1}) \quad \text{(Eq. 5-3)}$$

where $C_n^{\,l}$ is the corrected concentration of the nth sample, C_n is the measured concentration of PTX in the *n*th sample, C_{n-1} the measured concentration of the *(n-1)*th sample, V_T is the volume of receiver fluid, and V_S represents the volume of sample drawn (1 mL).

Loading content and loading efficiencies were determined by applying the following equations:

PTX Loading content = (weight of the loaded PTX/weight of the NC)×100 (Eq. 5-4)

PTX Loading efficiency = (amount of PTX in the NCs/initial amount of the PTX) ×100 (Eq. 5-5)

Water-insoluble FITC was applied to form fluorescent NCs, which were traceable via FACS, in order to study distribution of the NCs in macrophages. Then these water-

insoluble FITCs were encapsulated inside the NCs during their formation in the microfluidic platform. The abovementioned water-insoluble FITC were synthesized as reported earlier.[S11] In brief, FITC (53.5 mg, Sigma), oleylamine (115.5 mg, Sigma), and sodium hydroxide (1.34 mg, Sigma) were mixed in toluene (10mL, Sigma). Then the mixture was heated up to 120°C for 2 h. After that, toluene was removed under vacuum overnight. Finally, the solid remnants were washed three times with HCl (0.1N, Sigma) followed by distilled water and in a dark environment at 60°C the residues were dried for 2 days.

Macrophage Culture.[S12] RAW264.7 murine macrophages were monolayer cultured in a humidifier incubator (5% CO_2) at 37°C, then maintained in Dulbecco's minimum essential medium (DMEM, Sigma-Aldrich) supplemented with 10% heat-inactivated fetal bovine serum albumin (FBS, Invitrogen), 1% L-glutamine, and 1% penicillin G/ streptomycin (Invitrogen). Phagocytosis experiments were done with the cell density of about 5×10^5 cells.ml^{-1}. The plates containing macrophages were put and stirred in a humidified incubator at 37°C, at the final concentration of 5 μM of FITC-conjugated NC for 3 h. Afterward, the cells were rapidly cooled down (4°C) and washed three times with iced PBS. Then, for FACS analysis, they were fixed with formalin/PBS 1% (v/v), scrapped, and resuspended in PBS and then analyzed using flow cytometry, on a CyAn ADP Analyzer (FACS, Beckman Coulter, Inc) in triplicate. Finally the results are expressed as the normalized mean phagocytic capacity.

The human breast adenocarcinoma cell line (MCF-7) was used for the cytotoxicity experiments. *In vitro* cytotoxicity assay was performed using HMCS NPs against MCF-7 cells. MCF-7 cells were cultured in DMEM (Sigma-Aldrich) without phenol red and supplemented with 10 % fetal bovine serum. The cell cultures were cultivated at 37 °C in an incubator maintained at 5% CO_2.

The cytotoxicity tests were performed using MTT colorimetric assays.[S13] Cytotoxicity of the NCs was determined after 72 h incubation with MCF-7 cells. To determine cell cytotoxicity/viability, the cells were plated at a density of 10,000 cells per well in 96 well plates and then incubated overnight at 37 °C in 5 % CO_2 atmosphere. For PTX treatment, a stock solution of PTX (10 mg·mL^{-1} in DMSO) was diluted to the defined concentration in culture medium. After treating the samples for 72 h, the MTT solution (20 μL, 5 mg·mL^{-1} in phosphate buffer, pH 7.4) was added. The incubation was continued for another 2 h at 37 °C and 5 % CO_2 for exponentially growing cells. The absorbance of the purple MTT formazan solubilized in DMSO was then measured using a plate reader (Safire II, Tecan Sales Switzerland AG, Mannedorf, CH) at 570 nm.

The control experimental medium contained no NCs. The samples were maintained with uniform drug concentration. The spectrophotometer was calibrated to zero absorbance using culture medium without cells. The relative cell viability (%) related to the control wells, containing cell culture medium without NCs, was calculated by $[A]_{test}/[A]_{control} \times 100$, where $[A]_{test}$ is the absorbance of the test sample and $[A]_{control}$ is the absorbance of control sample.

All the experiments were conducted in triplicate at the minimum. The statistical analyses of the experimental data were done using the Student's t-test, and the results are presented as mean ± SD. Statistical significance was accepted at a level of $p < 0.05$.

5.3 Results and Discussion:

In this study, poly(ethylene glycol)$_{106}$-*b*-poly(propylene glycol)$_{70}$-*b*-poly(ethylene glycol)$_{106}$ copolymer (Pluronic® F-127; BASF) was self-assembled with dPE chains to make soluble nanocapsules (NCs). Hydroxyl-terminated dendrimers have been shown to be less toxic than those functionalized with other moieties, such as carboxyl or amine groups.(*190*) With this general microfluidic assembly method, which can be extended to

the other di- or multiblock copolymers, self-assembly of polymers occurs as a consequence of controlled changes in local water content, which results in monodisperse PEGylated dPEs with tunable sizes. The primary advantage of microfluidic mixing over bulk mixing is the additional control over final NC properties. Microfluidics can induce rapid mixing, has high flexibility for fine-tuning particle properties with high reproducibility, and is independent of user skill; all of these aspects are difficult to achieve using traditional techniques.(*14-17, 20, 23, 191*) Microfluidics has made fine control over NP features more accessible by introducing formation parameters, such as flow ratio, mixing time, and chip architecture.(*192*) Even small changes in these parameters can yield particles with completely different properties that are applicable in many fields.(*102, 160, 193*) Having control over many adjustable parameters enhances the precision and tunability of the resulting NPs.(*168*)

The dPE used in this study was synthesized according to previously reported procedures.(*194*) Briefly, a α-diimine palladium(II) catalyst was used to polymerize high molecular weight (MW), hyperbranched PE with the chain-walking mechanism. The resulting dPE was characterized with a triple detector gel permeation chromatograph (GPC), ^{1}H and ^{13}C NMR spectroscopy, differential scanning calorimetry (DSC), dynamic light scattering (DLS), atomic force microscopy (AFM), and rheological measurements. The viscous dPE is completely amorphous at room temperature and has a MW of 155 $kg \cdot mol^{-1}$ (~100 branches per 1000 carbon atoms), and is almost entirely free of entanglements. However, the MW is 170 times greater than the entanglement MW M_e, and the radius of gyration, $<R_g^2>^{0.5}$, is about 15 nm, which is considerably lower than linear analogues.

The poly(dimethylsiloxane)-based microfluidic device consists of perpendicular channels (cross-junction), which creates a focused THF solution flow in a stream of water (Figure 5-2a). The water streams act as a nonsolvent, and drives NP self-assembly during lateral

stream mixing. Since the mixing time is such an important parameter in determining NP properties, a stable flow is vital in order to guarantee that mixing is controlled exclusively by the interfacial diffusion between the polymer flow and the surrounding water. Fluorescein sodium (1 $mg \cdot mL^{-1}$ aqueous solution) and water were used to mimic the flows so that we were able to study the microfluidic device's hydrodynamic flow focusing ability and determine the range of stable flow rates in the focused flow region. As shown in Figure 5-2a (inset), the fluorescein stream (middle channel, 1 mL min^{-1}) is hydrodynamically focused between the side water streams. To vary the degree of focusing, and consequently the mixing time, the flow ratio between the polymer and water streams can be easily adjusted.(*167*)

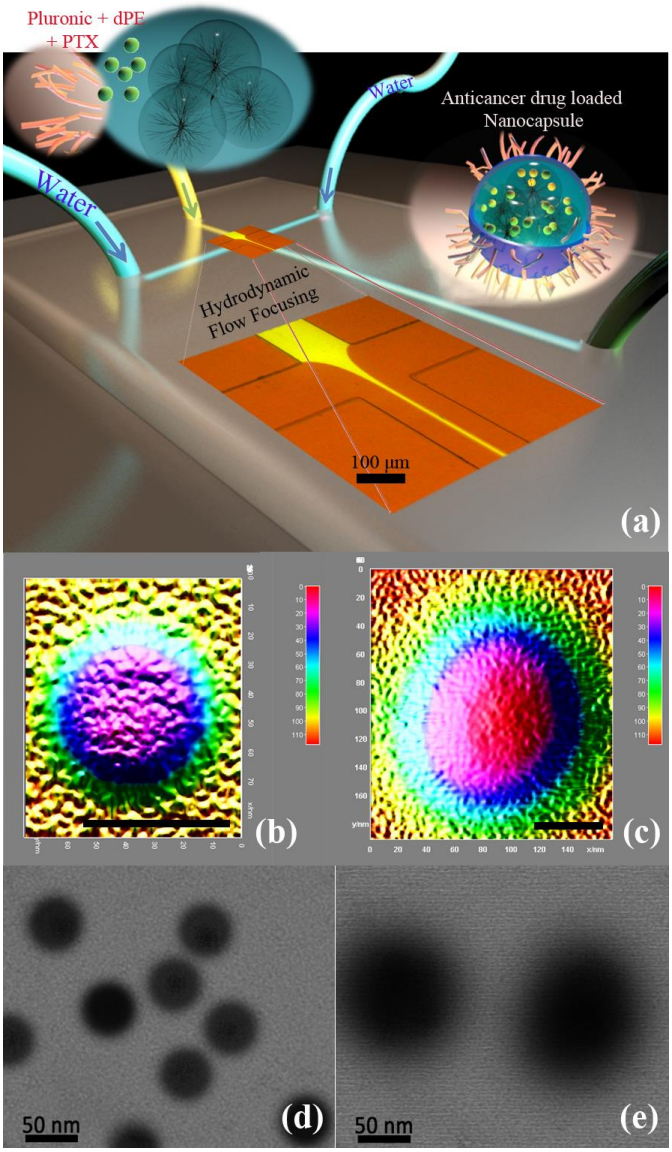

Figure 5-2 (a) Schematic representation of a t-shaped cross-junction microfluidic device, which is used to hydrodynamically focus the flow of Pluronic, dPE, and PTX in THF using a sheath flow of water. The inset is a fluorescence image of Fluorescein hydrodynamically focused with water streams (scale bar 100 µm). AFM (b, c) and TEM (d, e) images of Pluronic/dPE NCs synthesized at a flow ratio of 0.03 (b, d) in comparison with bulk synthesized NCs (c, e).

Precipitation of the dPE and Pluronic molecules is initiated by the presence of water molecules, which is controlled by molecular diffusion at the interface of the polymer and water streams. As this is the first report of dPE-Pluronic NC self-assembly via a microfluidic platform, we describe the process in detail here: by changing the flow ratio

between the THF and water streams from 0.03 to 0.2, the mixing time, τ_{mix}, for self-assembly was kept in the millisecond range. The mixing time varies from approximately 2.5 to 75 ms (Eq. S2). For $\tau_{mix} < \tau_{agg}$ (the aggregation time), NC formation is kinetically restricted, and the particles have smaller sizes and are more monodisperse than those prepared through bulk mixing.(*14, 168*) DLS (DLS; Zetasizer 3000HS, Malvern Instruments Ltd., Worcestershire, UK) results indicate that longer mixing times lead to larger NCs (Figure 5-3a). Furthermore, the polydispersity index (PDI) of the core-shell NCs is approximately 0.10, five times lower than those produced with bulk synthesis techniques (0.49).

In vitro evaluation of complement activation in the presence of fabricated NCs can be considered as a prediction of their fate after intravenous injection *in vivo*.(*195*) In fact, most of the NCs which induce strong complement activation are rapidly taken up by macrophages of the mononuclear phagocyte systems, while NPs exhibiting low or non-activators of the complement systems are not recognized by macrophages and could remain in the bloodstream.(*196*) In the current work, activation of the complement system induced by microfluidic/bulk synthesized NCs is studied in comparison with the control samples. It has been shown that molecules comprising PEG moieties such as Pluronic on the surface of mico-/nanoparticles, can strongly activate complement systems by three well-known pathways.(*195, 197*) Our results, as presented in Figure 5-3, show the effective inhibition of C3 cleavage and consequently, suppression toward complement activation. It seems that complement activation of the microfluidic synthesized NCs are proportional to their size, and can be conveniently controlled using this technique.

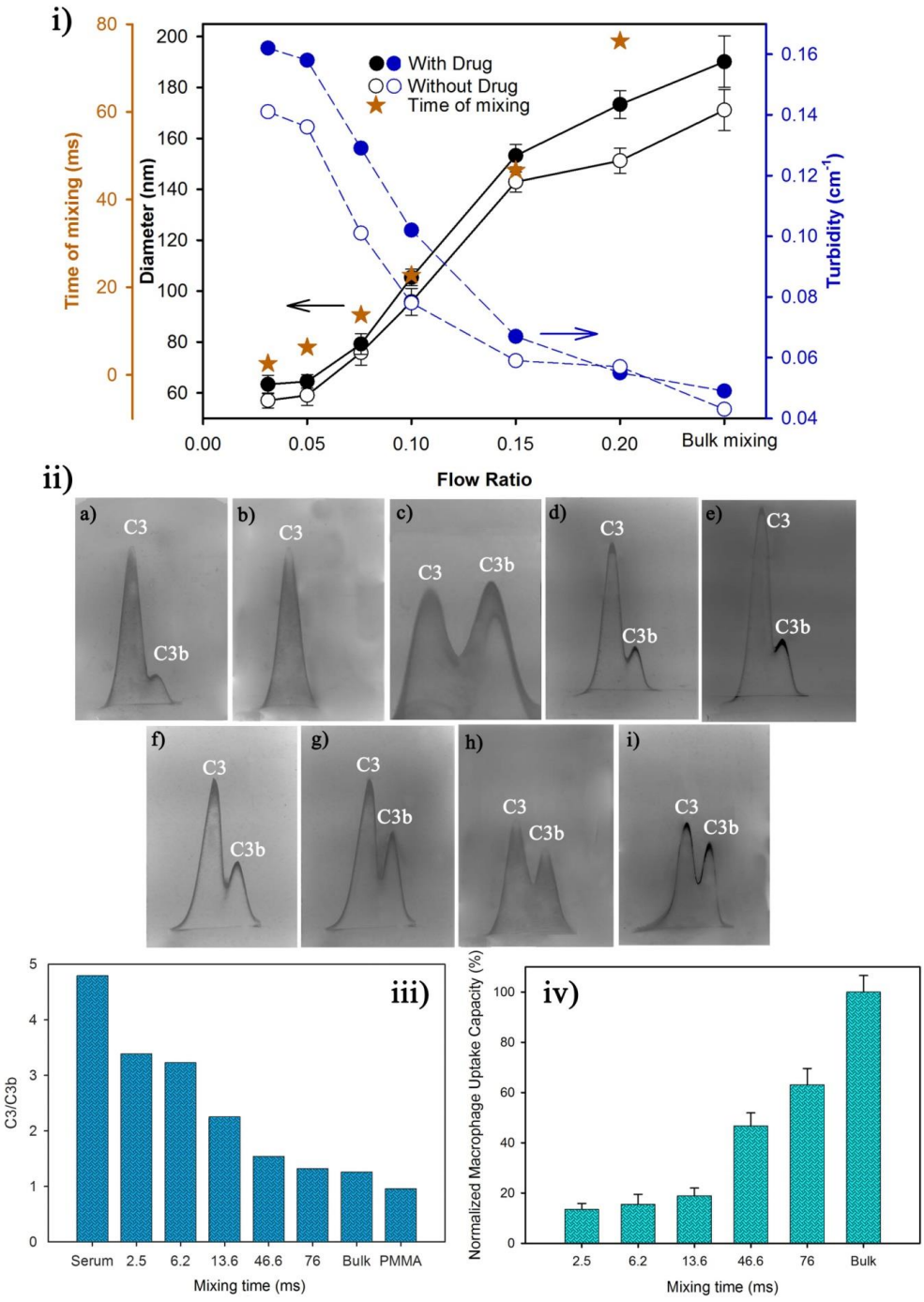

Figure 5-3 (i) Effects of flow ratio on diameter (based on DLS results) and turbidity of synthesized NCs with and without the drug paclitaxel (PTX). The theoretical mixing time is also shown. (ii) Crossed immunoelectrophoresis of C3 antigens in human serum diluted 1/4 in VBS^{2+} after 60 min incubation with NC suspensions. (a) Serum/VBS^{2+} as positive control (C3/C3b = 4.79); (b) serum/EDTA 10mM 1:3 v/v; (no Ca^{2+} → no C3 cleavage); (c) PMMA NCs as negative control (C3/C3b = 0.96); (d) PLdPE-FL0.03 (2.5 µs) (C3/C3b = 3.38); (e) PLdPE-FL0.05 (6.2 µs) (C3/C3b = 3.22); (f) PLdPE-FL0.076 (13.6 µs) (C3/C3b = 2.25); (g)

PLdPE-FL0.15 (47.0 μs) (C3/C3b = 1.54); (h) PLdPE-FL0.2 (76.0 μs) (C3/C3b = 1.32); (i) PLdPE-Bulk (C3/C3b = 1.25). (iii) Plot of C3/C3b ratio as a function of mixing time. (iv) Phagocytosis of the different microfluidic and bulk NCs by RAW 264.7 murine macrophages at 37°C.

It is understood that particle size and curvature affect the complement activation.(*195, 198*) The role of curvature becomes more significant for particles with sizes similar to the cross-sectional diameter of complement proteins such as ~40 nm for IgM(*198*) and ~30 nm for C4b2a.(*195*) In view of this, assembly and deposition on to the surface of particles with high curvature is rather difficult. Despite the fact that C3 protein has the smaller size relative to the other complement proteins, and its surface-bound compartment (C3b) is assumed to occupy an area of 40 nm^2,(*199*) but it has been shown here having smaller NCs (higher curvature value) has resulted in decreased activation of complement activation (Figure 5-3). The macrophage uptake of the NCs is also evaluated as an indicator of the immune system response. As shown in Figure 5-3 (iv), phagocytic uptake of NCs is size dependent and low for the microfluidically prepared NCs. These results are in agreement with the demonstrated complement activation results, which imply the considerable capability of the designed NCs to escape from the immune systems for various *in vivo* applications.

The hydrophobic-core, hydrophilic-shell structure of the dPE/Pluronic NCs provides an ideal environment for encapsulating hydrophobic molecules. This ability is demonstrated with paclitaxel (PTX), a powerful hydrophobic anticancer drug. To encapsulate the drug, a 0.5 $mg \cdot mL^{-1}$ solution of PTX in THF was mixed with a solution of dPE and Pluronic and was then injected into the central channel of the microfluidic device. During NC formation, the hydrophobic PTX molecules associate with the hydrocarbon structure of dPE and become entrapped in the hydrophobic cores of the core-shell NCs. As shown in Figure 5-2a, the incorporation of PTX leads to an increase in the size of the NCs. However, the PTX loaded NCs (57–171 nm) remain within the ideal size window for increased NC

permeability and retention (50–200 nm).(*171*) The morphology of dPE/Pluronic NCs prepared at a flow ratio of 0.03 is shown in Figure 5-2c. All of the prepared NCs are spherical in shape (54 ± 7 nm based on TEM image) and do not aggregate in an aqueous environment.

In order to quantify the ability of PEGylated dPE to encapsulate significant amounts of hydrophobic anticancer drugs, we loaded the dPE/Pluronic NCs with different concentrations of PTX (5, 10, 15, and 20 wt%). As expected, PTX loading was very efficient for microfluidic synthesized NCs. For example, at 10 wt% of initial drug loading efficiency increased from 69.1% ± 19.3 wt% (for bulk mixing) to 99.1% ± 4.5 wt% for NCs fabricated in the rapid mixing regime (0.03 flow ratio). This resulted in weight percent loading values that are among the highest reported in literature for PTX.(*200, 201*) As shown in Figure 5-4 and 5-5, the loading content of dPE/Pluronic NCs can be controlled through operational parameters in the microfluidic device. A relatively small increase in flow ratio, and therefore in mixing time, results in larger particles and decreased drug loading. Maximum PTX loading (9.906 wt%) occurred for NCs with the lowest flow ratio. Despite the high PTX loading efficiencies, no significant change of the size of NCs was observed, suggesting that the hyperbranched nature of dPE creates a high level of free volume in the self-assembled dPE/Pluronic NCs.

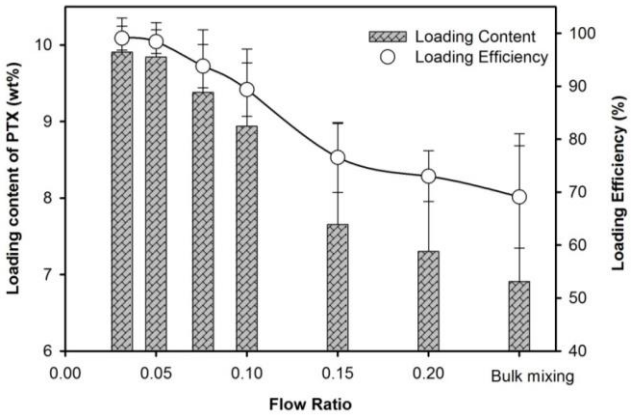

Figure 5-4 The change in paclitaxel (PTX) loading contents/efficiency as a function of flow ratios in comparison with that of bulk mixing at 10 wt% of initial loading of the drug. (Mean ± SD, n = 5 independent experiments).

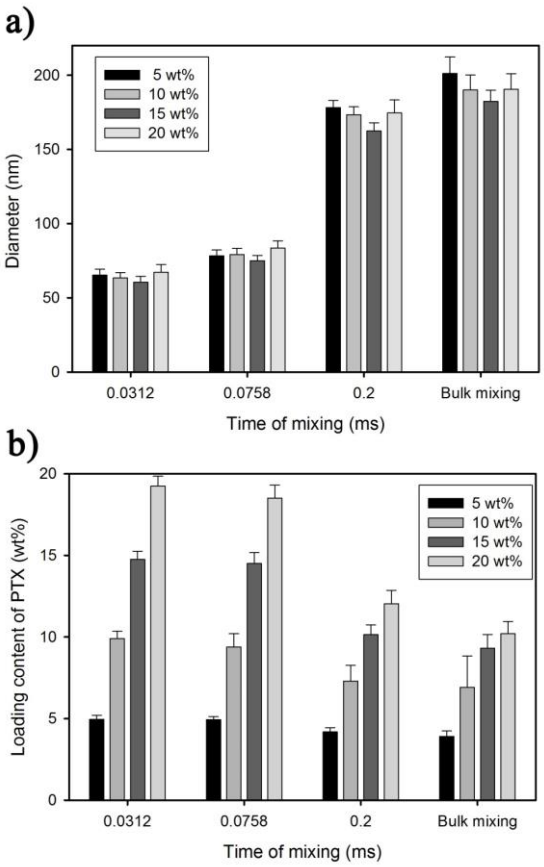

Figure 5-5 The change in size (a) and PTX loading contents (b) of prepared NCs as a function of flow ratios in comparison with that of bulk mixing at 5, 10, 15, and 20 wt% of initial loading of the drug. (Mean ± SD, n > 3 independent experiments).

Relative activities of PTX were estimated by calculating the maximum rate of tubulin protein polymerization relative to the standard samples (Figure 5-6). Stabilities of the free and encapsulated PTX inside different types of NCs were evaluated by measuring the variations of their activities using the tubulin assay after storage at 25 °C and 37 °C for 1–14 d in 96-well microtiter plates according to previously established protocols. Briefly, at defined time intervals, NCs were separated using centrifugation and redispersed in water at pH 4.5 to extract PTX from NCs, and then PTX was separated using HPLC to perform a tubulin protein assay. Then, select concentrations of PTX were reacted with tubulin protein solution (general tubulin buffer, tubulin glycerol buffer, 1 mM GTP), and the reaction was followed by measuring the increase in apparent absorption at 350 nm over a 1 h period at 37 °C using an ELISA plate reader (Safire II, Tecan Sales Switzerland AG, Mannedorf, CH).

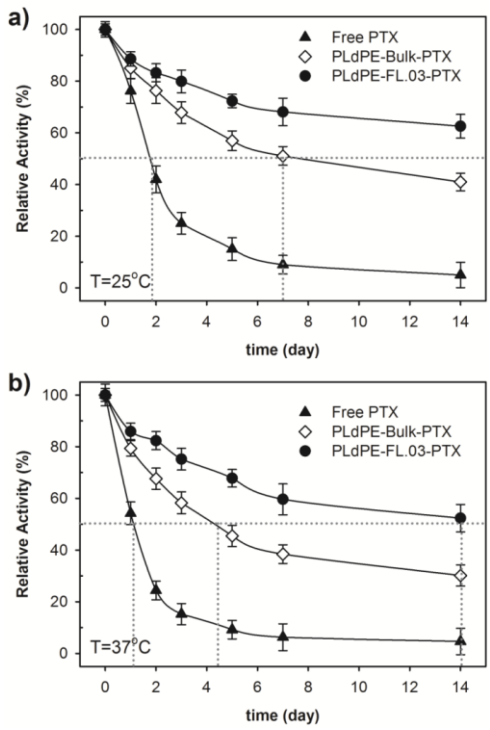

Figure 5-6 Relative activity of PTX drug using a tubulin protein polymerization assay for both free and encapsulated PTX at 25 °C and 37 °C. (Mean ± SD, n = 4 independent experiments).

As shown in Figure 5-6, drug degradation is generally considered as a first order process and can be described by the following equation: $ln(a/a_0) = kt$, where a is the activity of drug at time t, a_0 is the initial drug activity, k is the degradation rate constant. At half-life of drug ($t_{1/2}$), we have $a=a_0/2 \Rightarrow t_{1/2}= 0.693/k \Rightarrow k=0.693/t_{1/2}$. The results of PTX half-life ($t_{1/2}$) and degradation rate constant (k) are shown in Figure 5-7 and Figure 5-8a, respectively.

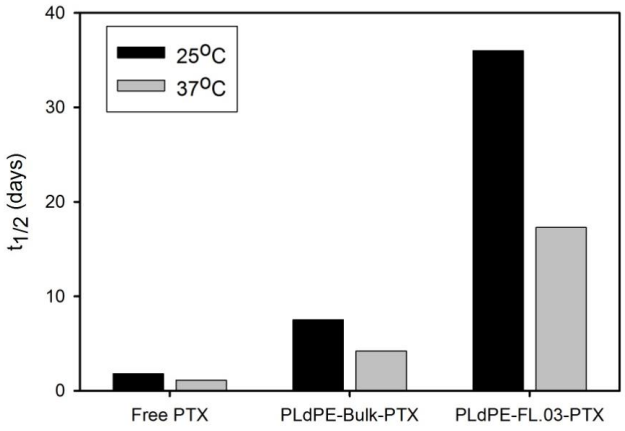

Figure 5-7 PTX half-life ($t_{1/2}$) for the various drug formulations at two different temperatures of 25°C and 37°C.

Figure 5-8 shows the *in vitro* release profiles of PTX in PBS (phosphate buffered solution, pH 7.4) at 37 °C from NCs formed using both microfluidic and bulk mixing. The profiles exhibit relatively fast releases during the early stages (day 1), then followed by slow asymptotic releases, which are typical for PTX-loaded, self-assembled NCs.(*122, 201, 202*) Figure 5-8 also demonstrates that NCs formed through microfluidics have a slower and more sustained release rate than the bulk synthesized NCs. Within two weeks, almost 100% of the PTX was released from bulk synthesized dPE/Pluronic NCs, whereas about 86%, 76%, and 98% of the PTX was released from NCs formed at flow ratios of 0.03, 0.075, and 0.2, respectively.

For dPE/Pluronic NCs formed in the rapid mixing regime (time of mixing 2.5 and 13 ms with NC sizes of 63 and 79 nm, respectively), larger NCs have slower release profiles. These results are in agreement with recent reports that smaller NCs, due to their greater surface area to volume ratio, have faster release rates.(*203*) Additionally, with the decrease in flow ratio comes a shorter mixing time (2.5 ms for R = 0.03), smaller NCs, and higher drug encapsulation efficiency (Figure 5-8b).

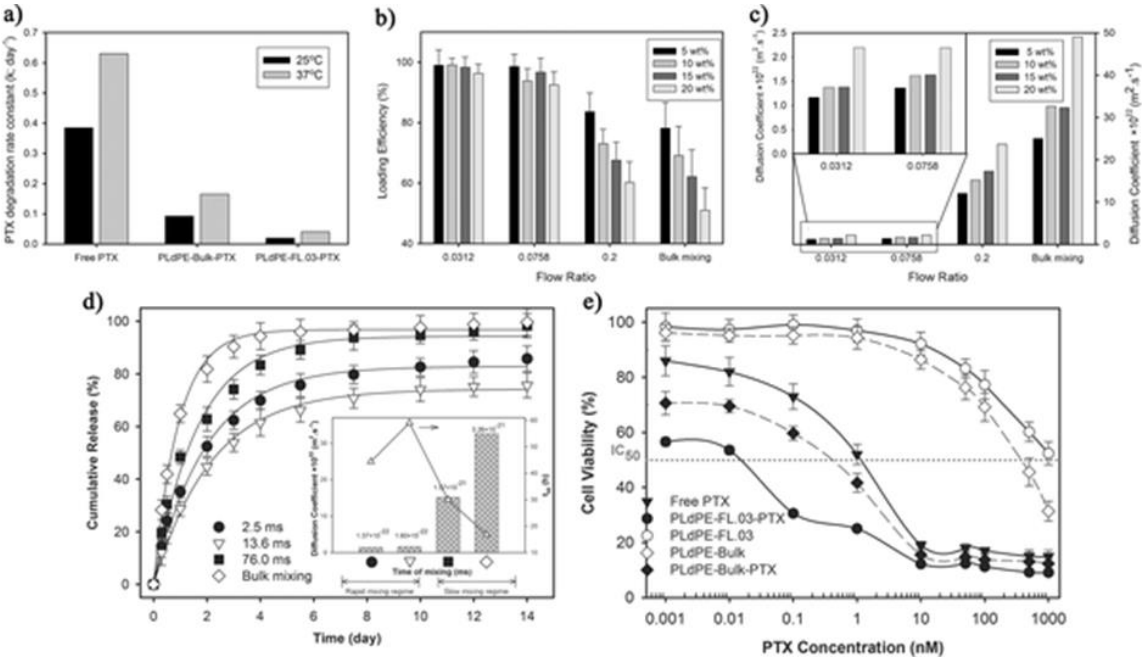

Figure 5-8 (a) Paclitaxel (PTX) degradation rate constant (*k*) for the various drug formulations at two different temperatures of 25°C and 37°C. (b) The change in PTX loading efficiency as a function of flow ratios in comparison with that of bulk mixing at 5, 10, 15, and 20 wt% of initial loadings of the drug. (Mean ± SD, n = 5 independent experiments). (c) Calculated diffusion coefficients of PTX within NCs as a function of mixing time at different initial loading weights of 5, 10, 15, and 20 wt%. (d) Cumulative *in vitro* release of PTX from designed NCs at 37 °C and pH 7.4 (Mean ± SD, n = 4 independent experiments.) Curves are fitted first-order release equations (R^2> 0.98). The inset depicts calculated diffusion coefficients of PTX within NCs and relevant times for releasing 50% of the loaded drug. (e) MTT-based cell viability assay of MCF-7 cells after 72 h of exposure to free PTX, PTX loaded NCs, and unloaded NCs at 37°C. Unloaded NCs were used as a negative control to the PTX loaded NCs and are plotted on the abscissa so that the number of NCs in corresponding trials is the same.

The diffusion coefficient of PTX molecules within the dPE NCs was determined through analysis of the drug release profiles. The calculated values for the diffusion coefficient and

the time needed for 50% drug release (t_{50}) are shown in Figure 5-8. The NCs formed with microfluidics have considerably lower diffusion coefficients and an extended t_{50} release compared to NCs created with bulk mixing. This prolonged, controlled release is highly desirable for treatment applications. Although the diffusion coefficient was found to increase with mixing time, the longer t_{50} for NCs formed with a 13.6 ms mixing time may be ascribed to the higher number of hydrophobic carriers (dPE) in the corresponding NCs. These results confirm the important role of self-assembly time in determining drug loading density and release behavior of the polymeric NCs.

Pluronic F127-PTX NPs were evaluated as control samples. These NPs were prepared using the same microfluidic platform at flow rate of 0.076 without incorporation of dPEs. As shown in Figure 5-9a, the size of resultant NPs is larger than dPE incorporated ones. These results confirm the efficient role of dPEs on formation of more compact nanostructures. As shown in Figure 5-9b, the presence of dPEs in the core of NCs have provided the sustained release of PTX. Diffusion coefficient of drug molecules from Pluronic F127-PTX complexes was calculated to be 2.45×10^{-21} $m^2.s^{-1}$, which is about 15 times more than that of for Pluronic F127/dPE-PTX (1.61×10^{-22} $m^2.s^{-1}$).

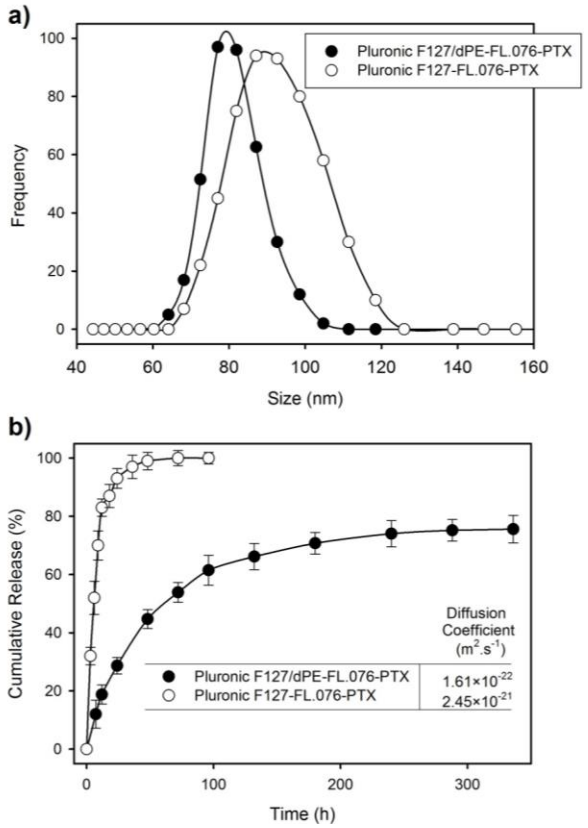

Figure 5-9 (a) DLS results for Pluronic F127/dPE-PTX NCs and Pluronic F127-PTX NPs, which were synthesized using cross-junction microfluidic platforms at the same flow ratio of 0.076. (b) Cumulative release profiles the corresponding nanocarriers.

Although the PTX encapsulation efficiency inside the NCs can be tuned through the microfluidic assembly platform, it is equally important that the encapsulated PTX retains its functional activity during the storage. Measured by tubulin polymerization assays, PTX was found to degrade much slower, at both 25 and 37°C, when encapsulated in microfluidic NCs compared to both free PTX and PTX encapsulated *via* bulk mixing (Figure 5-9). As shown in Figure 5-8a, the degradation rate constant (*k*) value, which is calculated at 25 and 37°C, is much lower for microfluidic synthesized NCs in comparison with the free and bulk encapsulated NCs. This prolonged stability can extend the effective circulation time of drug-loaded NCs in the human body. The relative activity of free PTX decreased considerably and reached half of its initial value after the second day of storage, whereas the encapsulation of PTX prevented degradation and prolonged its activity for weeks,

probably due to the hydrophobic dPE molecules protecting the PTX from direct contact with water molecules.

One requirement for a good cancer-therapy delivery vehicle is to maximize the lethal effects of the drug in the proximity of tumor cells. As is seen in Figure 5-8, the toxicity of plain NCs, as defined by the half-maximum inhibiting concentration (IC_{50}) for MCF-7 cells, is on the order of 300–1000 nM. We found little difference between the toxicity of bulk and microfluidically generated NCs. The IC_{50} toxicity for free PTX is on the order of 1 nM, but PTX toxicity is enhanced by almost two orders of magnitude through encapsulation into dPE-based microfluidic NCs. This dramatic effect may be due to increased cellular uptake of the microfluidic NCs.

Our results demonstrate the feasibility and importance of rapid mixing for the facile fabrication of complex dPE/Pluronic-based NCs, as well as controlling their self-assembly, drug loading, and release characteristics. Due to the olefinic nature of the synthesized NC cores, they are highly capable of carrying hydrophobic drugs while prolonging their release behavior. Nevertheless, further research on their *in vitro* and *in vivo* behaviors is needed, especially in NC surface modification for targeting.

5.4 Conclusion

In summary, we have developed a microfluidic-assisted fabrication of complex dPE/Pluronic-based NCs showing highly efficient encapsulation capacity of hydrophobic drugs. The monodisperse NCs in the range of 50–200 nm, ideal sizes for drug delivery, consist of a dendritic polyethylene core and a Pluronic copolymer shell. The resultant nanocarriers encapsulating a large amount of anticancer drug (say hydrophobic PTX) provide a low complement activation as well as sustained release profile with high tunability. This approach can be extended for the syntheses of other types of tailored, drug-loaded, dPE-based NCs with various shells for the emerging field of nanomedicine.

CHAPTER 6. NON-SPHERIVAL NANOMEDICNE: MICROFLUIDIC-ASSISTED SELF-ASSEMBLY OF ONE-DIMENSIONAL DRUG DELIVERY NANOSTRUCTURES FOR COMBINATORIAL CANCER THERAPY[5]

Except traditional design criteria like high loading efficiency, the importance of nanocarriers shape on its blood circulation and cell internalization is one of the critical factors which attracted considerable attention of scientists and added more complexity to design an ideal drug cargo. Moreover, combinatorial cancer therapies offer big potentials to increase the treatment efficiency and decrease the side effects. In this study, we demonstrate a simple microfluidic-assisted approach for controlled self-assembly of carbon nanotube (CNT)-templated 1D hybrid nanostructures for combinatorial cancer therapy. The nanostructures have a narrow size distribution and consist of a CNT-templated dendritic polyethylene (dPE) core and polymeric shell. The designed nanocarriers were shown to be highly efficient for combinatorial cancer therapy. While CNTs can be used for hyperthermia therapy, the decorated dPE nanoparticulate layer provided efficient loading of hydrophobic anticancer drugs. The developed hybrid one-dimensional nanostructures showed high cellular uptake, a sustainable release profile, and high tunability.

6.1 Introduction

Despite great advances in the field of nanomedicine, cancer remains one of the deadliest and most feared diseases. A nanocarrier platform capable of targeting and curing a variety of cancers with marginal side effects has not been developed.(*204*) An ideal nanoscale

[5] *This work has been submitted for publication by M.M. Hasani-Sadrabadi, V. Karimkhani, G. Bahlakeh, E. Dashtimoghadam, F.S. Majedi, F.J. Stadler, I. Kim, K.I. Jacob (2017)*

nanocarrier should meet a number of critical criteria, including sufficiently long circulation time in the body, efficient targeting, accumulation in target cells, high capacity of drug loading, nontoxicity to normal cells, and high cellular uptake. Recent studies demonstrated that non-spherical nanostructures have numerous desirable properties and thus these particles have gained increasing attention. Non-spherical drug delivery vectors for cancer therapy increase cellular uptake and show long circulation times, large tumour accumulation, long tumour inhibition time, high drug-loading capacity, and high maximum tolerated dose.(*204*) In addition to size, nanoparticle geometry has a large impact on the margination dynamics of vascular walls.(*205-207*) Spherical nanoparticles show minimal lateral drift, decreasing their probability of entering the vicinity of vessel walls and creating contact/binding points with endothelial cells. This dramatically decreases the effectiveness of both passive-targeting mechanisms (*i.e.* enhanced permeability and retention) and active targeting strategies. In contrast, non-spherical particles are more susceptible to tumbling and oscillations in the vasculature. Such features significantly enhance the tendency of achieving nanoparticle/cell wall contact, offering a higher potential for extravasation through vasculature fenestrations.(*206*)

Combinatorial cancer therapies exploit several therapeutic strategies that synergistically promote anti-cancer effects to overcome drug resistance. This can be accompanied by reducing the concentrations of active reagents to mitigate side effects.(*208-212*) Carbon nanotubes (CNTs) and their polymeric hybrid materials have attracted considerable attention in biomedical applications, particularly in the treatment and diagnosis of disease. The potential of CNTs originates from their one-dimensional nanoscale morphology with lengths ranging from the nano- to the microscale.(*213, 214*) Drug delivery arrays, photothermal therapy, and *in vivo* imaging have been extensively investigated based on CNT systems for cancer treatment.(*214-218*) However, the fabrication of combination

therapeutic nanostructures and hybrid CNT/polymer nanostructure systems requires complicated multistep procedures and reactions.(*212-214, 219*)

Bottom-up processes involved in self-assembly of nanoparticles *via* intermolecular forces can be used to create complex structures and tailor and tune particle structure and properties.(*11*) Recently, dendritic polyethylene nanoparticles (dPEs) were shown to be effective for various materials science applications(*52, 181, 182, 220-223*) because of their unique and interesting properties. dPEs are composed of highly branched PE chains that can be synthesized in a simple one-pot protocol.(*220*) dPEs are very different from their linear equivalents, as they are soluble in common organic solvents such as tetrahydrofuran (THF) and chloroform. Because they are bulky hydrophobic molecules, dPEs show great potential as nanocarriers for hydrophobic molecules and drugs.(*52, 223-225*) To create monodisperse well-defined and large nanoparticles (NPs) with dPE, multistep cascade chemical reactions are needed.(*225, 226*) Moreover, to achieve dispersion of highly hydrophobic dPEs in aqueous environments such as the blood, (homo-/co)polymerization(*186, 227*) reactions or "grafting-to" methods(*223, 228*) are required. Although these techniques simplify the design and tune the elegant and complex dPE structures for bioconjugation and drug delivery,(*188, 189*) the process is very tedious, labour-intensive, and commonly supplemented by reduction of catalytic activity. To overcome these limitations, we recently developed a microfluidic-assisted self-assembly approach for fabricating monodisperse PEGylated hydrophobic-hydrophilic core-shell structures of dPEs.(*52*)

One of the unique characteristics of dPEs, first developed by Ye and co-workers, is their ability to solubilize CNTs and graphene nano-sheets in conventional low-polarity organic solvents with low-boiling points such as chloroform and THF.(*229-232*) This occurs through non-covalent and non-specific CH−π interactions of dPE molecules with CNT or graphene surfaces. Given the biocompatibility and encapsulation capacity of hydrophobic

anticancer drugs as well as their ability to assemble on CNTs, dPE/CNT hybrid nanostructures show the potential for flexible design of customized 1D nanocarriers. Such dPE/CNT designs broaden the loading capacity of the nanohybrid carrier, which are typically loaded into CNTs through π−π stacking.(*216*)

The aim of present study was to conduct microfluidic-assisted synthesis and characterization of fine-tuned dPE/CNT hybrid nanocarriers loaded with paclitaxel (PTX) that is poorly soluble in water. To achieve these goals, CNT, dPEs, and poly(ethylene glycol)-*block*-poly(propylene glycol)-*block*-poly(ethylene glycol) copolymer (Pluronic F-127) with an average molar mass of 13,000 were self-assembled on a microfluidic platform to develop water-dispersible 1D drug-delivery systems. It has been reported that neutral hydroxyl-terminated NPs show lower toxicity than other charged functional moieties such as amine or carboxyl groups.(*190, 205*) Thus, the proposed microfluidic-directed assembly was used to prepare a PEGylated, non-spherical, dPE-decorated CNT nanostructure. This approach can be extended to other di- or multi-block hydrophilic-hydrophobic copolymers as well as brush-like copolymers.

6.2 Materials and Methods

Synthesis of dPE. Synthesis of dendritic polyethylene (dPE) nanoparticles and their characterization were reported in the previous chapter. In summary, dPE is a Newtonian fluid with zero shear viscosity η_0 near 56 Pa·s at room temperature. The average molecular weight (MW) is 157 kg·mol^{-1} and mean radius of gyration is approximately 15 nm. The nanoparticles are highly branched (~ 100 branches/1000 carbons) and fairly spherical.

Purification of single-walled carbon nanotubes (SWCNTs). We developed 200-nm long SWCNTS by controlled sonication and then separated them based on length using size-exclusion chromatography and ultracentrifugation. Length separation of single-walled carbon nanotubes was performed as previously described.(*233-235*) For size-exclusion

chromatography 25 mg of HiPco Carbon SWCNT (NanoIntegris Technologies, Inc., Quebec, Canada) as raw material was suspended in 50 mL of sodium cholate (1 wt% in D_2O) using a Q500 Sonicator (500 W; 3.2 mm probe; Qsonica, LLC., Newtown, CT, USA) at 7.5%. Size-exclusion chromatography was performed using Sephacryl High-Resolution gel filtration media (Sephacryl S-500 HR; GE Healthcare Life Sciences, Little Chalfont, UK) as reported previously.(*234*) The early fraction of nanotubes with known length distribution was diluted (10X) with sodium cholate solution and sonicated for 120 min. Glacial acetic acid (PharmaGrade, Sigma, St. Louis, MO, USA) was used to remove sodium cholate from the SWCNTs as previously described. This acid neutralizes the surfactant to form the corresponding acid, which is immediately immiscible with acetic acid, leading to breakdown of the stable sodium cholate helices. The carbon components then form networks under the influence of gravitational forces and van der Waals interactions and the sample was further solubilized in THF. The final solution was centrifuged at 17,000 ×g for 45 min.

6.2.1 Microfluidic-assisted fabrication of CNT-based nanohybrids.

Microfluidic devices were fabricated with poly(dimethylsiloxane) (PDMS; Sylgard 184 Silicone Elastomer Kit, Dow Corning Co., Freeland, MI, USA) using a standard micromoulding process as reported previously.[S1] To form the master moulds, silicon wafers were spin-coated with a Microchem (Westborough, MA, USA) negative epoxy resist (SU-8) to a thickness of 60 μm. Baking, lithography, and development procedures were performed at the EPFL Center for Micronanotechnology (Lausanne, Switzerland) to obtain negative microchannels on the wafer. The wafers were annealed at 150 °C to eliminate surface cracks in the SU-8. After thermal annealing, the surfaces of the resulting moulds were coated with a self-assembled monolayer of trimethylethoxy silane by vapor exposure for 40 min. The self-assembled monolayer prevents sticking of PDMS to the mould. Sylgard 184 monomer and curing agent were mixed in a weight ratio of 10:1,

poured over the mould, degassed in desiccators, and cured in an oven at 80 °C for 1 h. After curing, PDMS was removed from the mould and outlet holes were punched using a 150-μm diameter punch. The PDMS was then bonded to a glass slide using an oxygen plasma cleaner (100 mW; 1 min) from Harrick Plasma Inc. (Ithaca, NY, USA) The PDMS-based microfluidic device had two inlets for neutral pH water, one for the CNT/Pluronic/dPE solution in THF and one outlet. The water stream was split into two to achieve two water streams at the flow focusing (T-) junction. The mixing channel was 150 μm wide, 60 μm high, and 1 cm long. For drug-loaded NCs, paclitaxel (PTX, Sigma-Aldrich) was dissolved in THF and mixed with the CNT, dPE, and Pluronic F-127 solution.

6.2.2 Characterizations

Microscopic morphology of nanostructures. Atomic force microscopy (Bruker's Dimension FastScan, Billerica, MA, USA) and transmission electron microscopy (CM200-FEG-Philips, Amsterdam, Netherlands) were used to characterize the morphology of the nanostructures. A dilute suspension of NCs was prepared and deposited onto the Cu grid with a carbon film. The shape and size of the nanohybrids were characterized by diffraction (amplitude) contrast and (for crystalline materials) through high-resolution (phase contrast) imaging. The transmission electron microscopy used an LaB6 source operating at 100 kV accelerating voltage. The images were characterised using ImageJ software (NIH, Bethesda, MD, USA) with at least 20 different measurements. Dynamic light scattering and zeta potential measurements were performed using a Zetasizer (Zetasizer 3000HS, Malvern Instruments Ltd., Malvern, UK) in backscattering mode at 173° for water-diluted systems.

***In vitro* drug release measurement.** To determine the *in vitro* drug release profile, lyophilized PTX-loaded CNT-based nanohybrids (1 mg) were dispersed in 1 mL of phosphate buffered saline (1X PBS, pH 7.4). The solutions were placed in a 3500 Da

MWCO dialysis cartridge (Thermo Scientific, Waltham, MA, USA). The cartridge was immersed in 1 L PBS and gently shaken in a 37 °C water bath. At predetermined intervals, buffered solutions were collected and replaced with an equivalent volume of fresh PBS. The PTX concentration was measured by high-performance liquid chromatography by mixing 1 mL sample with 1 mL of acetonitrile. A reverse-phase C_{18} column was used as the stationary phase and the mobile phase consisted of acetonitrile/water (60:40 vol/vol). Separation was carried out at a flow rate of 1 $mL \cdot min^{-1}$ and PTX was detected at a wavelength of 230 nm. This method was evaluated over a linear range of 1–100 $\mu g \cdot mL^{-1}$. In this range, the percent deviation from theoretical value was found to be less than 5% and coefficients of linearity remained greater than 0.96 using clean PTX standards. The PTX concentration in the solution was corrected for sampling effects according to following equation:

$C_n^l = C_n[V_T/(V_T-V_S)](C_{n-1}^l/C_{n-1})$; where C_n^l is the corrected concentration of the nth sample, C_n is the measured concentration of PTX in the *n*th sample, C_{n-1} the measured concentration of the $(n-1)^{th}$ sample, V_T is the volume of receiver fluid, and V_S represents the volume of sample drawn (1 mL).

Encapsulation efficiency of the nanostructures and loading efficiencies were determined by applying the following equations:

PTX Loading content = (weight of the loaded PTX/weight of the nanohybrids) × 100

PTX Loading efficiency = (amount of PTX in the nanohybrids /initial amount of PTX) × 100

6.2.3 Cytotoxicity and cellular assays

Cytotoxicity of the nanohybrids. A standard MTT colorimetric assaying was carried out using HeLa cells to examine the cytotoxicity of the fabricated nanostructures. To determine cell cytotoxicity/viability, the cells were plated at a density of 10,000 cells per well in 96-

well plates and then incubated overnight at 37 °C in an incubator maintained at 5% CO_2. The cells were then incubated with NC-CNTs and PL-CNTs over a concentration range of 0.5–50 $\mu g \cdot mL^{-1}$. The culture medium was discarded after 24 h and the cells were washed with PBS (pH 7.4) followed by incubation for 2 h with 100 µL of 3-(4,5-dimethylthiazol-2-yl)-2,5-diphenyltetrazolium bromide (MTT) solution in Dulbecco's Modified Eagle's medium (DMEM; 500 $\mu g \cdot mL^{-1}$ in phosphate buffer pH 7.4). The medium containing MTT was replaced with 150 µL of dimethyl sulphoxide in each well. After shaking the plates for 10 min, the absorbance values of the wells were recorded with a microplate reader (Bio-Tek Synergy HT, Winooski, VT, USA) at a wavelength of 570 nm. The control culture medium contained no nanoparticles. All measurements were performed at room temperature. The spectrophotometer was calibrated to zero absorbance using control culture medium containing no cells. The relative cell viability (%) related to the control wells, containing cell culture medium without nanoparticles, was calculated as $[A]_{test}/[A]_{control} \times 100$, where $[A]_{test}$ was the absorbance of the test sample and $[A]_{control}$ was the absorbance of the control sample.

Cellular uptake. For cellular uptake experiments, the HeLa cell line was used to investigate the uptake of FITC-labelled NC-CNTs and PL-CNTs. The particles were incubated with cells from 0 to 5 h (incubator 37 °C, 5% CO_2) at a concentration range of 0.5–50 $\mu g.mL^{-1}$. After incubating the cells with the particles, the cells were rinsed three times with PBS and trypsinised to detach from the plates. The resulting cells were centrifuged and suspended in a 0.4% trypan blue solution in Dulbecco's Phosphate Buffers Saline (DPBS) solution to quench extracellular FITC fluorescence. The cells were centrifuged again and the dye solution was withdrawn. Next, the cell pellets were resuspended in DPBS. All samples were kept on ice until fluorescence-activated cell sorting analysis. These samples were analysed by flow cytometry (CyAn ADP, Beckman

Coulter, Inc. Brea, CA, USA) to detect green and red fluorescence. The process was repeated for cells positioned in an inverted configuration as described previously.

For microscopy, 1×10^5 cells per well were seeded on round glass cover-slips in 12-well plates. After reaching 80% confluency, the growth media was aspirated and 400 μL of FITC-labelled NC-CNTs and PL-CNTs in PBS were added to each well at a concentration of 10 $\mu g \cdot mL^{-1}$. Cells were then incubated for 4 h at 37°C and 5% CO_2. The samples were washed five times with PBS and fixed with 3% paraformaldehyde solution. Cell nuclei were stained with propidium iodide and then fluorescent microscopy measurements were performed using a ZEISS LSM700 UP2 (Jena, Germany) confocal laser scanning microscope.

A thermal imaging camera (FLIR Systems; Nashua, NH, USA) was used to record the NIR laser irradiation (808 nm; 1.5 $W \cdot cm^{-2}$)-induced increase in temperature. For photothermal ablation of cancer cells, HeLa cells were seeded in tissue culture dishes at a density of 40,000 cells/cm^2 and were cultured for 24 h at 37°C in an incubator maintained at 5% CO_2 until reaching 80% confluence. Next, the medium was replaced with nanohybrid-containing medium (0.5, 1, 5, 10, 25, and 50 □$g \cdot mL^{-1}$). After incubation for 4 h, the cells were rinsed three times with PBS to remove the free nanostructures. Fresh medium was added and then laser light at 808 nm; 1.5 $W \cdot cm^{-2}$ with a 250 □m diameter spot-size was irradiated for 6 min. Cell viability was characterised by using the live/dead assay and MTT assay as described above after 24 h.

RAW264.7 macrophage-like cells (ATCC, Manassas, VA, USA) were seeded 48 h prior to the experiment in 96-well culture plates at a density of 1×10^5 cells per well in culture medium supplemented with 5% foetal bovine serum. The cells were incubated in medium containing NC-CNTs and PL-CNTs (10 $\mu g \cdot mL^{-1}$) for 5 h. As a positive control, cytokine production was stimulated with LPS (50 $ng \cdot mL^{-1}$). Cytokine ELISA kits obtained from BD

Biosciences (Franklin Lakes, NJ, USA) were used to evaluate the expression levels of TNF-α and IL-10 in the medium according to the manufacturer's protocols. For pharmacokinetics (blood circulation) studies, six female BALB/c mice (18–22 g) were randomly divided into two groups for the two different kinds of designed nanostructure NC-CNTs and PL-CNTs. All mice were fed a commercial diet and water *ad libitum* and were on alternating 12-h light/dark cycles. Both groups were injected *via* the tail vein at the same dose of 2 mg per kg of mice's body weight. Blood samples were drawn from the retro-orbital sinus at different times, 0 and 30 min and 1, 1.5, 3, 5, 7, 9, and 12 h, into heparinized tubes and the samples were centrifuged for 15 min. The plasma was separated and stored at −20°C in the dark before analysis. The plasma concentration of NPs was defined based on the fluorescence intensity of the FITC groups using a Bio-Tek Microplate Reader. The normalized plasma concentrations of applied nanostructures are shown as a function of time.

All experiments were conducted in at least triplicate. Statistical analyses of the experimental data were conducted using the *t*-test, and the results are presented as the mean ± SD. Statistical significance was accepted at a level of $p < 0.05$.

6.2.4 Simulation Methods

***Ab initio* calculations.** High-level electronic structure calculations based on *ab initio* quantum mechanics tools were employed to obtain dPE molecules with equilibrium structures for use in subsequent MD simulations. The chemical structure of dPE molecules was taken from work reported by Ittel et al.(*236*) *Ab initio* calculations of dPE molecules were carried out using Hartree-Fock (HF) theory with 6-31G** basis functions(*237*) without any constraints. The final geometry-optimized dPE molecule is shown in Figure 6-1. Partial charges centred on dPE atoms were determined via electrostatic potential-based

method of CHELPG.(*238*) All *ab initio* electronic structure computations were performed using the Gaussian 09 suite of programs.(*239*)

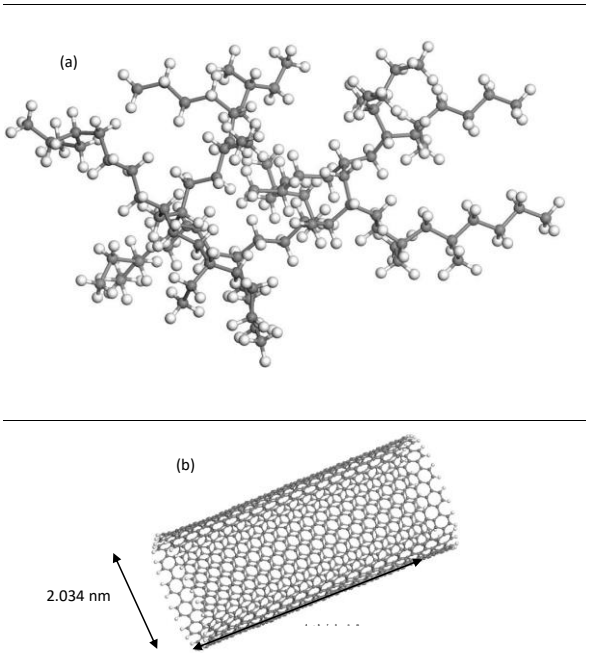

Figure 6-1 (a) HF/6-31G optimized geometry of dPE, and (b) chemical structure of SWCNT (15,15) applied for MD simulations. All atoms are shown in ball and stick model (colour code: carbon, gray and hydrogen, white).**

Molecular dynamics (MD) simulations. To qualitatively and quantitatively evaluate the affinity between CNT and dPE, classical MD simulations were conducted for the CNT-dPE complex. MD simulation approaches were conducted on a simulation box comprising dPE molecules and SWCNTs. An armchair SWCNT of chirality (15,15) with a diameter of 2.034 nm and length of 4.673 nm (shown in Figure 6-1b) was taken into consideration for simulation characterisation of the central CNT molecule, as CNTs of the same diameter were utilized in our experiments. The terminal carbon atoms in SWCNTs were saturated by hydrogen atoms. Next, the constructed SWCNT was placed at the centre of a simulation cell of dimensions $4.8 \times 7.0 \times 7.0$ nm^3, and then surrounded by 17 dPE molecules obtained from calculations at the HF/6-31G** level of theory. These dPE molecules were randomly positioned around the SWCNT, as illustrated in panels (a) and (b) in Figure 6-2.

The three-dimensional simulation box was energy-minimized using the Steepest Descent algorithm. Subsequently, the minimum energy SWCNT-dPE configuration was subjected to a 10-ns MD simulation performed in the constant volume and temperature (NVT) ensemble, where all SWCNT atoms were position-restrained and kept fixed at the centre of MD cell. The Berendsen thermostat was used to control the temperature at the desired value of 300 K. OPLS-AA force field parameters were adopted to describe the interactions between dPE and CNT.(*240, 241*) A leapfrog approach with a time step of 1 fs (10^{-15} s) was employed to integrate the Newton motion equation. The LINCS method was utilized to maintain all bonds fixed at their equilibrium values. Non-bonded interactions were truncated using a 1.2 nm cut-off distance. Periodic boundary conditions were imposed in all three directions of the simulation box. All atomistic MD simulations were executed using GROMACS simulation code (version 4.5.4).(*242, 243*) Dynamic trajectories from the last 5-ns NVT simulations were saved every 10 ps and used for later visual and quantitative analyses of chemical affinities between SWCNT and dPE molecules (Figure 6-2).

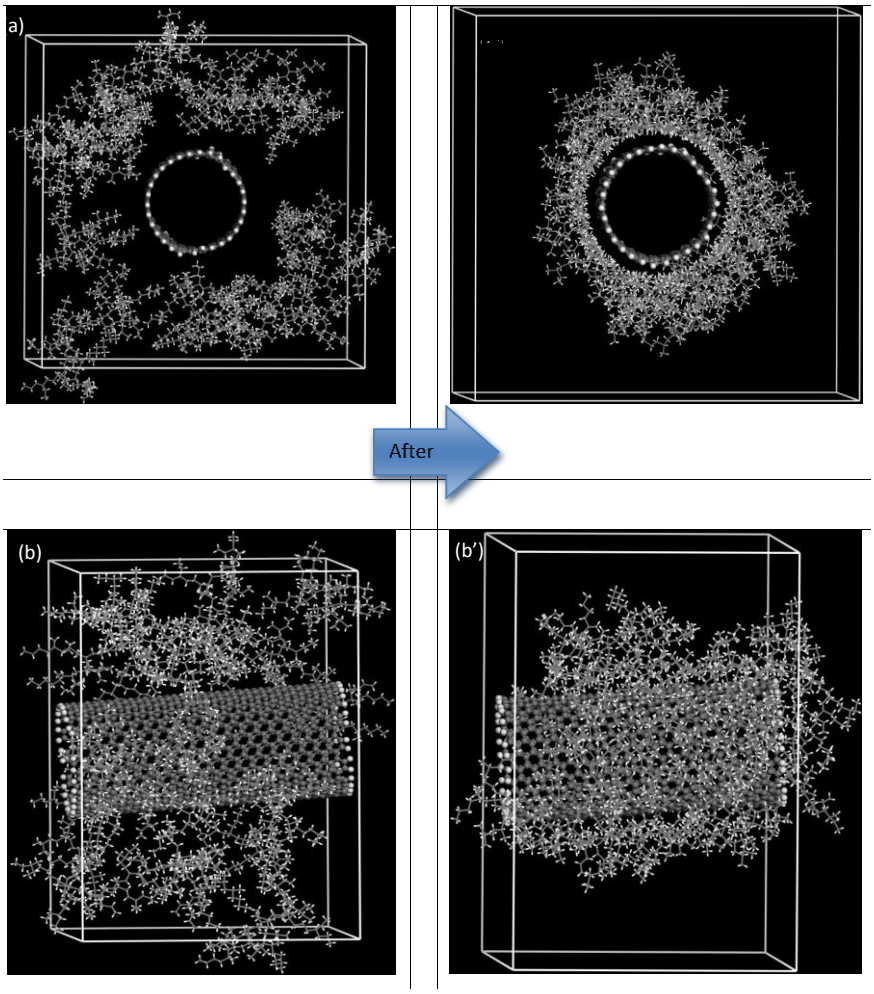

Figure 6-2 Initial simulation cell of SWCNT-dPE: (a) front view, and (b) side view; final simulation cell of SWCNT-dPE obtained at the end of 10-ns MD simulations: (a′) front view, (b′) side view. CNT is in ball and stick model, and dPE molecules are shown in line model (colour code: carbon, gray; hydrogen, white).

6.3 Results and Discussion

dPEs were synthesized based on previously reported procedures.(*52, 194, 222*) A Brookhart type α-diimine palladium(II) catalyst was synthesized and used to polymerize high-molecular weight (MW), highly branched PE NPs *via* the so called chain-walking mechanism (see Supplementary Information). The synthesized dPEs were characterized by triple-detection size exclusion chromatography, ^{1}H and ^{13}C NMR spectroscopy, dynamic light scattering, atomic force microscopy, rheological measurements, and differential

scanning calorimetry. The obtained dPE with honey-like viscosity was completely amorphous at 25 °C with MW of approximately 155 $kg \cdot mol^{-1}$ (approximately 100 branches per 1000 carbon atoms based on NMR characterization). Rheological measurements showed that dPEs are free of entanglements because of the large number of closely packed branches.(*244, 245*) although the MW is approximately 170-fold greater than the entanglement molecular weight (M_e) for linear PE, while its radius of gyration, $<r_g^2>^{0.5}$ is approximately 15 nm, which is considerably smaller than linear analogues of the same MW.(*246, 247*)

Short-length, single-walled CNTs were prepared by controlled sonication and subsequent separation based on length using size-exclusion chromatography and ultracentrifugation (see Supporting Information). To synthesize nanohybrids, CNT/dPE/Pluronic F-127 were pre-mixed with THF at room temperature and then introduced into the microchip as the core flow using a syringe micropump (Figure 6-3a). The water streams, used as the non-solvent, were introduced onto the chip with lateral flow. To vary the degree of flow focusing, the flow ratios of the core dispersion and water streams were adjusted using micropumps for THF solutions and water. The generated nanostructures composed of self-assembled dPE/Pluronic decorating CNTs were designated as nanocapsule-CNTs (NC-CNTs). For drug-loaded nanostructures, PTX was dissolved in THF at an initial loading of 10 wt/v% mixed with the polymer/CNT solution.

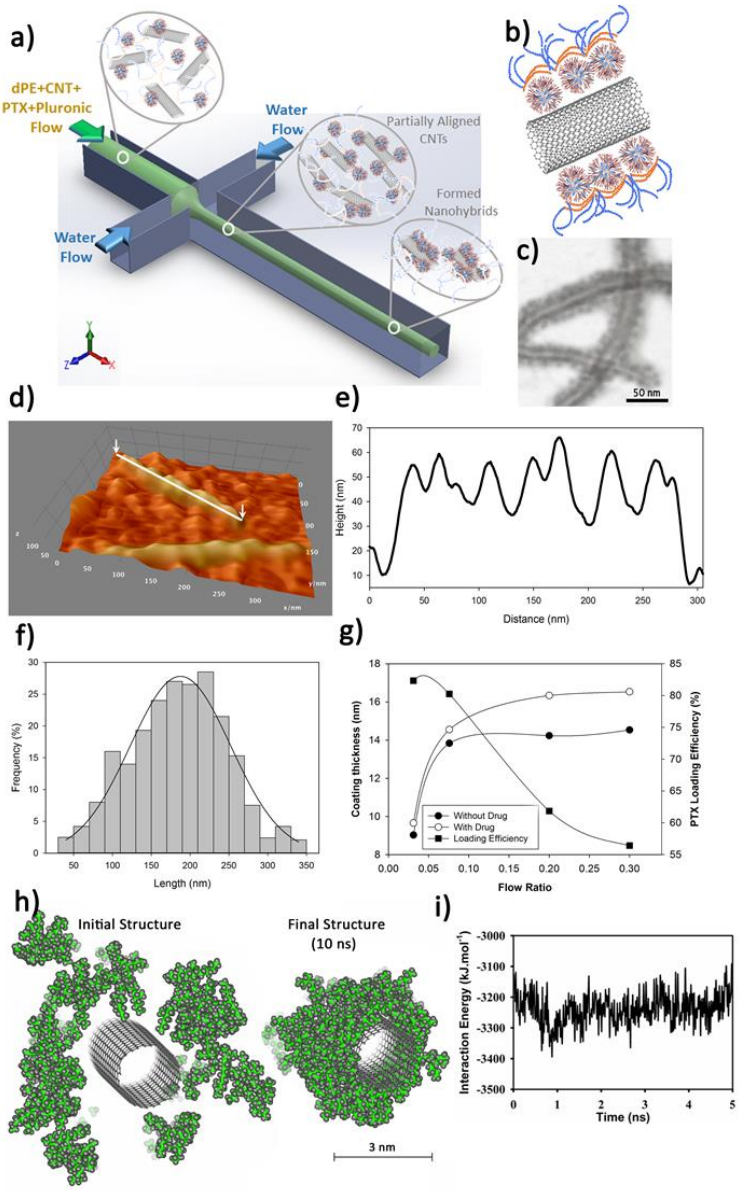

Figure 6-3 Physical characteristics of microfluidic synthesized nanohybrids. (a) Schematic representation of cross-junction microfluidic device used for controlled formation of CNT-based nanohybrids. Pre-mixed solution of dPE, CNT, Pluronic F127, and anticancer drug (PTX) in THF (main flow) was focused using two streams of water (lateral flow) at different flow rates. (b) Hypothetical arrangement of molecules around CNT. (c) Transmission electron micrograph (TEM) of the self-assembled nanohybrid nanoparticles; FR = 0.03, Scale bar: 50 nm. (d) Atomic force macroscopic image of single nanohybrid formed at FR = 0.03 and deposited on mica (e) with its representative height distribution profile. (f) Length distribution of CNT-based nanohybrids (n = 300). (g) Coating thickness of microfluidic-assisted synthesized nanohybrids at different flow rates with (filled spheres) and without (open spheres) anticancer drug (PTX). The loading efficiency of PTX is also plotted (filled square). (h) Initial simulation cell (left) and final simulation cell (right) of CNT-dPE after 10-ns MD simulations. (i) Time evolution of van der Waals (vdW) interaction energy between CNT and dPE molecules during the final 5-ns of molecular dynamics (MD) simulations.

The main benefit of self-assembly by microfluidic mixing in comparison with that of conventional bulk methods is the precise control over time of mixing, and, consequently, tunability of the final assembled nanostructure properties. It has been proven that microfluidics gives great flexibility in adjusting and tuning shape, size and, therefore, properties of the nanostructures, ultimately leading to superior reproducibility and uniformity of the resultant particles.(*14-17, 23, 52, 167, 248-251*)

To better understand the formation of the nanocarriers, we evaluated the intrinsic affinity of dPE to CNTs using molecular dynamics simulation. The final equilibrated configuration of the dPE-CNT complex attained from the canonical ensemble, constant-temperature; constant-volume ensemble (NVT), is shown in Figure 6-3h. Compared with the initial state, dPEs clearly moved towards the CNT surface and localized near their outer surface. Moreover, dPEs wrapped CNTs with neighbouring CH groups pointing towards their external surface, thus maximizing surface coverage. This enabled dPE molecules to form a layer around the CNTs *via* methyl (CH)-π interactions. The delocalized π electrons in aromatic benzene rings of CNT strongly interacted with numerous CH groups in dPE, enabling the dPEs to interact with the surface of CNTs. To quantify the extent of intermolecular interactions governing the behaviour of the CNT-dPE complexes, van der Waals interactions (vdW) were predicted within the last 5 ns of the simulations. Figure 6-3i presents the calculated interaction energy versus simulation time. The CNT-dPE interaction energy showed negligible fluctuations, indicating that dPE adsorption and subsequent wrapping around the CNT stabilized the nanohybrids, likely by strengthening the vdW interactions. The increased binding energy was reflected by the negative sign, quantitatively confirming the affinity between CNT and dPE molecules, leading dPEs to localize near the CNT surface. CH−π interactions appeared between CNT and dPEs significantly contributed to the vdW interactions.

Drug-loading efficiency measurement revealed that NC-CNTs encapsulated more than 80% of the drug. This high encapsulation efficiency, which is similar to that of our recently reported spherical dPE-based nanocapsules,(*52*) is among the highest value reported for micellar systems.(*225*) One of the main factors determining the efficiency of drug delivery nanocarriers is *in vivo* fate of the nanocarrier, which may be related to immune system activation. We evaluated the effect of nanostructures on stimulation of the immune system *in vitro* to predict the fate of NC-CNTs under physiological conditions. Tumour necrosis factor alpha (TNF-α) and interleukin-6 (IL-6) are two the most common cytokines produced by macrophages, which enter the bloodstream under abnormal conditions to provoke an immune system response. Lipopolysaccharides (LPS) are bulky organic molecules formed by covalent attachment of a lipid and polysaccharide, which can stimulate a strong immune response. Thus, LPS is useful as a negative control to evaluate the sensitivity of the immune system to the fabricated nanostructures. As shown in Figure 6-4, the data confirmed that Pluronic-coated CNTs (PL-CNTs) and NC-CNTs stimulated approximately one order of magnitude lower TNF-α and IL-6 expression than the control LPS.

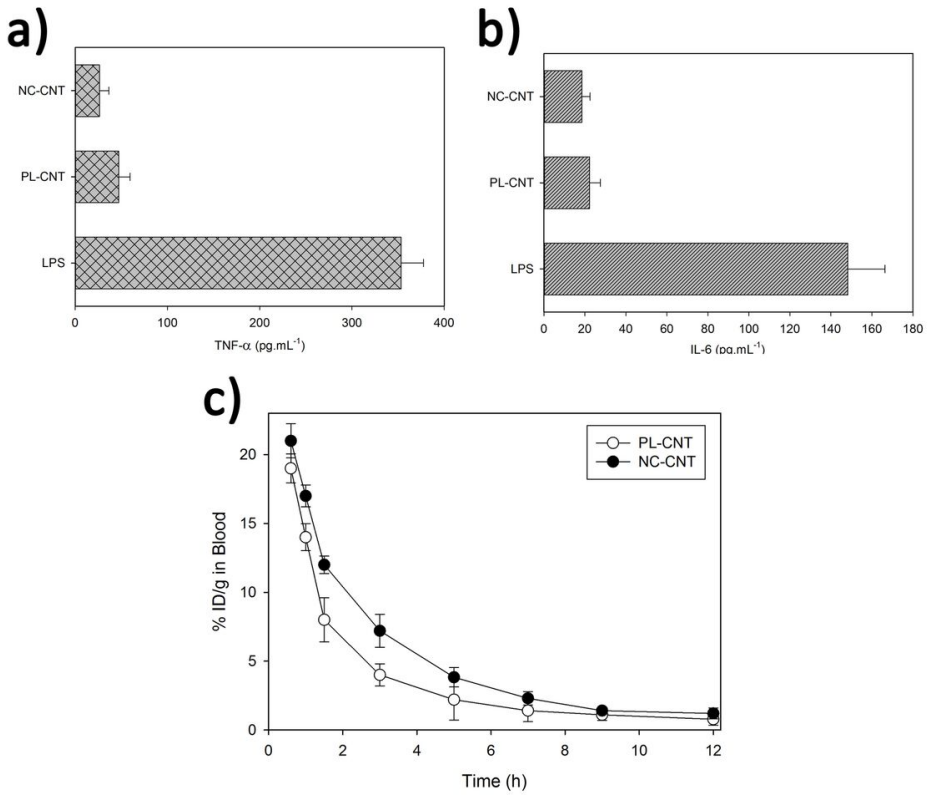

Figure 6-4 Determination of immune response of nanohybrids after incubation with RAW 264.7 macrophages by evaluating TNF-α (a) and IL-6 (b) cytokine expression using ELISA. (c) *In vivo* pharmacokinetic data represent percentage of remaining NPs at several time points after intravenous injection of NPs into BALB/c mice. Data include background subtraction of blood auto-fluorescence. Two-compartment model was used to determine nanohybrid half-lives.

Previous studies showed that PEGylation (PEG, polyethylene glycol) of NPs, which increases circulation time in the bloodstream, is an efficient modification for avoiding activation of the immune system against NPs.(*252*) This strategy was used for make CNTs stealth for surveillance of the immune system, but Moghimi and co-workers showed that PEGylation of single-walled CNTs (SWCNTs) and multi-walled CNTs (e.g. different PEG chain length, PEG adsorption versus covalent linkage) do not completely stop complement activation against them.(*253*) Complement activation occurs both *in vitro* and *in vivo* for PEGylated CNTs via the lectin pathway. Surprisingly, PEGylated SWCNTs with a branched PEG architecture activated the lectin pathway through only *L*-ficolin recognition, that did not generate anaphylatoxins or did not induce the complement system affect or

arm triggering.(*254*) Very recently, Lee et al. showed that covalent conjugation of virus-like NPs with branched polynorbornene increases their shielding efficiency from antibody recognition.(*252*) These results suggest that complement activation can be minimized.

Figure 6-4c shows that the bioavailability of NC-CNTs was higher than for PL-CNTs. This may be associated with the higher softness of NC-CNTs. As described above, dPEs are rubbery and soft NPs; room temperature is significantly higher than their glass transition temperature. Thus, dPE-decorated CNTs form softer exterior compared with pristine CNTs. Numerous recent studies have evaluated the impact of elasticity on NP fate in the body.(*255-258*) By using soft and hard PEG-based hydrogel NPs, Anselmo *et al.* (*255*) showed that softer NPs have significantly reduced uptake in immune cells, endothelial cells, and cancer cells, but they showed enhanced circulation times and improved targeting. Key *et al.* (*256*) showed that soft discoidal polymeric NPs were more resistant to macrophage uptake compared with their hard counterparts. As a result, the NC-CNT system not only provides flexibility in anticancer drug selection, but also may enable tuning of the fate of NPs by changing the surface's mechanical properties. As shown in Figure 6-5, the internalization of fluorescein isothiocyanate (FITC)-labelled nanohybrids in HeLa cells was measured to determine the targeting capability of our proposed system. Figure 6-5a shows receptor-mediated endocytosis measured by FITC-labelling. There was a significant increase in FITC intensity of treated samples with NC-CNT compared to PL-CNTs. Moreover, internalization of NC-CNTs was higher than for PL-CNTs. Figure 6-5b shows the temperature dependency of NC-CNT endocytosis.

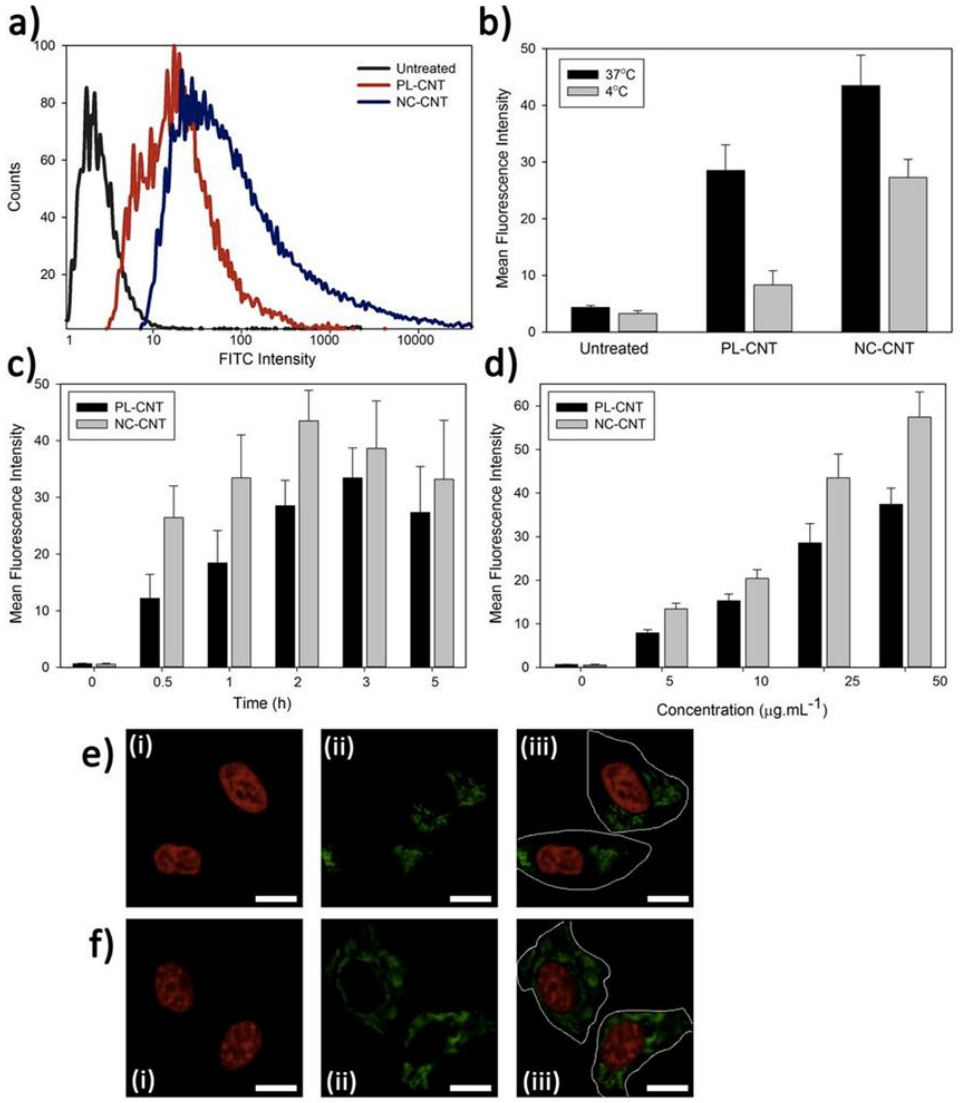

Figure 6-5 (a) Cellular uptake of FITC-labelled PL-CNT and NC-CNT nanohybrids after 2 h incubation with nanohybrids at 25 □g·mL^{-1} in a 10% foetal bovine serum (FBS) containing culture and measured by flow cytometry. b) Temperature-dependent cellular uptake based on median fluorescent intensity at 4 °C (black) and 37 °C (grey) (2 h; 25 μg·mL^{-1}; 10% FBS). c) Uptake kinetics of nanohybrids incubated with the HeLa cancer cells (25 μg·mL^{-1}; 10% FBS). d) Cellular uptake of nanohybrids as a function of nanohybrid concentration (2 h; 10% FBS). Values indicate mean ± one standard deviation from three independent measurements performed in triplicate. Confocal laser scanning microscopy images showing cellular uptake of FITC-labelled PL-CNT (e) and NC-CNT (f) nanohybrids, after 2 h incubation with HeLa cells in culture containing 10% FBS. The cell nuclei were stained with propidium iodide (red). The green dots represent internalized nanomaterials. The scale bar is 10 μm.

Internalization tests were performed on samples incubated at 4 and 37 °C. It is well-known that endocytosis is strongly inhibited at 4 °C.(*259*) As endocytosis is an energy-activated

process, internalization is expected to be higher at elevated temperatures for both PL-CNT and NC-CNT nanohybrid systems. However, we found that the relative decrease in endocytosis for the developed nanohybrids at 4 °C was significantly lower than that for other nanoparticle drug-delivery systems.(*260*) Kostarelos *et al.*(*261*) showed that different functionalized SWCNT can be internalized by mammalian and prokaryotic cells *via* energy-independent mechanisms. Internalization was found to be higher for NC-CNTs than for PL-CNTs and, surprisingly, a more pronounced difference was observed at lower temperatures. Figure 6-5c shows the kinetics of internalization over 5 h. During the test, internalization of NC-CNTs was higher than for PL-CNTs. As shown in Figure 6-5d, the amount of internalized nanohybrid structures increased with increasing dosage for both PL-CNT and NC-CNT samples. In accordance with the above results, for all concentrations, internalization was higher for NC-CNTs than for PL-CNTs. Figure 3e and 3f shows the confocal microscopy images of HeLa cells containing internalized PL-CNTs and NC-CNTs. Red and green areas represent the cell nucleus and CNTs, respectively. Figure 6-5e(iii) and 3f(iii) are the merged images of Figure 6-5e(i) with 6-5e (ii) and 6-5f(i) with 6-5f(ii), respectively. These figures clearly show the higher internalization of NC-CNTs than that of PL-CNTs.

One of the characteristics of CNTs is their photothermal effect in the near-infrared (NIR) region, while biological systems are transparent in this range.(*262*) Here, we attempted to exploit this potential for developing a 1D nanostructure platform for combinatorial cancer therapy. Figure 6-6a shows the temperature change of the media over time after laser irradiation. While the maximum temperature increase for PBS was less than 5 °C, both the PL-CNT and NC-CNT systems showed more than 20 °C increases after irradiation. Throughout the experiment, the temperature increase was higher for PL-CNTs than for NC-CNTs. This may be because of the thermal insulating effect of dPE. Figure 6-6b shows the *in vitro* release profile of PTX-loaded NC-CNTs in PBS (pH 7.4) at different

temperatures. The release profiles at 37 and 45°C revealed reasonably fast releases during early stages, followed by sustained asymptotic release, which was previously observed for PTX-loaded self-assembled NCs.(*52, 263-265*) As expected, the release rate was higher at elevated temperatures. To examine the effect of laser radiation on PTX release, two pulses of irradiation (808 nm; 1.5 $W.cm^{-2}$) were applied to the sample maintained at 37 °C (indicated by arrows in Figure 6-6b). Laser exposure caused increased release compared to the corresponding samples without laser exposure. Thus, fine-tunable drug release in combination with photothermal therapy is expected using NC-CNT nanohybrid structures.

One of the main prerequisites for an ideal anti-cancer nanomedicine is its ability to maximize toxic effects near tumour cells. Here, we examined the toxicity of unloaded and PTX-loaded NC-CNTs with and without laser irradiation. As expected, Pluronic F127-assembled nanostructures did not show cytotoxic effects. Both PL-CNTs and NC-CNTs without laser exposure showed similar toxicities in a concentration-dependent manner and more than 75% cell viability at all examined CNT concentrations. After applying the laser, the death rate of cancer cells significantly increased. This effect was more pronounced at higher CNT concentrations and more notable for NC-CNTs, which showed more than 90% cytotoxicity at 50 $\mu g \cdot mL^{-1}$ of CNT. This can be ascribed to the higher cellular uptake of NC-CNTs compared to that of PL-CNTs. Figure 6-6b shows the effect of PTX on the toxicity of nanohybrids. Interestingly, NC-CNTs without a drug were not toxic up to very high concentrations. Moreover, the efficiency of laser irradiation in the system without PTX was significant at higher CNT concentrations. However, the toxicity of PTX-loaded NC-CNTs was very high, which was associated with the higher PTX concentration inside the cells after high internalization of NC-CNTs. The results revealed a synergistic cytotoxic effect for PTX-loaded NC-CNTs after laser exposure. In fact, one order of magnitude less PTX is required to achieve equivalent toxicity when nanohybrid structures are exposed to laser light.

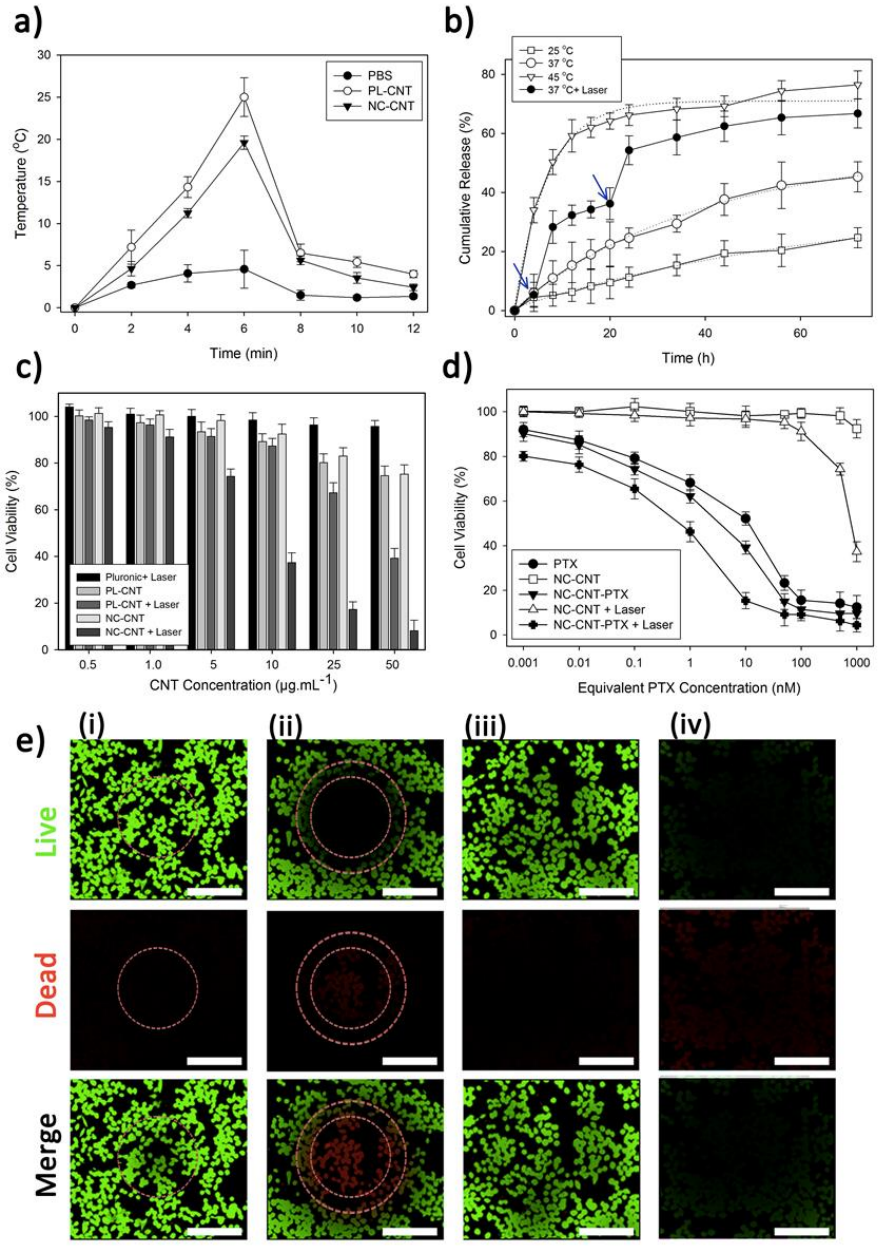

Figure 6-6 (a) *In vial* heat generation in PBS suspensions containing 10 μg·mL^{-1} of various types of designed CNT-based nanohybrids after NIR-irradiation (808-nm laser; 1.5 W·cm^{-2}; 6 min). (b) Cumulative *in vitro* release profiles of PTX from designed nanohybrids at pH 7.4 PBS solution and at different temperatures. Arrows indicate the time of laser exposure (mean ± SD, n = 3 independent experiments). MTT-based cell viability assay of HeLa cells after 72 h of exposure to PTX-loaded (d) and unloaded (c) NPs as a function of concentration at 37 °C. The effect of laser exposure on cellular viability of HeLa cells. (e) Visualized evaluation of cellular viability of HeLa cancer cells after various treatments *via* live-dead assay (scale bar 200 μm). Photothermal destruction of HeLa cells (i) without and (ii) with presence of 10 μg.mL^{-1} NC-CNTs (without PTX) after 6 min NIR irradiation (808 nm; 1.5 W·cm^{-2}), solid marked circle indicates laser irradiation spot. 10 μg·mL^{-1} of PTX-loaded NC-CNTs cultured

with cells for 4 h (iii) and 72 h (iv) and then removed by changing the media. All images were taken 24 h post (photothermal/PTX) treatment. Dead cells are red while viable cells are green.

The photothermal cytotoxicity was consistent with the results of the intracellular uptake of nanohybrids (Figure 6-5). The importance of localized and precise photodestruction of cancer cells or cancerous tissue has been emphasized in numerous previous studies. In CNT-treated cells, significant cell death was observed after 6 min of irradiation due to heat accumulation inside cells and sufficient temperature increase to initiate DNA damage. Comparison of the laser-irradiated area *versus* that of the non-irradiated region showed increased localized cell death.

6.4 Conclusion

In conclusion, we demonstrated the potential of using a microfluidic-assisted approach for synthesizing complex hybrid nanostructures based on carbon nanotubes. Through non-covalent non-specific CH−π interaction, hydrophobic dPE molecules decorated on the CNT surface and later block copolymers used to hydrophilic functionalized nano-kit. The designed dPE-CNT hybrid nanostructures with a narrow size distribution were shown to have a high capacity for loading anticancer drugs, which can be precisely tuned to provide a sustainable release pattern. Moreover, this simply fabricated but complex nanostructure showed high cellular uptake. The resultant nanocarriers showed remarkable efficiency for delivery of combinatorial cancer therapeutics based on photodynamics and chemotherapy. Regarding the employed interactions, the accessible nanostructures are not limited to 1D and with choosing other carbon-based materials like graphene and/or other simple or complex copolymer (e.g. containing targeting moieties), broader library of nanostructures with higher accuracy and efficiency can be synthesized.

CHAPTER 7. VIRUS-INSPIRED MECHANOBIOLOGICAL DESIGN OF CANCER NANOMEDICINES

Here we have tried to address the importance of mechanobiological properties of polymeric nanoparticles as they engage with biological systems. A microfluidic system was used to generate monodisperse nanoparticles with broad ranges of mechanical stiffness. A 3D tumor-on-chip device was then developed to mimic the dynamic and 3D microenvironment near the tumor spheroids *in vitro* which is further used to screen the targeting properties of engineered nanoparticles, too. We tried to optimize the mechanical properties and accordingly design a nanotherapeutics agent with prolonged blood circulation, enhanced tumor penetration and apoptosis promoting capability. Finally, we designed virus-mimicking NPs that can switch their mechanical stiffness to maximize their therapeutic efficacy.

7.1 Introduction

Mimicking features of a natural material is not a trivial undertaking. Natural particles such as pathogens (esp. viruses) are highly optimized for their specific functions *in vivo*. Such systems possess features desired in designing drug delivery vehicles. This approach enables us to satisfy the central dogma of drug delivery, which is to design bio-inspired vehicles that target tissues and cells with maximal therapeutic efficacy. Human immunodeficiency virus (HIV) is one of the most professional biological hijackers (*266*). These nanomaterials can circulate long enough through the blood to find their potential targets. It has been reported that immature HIV particles are more than four to 14-folds stiffer than mature ones (*266, 267*). Moreover, there is a striking correlation between the softness of HIV viruses during maturation and their ability to enter cells. Reported results show that HIV regulates its mechanical properties and turns stiff

when entering or leaving the cells, whereas being soft during blood circulation and undergoes maturation-induced stiffness switch during the infection process (*267*). Based on these findings, it is logical to consider mechanical properties as one of the cornerstones of nanoparticles' (NPs) pharmacokinetics, tumoral distribution pattern, cellular uptake rate and their mechanism of internalization. There are few reports that confirm the effects of micro-/nanoparticles' elasticity on pharmacokinetics and their cellular internalization in various cell lines (*255, 268, 269*). However, there is no systematic study to investigate the mechanobiological properties of NPs by keeping all the other physical variants such as size, surface charge, and ligand density constant. Therefore, this calls for the studies aimed at evaluating the effect of elastic deformation of NPs on their biological behavior. Here we proposed engineering strategies for enhancing the efficacy of cancer nanotherapeutics by controlling their physico-mechanical properties. As a robust synthesis tool that provides a controlled mixing regime, we used microfluidics platforms to synthesize monodisperse NPs with adjustable physicochemical properties. The central hypothesis is that mechanical properties of NPs, which is often ignored in nano-bio interface, significantly affect their therapeutic efficacies. Therefore, we systematically investigated the effects of mechanical characteristics of NPs on their biological functionalities both *in vitro* and *in vivo*, and then inspired by viruses, we offered a way to remotely switch the mechanical properties of NPs from soft to hard.

7.2 Materials and Methods

7.2.1 Chemicals and Biologicals

Unless noted otherwise, all chemicals were purchased from Sigma-Aldrich, Inc. (St. Louis, MO). All glassware was cleaned overnight using concentrated sulfuric acid and then thoroughly rinsed with Milli-Q water. human umbilical vein endothelial cells (HUVEC), U87MG human glioblastoma, human embryonic kidney cells 293 (HEK-293), human

breast adenocarcinoma (MCF-7) were purchased from American Type Culture Collection (ATCC). All other cell culture reagents, solutions, and dishes were obtained from Thermo Fisher Scientific (Waltham, MA) except as indicated otherwise.

7.2.2 Experimental

Hydrophobic modification of chitosan was performed according to our previous reports (*44*, *248*). In brief, 1 gr chitosan (CS; medium molecular weight, 280,000 g/mol, degree of deacetylation 83%, Fluka) was stirred for 12 h in aqueous acetic acid (50 mL, 1% w/v). Once dissolved, the solution was filtered with a 0.2 µm Nylon syringe filter. The pH was then adjusted to 5.5 by addition of sodium hydroxide. An ethanolic solution of 300 mg palmitic acid N-hydroxysuccinimide ester was added drop-wise to the chitosan solution at 98 °C under reflux and reacted for 48 h. The solution was then cooled down to room temperature and, after adding acetone, was precipitated by adjusting the solution pH to 9.0. The precipitated polymer was then filtered twice, washed with an excess of acetone, and lyophilized. The prepared hydrophobically modified chitosan (HMCS) was analyzed by ^{1}H NMR (Bruker 400 MHz).

The degree of substitution (DS) of palmitoyl groups on chitosan was determined using the ninhydrin assay (*44*). HMCS was dissolved in an aqueous acetic acid and then 0.5 mL of 4 M acetic acid in acetate buffer (pH= 5.5) was added into 0.5 mL of the prepared solution. 1 ml of ninhydrin reagent was then added and test tubes were placed in a boiling water bath for 20 min. The solutions were then cooled and absorbance at 570 nm was measured. The unmodified chitosan solution was used as control and the acetic acid/acetate buffer was used as the blank solution.

Fluorescein-modified hydrophobically modified chitosan (FITC-HMCS) were synthesized based on the reaction between fluorescein isothiocyanate (FITC) and the chitosan as described elsewhere (*270*). In brief, FITC was dissolved in methanol (2 $mg.ml^{-1}$) and then

added drop-wise to the solution of HMCS in 1% w/v acetic acid. After 5 h reaction in darkness, at ambient temperature, the FITC-labeled chitosan was precipitated in 0.2 M NaOH and separated from unreacted FITC in a Sephadex G-50 column with 1/15 M phosphate buffer/0.2 M NaCl as an elution solvent. Fractions containing the labeled polymer were collected and dialyzed using a 3500 Da molecular weight cut-off dialysis cartridge (Thermo Scientific, Rockford, IL) against deionized water for four days until no fluorescence was detected in the supernatant before freeze drying. The resultant FITC-HMCS was used to prepare the fluorescent labeled NPs as described above.

Microfluidic devices were fabricated with poly(dimethylsiloxane) (PDMS) using a standard soft-lithography process (*271*). To make the master molds, silicon wafers were spin-coated with SU-8 photocurable epoxy to a thickness of 60 μm. Baking, lithography, and development procedures were performed at the clean room facilities to obtain negative channels on the wafer. The wafers were then annealed at 150 ºC to eliminate surface cracks in the SU-8. After annealing, the surface of molds was coated with a self-assembled monolayer of trimethylethoxy silane by vapor exposure for 40 min. The SAM prevents PDMS from sticking to the mold. PDMS (Sylgrad 184) monomer and curing agent were mixed in a weight ratio of 10:1, poured into the mold, degassed in desiccators and cured in an oven at 80 ºC for 1 h. After curing, the PDMS was removed from the mold and in-/outlet holes were punched using a 150 μm diameter punch. The PDMS was then bonded to a glass slide using oxygen plasma (100 mW, 1 min). The PDMS microfluidic device had two inlets for alkaline water (pH 9), one for the aqueous solution of HMCS with the pH of 5.5 at four different initial concentrations of 0.5, 1.0, 2.0, and 5.0 $mg.ml^{-1}$), and one outlet. Water stream is split into two, in order to achieve two water streams at the flow focusing cross-junction. The mixing channel was 150 μm wide, 60 μm high and 1 cm long. The flow rates were adjusted for each concentration individually as shown in Table 7-1.

Table 7-1 Microfluidic processing conditions for making HMCS-based nanoparticles at different initial polymer concentrations.

	Polymer Conc. ($mg.ml^{-1}$)	Main Flow Rate ($\mu l.min^{-1}$)	Sheath Flow Rate ($\mu l.min^{-1}$)	Flow Ratio	Time of Mixing (ms)
FR-1	0.5	0.5	15	0.03	2.8
	1	0.5	16	0.03	2.5
	2	0.4	14	0.03	2.1
	5	0.7	20	0.04	3.1
FR-2	0.5	0.5	7	0.07	12.2
	1	0.5	6.5	0.08	14.0
	2	0.5	7.1	0.07	11.9
	5	0.4	5.5	0.07	12.6
FR-3	0.5	0.5	5	0.10	22.6
	1	0.5	5	0.10	22.6
	2	0.4	4.3	0.09	19.8
	5	0.6	5.5	0.11	26.5
FR-4	0.5	0.5	2.5	0.20	76.1
	1	0.5	2.5	0.20	76.1
	2	0.4	1.9	0.21	82.8
	5	0.6	2.9	0.21	80.5

For bulk synthesis of HMCS nanoparticles, polymeric solutions were prepared by dissolving 2.5 $mg.ml^{-1}$ polymer in 1% w/v acetic acid solution under constant stirring. HMCS nanoparticles were synthesized through nanoprecipitation by drop-wise addition of 1M sodium hydroxide to adjust the pH to 7.4.

To make photocrosslinkable nanoparticles, chitosan (1 mg/ml) chains first modified with poly (ethylene glycol) diacid (PEG-(COOH)2; 600 Da) (5 mg/ml) after activation with EDC/Sulfo-NHS for 5 min. The reaction was performed at pH 5 for 3 h. After purification of the product via dialysis and subsequent lyophilization, the carboxylic acid groups were reacted with diamine again using EDC/Sulfo-NHS chemistry for 5 h. These hydrazine groups are necessary for photocontrollable reaction with functionalized multi-arm PEGs. Functionalization of 4-arm PEG amine (5,000 Da; Creative PEGWorks, Chapel Hill, NC) was performed as previously reported by Anseth and coworkers (*272*). Incorporation of

photoreactive 2-nitrobenzyl-alcohol groups on PEG molecules form 2-nitrosobenzaldehyde (*272*) upon UV exposure using a laser diode at the wavelength of 405 nm with the intensity of 20 mW/cm^2 that can react with hydrazine groups of slightly modified chitosan chains (Figure 7-1).

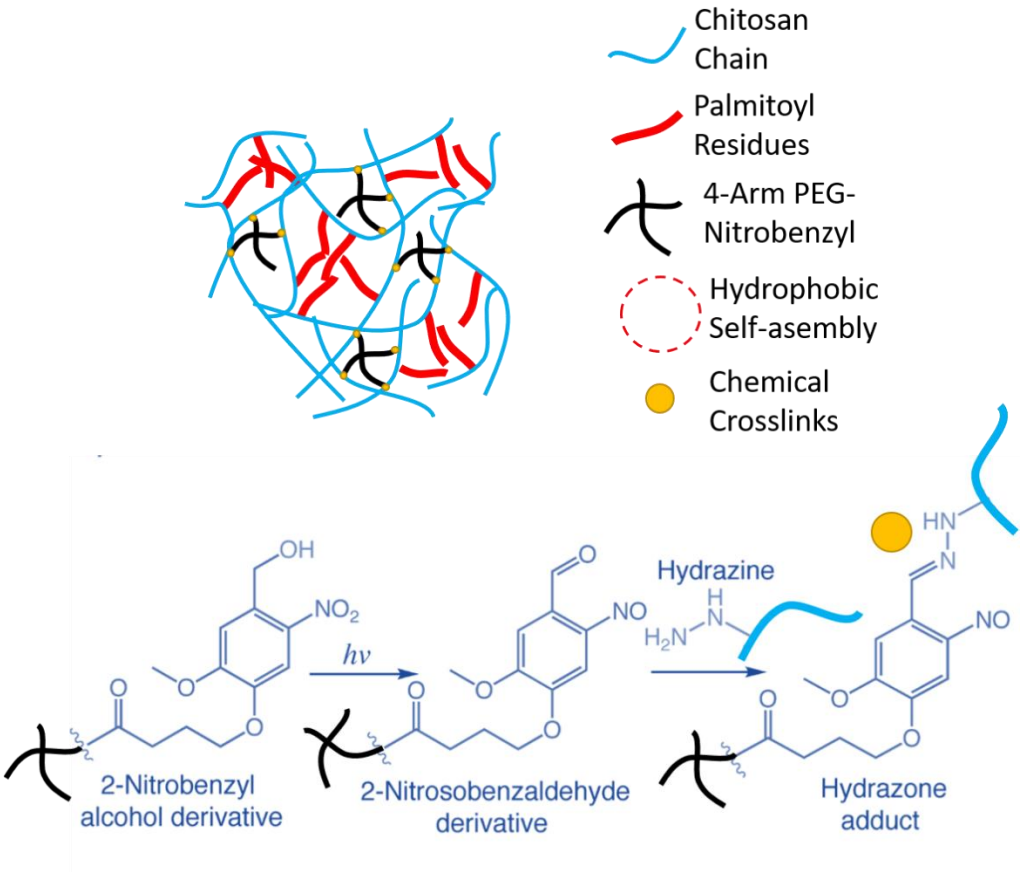

Figure 7-1 Schematic of proposed reaction between 2-nitrobenzyl-alcohol groups on 4-arm PEG with hydrazine groups of modified chitosan after UV exposure.

For drug loading into nanoparticles, Paclitaxel was dissolved in acidic water (pH 4.5) and mixed with the polymeric solution. Then, the nanoparticles synthesis was followed as detailed above.

Transmission electron microscopy (TEM; CM200-FEG-Philips) was used to characterize size and morphology of the nanoparticles. To this end, a dilute suspension of nanoparticles

was prepared and deposited onto a Cu TEM grid with a carbon film. The shape and size of the particles was characterized via diffraction (amplitude) contrast and, for crystalline materials, through high resolution (phase contrast) imaging. The TEM used a LaB6 source operating at 100 kV. The images were characterized using ImageJ software with at least 20 different measurements.

Dynamic light scattering (DLS) as well as zeta potential measurements were performed using a Zetasizer (Zetasizer 3000HS, Malvern Instruments Ltd., Worcestershire, UK) in backscattering mode at 173˚ for water diluted systems.

Transmittance of the prepared samples was measured at room temperature (20 °C) with a Shimadzu UV mini 1240 UV/visible spectrophotometer with a wavelength of 550 nm. Turbidity (τ) was calculated from the transmittance using Lambert-Beer's law:

$$\tau = -\frac{1}{L}\, ln\left(\frac{I_t}{I_0}\right) \qquad (Eq. 7-1)$$

where L is the length of light path in the sample cell (1.0 cm quartz cuvette), I_t is the intensity of the light transmitted through the sample, and I_0 is the intensity of the light transmitted through the solvent (deionized water). Each measurement was performed at least three times.

A PTR 46 refractometer (Index Instruments, UK) was used to measure the refractive index of 1% v/v aqueous acetic acid solution which was obtained as n_0 =1.332. The values of the refractive index increment (*dn*/*dc*) of the polymer solutions were determined through the asymmetric flow field-flow fractionation (AFFFF) method using AF2000 FOCUS system (Postnova Analytics, Landsberg, Germany). The *dn/dc* was measured at the wavelength of 635 nm.

For mechanical characterization of nanoparticles, standard V-shaped gold-coated silicon nitride tipless AFM cantilevers (Bruker/Veeco, Veeco Metrology Inc., now BrukerNano, Camarillo, CA) were used in this study. The cantilever spring constant was measured using the thermal fluctuations method. The spring constant of the cantilevers was found to be 0.105 N/m. Measurements were performed using a Veeco AFM II Dimension 3100 (Veeco Metrology Inc., now BrukerNano) instrument in liquid mode (ultrapure water) after drying the nanoparticles on poly (acrylic acid)-treated mica surface and re-hydrated with ultrapure water before test. To minimize viscoelastic effects, force-indentation curves were recorded at the frequency of 1 Hz.

To functionalized HMCS nanoparticles with cyclic RGD (Arg-Gly-Asp-d-Phe-Lys), carboxylic acid terminated cRGD-PEG reacted with amine-containing chitosan nanoparticles via 1-Ethyl-3-[3-dimethylaminopropyl] carbodiimide (EDC)/ N-hydroxysuccinimide (NHS) chemistry. After 5 h of reaction nanoparticles were dialyzed (Float-A-Lyzer, MWCO: 20kDa; Spectrum Laboratories, Inc., Rancho Dominguez, CA) for two days against PBS to remove unreacted cRGD-PEG molecules. The nanoparticles suspension was lyophilized and kept refrigerated before further use.

Quantification of RGD groups on the nanoparticles' surface wasw assessed using the LavaPep Peptide Quantification Kit (Gel Company Inc, San Francisco, CA, USA) as reported elesewhere (*273*). In brief, 100 µl of cRGD-PEG-HMCS nanoparticles (1 mg/ml) was mixed with 100 µl of the LavaPep working reagent and incubated for 1 h under dark condition and the fluorescence intensity was measured using a plate reader (Safire II, Tecan Sales Switzerland AG, Mannedorf, CH). The number of cRGD groups was estimated using a calibration curve of free peptides.

To determine the *in vitro* drug release profile, lyophilized PTX-loaded nanoparticles (1 mg) were dispersed in 1 ml of phosphate buffered saline (1X PBS, pH 7.4). The solutions

were placed into a 3.5 kDa molecular weight cut-off dialysis cartridge (Float-A-Lyzer). The cartridge was immersed in 1 L PBS and gently shaken in a 37°C water bath. At predetermined intervals, buffer solution samples were collected and replaced with an equivalent volume of fresh PBS. A Sequential pH change (from 7.4 to 6.5 or 5.5) in PBS medium was applied to study the effect of pH on release profiles. The PTX concentration was measured with reversed-phase high-performance liquid chromatography (HPLC) by mixing 1 ml of sample with 1 ml of acetonitrile as follows: A C18 column was used as the stationary phase, while the mobile phase consisted of acetonitrile:water (60:40 vol/vol). Separation was carried out at a flow rate of 1 $mL.min^{-1}$. PTX was detected at a wavelength of 230 nm. This method was evaluated over a linear range of 1-100 $\mu g.ml^{-1}$. In this range, the deviation from theoretical values was less than 5% and the R-square values remained less than 4% using clean PTX standards.

The PTX concentration in the solution was corrected for sampling effects according to [ref AFM]:

$C_n^l = C_n[V_T/(V_T-V_S)](C_{n-1}^l / C_{n-1})$, where C_n^l is the corrected concentration of the n^{th} sample, C_n is the measured concentration of PTX in the n^{th} sample, C_{n-1} the measured concentration of the $(n-1)^{th}$ sample, V_T is the volume of the receiver fluid and V_S represents the volume of the drawn sample (1 ml).

Encapsulation efficiency of the nanoparticles and loading contents were determined by applying the following equations:

PTX Loading content = (Weight of the loaded PTX / Weight of the NPs)×100

PTX Loading efficiency = (The amount of PTX in the NPs/ Initial amount of the PTX in NPs) × 100

Relative activities of PTX were estimated by calculating the maximum rate of tubulin polymerization relative to the standard samples as reported before (*44*, *274*). Stability of the free and encapsulated PTX inside different types of nanoparticles was evaluated by measuring the variations of their activities using the tubulin protein assay after storage at 25°C and 37°C for 1-14 days in a 96-well microtiter plates according to previously established protocols. Briefly, at defined time intervals nanoparticles were separated using centrifugation and redispersed in water at pH 4.5 to extract the PTX from the nanoparticles. The PTX was then separated using HPLC to perform a tubulin protein assay. PTX at defined concentrations was reacted with tubulin protein solution (general tubulin buffer, tubulin glycerol buffer, 1 mM GTP) and the reaction was followed by measuring the increase in apparent absorption at 350 nm over 1 h at 37°C using a Safire II plate reader.

To analyze expression of integrin receptor using Western blot, HUVEC, U87 MG, HEK-293, and MCF-7 cells were lysed using protein extraction buffer (Bio-Rad, Irvine, CA). The extracted proteins were fractionated in 10% sodium dodecyl sulfate-polyacrylamide gels (PAGE) and electrophoretically transferred to a nitrocellulose membrane (Bio-Rad). The membranes were then incubated with antibodies against avb3 as well as GAPDH which was used as the housekeeping protein. For flow cytometry analysis, antibodies to integrin αvβ3 were purchased from Abcam. Cells were analyzed on FACSVerse using FlowJo software (Treestar).

The cellular uptake of different types of FITC-labeled HMCS nanoparticles were measured using flow cytometry, FACSVerse Analyzer (BD Biosciences). For the FACS analysis1 10^6cells (each type) were dispersed into Eppendorf tubes. Then nanoparticles were added at different concentrations of 100 $\mu g.ml^{-1}$, except for the unstained negative control, and the cells were incubated for 2 h in normal medium in a tissue culture incubator. The cells were then washed using ice-cold PBS containing 10% FBS, and transferred into FACS tubes. All samples were kept on ice until FACS analysis.

The cells were seeded in a T-25 flask and treated with 0.1% NaN_3 and 80 μM Dynasore in a serum-free MEM for 1 h before incubation of the nanoparticles at 37°C/5% CO_2. For the action of chlorpromazine, the cells were pre-incubated in a serum-free MEM containing 10 μg/ml chlorpromazine (ChemBridge) for 15 min at 37°C and 5% CO_2. The medium was then replaced with a fresh media containing the inhibitors and particles. These cells were further incubated for 30 min at 37°C and 5% CO_2. The cells were washed with D-PBS and trypsinized and processed for the flow cytometry test. Further, to examine the contribution of macropinocytosis in the uptake cascade, the cells were incubated with a macropinocytosis inhibitor, 5-(N-ethyl-N-isopropyl) amirolide (EIPA), at the concentration of 100 μM for 30 min. Then, the cells were incubated with a fresh medium containing the nanoparticles. Then, the cells were washed after 1 h (*50*). The resulting cells were analyzed via FACS. To further explore the mechanism through which these nanoparticles entered the cells, we performed an internalization experiment at 4°C to block the active endocytosis cascade.

Effect of different formulations of nanoparticles on proliferation of cancer cell lines was evaluated by MTT assay. In brief, cells were cultured on standard 96-well plate at a density of 10,000 cells per well. The cells were cultured at 37 °C in a 5% CO_2 incubator. After incubating for 24 h, the culture medium was replaced by fresh medium containing specific concentrations of nanoparticles representing PTX concentrations of 0.001-1000 nM and incubated for 72 h. For paclitaxel treatment, a stock solution of paclitaxel (10 $mg.ml^{-1}$ in DMSO) was diluted to the defined concentration in culture medium. Then, tetrazolium salt (M2128) was added for an additional 4 h. Thereafter, formazan crystals were dissolved in dimethyl sulfoxide while shaking for 20 min. Absorbance at 570 nm was measured by utilizing a microplate reader at 570 nm. The control medium contained no nanoparticles. The samples were maintained with uniform drug concentration. The spectrophotometer was calibrated to zero absorbance using culture medium without cells. The relative cell

viability (%) related to the control wells, containing cell culture medium without nanoparticles, was calculated by $[A]_{test}/[A]_{control} \times 100$, where $[A]_{test}$ is the absorbance of the test sample and $[A]_{control}$ is the absorbance of the control sample. To evaluate the viability of the encapsulated U87 MG cells in 3D collagen-based matrix, a live-dead assay (Calcein AM/ethidium bromide homodimer-1) was utilized after treating the encapsulated cells with different formulation of nanoparticles at different concentrations. NIH ImageJ software (NIH, Bethesda, MD) was used to quantify the percentage of live cells.

The role of PTX-loaded nanoparticles' treatment on migration of HUVECs toward VEGF gradient was performed using Transwell migration assay as reported elsewhere (*275, 276*). The migrated cells were stained on the bottom sides of the membrane and counted to assess the migration of HUVEC cells.

Matrigel-based angiogenesis assay was done according to the manufacturer's protocol (Corning; Santa Barbara, CA) (*277, 278*). In brief, Matrigel (10 µl) was added to 96-well plates and kept in cell culture incubator for 1 h. GFP Expressing HUVECs were seeded at a density of 2.5×10^5 cells per well. All HUVEC experiments were conducted in EBM2 medium (Lonza) supplemented with 25 ng/ml VEGF (Abcam) and 2.5 ng/ml epidermal growth factor (Abcam). A formulation array of PTX-loaded and unloaded nanoparticles containing PTX were added to media and co-cultured with cells for 72 h. Afterward, wells were washed twice with DPBS and the formation of tube-like structures in 3D matrix was evaluated using a confocal laser scanning microscope (Confocal Leica SP5 Blue).

Cell aggregates were made using a force aggregation method as reported elsewhere (*279*). Micropatterned wells were kindly provided by Mark Ungrin group at University of Calgary. Square pyramidal microwells with 400 µm side-wall dimension of each square pyramidal well (AggreWell, Stem Cell Technologies; 400 µm side-wall dimension of each square pyramidal micro-well) were used as described previously (*279, 280*). U87 MG cells

trypsinized and seeded on micropatterned wells at a concentration of 1.2×10^6 cells per well.

Well plates were centrifuged at 200×*g* for 5 min. Plates were visualized under the microscope to confirm cells have spun to the bottom of each microwell. The plate was incubated for 24 h at 37 °C in an incubator, aggregates were then harvested from each well, and finally the aggregate suspension was collected in a 15 mL conical tube before injection into the on-a-chip platform. At this seeding density, aggregates containing 800-1200 cells were formed.

Soft lithography procedures were used to fabricate the aggregate trap microfluidic device. The same procedure was used as described above to make PDMS-based microfluidic chip. Before use, the device was flushed with Pluronic F-127 copolymer solution (0.2 mg/ml) to prevent unspecific protein/cell interactions with PDMS walls. The capture efficiency of the chip was first optimized with 150 µm fluorescent polystyrene beads. In brief, aggregates suspension was introduced to the device at concentration of 1000 aggregates per ml *via* a syringe pump. The number of captured aggregates was visualized *via* fluorescence microscopy after immunostaining of cells with anti-integrin β_3-FITC antibody. To evaluate association of nanoparticles with cancer cell aggregates, the device placed in microscope incubation chamber and the flow of nanoparticles was controlled with a precision micro peristaltic pump (Cole-Parmer). Accumulation of nanoparticles was visualized over time using a confocal laser scanning microscope. Distribution of FITC-labeled nanoparticles through the cell aggregates was evaluated using ImageJ software after normalizing the fluorescence signal to the surrounding media.

Soft lithography method was conducted to develop a multilayer microfluidics device to represent the main features of tumor microenvironment *in vitro*. The upper and lower layers were fabricated by casting PDMS resin (10 resin: 1 curing agent) on master molds contains

positive patterns. The height of the channels was 300 μm. Thin nanoporous glass membranes with 500 nm pores (SiMPore's G-FLAT™ Microporous Glass Membranes; West Henrietta, NY) were used between the upper and lower channels.

The membrane surface was treated with oxygen plasma and irreversibly bond to upper and lower PDMS substrates sequentially after manual alignment. Aggregates suspension was introduced to the device at concentration of 1000 aggregates per ml *via* a syringe pump (green channels) and then collagen solution was injected. Collagen hydrogels were prepared by mixing the rat tail collagen I, sodium hydroxide and EDTA on ice as reported elsewhere (*281*). The final concentration of collagen was 2.5 and 5.0 mg/ml. After vortex mixing for 30 s, the gel solution was injected to the lower chamber of 3DToC device *via* a syringe pump while providing the flow of ice-cold PBS in the other channels, then incubated overnight at 37 °C.

Different hydraulic pressure conditions have been applied at capillary, interstitial and tumor microchannels as proposed before (*282*). Here, 10, 5, and 20 mmHg pressures were applied at both ends of interstitial, tumor, and capillary channels, respectively. These pressures were selected to represent physiologically relevant conditions. Penetration of FITC-labeled nanoparticles in collagen hydrogel monitored using a confocal laser scanning microscope at different time points (30 min-12 h). Daily investigation of aggregate size was performed over the time course of 7 days.

Flow cytometry analysis (FACSVerse, BD Bioscience) was performed to evaluate apoptosis of U87 MG cell after treatment with different nanoparticle formulations inside the 3D tumor-on-chip device. Cell aggregates were extracted from device after digestion of collagen hydrogel. Relative number of apoptotic cells was evaluated using Annexin V-PE Apoptosis Detection Kit (BD Bioscience).

Protein corona experiment performed as reported elsewhere (*283, 284*). In brief, blood was taken from ten healthy donors in accordance with institutional policy. Plasma was separated and the protein aggregates further removed by ultracentrifugation. Soft (sample A) and hard (sample B) nanoparticles were incubated with human plasma under gentle shaking for 3 h, separated using ultracentrifugation at 20,000×g for 1 h, and then washed thee times. The ratio of particles to plasma was calculated to represent approximately constant surface area. Proteins then eluted after dissolving HMCS nanoparticles by reducing the pH to 3.0 and shaking the solution for 30 min. proteins concentration was assessed by micro BCA protein assay after correcting the values for chitosan chains. Then, proteins were digested following the reported protocols (*285*). Quantitative analysis of protein samples was performed by liquid-chromatography mass-spectrometry (LC-MS) technique. LTQ Orbitrap XL Mass Spectrometer (Thermo Fisher Scientific) coupled with Eksigent NanoLC-2D HPLC and Autosampler was used after 10-fold dilution of digested protein samples in 0.1% formic acid. The experimental details were followed as reported by Schöttler et al. (*283*). MS spectra were collected over an m/z range of 300-2000 Da. All samples were analyzed in triplicate and quantitative data were made to estimate the amount of each protein in fmol.

All experiments on mice were performed in accordance with institutional policy on human and ethical treatment of animals. For *in vivo*, female BALB/c mice (18–21 g) were used. For all the experiment, U87 MG human glioblastoma tumor model were generated by subcutaneous injection of 5×10^6 cells in 50 ml PBS into the front left legs of the mice. When the tumor diameter reached 5 mm (after about three weeks), the mice randomly assigned for the experiments. All mice were fed with a commercial diet and water *ad libitum* and were on alternating 12 h light/dark cycles.

For *in vivo* pharmacokinetic (blood circulation) studies, six tumor-bearing BALB/c mice were randomly divided into two groups for the two different types of nanoparticles (n=3)

and free drug. Both groups received injections via the tail vein at a dose of 2 mg nanoparticles per kg of body weight. Blood samples were drawn into heparinized tubes from the retro-orbital sinus at different time points and then centrifuged for 15 min. The plasma was separated and stored at −20 °C in the dark before analysis. The plasma concentration of blood containing particles was defined based on the fluorescence intensity using microplate Reader. The normalized plasma concentrations of the applied particles were plotted as a function of time. The data were fit to a two-compartment model, from which the half-lives characterizing the nanoparticle formulations can be extracted.

Tissue accumulation of nanoparticles in tumor and other organs including bone, heart, kidney, liver, muscle, and spleen also evaluated by measuring the tissue's fluorescence signal 48 h after tail vein injection of FITC-labeled nanoparticles to determine the percentage of injected dose per gram (%ID/g) for each sample (n=4).

In order to assess tumor suppression and survival rates, mice were randomly assigned to experimental groups (n=5) to receive physiological Saline (PBS), free PTX, and PTX-loaded nanoparticles with different formulations *via* tail vein injection on the first and seventh days of the experiments. The paclitaxel dose kept constant to 10 mg/kg body weight across all the formulations. Tumor volume was monitored using a digital caliper at different timepoints and the volume was mounted as length×$(\text{width})^2/2$. The serial measurements of tumor volume were followed for two weeks on which the animals were sacrificed. The survival times of tumor-bearing mice were also investigated by the same procedure as described above but after treatment of animals at 0, 7, 14, and 21 days with free PTX, and PTX-loaded nanoparticles with different formulations. The survival time was assessed (n=5) over period of two months.

To evaluate angiogenesis in the presence of different types of nanoparticles *in vivo*, the Matrigel assay was performed according to procedure reported elsewhere (*286, 287*). In

brief, mice (n=5) were injected subcutaneously on the flank of mice with 400 µl of VEGF-containing Matrigel encapsulating 4×10^6 HUVECs. After 48 hours, mice were received injections of PTX-loaded nanoparticles (10 mg of equivalent PTX mass per kg of body weight) *via* the tail vein. After 48 h, 100 µl of tetramethylrhodamine isothiocyanate–Dextran (TRITC-Dextran; 155 kDa) was injected intravenously (50mg/ml) via the tail veins (*288*). After 10 minutes, animals were sacrificed and the Matrigel plugs were removed, fixed and imaged by confocal fluorescence microscope. The relative fluorescence intensities were quantified using ImageJ software. After identifying the vessels' borders the extravascular TRITC content was quantified. Vascular leakage was defined as extravascular TRITC/total TRITC (*288*).

The retrieved tumor tissue samples were prepared (fixed, paraffin embedded, and sectioned). For immunofluorescence staining, the prepared specimens were treated with TUNEL kit (Click-iT® TUNEL Alexa Fluor® Imaging Assay) to detect the apoptosis according to manufacturer's instruction. The images were taken using a fluorescent microscope (Leica Microsystems).

All experiments were conducted at least in triplicate. The statistical analysis of the experimental data was done using the Student's t-test or ANOVA, and the results were presented as mean ±S.D. For all the tests, the threshold was set to $p < 0.05$ for "statistically significant", $p < 0.01$ for "statistically very significant" and $p < 0.001$ for "statistically extremely significant".

7.3 Results and Discussion

Polymeric NPs can be synthesized either by top-down or bottom-up approaches. Since the bottom-up process involves self-assembly of particles *via* intermolecular forces, it offers great opportunities for tailoring structure and properties of particles. However, having control over the synthesis procedure can be really challenging in this approach.

Thanks to the microfluidic techniques (Figure 7-2a), we can reproducibly create small monodisperse NPs through the well-controlled mixing regimes that form *via* hydrodynamic flow focusing. Our previous results confirm the possibility of controlling the main physical and biological characteristics of NPs such as size (50-250 nm), Zeta potential (1-14 mV), drug loading efficiency (>95%), and drug release profiles ($\approx 3\times10^{-22}$ $m^2.s^{-1}$) (*44, 248, 270, 274, 289, 290*) simply by playing with flow rates. However, in order to keep all the NPs' features constant and play with just a single physical property (*e.g.,* mechanical stiffness) we cannot rely just on flow ratio as the tuning factor. Here, by introducing the second controlling factor, polymer initial concentration, we have provided two degrees of control over the physical properties of NPs. We have used hydrophobically-modified chitosan (HMCS) with N-palmitoyl groups in the current work. We have shown HMCS can form nanoparticle through self-assembly and encapsulate hydrophobic anticancer drugs (*44, 248*). As demonstrated in Figure 7-2 b-c, we synthesized an array of HMCS NPs with desired properties by tuning polymer concentration and flow rates.

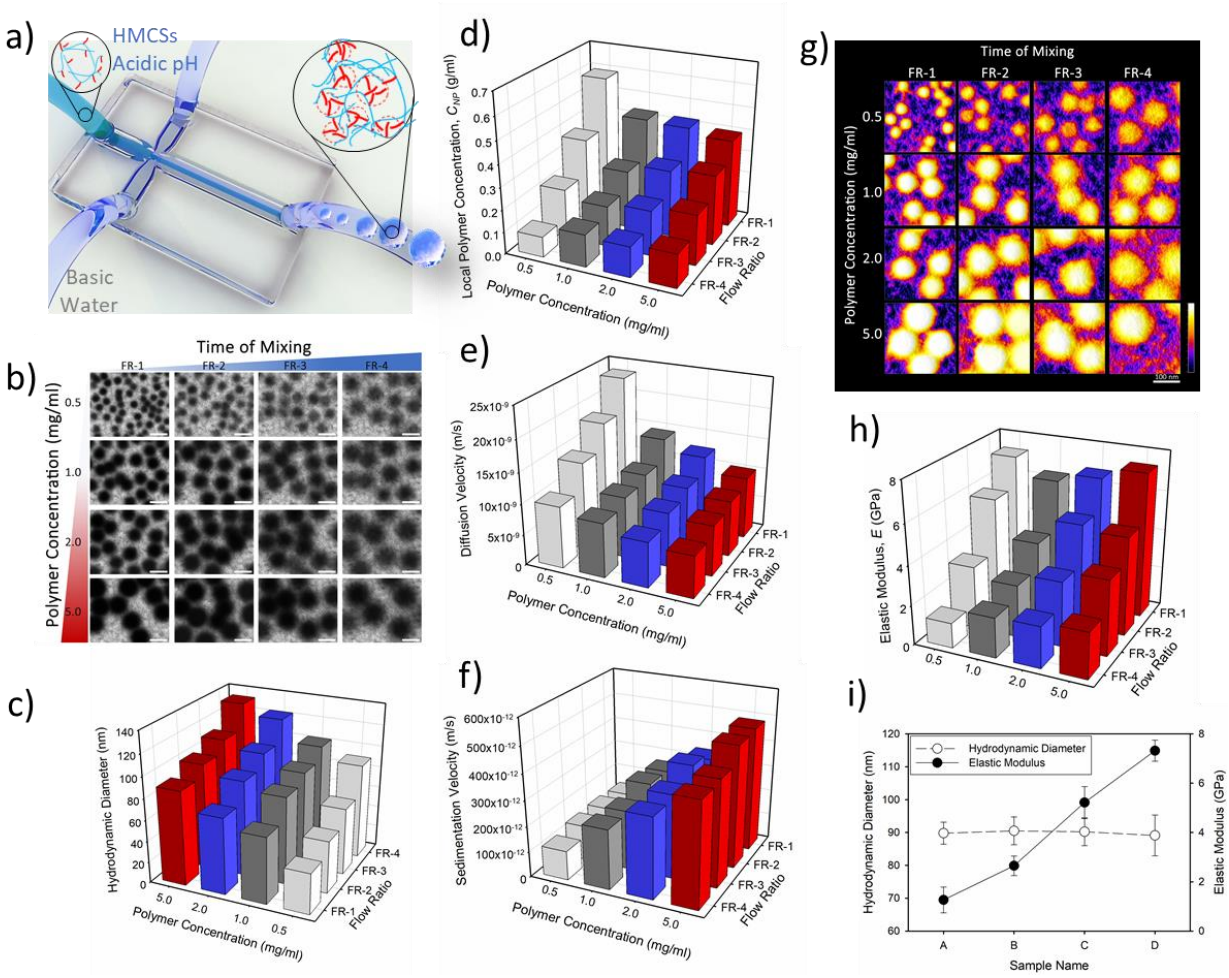

Figure 7-2 Schematic representation of cross junction microfluidic used for hydrodynamic flow focusing of hydrophobically-modified chitosan (HMCS) stream using sheath flow of water at basic pH. The effect of flow ratio and initial polymer concentration on (b) morphology and (c) hydrodynamic diameter (based on the DLS measurements) for synthesized NPs. (d) The calculated compactness of NPs (local polymer concentration; c_{NP} inside the NPs). (e) The diffusion[1] and (f) sedimentation[2] velocities of the synthesized NPs. (g) AFM-nanoindentation images and (h) calculated Young's modulus (E) of prepared NPs at different conditions. (i) Having an array of NPs enabled us to select series of NPs with same sizes, but different mechanical properties.

[1]**Diffusion velocity: $V_D=2D/x$;** x: certain distance of travel (culture medium height); [2]**sedimentation velocity: $V_s=2gr^2c_{NP}(\rho_P-\rho_0)/9\eta\rho_P$**; g: gravitational acceleration, c_{NP}: NPs compactness.

In addition to the initial polymer concentration, degree of substitution (*i.e.*, palmitoyl group) affects the overall physical properties of HMCS NPs. Based on transmission

electron microscopy (TEM) images and turbidity results (Table 7-2), it is evident that prepared NPs have different levels of compactness.

Table 7-2 Turbidity values for HMCS nanoparticles prepared with microfluidics technique.

Turbidity (cm^{-1})	Initial Polymer Concentration; C_t ($mg.ml^{-1}$)			
	0.5	**1.0**	**2.0**	**5.0**
FR-1	0.231	0.272	0.311	0.361
FR-2	0.188	0.220	0.276	0.319
FR-3	0.141	0.171	0.212	0.253
FR-4	0.084	0.150	0.170	0.203

The local polymer concentration inside the NPs, c_{NP}, was calculated (*see Chapter 2 for details*) as an indicator of compactness. As seen, compactness of NPs was found to increase as flow ratio decreased. In fact, in shorter mixing times, higher probability of hydrophobic segments to form intermolecular association leads to formation of more compact NPs (Figure 7-2d). By having the c_{NP}, molecular weight of NPs, M_{NP}, number of the polymer chains aggregated to form NPs, N_{agg}, number density of NPs, N, as well as the average mass of individual NPs were calculated and presented in Table 7-3 *(see Chapter 2 for calculation details).* The obtained results revealed that number of the aggregated chains rises with increase in the time of mixing. Such observation suggests that at lower flow ratios and on account of rapid mixing regime, chains have limited time to aggregate, which results in lower number of kinetically assembled chains forming NPs, which is also affected by the initial polymer concentration. The obtained results for compactness and aggregation number converge to indicate that at lower flow ratios (fast mixing regimes; FR-1 and FR-2) smaller and more compact NPs form that are composed of relatively higher number of aggregated chains. In view of this, formation of NPs at higher flow ratios (slow mixing regimes) results in bigger hydrodynamic sizes and lower compactness values due to the arrangement of HMCS chains at longer time of mixing.

Table 7-3 The calculated NPs' molecular weight (M_{NP}) (a), the concentration of NPs (N_{NP}) (b), and aggregation number (N_{agg}) of the polymer chains in the corresponding NPs (b).

a)

M_{NP} (g.mol^{-1}) ×10^{7}	Initial Polymer Concentration; C_t (mg.ml^{-1})			
	0.5	**1.0**	**2.0**	**5.0**
FR-1	5.697	6.802	7.692	8.882
FR-2	4.624	5.411	6.805	7.880
FR-3	3.494	4.159	5.240	6.230
FR-4	2.073	3.749	4.233	5.060

b)

N_{NP} ($\#_{NP}$.ml^{-1}) ×10^{12}	Initial Polymer Concentration; C_t (mg.ml^{-1})			
	0.5	**1.0**	**2.0**	**5.0**
FR-1	3.584	2.245	3.001	4.268
FR-2	2.663	1.631	2.174	3.881
FR-3	2.155	1.768	2.199	4.051
FR-4	1.802	1.544	1.904	3.403

c)

N_{agg} (#)	Initial Polymer Concentration; C_t (mg.ml^{-1})			
	0.5	**1.0**	**2.0**	**5.0**
FR-1	380	453	513	592
FR-2	308	361	454	525
FR-3	233	277	349	415
FR-4	138	250	282	337

Diffusive and sedimentation behavior of NPs evaluated based on the calculated parameters and the results of sedimentation and diffusion velocities are plotted in Figure 7-2 e,f. Diffusive properties, velocity (Figure 7-2e) and coefficient (Table 7-3a) are scaled with the size of NPs but the sedimentation characteristics, velocity (Figure 7-2f) and coefficient (Table 7-4b), are much more depending on the compactness and weight (Table 7-4d) of NPs.

Table 7-4 The nanoparticles' diffusion (a), sedimentation (b), and drag coefficients as well as calculated mass of NPs.

a)

Diffusion Coefficient; D ($m^2.s^{-1}$) $\times10^{-12}$	Initial Polymer Concentration; C_t ($mg.ml^{-1}$)			
	0.5	**1.0**	**2.0**	**5.0**
FR-1	11.71	7.16	6.23	5.05
FR-2	9.10	5.44	4.98	4.53
FR-3	7.11	4.97	4.40	4.12
FR-4	5.01	4.41	3.68	3.40

b)

Sedimentation Coefficient; S (s^{-1}) $\times10^{-9}$	Initial Polymer Concentration; C_t ($mg.ml^{-1}$)			
	0.5	**1.0**	**2.0**	**5.0**
FR-1	6.86	10.18	13.04	17.51
FR-2	4.78	6.73	10.54	14.07
FR-3	2.84	4.06	6.41	9.00
FR-4	1.03	3.33	4.26	6.06

c)

Drag Coefficient; f ($g.s^{-1}$) $\times10^{-10}$	Initial Polymer Concentration; C_t ($mg.ml^{-1}$))			
	0.5	**1.0**	**2.0**	**5.0**
FR-1	3.66	5.98	6.88	8.48
FR-2	4.71	7.86	8.59	9.45
FR-3	6.02	8.61	9.73	10.40
FR-4	8.55	9.71	11.63	12.59

d)

NP Mass; m (g) $\times10^{-17}$	Initial Polymer Concentration; C_t ($mg.ml^{-1}$)			
	0.5	**1.0**	**2.0**	**5.0**
FR-1	1.74	5.57	8.33	14.64
FR-2	2.35	7.66	11.50	16.10
FR-3	2.90	7.07	11.37	15.43
FR-4	3.47	8.10	13.13	18.36

These parameters have been adjusted to enable us to have NPs with similar sizes but different compactness; and as a result, they possess different mechanical properties as measured by atomic force microscopy (AFM) nanoindentation (Figure 7-2 g-h). Interestingly, by moving diagonally along these graphs, we have NPs with quite the same hydrodynamic radiuses (89-91 nm), but as they are formed in different regimes, the mechanical properties are different by about 7 folds (Figure 7-2 h,i). From now on, we call these NPs as *A*-*D* from softest (C_{HMCS} =0.5 and FR-4) to stiffest one (C_{HMCS} =5.0 and FR-1) (Figure 7-2 i). The selected sizes are in the acceptable range for passive targeted drug delivery, which helps to achieve enhanced penetration and accumulation of particles in tumor sites. [2,4-5] However, as these particles possessed variable surface charges (zeta potential: 5-19 mV) poly (ethylene glycol) (PEG) modification was implemented to eliminate the effect of surface charge on biological behaviors of these particles. Since modification with pristine PEG significantly reduces the potential of NPs to associate with cells, we used cyclic-RGD (cRGD) modified PEG (cRGD-PEG) for decorating our particles at optimized surface densities (Figure 7-3 a-c). The optimized ligand density is

measured to be 20,000 cRGD.μm^{-2} which equals to about 500 ligands per NPs. This level is shown to have low phagocytosis by macrophages (RAW264.7) as well as high cellular uptake by integrin expressing cells (*e.g.* HUVEC) (Figure 7-3 d-e).

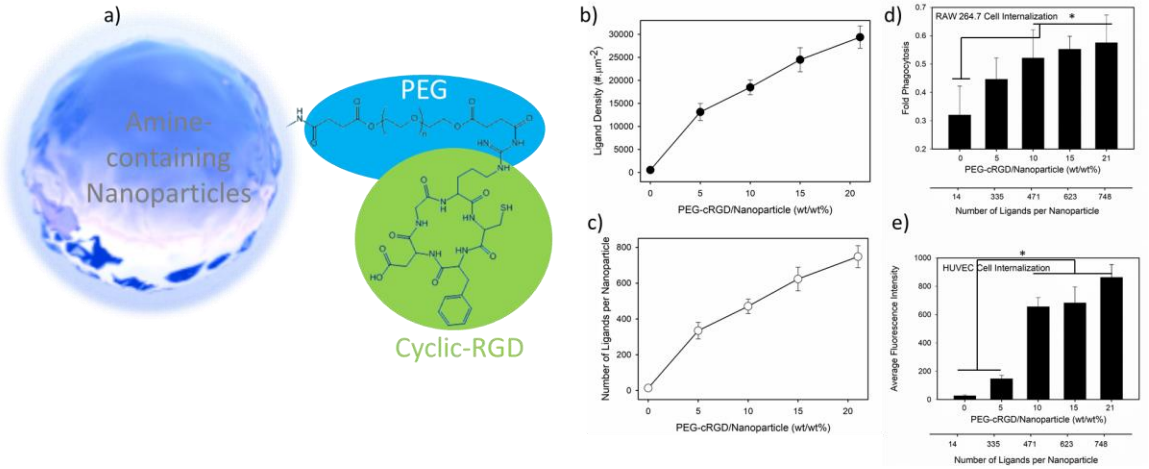

Figure 7-3 (a) Schematic representation of bioconjugation of chitosan-based NPs with cyclic-RGD-based poly (ethylene glycol) (cRGD-PEG). (b) Quantification of cRGD surface density and (c) the number of conjugated cRGD per NPs as a function of initial cRGD-PEG in reaction. Association of NPs in RAW 264.7 (d) macrophages and (e) endothelial cells (HUVEC) which examined to select the optimized number of ligand per NPs. The presented data are expressed as average ± SD. The results were statistically analyzed using unpaired t tests. Statistical significance is indicated by * ($p < 0.05$).

As seen in Figure 7-4a, PEGylation process is optimized to provide nanoparticles with the same level of cRGD ligand. Surface charge (Figure 7-4b) of NPs are studied and the values of Zeta potentials are reported in Figure 7-4b. NPs with lower surface charges needed more cRGD-PEG to present the same level of ligand. Although functionalization of NPs with PEG was used to eliminate the effect of surface charge of NPs, is may not be able to react with all the primary amines due to the steric hindrance. To confirm that the remaining free amines will not interfere with the biological properties of NPs, we further treated them with citraconic anhydride to covalently block the remaining amine groups. As shown in Figure 7-4c, chemical blockade of amine groups did not affect the surface charge and internalization of nanoparticles so further blocking was not required.

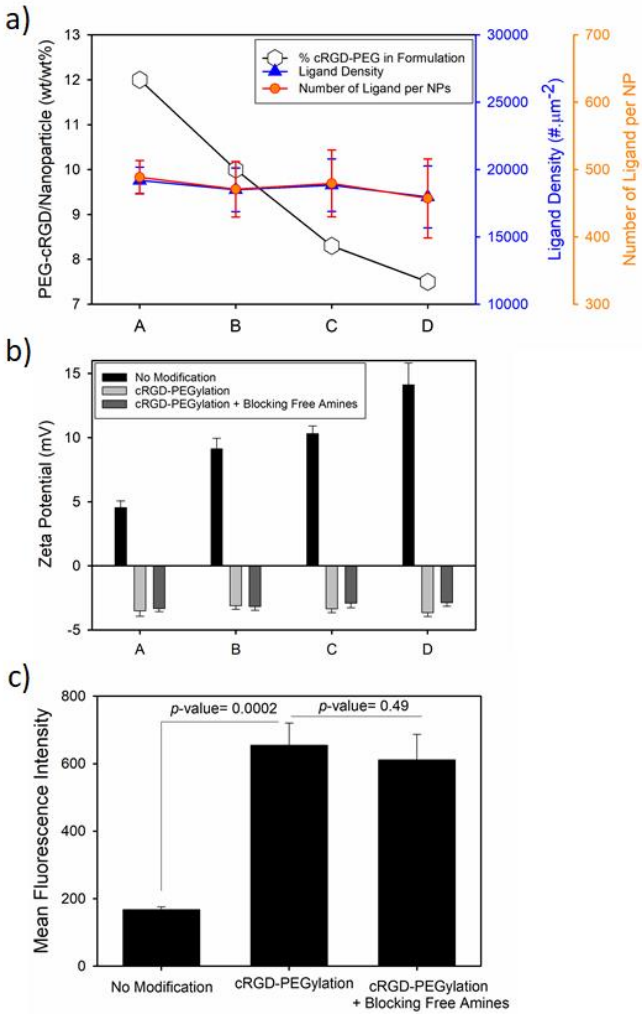

Figure 7-4 (a) Optimizing of the formulation by changing the ratio of reactive cRGD-PEG to NPs to have nanoparticles with same density of ligands. Zeta potential measurements (b) and HUVEC internalization experiments (c) confirmed sufficient coverage of primary amine groups on HMCS surface and further blockade of amine groups with Citraconic Anhydride did not affect surface charge and internalization of nanoparticles.

Due to amphiphilic nature of HMCSs, we can encapsulate both hydrophobic and hydrophilic agents (*44*, *270*, *290*). Here, we have tried to encapsulate paclitaxel (PTX), as a hydrophobic anticancer drug, during the formation of NPs [*Note 1:* An acidic condition during the injection of HMCS/PTX prevents PTX epimerization and prolongs its activity]. PTX loading content (Figure 7-5a) and efficiencies were evaluated at different initial drug contents of 5-20 wt%/$wt_{Polymer}$. It seems that in the case of more compact NPs (D and C), more hydrophobic moieties were involved and interacted with PTX molecules during the

formation of NPs, resulting in higher encapsulation efficiencies. This high level of interactions can also protect the drug molecules from degradation (*i.e.*, epimerization) both at shelf temperatures and inside the body as confirmed by evaluating the functionality of encapsulated PTX molecules to inhibit tubulin polymerization (Figure 7-6). The *in vitro* release profiles of NPs containing same content of drug were compared in phosphate buffer saline (PBS) at different pH range of 7.4, 6.5, and 5.5 over two weeks (Figure 7-5). As shown in Figure 7-5, more compact NPs showed slower releases compared to the softer ones with less sensitivity to pH reduction (pH 6.5 mimicking the tumor microenvironment and pH 5.5 as an indication of intracellular (lysosomal) pH). Estimation of the required time to release half of the loaded PTX (t_{50}) from the NPs and calculation of diffusion coefficients (Figure 7-b inset) confirmed the idea.

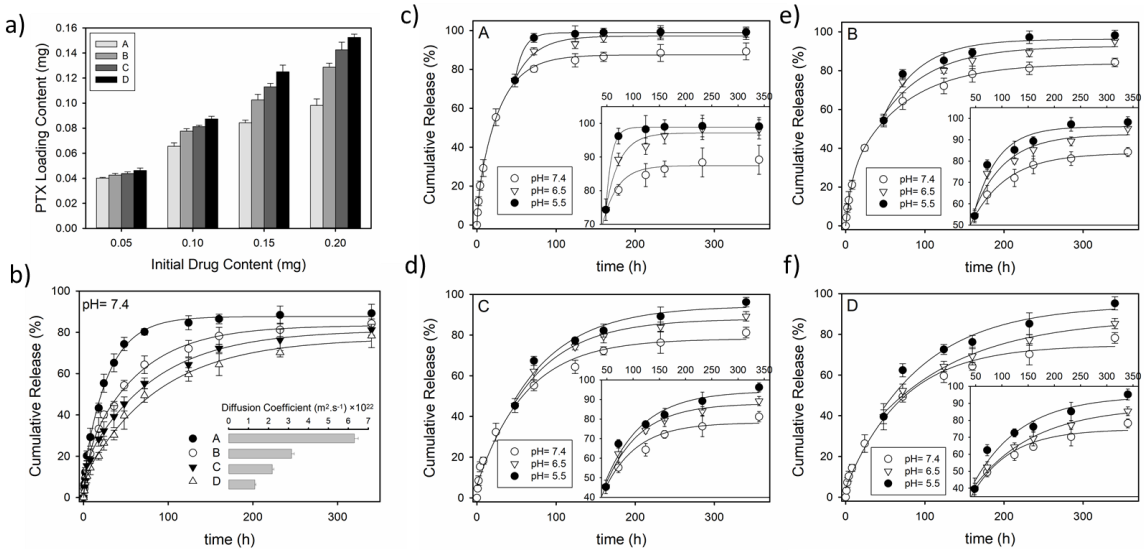

Figure 7-5 (a) The change in paclitaxel (PTX) loading content as a function of initial PTX loading concentration for NPs with different compactness. (b) Cumulative *in vitro* release of PTX from different formulations of microfluidic synthesized NPs at 37 °C and pH 7.4. Calculated diffusion coefficients are illustrated in subset. (c-f) Controlled release of PTX from microfluidic-synthesized NPs after changes in pH of the media from 7.4 to 6.5 and 5.5 at 37 °C (Mean ± SD, n = 4 independent experiments.).

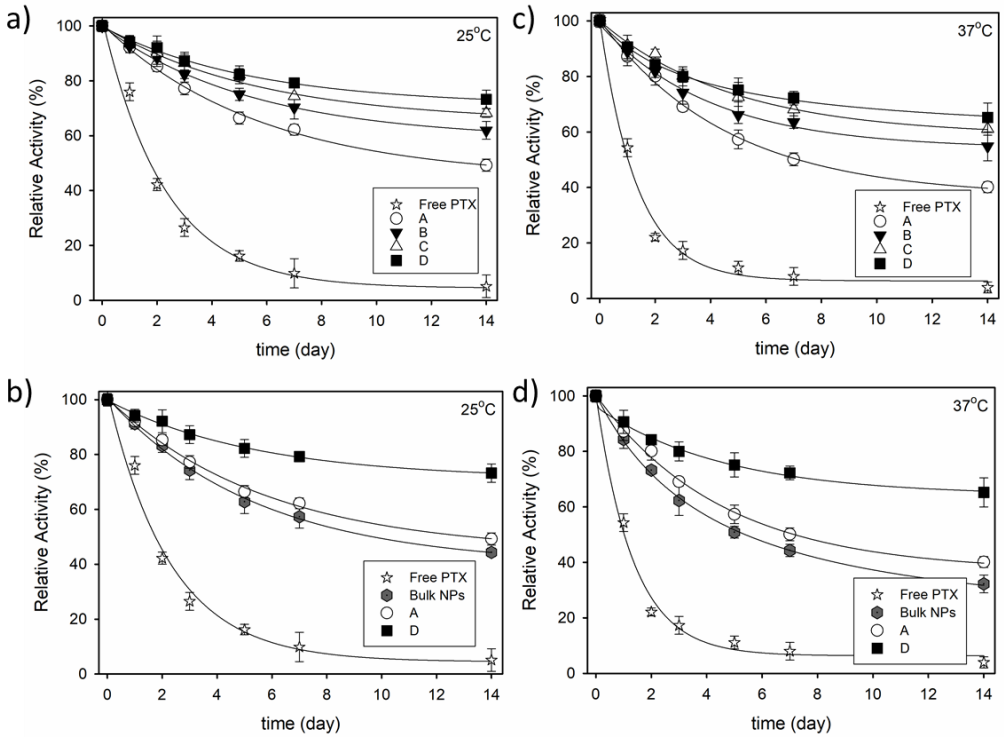

Figure 7-6 Relative activity of PTX at (a,b) 25°C and (c,b) 37 °C for free drug and PTX loaded NPs A-D with different compactness compared to PTX loaded bulk synthesized NPs.

To evaluate whether cRGD-PEG functionalized NPs could recognize αvβ3 integrins on endothelial cells, the association of these NPs were examined on HUVECs using flow cytometry. HUVECs were chosen as a model cell line with overexpression of integrin (*e.g.*, αvβ3) receptors as confirmed by flow cytometry and Western Blot assays (Figure 7-7a). Presented cRGD molecules on the NP surface are assumed to induce multivalent associations with the integrin receptors resulting in increased NPs binding and uptake (Figure 7-3 d,e). Designed NPs with different mechanical stiffness were incubated with HUVECs and the internalization levels were assessed (Figure 7-7 b-d). NPs without modification with PEG-cRGD also presented high levels of internalization compared to the PEGylated counterparts in the absence of cRGD (Figure 7-7b, $p<0.001$) due to the presence of primary amines on the surface of NPs that can be protonated and internalized as reported before (*44*, *291*). Specificity of binding was evaluated via competition assay by adding free

cRGD and monoclonal antibody against αvβ3 integrin as well as via NPs functionalized with a scrambled ligand (RDG). The quantitative endothelial cell uptake assay confirmed the importance of the active targeting achieved by cRGD. The uptake level of cRGD-functionalized NPs was enhanced with increase in the mechanical stiffness of NPs (Figure 7-7c, $p<0.01$), indicating the importance of mechanical properties in cell internalization. All four groups of tested NPs internalized the HUVECs, but their internalization kinetics was different. Indeed, less internalization took place for softer NPs (Figure 7-7d). Blank synthesized NPs, particles without PTX loading were not toxic even at high concentrations (Figure 7-7e). However, free PTX is toxic, and the half-maximal inhibitory concentration (IC_{50}) for HUVECs is about 3 nM. PTX toxicity was significantly enhanced through encapsulation in engineered NPs. This phenomenon is likely due to protecting drug from degradation that particle encapsulation provides and also high-levels of cellular internalizations. Consequently, drug release mainly occurs inside the cells which effectively enhances therapeutic efficacy.

In addition to the capability of PTX-loaded NPs to internalize and kill HUVECs, they can also inhibit cellular functions. We tested HUVECs migration inhibition due to the VEGF gradient in the presence of various nanoparticle-treatment strategies using transwell assay after 48 h of incubation (Figure 7-7 g-i). With increasing PTX concentration, all PTX-based treatments exhibited HUVEC migration inhibition. However, the highest inhibitory behavior was observed in the case of hard NPs functionalized with cRGD ligands especially at lower drug concentrations. At high drug concentrations, the difference between the inhibition rates was not significant. Compared to the free drug, drug-loaded NPs exhibited much higher migration inhibition at lower PTX concentrations (< 1nM). The same trend was observed in the test of HUVECs tube formation in 3D matrigel in the presence of VEGF (Figure 7-7 h-j). PTX carrying NPs effectively targeted and inhibited the angiogenesis ability of endothelial cells. The blank NPs, nontoxic to HUVECs,

displayed very low inhibitory effects on migration and tube formation of endothelial cells. Stiff cRGD-functionalized NPs exhibited significant inhibitory activity even at very low drug concentrations, which is related to the higher internalization potential of stiffer NPs as well as the positive effect of presented cRGD on the particle surface.

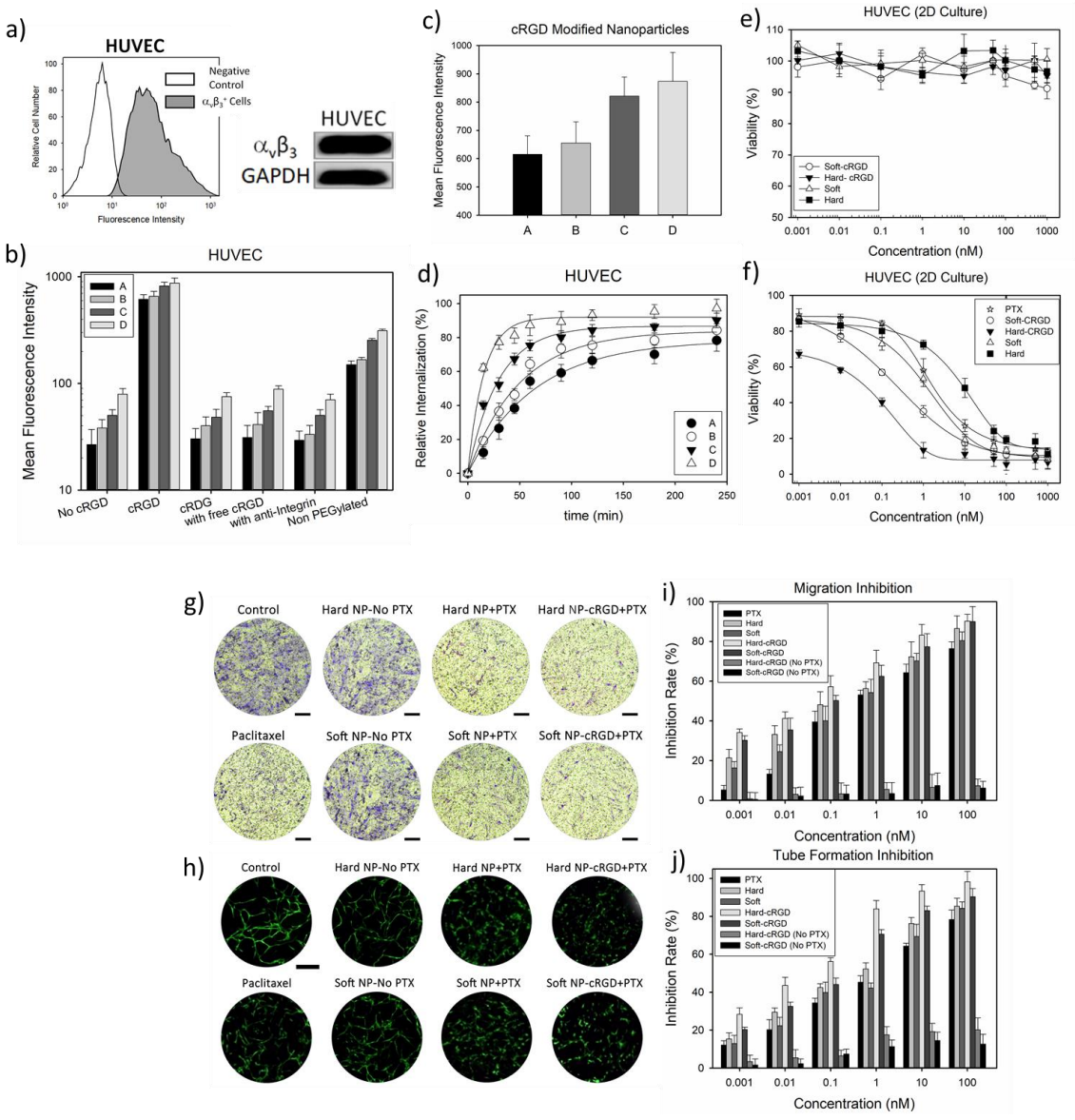

Figure 7-7 (a) Flow cytometry and Western Blot analysis that confirms overexpression of integrin αvβ3 by HUVECs. (b) Cellular uptake of the FITC-labeled NPs for different formulations after 2 h incubation with the HUVECs. (c) HUVEC uptake for cRGD-functionalized NPs with different stiffness. (d) The uptake kinetics of NPs incubated with the HUVECs. MTT cell viability assay of HUVECs after 72 h of exposure to (e) unloaded NPs,

(f) free PTX, and PTX loaded NPs at 37 °C. Unloaded NPs are plotted on the abscissa so that the number of NPs in the corresponding trials was the same. (g) Representative photographs of stained (blue) migrated HUVECs and Transwell assay results of endothelial cell migration after 12 h of treatment with different concentrations of NPs with/without PTX. (h) *In vitro* angiogenesis results of endothelial cell's (GFP-positive HUVECs) tube formation in a 3D Matrigel after 12 h of treatment with different NPs formulation.

In order to study the effects of mechanical properties of designed targeting NPs on cancer cell lines, we chose three different cell lines with different level of integrin expressions. Human glioblastoma (U-87 MG), kidney cancer (HEK-293), and breast cancer (MCF-7) cell lines with high, moderate, and very low expressions of αvβ3 integrin, respectively were tested (Figure 7-8a**)**. Here, only two sets of NPs, softest (sample A) and stiffest (sample D), were evaluated. As shown in Figure 7-8b, stiffer targeted NPs showed greater tendency for internalizing the cells with high level of integrin receptor expression. Difference in uptake quantities was also seen for non-PEGylated NPs; since both stiffness and surface charges of particles varies, the changes in uptake cannot be related solely to their mechanical properties.

Combination of mechanical stiffness and active targeting attributes to offer a synergetic effect in potential cancer treatment. Another feature that is expected from an efficient cancer nanomedicine is to offer maximum lethal effects at the lowest possible dosage of the drug. Here toxicity of PTX-loaded NPs was studied against three cell lines of interest and the half-maximal inhibitory concentrations (IC_{50}) were estimated (Figure 7-8 e-h). In the case of cells with high levels of integrin expression, as the particles can effectively engage with cell surface and internalize, stiffer NPs (C and D formulations) had the lowest IC_{50} (highest toxicity). However, when internalization is not probable (MCF-7 cells), soft NPs (A and B formulations) showed higher efficiency as they released drug faster and affected the cellular viability in shorter periods of time while the PTX loaded in stiffer NPs remained unleashed (Figure 7-8h).

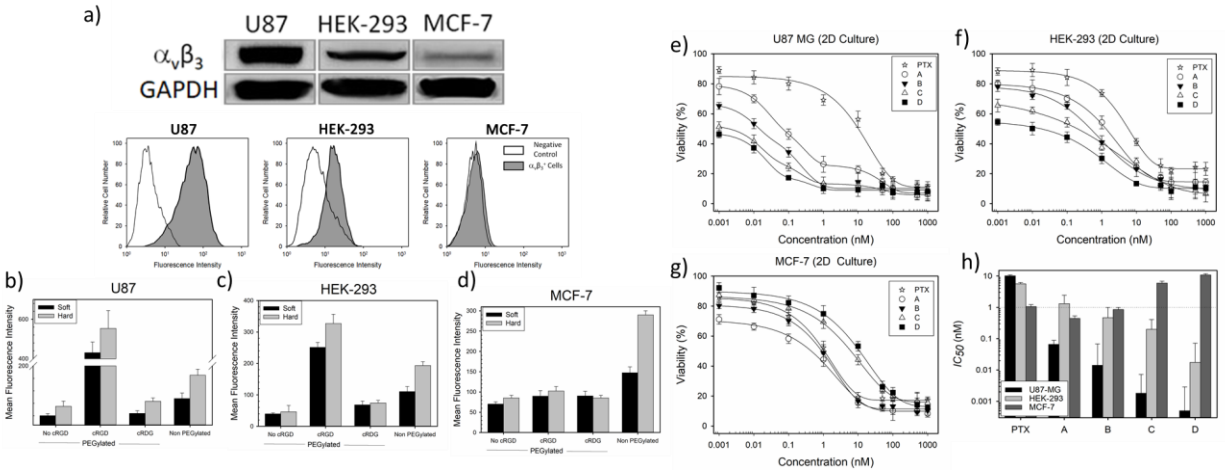

Figure 7-8 (a) Flow cytometry and western Blot analysis of integrin αvβ3 expression. U87 MG, HEK-293, and MCF-7 cells were confirmed to have strong, moderate, and extremely weak expression of integrin αvβ3. GAPDH was used as a control. Cellular uptake of the FITC-labeled NPs for different formulations after 2 h incubation with the U87 MG (b), HEK-293 (c), and MCF-7 (d) cells. MTT based cell viability assay of U87 MG (e), HEK-293 (f), and MCF-7 (g) cells after 72 h of exposure to unloaded NPs in 2D culture at 37 °C. (h) Plot of estimated half-maximal inhibitory concentration (IC50) of different PTX-loaded nanoparticle-based treatment for U87 MG, HEK-293, and MCF-7 cells.

As tumor tissues are 3D microenvironments, and the results of nanoparticle-cell interactions in cell monolayers (Figure 7-8) may not be predictive enough to evaluate the clinical outcomes of nanomedicines, inspired by the pioneer work by Warren Chan group (*292*); hence, we tried to address this challenge by testing 3D cell aggregates and dynamic flow conditions inside a microfluidic chip (Figure 7-9a). We used forced aggregation technique (*279*) to form monodisperse aggregates, with sizes around 100-150 um, from U87 MG cells inside the microfabricated microwells (Figure 7-9b). The aggregates were then loaded into the microfluidic chips which were designed to have "traps" for holding aggregates in place (Figure 7-9c). Aggregates can be easily studied using inverted optical or fluorescence microscopy to evaluate their size and shapes in real time (Figure 7-9d). The developed tumor aggregates-on-chip platform was then subjected to a flow of NPs with different mechanical properties or active cellular targeting. As shown in Figure 7-9 e,f, average fluorescent intensity in the aggregates confirm higher accumulation levels of stiff

NPs (Sample D) compared with soft NPs (Sample A), while integrin receptor targeting enhanced accumulation and retention of NPs. PEGylated but not cRGD-conjugated particles were found to show minimal interactions with cell aggregates.

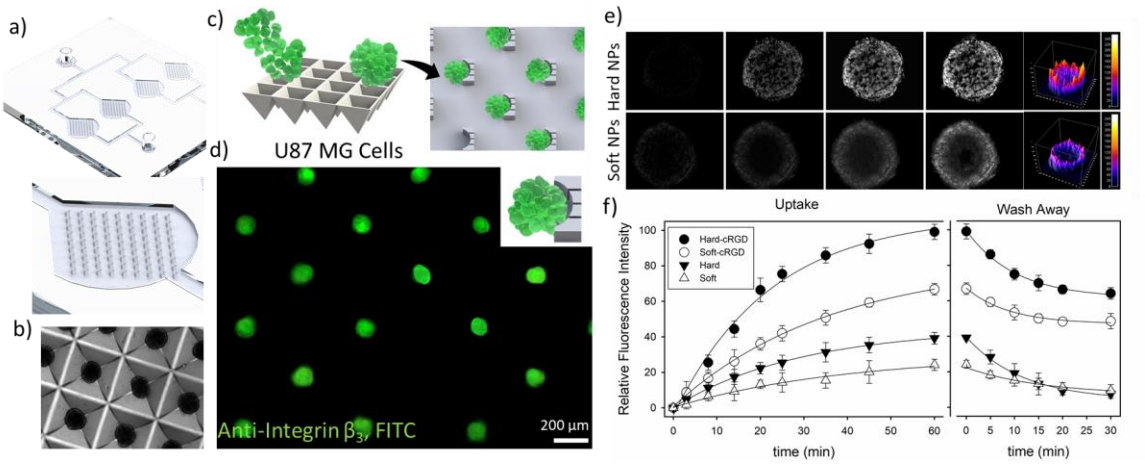

Figure 7-9 (a) Schematic of the PDMS-based microfluidic chip (aggregate-on-chip) to trap the cell aggregates. (b) Bright-field microscopy of formed aggregates on the designed 400 um microwells. (c) U87 MG cell aggregates were formed using force aggregation and were then injected in aggregate-on-chip device. (d) Fluorescent image of physically trapped cell aggregates after staining by anti-integrin β3. (e) Confocal fluorescent image and intensity profile of penetration of fluorescently-labeled stiff (upper panels) and soft (lower panels) NPs to a cell aggregate after 30 min, 2 h, 4 h, and 12 h of flow at 30 µl /h. (f) Average fluorescent intensity calculated from aggregate accumulation of targeted and non-targeted NPs as a function of time (left graph) and after flushing with PBS.

Although, targeted NPs accommodated higher than non-targeted ones, but even in the case of targeted NPs, stiffer particles penetrated more into the central regions of cell aggregates in comparison with softer counterparts (Figure 7-10). Flushing the chip with media caused a minor decrease in fluorescence level, which was more pronounced in the case of non-targeted NPs as they could not properly integrate with cells and can simply be washed away compared with cRGD-functionalized NPs (Figure 7-9f).

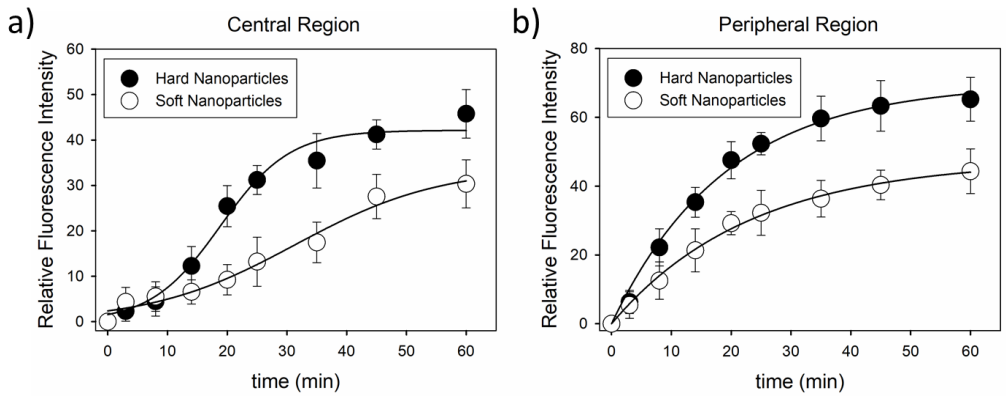

Figure 7-10 Average fluorescent intensity of targeted NPs at central (a) and peripheral (b) regions of aggregates as a function of time.

The proposed simple microfluidic platform (Figure 7-9) can mimic the 3D organization of tumor cells while enabling the cell-nanoparticle interaction under flow conditions. On the other hand, the *in vitro* results showed significant difference in cytotoxicity of particles in 2D cultures and encapsulated in 3D collagen gel (Figure 7-11 a,b). Further, NPs need to pass through the nanoscale tight junctions between the endothelial cells to reach tumor tissues; so, we designed a physiologically relevant tumor-on-chip (*3DToC*) platform to address these criteria and also engulf cancer cell aggregates. Schematic of the multilayer microfluidic device designed to systematically characterize the effects of tumors pathophysiological conditions on NP penetration is presented in Figure 7-11c. This platform has been designed based on the previous works reported elsewhere (*282, 293-295*) with some modifications to trap cell aggregates in the designated places. To mimic the transportation around the tumor tissue, the platform was designed to have a capillary channel for delivering NPs (blue; upper channel), two interstitial side channels to provide negative pressure (red; lower channel) and a tumor chamber in between where the tumor tissue, consisting of cell aggregates in a 3D collagen, (green; lower channel) is placed (Figure 7-11c). There is also a porous membrane with 400 nm pores sandwiched between the upper and lower fluidic channels.

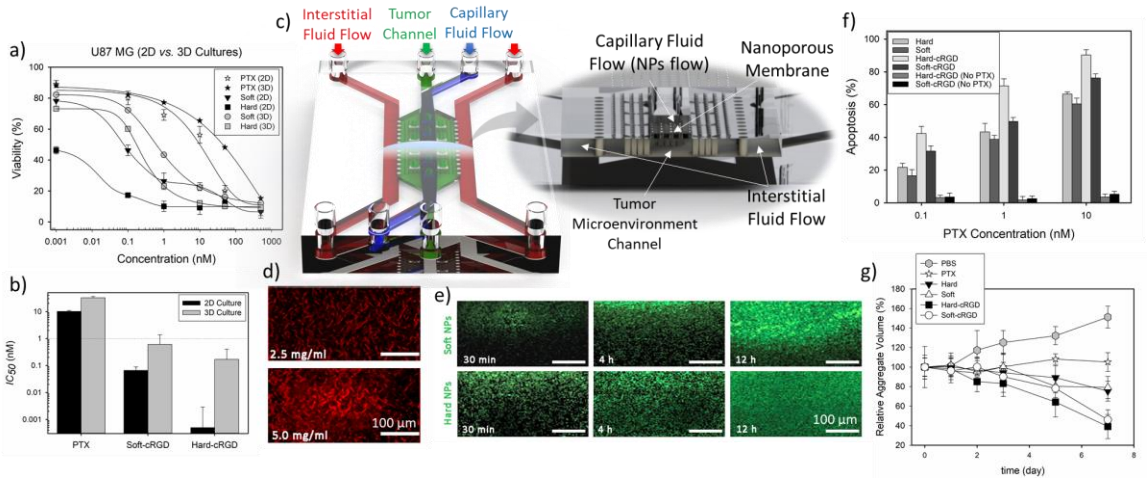

Figure 7-11 (a) MTT cell viability assay (b) and estimated half-maximal inhibitory concentration (IC50) of U87 MG cells after 72 h exposure to unloaded NPs in 2D vs. 3D cultures at 37 °C. (c) Schematic representation of designed 3D tumor-on-chip (3DToC) device used to mimic tissue microenvironment *in vitro*. 3DToC is designed to have capillary channel for delivering NPs (blue; upper channel), lymphatic channels (red; lower channel) where tumor tissue, cell aggregates in 3D collagen matrix, (green; lower channel) is placed between them. There is a porous membrane (400 nm) sandwiched between upper and lower PDMS layers. (d) Fluorescent signal shows the microstructure of collagen matrix formed with different initial concentrations of 2.5 and 5 mg/ml. (e) Penetration of FITC-labeled soft (upper panels) and hard (lower panels) NPs in a collagen gel (2.5 mg/ml) as a function of time under the flow. (f) Flow cytometry assessment of U87 MG cells apoptosis after digestion of collagen matrix and extracting cells from 3DToC device after 7 days. (g) Time-related evaluating average volume of tumor aggregate after treatment with different formulations of NPs at similar dose (1 nM).

Due to the high affinity of targeted NPs to endothelial cells (Figure 7-7), we could not culture HUVECs cells on top of membrane to simulate of the endothelium layer, so the porous membrane was used to control the cut-off size. The 3DToC platform was connected to pressure controllers to independently control the capillary, interstitial, and lymphatic fluid pressures. We also made a collagen gel inside the tumor channel at two different concentrations of 2.5 and 5.0 mg/ml as proposed before (*281*) to simulate the tumor's ECM at different tortuosity which affect penetration of NPs to the tumor cells (Figure 7-11d).

To evaluate the functionality of proposed NPs *in vitro*, we first designed a tumor on chip (ToC) model to mimic the main characteristics of tumor microenvironments. The ToC was designed to let the NPs accumulate in tumor regions under the flow and at physiologically

relevant velocity and pressure through the capillary channels and pass the porous membrane layer which simulate the gap junctions between the endothelial cells in leaky tumor vasculatures.

This 3DToC also provide an optical window for real time study of NP's penetration into a 3D tumor microenvironment as well as analyzing the tumor size in a way which has not been possible *in vitro* so far. As shown in Figure 7-11e, stiffer NPs can penetrate faster and distribute better through the collagen matrix after passing the 400 nm pores.

Moreover, after the experiments we restored the cells from aggregates by digesting the collagen matrix and detected substantial amount of hard targeted NPs inside the U87 cells. The flow cytometry (Annexin V apoptosis assay) evaluation of restored cells confirmed successful killing of cancer cells with drug loaded NPs, which highlights the importance of mechanical properties of a therapeutic nanomedicine. A real-time optical non-invasive evaluation of aggregate size over time revealed the capabilities of the targeted NPs in suppressing tumor growth *in vitro*.

Further, the effects of mechanical properties of NPs on their biodistribution and pharmacokinetics (PK) were studied. To this end, mice bearing subcutaneous integrin αvβ3-positive U87MG tumors were intravenously injected with different formulations of NPs. At selected time points after intravenous injection into healthy and tumor bearing mice, animals were sacrificed and organs were retrieved to estimate biodistribution of NPs with different stiffness (Figure 7-12a). As anticipated, NPs mainly accumulated in the well-perfused liver and spleen tissues due to their discontinuity in endothelium gaps. Stiffer NPs (targeted and non-targeted) exhibited higher liver affinity while softer particles showed higher tumor accommodation. The latter finding is attributed to higher blood circulation times of softer particles, which is defined as the ability of NPs to remain in the blood circulation for extended intervals and avoid clearance by the immune system. Additionally,

for both hard and soft NPs, tumor accommodation was significantly higher where cRGD targeting moieties were present. It could be inferred that softness plays a pivotal role in controlling biodistribution of NPs, and this effect can be boosted by active targeting.

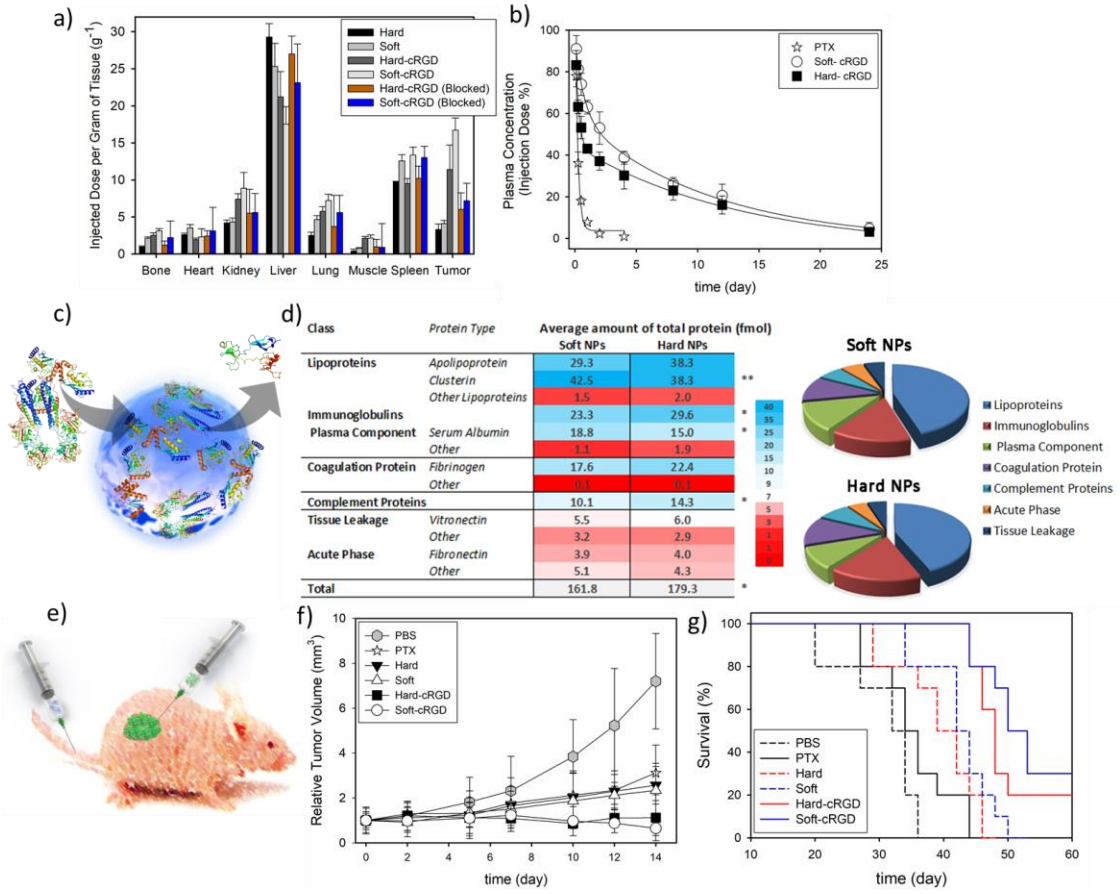

Figure 7-12 (a) Quantitative tissue accumulation of NPs in tumor and other organs in 48 h after tail vein injection of fluorescently-labeled NPs. (b) Pharmacokinetic data on blood clearance of free PTX drug PTX loaded in soft and hard NPs (n = 5). (c) Schematic representation of presumptive interactions with plasma proteins and NPs. (d) Heat map of the adsorbed proteins on PEGylated stiff and soft NPs, evaluated by proteomic mass spectrometry and ordered based on their abundances. The average amounts are illustrated in fmol. Percentage of identified proteins is grouped according to their biological class. (e) *In vivo* Anti-tumor effect of free and nanoparticle-loaded PTX based formulations (PTX concentration: 1 mg/kg) on U87MG tumor-bearing mice. (f) Suppression of tumor growth by assessing the mean volume of tumor (n=6). (g) Survival rates of tumor-bearing mice.

A two-compartment PK model was fitted on the circulation data to estimate blood circulation time of NPs (Figure 7-12b). PK analysis demonstrated that stiff NPs rapidly cleared from blood while softer NPs sowed longer circulations. Further, it was found that free PTX formulation was quickly removed from the circulating system in about 2 h after injection. This finding is in agreement with the presented macrophages uptake results (Figure 7-3) which showed lower cellular association than their unmodified (amine) counterparts.

In this study, the main goal of PEGylation was to eliminate the effects related to NPs' surface charge; however, PEGylation concurrently act as a stealth agent to improve blood circulation half-life as mentioned before. Our previous results (see Chapter 2 for details) revealed the effects of protein adsorption on cellular uptake of chitosan-based NPs. Here, we found higher uptake of NPs in the protein-free medium. To further assess this observation and to check whether mechanical properties of NPs plays any role in protein adsorption (Figure 7-12c), we analyzed the adsorption of over 100 proteins using liquid chromatography–mass spectrometry (LC-MS). Figure 7-12d**,** demonstrates the most adsorbed proteins identified (hard corona). Clusterin and other apolipoproteins were found to be the major proteins in hard corona for both NPs. High levels of clusterin adsorption were previously reported for other PEG- and poly(phosphoester)- (*283*) functionalized, silica(*285*)- and lipid-based (*296*) NPs. High adsorption levels of lipoproteins have been reported previously for NPs with hydrophobic nature (*297*, *298*). Similarly, high adsorption levels of several lipoproteins have been reported for more hydrophilic NPs like amine-modified quantum dots (*297*), PEGylated and poly(phosphoester)-functionalized gold NPs (*283*, *298*). The amphiphilic nature of HMCS NPs can be the reason for high levels of apolipoproteins adsorption. In the case of soft, less compact structures this phenomenon may be due to the more exposed hydrophobic groups that cause more adsorption of lipoproteins. The lower level of complement proteins adsorption on the surface of soft NPs

can elucidate their higher blood circulation times (*39*). In this case, complement activation can be attributed to the opsonization and cleavage of NPs from the blood (*52*). It is reported that in 2D surfaces proteins have less tendency to be adsorbed on substrates with lower mechanical stiffness (*299*), which is consistent with our observations for spherical NPs.

After intravenous injection of NPs in U87MG (integrin αvβ3-positive) tumor bearing mice, tumor size was analyzed at different time points (Figure 7-12 e,f). As shown in Figure 7-12f, all PTX-based formulations exhibited significant inhibitory effects on glioblastoma growth compared to the control groups (PBS; physiological saline). *In vitro* results in 2D and 3D cultures (Figure 7-11), confirmed the lethal effects of PTX on tumor cells while this drug was less effective *in vivo* due to the short blood circulation and fast degradation of PTX.

Nontheless, targeted NPs showed the strongest inhibitory effects amongst all the other groups which was in agreement with our *in vitro* results (Figure 7-11 f,g). These NPs not only are capable of targeting tumor cells and their neovasculatures (endothelial cells), but also they highly accumulated in tumor tissues by taking the advantage of enhanced permeability and retention (EPR) effect. This was also confirmed using our tumor-on-chip platform. However, the difference between hard and soft NPs was not statically significant in this case.

Compared to PBS and free PTX formulations, nanotherapeutics significantly prolonged the survival time, which was further enhanced in the presence of the targeting moiety. Such an *in vivo* enhancement may be due to the protection of drug from degradation while prolonging its blood circulation and providing a sustained release of the drug near the integrin over-expressed tumor/neovascular cells. However, in contrast to what was seen *in vitro*, the soft NPs showed better *in vivo* outputs. This highlights the importance of PK and biodistribution in defining the therapeutic efficacy of nanomedicines.

Overall, it seems that soft NPs are ideal for blood circulation and offer improved tissue distributions while stiffer NPs show greater tendency to penetrate tumor microenvironment and expressed higher levels of cellular engagement. Stiffer NPs also provided superior protection of their loaded drug. To solve the controversy between the requirements, we tried to use a biomimetic approach. Viruses are highly optimized for *in vivo* targeting of their agents and this ability can be mimicked to some extend and help us design the next-generation of nanoscale therapeutics. For example, human immunodeficiency virus (HIV) can circulate in its soft form and as soon as reaching the target tissue/cell it irreversibly switch to a stiffer form to achieve more efficient penetration/internalization. Here, we aimed to develop NPs with switchable (dynamic) mechanical properties with prolonged circulation half-lives due to their extreme softness and enhance their targeting efficiency by remotely increasing their hardness when reach to the tumor site. Applying the synthesis strategy described in Figure 7-13a, we selected UV-activated nitrobenzene-amine reaction that could increase the crosslinking density inside the NPs and harden them in less than a minute. To do so, NPs were loaded with nitrobenzene-functionalized 4-arm PEG molecules during their synthesis to enable us to remotely trigger the crosslinking of NPs upon UV exposure at 365 nm (Figure 7-13a).

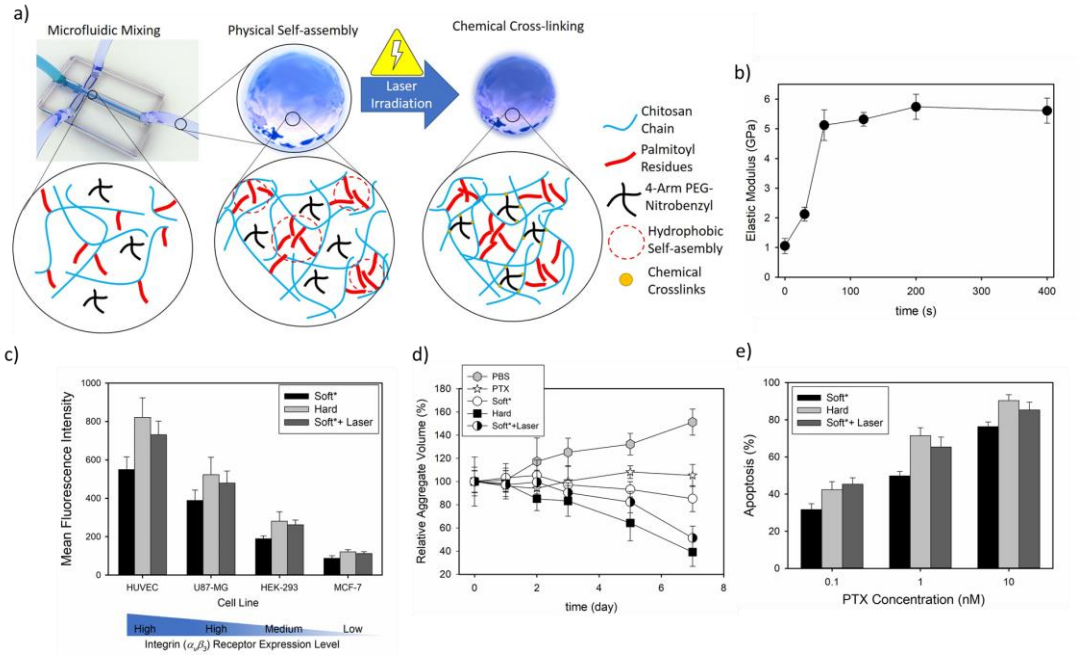

Figure 7-13 Schematic of the proposed approach to make NPs with switchable mechanical properties. Upon UV exposure (20 mW/cm^2) the pre-loaded 4-arm PEGs react with hydrazine groups of chitosans. (b) Change in the elastic modulus (E) of NPs as a function of UV irradiation time at 20 mW/cm^2. (b) Cellular uptake of the FITC-labeled NPs after 2 h incubation with the HUVEC, U87 MG, HEK-293, and MCF-7 cells. (d) Over time evaluation of the average volume of tumor aggregate after treatment with different formulations of NPs with and without UV exposure performed on a 3D tumor-on-chip platform. (e) Flow cytometry assessment of U87 MG cells apoptosis after digestion of the collagen matrix and extraction of cells from the 3DToC device after 7 days.

While there are other novel approaches like thiol–ene photoinitiated reactions (*300*) to spatiotemporally tune mechanical characteristics of polymer based structures, most of them require radical photoinitiators, which may not be favorable for *in vivo* applications. Here we are implemented the elegant approach proposed by Anseth and coworkers (*272*) to develop a photoinitiated method for tuning mechanical properties of our NPs. This way upon UV exposure the incorporated photoreactive 2-nitrobenzyl-alcohol groups on the PEG molecules form 2-nitrosobenzaldehyde (*272*) that react with hydrazine groups of slightly modified chitosan chains. The chains of chitosan were modified with PEG-diacid (600 Da) and then diamined via EDC/Sulfo-NHS chemistry to provide sufficient hydrazine groups for photocontrollable reaction with functionalized multi-arm PEGs. The kinetics of

hardening of NPs in the presence of UV-irradiation (20 mW/cm^2) were studied with AFM nanoindentation as shown in Figure 7-13b. Upon UV exposure, an instant increase in the elastic modulus (*E*) was observed, confirming the formation of hydrazone bonds between PEG and chitosan. Elastic modulus of our NPs were also in the same range as natural viruses (*301*).

The in vitro experiments were done on the newly synthesized soft NPs that incorporated photoreactive PEG molecules before (Soft*) and after UV-initiated hardening process (Soft*+ Laser). As shown in Figure 7-13c, the cRGD modified version of these switchable NPs provided the same levels of internalization as hard NPs. The same trend for internalization, as a function of integrin receptor expression, was observed for these newly formed NPs. Although, presence of the 4-arm PEG decreased the encapsulation efficiency of NPs at high PTX concentrations (data not shown). However, it loaded enough PTX to provide the desired therapeutic effects. Upon UV activation, these NPs illustrated same levels of 3D tumor penetration and cytotoxicity as their hard counterparts which was also confirmed by our 3D tumor-on-chip platform (Figure 7-13 d,e).

In vivo proof-of-concept experiments were also performed on U87 MG tumor bearing mice by having local UV exposure just on the tumor side (Figure 7-14a) to check the possibility of switch in the mechanical properties of NPs while they are inside the body. Pharmacokinetics results confirmed the same blood circulation profile for the switchable NPs (Figure 7-14b). Although harder NPs were better cases for of drug protection but since circulation period was short and upon reaching to the tumor site hardening took place, we had a good drug protection in the whole procedure. The biodistribution of NPs were also quite the same for the soft* NPs with and without local UV irradiation except for the tumor tissue. As shown in Figure 7-14c, local irradiation, in vivo, helped the NPs that were trapped near the tumor tissue switch to the stiff state and accommodate better with the tumor cells. Analysis of the survival rate of tumor bearing animals also confirmed the

enhancement in therapeutic efficacy of cancer nanomedicine by this virus-inspired approach. The problem associated with UV-penetration through the body will be overcome in the future works by replacing this photoinitiated reaction with near-infrared sensitive ones.

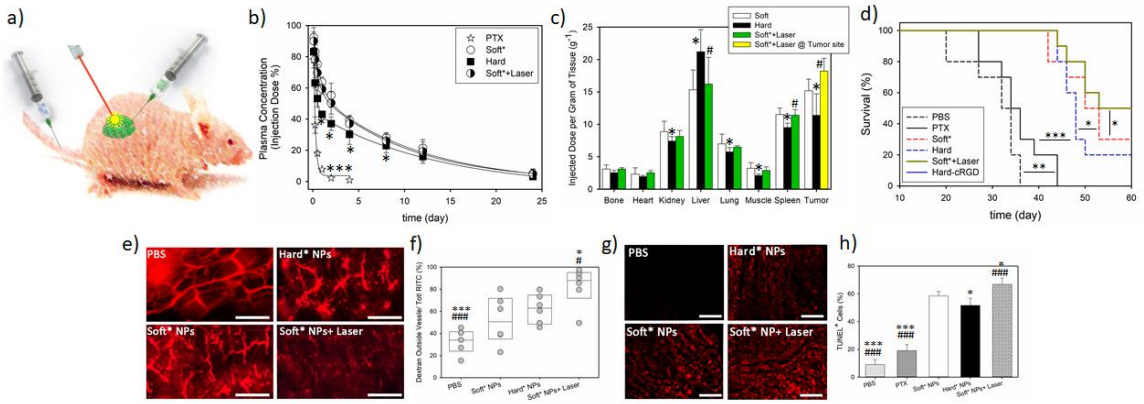

Figure 7-14 (a) *In vivo* Anti-tumor effect of mechanically switchable PTX-loaded nanoparticle on U87MG tumor-bearing mice. (b) Pharmacokinetic data on blood clearance of the free PTX and when loaded in soft* and hard NPs with and without UV irradiation (n = 5). (c) Quantitative tissue accumulation of NPs in tumor and other organs 48 h after tail vein injection of fluorescently-labeled NPs with and without UV irradiation. (d) Survival rates of tumor-bearing mice treated with different modularity of NPs. (e) In vivo vascular disruption in the subcutaneous matrigel model after treatment with targeted NPs with different formulations. The plugs were removed after the treatment and imaged by fluorescent microscopy. (f) Alteration in vessel morphology evaluated by measuring the RITC-Dextran leakage from the vasculatures. (g) Tumor tissue cross-section immunostained for TUNEL-positive cells. (h) Quantification of apoptosis by assessing the number of TUNE-positive cells.

The presented data are expressed as average ± SD. The results were statistically analyzed using unpaired t-tests. For all the tests, the threshold was set to $p < 0.05$ for "statistically significant", $p < 0.01$ for "statistically very significant" and $p < 0.001$ for "statistically extremely significant". Statistical significance is indicated by * (significant), ** (very significant), and * (extremely significant) for differences between each experimental group and the soft nanoparticles. Statistical significance is indicated by # (significant), ## (very significant), and ### (extremely significant) for differences between different treatments and the hard nanoparticles.**

We also evaluated the antiangiogenic effects of the designed targeted NPs in the mice carrying subcutaneous Matrigel plugs (*287*). The Matrigel also incorporated basic fibroblast growth factor (bFGF) and VEGF to promote angiogenesis. It is also important to mention that this model was designed to represent the normal angiogenesis induced by

proangiogenic factors (VEGF and bFGF) and may be different from the tumor angiogenesis process (*287*). After three days of subcutaneous transplantation, the mice were tail vein injected with PTX containing NPs in the presence and absence of UV-exposure on tumor side. Antiangiogenic effects were assessed after 7 days by studying the alteration in vessel morphology through measuring the increase in RITC-Dextran leakage (*288*) Figure 7-14 e,f).

TdT-mediated dUTP nick end labelling (TUNEL) staining, was used to stain the apoptotic cells in in the tumor tissue (Figure 7-14g). Nanoparticle-mediated delivery of PTX caused significant increase in the tumor cell apoptosis compared to the free PTX treatment. These results were in agreement with the improved survival rates of animals after treatment with targeted NPs. Interestingly, local triggering of mechanical switching significantly enhanced the number of TUNEL-positive cells in the tumor tissue ($p<0.05$) (Figure 7-14h). Our control experiments also indicated that UV-exposure itself in the absence of NPs or in the case of non-switchable hard or soft NPs had no effect on the apoptosis rate. The observed improvement in the case of virus-inspired NPs in comparison with other anti-tumor-treated groups, was probably as a consequence of local piling-up of PTX inside the tumor tissue as well as possible enhancement in the cellular internalizations, leading to the increased apoptosis.

7.4 Conclusion

Our results proved the importance of mechanical properties of the nanomedicine which can affects a broad range of biological behaviors from drug-carrier or particle-cell interactions to the protein adsorption pattern of these NPs in blood plasma, their circulation through the body and in different tissues, and tumor treatment efficiency. We tried to optimize the required mechanical properties and accordingly design a nanotherapeutics agent with

prolonged blood circulation, enhanced tumor penetration tendency and apoptosis promoting capability.

CHAPTER 8. CONCLUSION

8.1 Concluding Remarks

As a robust synthesis tool that provides a controlled mixing regime, we used microfluidic platforms to synthesize monodisperse nanoparticles (NPs) with adjustable physicochemical properties. Size and surface charge of these nanoparticulate systems strongly tune their nanobio interactions. Here, we first assessed the effects of hydrodynamic size and surface charge of NPs on their cellular internalization (*Chapter 2*). The role of the biomolecular corona that surrounds NPs upon entering biological fluids was also investigated in the modified 2D cultures and by considering sedimentation and diffusion properties of microfluidics-assisted synthesized NPs. Also, it should be considered that NPs face substantial changes in their environment before reaching their targets. Specifically, in the case of oral administration of cancer therapeutics, drug molecules should be protected during their passage from the gastrointestinal tract. In *Chapter 3*, for the first time, we presented a dual microfluidic system that enabled fabrication of core-shell drug nanocarriers with high tunability. Self-assembled biopolymer-based NPs were produced in a cross-junction microfluidic device followed by a fine coating with a pH- sensitive copolymer through a Tesla micromixer. We confirmed the molecular interactions between the layers using molecular dynamic simulation. Coating NPs with a pH-sensitive layer gave them the ability to bypass the acidic gastric fluid while protecting their cargo. Such a tunable drug delivery system that allows physiological-responsive release can be a potential carrier for colon cancer chemotherapeutics. Even with a cross-junction microfluidic device we can make complex nanoparticles. In *Chapter 4*, monodisperse and highly reproducible hybrid NPs were developed through a one-step

incorporation of magnetic NPs and an anticancer drug into nanoprecipitated poly(D,L-lactide-co-glycolide) (PLGA) chains. We also incorporated bisphosphonate-functionliazed PLGA in order to activly target bone-like tissues. NPs conjugated with bisphosphonate showed significantly higher bone binding affinity both *in vitro* and *in vivo*. Furthermore, molecular interactions between functionalized PLGA and hydroxyapatite surfaces were approved *via* computational molecular dynamics. *In vivo* results verified the prolonged circulation of engineered NPs and higher levels of tumor suppression in the case of a bone metastatic tumor. The versatile synthesis approach that is proposed here to tailor multifunctional NPs can be used for personalized theranostics including chemotherapy, magnetic resonance imaging and hyperthermia treatment, aswell. We also used the same platform to make nanocapsules with ultra-high capacity for anti-cancer drug loading. In *Chapter 5*, dendritic polyethylene (dPE) was encapsulated by a tri-block amphiphilic copolymer. Microfluidic-assisted nanocapsules that formed showed highly efficient encapsulation capacities for encapsulating hydrophobic drugs while providing sustained release profiles with great tunability. This approach can be extended for the syntheses of other types of tailored, drug-loaded, dendritic polymer-based nanocapsules for the emerging field of nanomedicine. Using the same components and by adding a hydrophobic template we were able to control formation of one-dimensional nanostructures. In *Chapter 6*, carbon nanotubes were used to provide non-covalent CH–π interaction sites with hydrophobic dPE molecules. These simply fabricated but complex nanostructures showed high cellular uptake in cancer cells. These nanostructures showed remarkable efficiency when used as combinatorial cancer therapeutics based on the photodynamics and chemotherapy. Considering the applied interactions, accessible nanostructures may not be limited to 1D and by choosing other carbon-based materials like graphene and/or other simple or complex copolymers (e.g. containing targeting moieties), broader library of nanostructures with higher accuracy and efficiency can be synthesized. The central hypothesis in *Chapter 7* was that mechanical properties of NPs, which is often ignored in

nano-bio interface, can significantly affect their therapeutic efficacies. Therefore, we systematically investigated the effects of mechanical characteristics of NPs on their biological functionalities both *in vitro* and *in vivo*. We also developed a 3D tumor-on-chip (3DToC) device in order to mimic transport phenomena near the tumor tissue. This 3DToC platform was designed to provide dynamic and 3D cultures for tumor cells in order to evaluate NPs-cells and NPs-matrix interactions in real-time. Our results demonstrated the importance of mechanical properties of the nanomedicine which can affects a broad range of biological behaviors from drug-carrier or particle-cell interactions to the protein adsorption pattern of these NPs in blood plasma, their circulation through the body and in different tissues, and their tumor treatment efficiency. We tried to optimize the required mechanical properties and accordingly design a nanotherapeutics agent with prolonged blood circulation, enhanced tumor penetration tendency and apoptosis promoting capability. In the end, we designed virus-mimicking NPs that can switch their mechanical stiffness. The working hypothesis was that by designing dynamic NPs, capable of switching their stiffness in response to an external stimulus, we can create a trade-off between low elasticity, which is mainly needed during the blood circulation, and high elasticity, which is most desirable for tumor penetration and cellular uptake. The switching can be triggered remotely by laser irradiation in the site of action. All in all, our findings point to the high potential of microfluidic systems on designing complex multifunctional nanoparticles with precise bottom-up approach for various biomedical applications. The presented results are expected to attract scientists in the fields of chemistry, soft matter, cell biology, pharmacy, and medicine.

8.2 Future perspectives

The major contribution of this thesis has been to develop a microfluidics-based approach for developing next-generation of nanoparticles as cancer therapeutics. While many new understandings have been gained during this research and it declared a promising outlook

toward this technology, many aspects remained untouched. The translation of these functional nanoparticles from academic labs to industrial scale needs mass production of these nanoparticles. This issue may be addressed by designing microfluidic devices with parallel channels rather than just increasing the characteristic dimension of the channels. In this sense, the fluidic system needs to be modified with industrial-scale fluid control systems.

Purification of these NPs also needs to be adapted for industrial use. New microfluidic platforms can be developed to purify fabricated particles effectively right after their production. However, since these purifications are required for high volumes of nanoparticles, currently available designs still need improvement for industrial applications.

The proposed (organic) solvent-free approach of making biopolymer-based nanoparticles can be really desirable for pharmacological companies, considering the growing interest in developing green chemistry methods for therapeutics. The user independent process and minor batch-to-batch variation make microfluidics-based approaches highly appropriate for creating a library of nanoparticles suitable for screening potential new therapeutics.

This microfluidics approach can be used for making various types of soft (polymeric) nanoparticles. However, this system has limited effectiveness in producing monodisperse metallic and ceramic nanoparticles. Further adjustment of the microfluidic design for producing non-polymeric nanostructures can lead to great advances in photothermal therapy as well as *in vivo* imaging.

As traditional 2D *in vitro* systems have limited success in predicting the efficacy of cancer nanomedicine. Here we developed a 3D tumor-on-chip platform to better real-time study of the *in vitro* performance of designed nanoparticles in *in vivo* mimicking conditions. This library of nanoparticles can also be used for high-throughput screening of the efficacy of

candidate drugs on various primary cancer cells or cancer cell lines. Our chip consists of tumor cell aggregates as well as their extracellular matrix to consider the effect of cell-matrix interactions. However, addition of other microenvironment components like fibroblasts and endothelial cells, as well as immune cells is critical to make the model more physiologically relevant. These chips can also be developed to use patient-derived tumor cells and make personalized nanomedicine possible.

Similarly, the use of microfluidic platform technologies to reproducibly synthesize and screen libraries of nanoparticles with different chemical compositions and/or physical and chemical properties can potentially advance nanoparticle discovery similar to what happened in medicinal chemistry that high-throughput screening of small molecules led to advanced small-molecule discovery.

REFERENCES

1. Y. Cheng, L. Zhao, Y. Li, T. Xu, Design of biocompatible dendrimers for cancer diagnosis and therapy: current status and future perspectives. *Chemical Society Reviews* **40**, 2673 (2011).

2. K. Riehemann *et al.*, Nanomedicine—Challenge and Perspectives. *Angewandte Chemie International Edition* **48**, 872 (2009).

3. A. Schroeder *et al.*, Treating metastatic cancer with nanotechnology. *Nat Rev Cancer* **12**, 39 (2012).

4. R. S. Schwartz, Paul Ehrlich's Magic Bullets. *New England Journal of Medicine* **350**, 1079 (2004).

5. M. A. Dobrovolskaia, S. E. McNeil, Immunological properties of engineered nanomaterials. *Nat Nano* **2**, 469 (2007).

6. D. Hanahan, Robert A. Weinberg, Hallmarks of Cancer: The Next Generation. *Cell* **144**, 646 (2011).

7. J. A. Hubbell, A. Chilkoti, Nanomaterials for Drug Delivery. *Science* **337**, 303 (2012).

8. A. Schroeder *et al.*, Treating metastatic cancer with nanotechnology. *Nature Reviews Cancer* **12**, 39 (2011).

9. R. P. Johnson *et al.*, Biocompatible Poly(2-hydroxyethyl methacrylate)-b-poly(L-histidine) Hybrid Materials for pH-Sensitive Intracellular Anticancer Drug Delivery. *Advanced Functional Materials* **22**, 1058 (2012).

10. R. P. Johnson *et al.*, Dual Stimuli-Responsive Poly(N-isopropylacrylamide)-b-poly(l-histidine) Chimeric Materials for the Controlled Delivery of Doxorubicin into Liver Carcinoma. *Biomacromolecules* **14**, 1434 (2013).

11. O. Ikkala, G. ten Brinke, Functional Materials Based on Self-Assembly of Polymeric Supramolecules. *Science* **295**, 2407 (2002).

12. E. K.-H. Chow, D. Ho, Cancer Nanomedicine: From Drug Delivery to Imaging. *Science Translational Medicine* **5**, 216rv4 (2013).

13. R. Langer, New methods of drug delivery. *Science* **249**, 1527 (1990).

14. R. Karnik *et al.*, Microfluidic platform for controlled synthesis of polymeric nanoparticles. *Nano Letters* **8**, 2906 (2008).

15. A. Jahn *et al.*, Microfluidic mixing and the formation of nanoscale lipid vesicles. *Acs Nano* **4**, 2077 (2010).

16. A. Jahn, W. N. Vreeland, D. L. DeVoe, L. E. Locascio, M. Gaitan, Microfluidic directed formation of liposomes of controlled size. *Langmuir* **23**, 6289 (2007).

17. F. S. Majedi *et al.*, Microfluidic synthesis of chitosan-based nanoparticles for fuel cell applications. *Chemical Communications* **48**, 7744 (2012).

18. D. Mark, S. Haeberle, G. Roth, F. von Stetten, R. Zengerle, Microfluidic lab-on-a-chip platforms: requirements, characteristics and applications. *Chemical Society Reviews* **39**, 1153 (2010).

19. G. M. Whitesides, The origins and the future of microfluidics. *Nature* **442**, 368 (2006).

20. F. S. Majedi *et al.*, Microfluidic assisted self-assembly of chitosan based nanoparticles as drug delivery agents. *Lab on a Chip* **13**, 204 (2013).

21. S. Chopra *et al.*, Design of Insulin-Loaded Nanoparticles Enabled by Multistep Control of Nanoprecipitation and Zinc Chelation. *ACS Applied Materials & Interfaces* **9**, 11440 (2017).

22. J.-M. Lim *et al.*, Parallel microfluidic synthesis of size-tunable polymeric nanoparticles using 3D flow focusing towards in vivo study. *Nanomedicine: Nanotechnology, Biology and Medicine* **10**, 401 (2014).

23. M. M. Hasani-Sadrabadi *et al.*, Morphological Tuning of Polymeric Nanoparticles via Microfluidic Platform for Fuel Cell Applications. *Journal of the American Chemical Society* **134**, 18904 (2012).

24. Y. Kim *et al.*, Mass Production and Size Control of Lipid–Polymer Hybrid Nanoparticles through Controlled Microvortices. *Nano letters* **12**, 3587 (2012).

25. Y. Wang, P. Brown, Y. Xia, Swarming towards the target. *Nature Materials* **10**, (2011).

26. A. E. Nel *et al.*, Understanding biophysicochemical interactions at the nano–bio interface. *Nature materials* **8**, 543 (2009).

27. R. A. Petros, J. M. DeSimone, Strategies in the design of nanoparticles for therapeutic applications. *Nature Reviews Drug Discovery* **9**, 615 (2010).

28. A. Du Toit, Endocytosis: A new gateway into cells. *Nat Rev Mol Cell Biol* **16**, 68 (2015).

29. F. R. Maxfield, T. E. McGraw, Endocytic recycling. *Nature reviews Molecular cell biology* **5**, 121 (2004).

30. T. Xia, L. Rome, A. Nel, Nanobiology: particles slip cell security. *Nature materials* **7**, 519 (2008).

31. A. Verma *et al.*, Surface-structure-regulated cell-membrane penetration by monolayer-protected nanoparticles. *Nature materials* **7**, 588 (2008).

32. J. Rejman, V. Oberle, I. Zuhorn, D. Hoekstra, Size-dependent internalization of particles via the pathways of clathrin-and caveolae-mediated endocytosis. *Biochem. J* **377**, 159 (2004).

33. V. P. Chauhan, R. K. Jain, Strategies for advancing cancer nanomedicine. *Nature materials* **12**, 958 (2013).

34. V. P. Chauhan *et al.*, Normalization of tumour blood vessels improves the delivery of nanomedicines in a size-dependent manner. *Nature nanotechnology* **7**, 383 (2012).

35. U. Prabhakar *et al.*, Challenges and Key Considerations of the Enhanced Permeability and Retention Effect for Nanomedicine Drug Delivery in Oncology. *Cancer Research* **73**, 2412 (April 15, 2013, 2013).

36. V. Torchilin, Tumor delivery of macromolecular drugs based on the EPR effect. *Advanced Drug Delivery Reviews* **63**, 131 (2011).

37. Y. Li, J. Wang, M. G. Wientjes, J. L. S. Au, Delivery of nanomedicines to extracellular and intracellular compartments of a solid tumor. *Advanced Drug Delivery Reviews* **64**, 29 (2012).

38. E. C. Cho, Q. Zhang, Y. Xia, The effect of sedimentation and diffusion on cellular uptake of gold nanoparticles. *Nature nanotechnology* **6**, 385 (2011).

39. V. Mirshafiee, M. Mahmoudi, K. Lou, J. Cheng, M. L. Kraft, Protein corona significantly reduces active targeting yield. *Chemical Communications* **49**, 2557 (2013).

40. M. Mahmoudi *et al.*, Cell "vision": complementary factor of protein corona in nanotoxicology. *Nanoscale* **4**, 5461 (2012).

41. M. J. Hajipour, S. Laurent, A. Aghaie, F. Rezaee, M. Mahmoudi, Personalized protein coronas: a "key" factor at the nanobiointerface. *Biomaterials Science* **2**, 1210 (2014).

42. M. P. Monopoli, C. Åberg, A. Salvati, K. A. Dawson, Biomolecular coronas provide the biological identity of nanosized materials. *Nature nanotechnology* **7**, 779 (2012).

43. S. Tenzer *et al.*, Rapid formation of plasma protein corona critically affects nanoparticle pathophysiology. *Nature nanotechnology* **8**, 772 (2013).

44. F. S. Majedi *et al.*, On-Chip Fabrication of Paclitaxel-Loaded Chitosan Nanoparticles for Cancer Therapeutics. *Advanced Functional Materials* **24**, 432 (2014).

45. M. M. Hasani-Sadrabadi *et al.*, Enhanced osteogenic differentiation of stem cells via microfluidics synthesized nanoparticles. *Nanomedicine: Nanotechnology, Biology and Medicine*.

46. Y.-L. Chiu *et al.*, pH-triggered injectable hydrogels prepared from aqueous N-palmitoyl chitosan: in vitro characteristics and in vivo biocompatibility. *Biomaterials* **30**, 4877 (2009).

47. S. Prochazkova, K. M. Vårum, K. Ostgaard, Quantitative determination of chitosans by ninhydrin. *Carbohydrate polymers* **38**, 115 (1999).

48. M. Huang, Z. Ma, E. Khor, L.-Y. Lim, Uptake of FITC-chitosan nanoparticles by A549 cells. *Pharmaceutical Research* **19**, 1488 (2002).

49. G. Ciapetti, E. Cenni, L. Pratelli, A. Pizzoferrato, In vitro evaluation of cell/biomaterial interaction by MTT assay. *Biomaterials* **14**, 359 (1993).

50. J. A. Swanson, C. Watts, Macropinocytosis. *Trends in Cell Biology* **5**, 424 (1995).

51. M. Lundqvist *et al.*, Nanoparticle size and surface properties determine the protein corona with possible implications for biological impacts. *Proceedings of the National Academy of Sciences* **105**, 14265 (2008).

52. M. M. Hasani-Sadrabadi *et al.*, Microfluidic-Assisted Self-Assembly of Complex Dendritic Polyethylene Drug Delivery Nanocapsules. *Advanced Materials* **26**, 3118 (2014).

53. V. Mailänder, K. Landfester, Interaction of Nanoparticles with Cells. *Biomacromolecules* **10**, 2379 (2009).

54. H. Jonassen, A.-L. Kjøniksen, Optical-scattering method for the determination of the local polymer concentration inside nanoparticles. *Physical Review E* **84**, 022401 (2011).

55. M. A. Dobrovolskaia, S. E. McNeil, Immunological properties of engineered nanomaterials. *Nature nanotechnology* **2**, 469 (2007).

56. R. R. Arvizo *et al.*, Effect of nanoparticle surface charge at the plasma membrane and beyond. *Nano letters* **10**, 2543 (2010).

57. M. Horie, H. Kato, K. Fujita, S. Endoh, H. Iwahashi, In vitro evaluation of cellular response induced by manufactured nanoparticles. *Chemical research in toxicology* **25**, 605 (2011).

58. P. Decuzzi, M. Ferrari, The role of specific and non-specific interactions in receptor-mediated endocytosis of nanoparticles. *Biomaterials* **28**, 2915 (2007).

59. A. Lesniak *et al.*, Nanoparticle adhesion to the cell membrane and its effect on nanoparticle uptake efficiency. *Journal of the American Chemical Society* **135**, 1438 (2013).

60. J. G. Teeguarden, P. M. Hinderliter, G. Orr, B. D. Thrall, J. G. Pounds, Particokinetics in vitro: dosimetry considerations for in vitro nanoparticle toxicity assessments. *Toxicological Sciences* **95**, 300 (2007).

61. P. M. Hinderliter *et al.*, ISDD: a computational model of particle sedimentation, diffusion and target cell dosimetry for in vitro toxicity studies. *Particle and fibre toxicology* **7**, 36 (2010).

62. Y. Li, X. Zhang, D. Cao, The Role of Shape Complementarity in the Protein-Protein Interactions. *Scientific reports* **3**, (2013).

63. A. A. Bogan, K. S. Thorn, Anatomy of hot spots in protein interfaces. *Journal of molecular biology* **280**, 1 (1998).

64. A. J. McCoy, V. Chandana Epa, P. M. Colman, Electrostatic complementarity at protein/protein interfaces. *Journal of molecular biology* **268**, 570 (1997).

65. Y. Yano, K. Matsuzaki, Measurement of thermodynamic parameters for hydrophobic mismatch 1: Self-association of a transmembrane helix. *Biochemistry* **45**, 3370 (2006).

66. A. I. Ivanov, in *Exocytosis and Endocytosis*. (Springer, 2008), pp. 15-33.

67. D. Vercauteren *et al.*, The use of inhibitors to study endocytic pathways of gene carriers: optimization and pitfalls. *Molecular Therapy* **18**, 561 (2009).

68. L. Pelkmans, T. Bürli, M. Zerial, A. Helenius, Caveolin-stabilized membrane domains as multifunctional transport and sorting devices in endocytic membrane traffic. *Cell* **118**, 767 (2004).

69. R. G. Parton, A. A. Richards, Lipid rafts and caveolae as portals for endocytosis: new insights and common mechanisms. *Traffic* **4**, 724 (2003).

70. M. Kirkham, R. G. Parton, Clathrin-independent endocytosis: new insights into caveolae and non-caveolar lipid raft carriers. *Biochimica et Biophysica Acta (BBA)-Molecular Cell Research* **1745**, 273 (2005).

71. J. A. Champion, S. Mitragotri, Shape induced inhibition of phagocytosis of polymer particles. *Pharmaceutical research* **26**, 244 (2009).

72. L. Rajendran, H.-J. Knölker, K. Simons, Subcellular targeting strategies for drug design and delivery. *Nature Reviews Drug Discovery* **9**, 29 (2010).

73. S. E. Gratton *et al.*, The effect of particle design on cellular internalization pathways. *Proceedings of the National Academy of Sciences* **105**, 11613 (2008).

74. B. R. Smith *et al.*, Shape matters: intravital microscopy reveals surprising geometrical dependence for nanoparticles in tumor models of extravasation. *Nano letters* **12**, 3369 (2012).

75. T. Whiteside, The tumor microenvironment and its role in promoting tumor growth. *Oncogene* **27**, 5904 (2008).

76. P. A. Netti, D. A. Berk, M. A. Swartz, A. J. Grodzinsky, R. K. Jain, Role of extracellular matrix assembly in interstitial transport in solid tumors. *Cancer research* **60**, 2497 (2000).

77. T. Stylianopoulos, K. Soteriou, D. Fukumura, R. K. Jain, Cationic nanoparticles have superior transvascular flux into solid tumors: insights from a mathematical model. *Annals of biomedical engineering* **41**, 68 (2013).

78. D. M. Muzny *et al.*, Comprehensive molecular characterization of human colon and rectal cancer. *Nature* **487**, 330 (2012).

79. A. Kreso *et al.*, Self-renewal as a therapeutic target in human colorectal cancer. *Nature Medicine* **20**, 29 (2014).

80. K. A. Paschos, N. Bird, Current diagnostic and therapeutic approaches for colorectal cancer liver metastasis. *Hippokratia* **12**, 132 (2008).

81. S. Van Schaeybroeck, W. L. Allen, R. C. Turkington, P. G. Johnston, Implementing prognostic and predictive biomarkers in CRC clinical trials. *Nature Reviews Clinical Oncology* **8**, 222 (2011).

82. S. S. Zeki, T. A. Graham, N. A. Wright, Stem cells and their implications for colorectal cancer. *Nature Reviews Gastroenterology and Hepatology* **8**, 90 (2011).

83. Z. Cheng, A. Al Zaki, J. Z. Hui, V. R. Muzykantov, A. Tsourkas, Multifunctional Nanoparticles: Cost Versus Benefit of Adding Targeting and Imaging Capabilities. *Science* **338**, 903 (2012).

84. B. C. Giovanella *et al.*, DNA topoisomerase I-targeted chemotherapy of human colon cancer in xenografts. *Science* **246**, 1046 (1989).

85. V. P. Torchilin. (2010), vol. 197, pp. 3-53.

86. M. Loeffler, J. A. Krüger, A. G. Niethammer, R. A. Reisfeld, Targeting tumor-associated fibroblasts improves cancer chemotherapy by increasing intratumoral drug uptake. *Journal of Clinical Investigation* **116**, 1955 (2006).

87. D. Shi, N. M. Bedford, H. S. Cho, Engineered multifunctional nanocarriers for cancer diagnosis and therapeutics. *Small* **7**, 2549 (2011).

88. M. Ferrari, Cancer nanotechnology: Opportunities and challenges. *Nature Reviews Cancer* **5**, 161 (2005).

89. K. Thanki, R. P. Gangwal, A. T. Sangamwar, S. Jain, Oral delivery of anticancer drugs: Challenges and opportunities. *Journal of Controlled Release* **170**, 15 (2013).

90. A. des Rieux, V. Pourcelle, P. D. Cani, J. Marchand-Brynaert, V. Préat, Targeted nanoparticles with novel non-peptidic ligands for oral delivery. *Advanced Drug Delivery Reviews* **65**, 833 (2013).

91. K. Yin Win, S. S. Feng, Effects of particle size and surface coating on cellular uptake of polymeric nanoparticles for oral delivery of anticancer drugs. *Biomaterials* **26**, 2713 (2005).

92. R. Khatik *et al.*, Toxicological evaluation and targeting tumor cells through folic acid modified guar gum nanoparticles of curcumin. *Journal of Biomaterials and Tissue Engineering* **4**, 143 (2014).

93. M. V. Srikanth, B. Janaki Ram, S. A. Sunil, N. Sreenivasa Rao, K. V. Ramana Murthy, Gastroretentive drug delivery systems: Novel approaches and its evaluation-A review. *International Journal of Pharmaceutical Sciences Review and Research* **10**, 203 (2011).

94. Y. Wang, P. Li, Z. Peng, F. H. She, L. X. Kong, Microencapsulation of nanoparticles with enhanced drug loading for pH-sensitive oral drug delivery for the treatment of colon cancer. *Journal of Applied Polymer Science* **129**, 714 (2013).

95. L. F. A. Asghar, M. Azeemuddin, V. Jain, S. Chandran, Design and in vitro evaluation of formulations with pH and transit time controlled sigmoidal release profile for colon-specific delivery. *Drug Delivery* **16**, 205 (2009).

96. C. A. Schoener, N. A. Peppas, pH-responsive hydrogels containing PMMA nanoparticles: An analysis of controlled release of a chemotherapeutic conjugate and transport properties. *Journal of Biomaterials Science, Polymer Edition* **24**, 1027 (2013).

97. W. Gao, J. M. Chan, O. C. Farokhzad, PH-responsive nanoparticles for drug delivery. *Molecular Pharmaceutics* **7**, 1913 (2010).

98. C. L. Peng *et al.*, Development of thermosensitive poly(n-isopropylacrylamide-co-((2- dimethylamino) ethyl methacrylate))-based nanoparticles for controlled drug release. *Nanotechnology* **22**, (2011).

99. F. S. Majedi *et al.*, On-Chip Fabrication of Paclitaxel-Loaded Chitosan Nanoparticles for Cancer Therapeutics. *Advanced Functional Materials* **24**, 432 (2014).

100. D. Ray, D. K. Mohapatra, R. K. Mohapatra, G. P. Mohanta, P. K. Sahoo, Synthesis and colon-specific drug delivery of a poly(acrylic acid-co-acrylamide)/MBA nanosized hydrogel. *Journal of Biomaterials Science, Polymer Edition* **19**, 1487 (2008).

101. M. M. Patel, A. F. Amin, Formulation and development of release modulated colon targeted system of meloxicam for potential application in the prophylaxis of colorectal cancer. *Drug Delivery* **18**, 281 (2011).

102. G. M. Whitesides, The origins and the future of microfluidics. *Nature* **442**, 368 (2006).

103. F. S. Majedi *et al.*, Microfluidic assisted self-assembly of chitosan based nanoparticles as drug delivery agents. *Lab on a Chip - Miniaturisation for Chemistry and Biology* **13**, 204 (2013).

104. S. Taranejoo, M. Janmaleki, M. Rafienia, M. Kamali, M. Mansouri, Chitosan microparticles loaded with exotoxin A subunit antigen for intranasal vaccination against Pseudomonas aeruginosa: An in vitro study. *Carbohydrate Polymers* **83**, 1854 (2011).

105. E. Dashtimoghadam, H. Mirzadeh, F. A. Taromi, B. Nyström, Microfluidic self-assembly of polymeric nanoparticles with tunable compactness for controlled drug delivery. *Polymer (United Kingdom)* **54**, 4972 (2013).

106. M. D. Rockville, *United States Pharmacopeia and National Formulary*. (United States Pharmacopeial Convention Inc., ed. 26th, 2003).

107. P. C. Hariharan, J. A. Pople, The influence of polarization functions on molecular orbital hydrogenation energies. *Theoret. Chim. Acta* **28**, 213 (1973).

108. P. Hohenberg, W. Kohn, Inhomogeneous Electron Gas. *Physical Review* **136**, B864 (1964).

109. W. Kohn, L. J. Sham, Self-Consistent Equations Including Exchange and Correlation Effects. *Physical Review* **140**, A1133 (1965).

110. A. D. Becke, Density-functional thermochemistry. III. The role of exact exchange. *J Chem Phys* **98**, 5648 (1993).

111. C. Lee, W. Yang, R. G. Parr, Development of the Colle-Salvetti correlation-energy formula into a functional of the electron density. *Physical Review B* **37**, 785 (1988).

112. A. D. McLean, G. S. Chandler, Contracted Gaussian basis sets for molecular calculations. I. Second row atoms, Z=11–18. *J Chem Phys* **72**, 5639 (1980).

113. M. J. Frisch *et al.*, Gaussian 09, Revision D.01. (2009).

114. S. D. Accelrys Software Inc., 2009.

115. H. Sun, COMPASS: An ab Initio Force-Field Optimized for Condensed-Phase ApplicationsOverview with Details on Alkane and Benzene Compounds. *J Phys Chem B* **102**, 7338 (1998).

116. H. Sun, P. Ren, J. Fried, The COMPASS force field: parameterization and validation for phosphazenes. *Computational and Theoretical Polymer Science* **8**, 229 (1998).

117. W. C. Swope, H. C. Andersen, P. H. Berens, K. R. Wilson, A computer simulation method for the calculation of equilibrium constants for the formation of physical clusters of molecules: Application to small water clusters. *J Chem Phys* **76**, 637 (1982).

118. P. Ingram, H. G. Jerrard, Measurement of relaxation times of macromolecules by the Kerr effect. *Nature* **196**, 57 (1962).

119. J. Fallingborg, Intraluminal pH of the human gastrointestinal tract. *Danish medical bulletin* **46**, 183 (1999).

120. G. Pye, D. Evans, S. Ledingham, J. Hardcastle, Gastrointestinal intraluminal pH in normal subjects and those with colorectal adenoma or carcinoma. *Gut* **31**, 1355 (1990).

121. Z. Du *et al.*, Paclitaxel-loaded micelles composed of folate-poly(ethylene glycol) and poly(γ-benzyl l-glutamate) diblock copolymer. *Colloids and Surfaces A: Physicochemical and Engineering Aspects* **353**, 140 (2010).

122. H. Kang Moo *et al.*, A new hydrotropic block copolymer micelle system for aqueous solubilization of paclitaxel. *Journal of Controlled Release* **126**, 122 (2008).

123. H. M. Ding, Y. Q. Ma, Controlling cellular uptake of nanoparticles with pH-sensitive polymers. *Scientific Reports* **3**, (2013).

124. J. Shi, N. M. Alves, J. F. Mano, Drug release of pH/temperature-responsive calcium alginate/poly(N- isopropylacrylamide) semi-IPN beads. *Macromolecular Bioscience* **6**, 358 (2006).

125. A. Popat, J. Liu, G. Q. Lu, S. Z. Qiao, A pH-responsive drug delivery system based on chitosan coated mesoporous silica nanoparticles. *Journal of Materials Chemistry* **22**, 11173 (2012).

126. W. Chen, J. Du, Ultrasound and pH dually responsive polymer vesicles for anticancer drug delivery. *Scientific Reports* **3**, (2013).

127. J. E. Liebmann *et al.*, Cytotoxic studies of paclitaxel (Taxol®) in human tumour cell lines. *British Journal of Cancer* **68**, 1104 (1993).

128. T. Yang *et al.*, Antitumor effect of paclitaxel-loaded PEGylated immunoliposomes against human breast cancer cells. *Pharmaceutical Research* **24**, 2402 (2007).

129. Z. Amoozgar, J. Park, Q. Lin, Y. Yeo, Low molecular-weight chitosan as a pH-sensitive stealth coating for tumor-specific drug delivery. *Molecular Pharmaceutics* **9**, 1262 (2012).

130. J. W. Loh, M. Saunders, L. Y. Lim, Cytotoxicity of monodispersed chitosan nanoparticles against the Caco-2 cells. *Toxicology and Applied Pharmacology* **262**, 273 (2012).

131. Z. G. Yue *et al.*, Surface charge affects cellular uptake and intracellular trafficking of chitosan-based nanoparticles. *Biomacromolecules* **12**, 2440 (2011).

132. T. Sato, T. Ishii, Y. Okahata, In vitro gene delivery mediated by chitosan. Effect of pH, serum, and molecular mass of chitosan on the transfection efficiency. *Biomaterials* **22**, 2075 (2001).

133. B. Sarmento, J. Das Neves, *Chitosan-Based Systems for Biopharmaceuticals: Delivery, Targeting and Polymer Therapeutics*. (2012).

134. T.-G. Iversen, T. Skotland, K. Sandvig, Endocytosis and intracellular transport of nanoparticles: Present knowledge and need for future studies. *Nano Today* **6**, 176 (2011).

135. M. Karsdal *et al.*, Osteoarthritis–a case for personalized health care? *Osteoarthritis and Cartilage* **22**, 7 (2014).

136. S. R. Cummings, L. J. Melton, Epidemiology and outcomes of osteoporotic fractures. *The Lancet* **359**, 1761 (2002).

137. L. P. Connolly, L. A. Drubach, T. S. Treves, Applications of Nuclear Medicine in Pediatric Oncology. *Clinical Nuclear Medicine* **27**, 117 (2002).

138. K. Wang *et al.*, Bone Scintigraphy in Common Tumors With Osteolytic Components. *Clinical Nuclear Medicine* **30**, 655 (2005).

139. A. G. Huvos, *Bone tunmors: Diagnosis, treatment, and prognosis*. (London: WB Saunders, 1997, 1997).

140. F. T. Çermik, A. Salan, F. M. Firat, A. S. Berkarda, Tc-99m MDP Bone Scintigraphy in a Patient with Multicentric Osteosarcoma. *Clinical Nuclear Medicine* **28**, 599 (2003).

141. V. Kubícek, I. Lukeš, Bone-seeking probes for optical and magnetic resonance imaging. *Future medicinal chemistry* **2**, 521 (2010).

142. A. Panahifar, M. Mahmoudi, M. R. Doschak, Synthesis and in Vitro Evaluation of Bone-Seeking Superparamagnetic Iron Oxide Nanoparticles as Contrast Agents for Imaging Bone Metabolic Activity. *ACS Applied Materials & Interfaces* **5**, 5219 (2013).

143. R. Torres Martin de Rosales *et al.*, 99mTc-bisphosphonate-iron oxide nanoparticle conjugates for dual-modality biomedical imaging. *Bioconjugate Chemistry* **22**, 455 (2011).

144. V. Lewington, Cancer therapy using bone-seeking isotopes. *Physics in medicine and biology* **41**, 2027 (1996).

145. A. S. Lübbe, C. Alexiou, C. Bergemann, Clinical applications of magnetic drug targeting. *Journal of Surgical Research* **95**, 200 (2001).

146. M. Mahmoudi *et al.*, Magnetic Resonance Imaging Tracking of Stem Cells in Vivo Using Iron Oxide Nanoparticles as a Tool for the Advancement of Clinical Regenerative Medicine. *Chemical Reviews* **111**, 253 (2011).

147. M. Mahmoudi, V. Serpooshan, S. Laurent, Engineered nanoparticles for biomolecular imaging. *Nanoscale* **3**, 3007 (2011).

148. S. Sengupta *et al.*, Temporal targeting of tumour cells and neovasculature with a nanoscale delivery system. *Nature* **436**, 568 (2005).

149. M. Mahmoudi, S. Sant, B. Wang, S. Laurent, T. Sen, Superparamagnetic iron oxide nanoparticles (SPIONs): Development, surface modification and applications in chemotherapy. *Advanced Drug Delivery Reviews* **63**, 24 (2011).

150. M. Mahmoudi, H. Hofmann, B. Rothen-Rutishauser, A. Petri-Fink, Assessing the in vitro and in vivo toxicity of superparamagnetic iron oxide nanoparticles. *Chemical reviews* **112**, 2323 (2011).

151. M. Mahmoudi, A. Simchi, M. Imani, A. S. Milani, P. Stroeve, Optimal Design and Characterization of Superparamagnetic Iron Oxide Nanoparticles Coated with

Polyvinyl Alcohol for Targeted Delivery and Imaging†. *The Journal of Physical Chemistry B* **112**, 14470 (2008).

152. F. Benyettou *et al.*, A multimodal magnetic resonance imaging nanoplatform for cancer theranostics. *Physical Chemistry Chemical Physics* **13**, 10020 (2011).

153. F. Matsuoka *et al.*, Hyperthermia using magnetite cationic liposomes for hamster osteosarcoma. *BioMagnetic Research and Technology* **2**, 3 (2004).

154. P. M. Valencia, O. C. Farokhzad, R. Karnik, R. Langer, Microfluidic technologies for accelerating the clinical translation of nanoparticles. *Nature Nano* **7**, 623 (2012).

155. W. J. Duncanson *et al.*, Microfluidic synthesis of advanced microparticles for encapsulation and controlled release. *Lab on a Chip* **12**, 2135 (2012).

156. M. M. Hasani-Sadrabadi *et al.*, Microfluidic-Assisted Self-Assembly of Complex Dendritic Polyethylene Drug Delivery Nanocapsules. *Advanced Materials* **26**, 3118 (2014).

157. R. Pignatello *et al.*, A novel biomaterial for osteotropic drug nanocarriers: synthesis and biocompatibility evaluation of a PLGA-ALE conjugate. (2009).

158. E. Cenni *et al.*, Biocompatibility of poly (d, l-lactide-co-glycolide) nanoparticles conjugated with alendronate. *Biomaterials* **29**, 1400 (2008).

159. A. Petri-Fink, M. Chastellain, L. Juillerat-Jeanneret, A. Ferrari, H. Hofmann, Development of functionalized superparamagnetic iron oxide nanoparticles for interaction with human cancer cells. *Biomaterials* **26**, 2685 (2005).

160. E. Dashtimoghadam, H. Mirzadeh, F. A. Taromi, B. Nyström, Microfluidic self-assembly of polymeric nanoparticles with tunable compactness for controlled drug delivery. *Polymer* **54**, 4972 (2013).

161. S. Sharma, T. Ganesh, D. G. I. Kingston, S. Bane, Promotion of tubulin assembly by poorly soluble taxol analogs. *Analytical Biochemistry* **360**, 56 (2007).

162. H. Chen *et al.*, Alendronate-Conjugated Amphiphilic Hyperbranched Polymer Based on Boltorn H40 and Poly (ethylene glycol) for Bone-Targeted Drug Delivery. *Bioconjugate Chemistry* **23**, 1915 (2012).

163. M. Kay, R. Young, A. Posner, Crystal structure of hydroxyapatite. *Nature* **204**, 1050 (1964).

164. X. Lu, Z. Zhao, Y. Leng, Calcium phosphate crystal growth under controlled atmosphere in electrochemical deposition. *Journal of crystal growth* **284**, 506 (2005).

165. R. Xin, Y. Leng, N. Wang, In situ TEM examinations of octacalcium phosphate to hydroxyapatite transformation. *Journal of crystal growth* **289**, 339 (2006).

166. S. Hauptmann, H. Dufner, J. Brickmann, S. M. Kast, R. S. Berry, Potential energy function for apatites. *Physical Chemistry Chemical Physics* **5**, 635 (2003).

167. M. M. Hasani-Sadrabadi *et al.*, A microfluidic approach to synthesizing high-performance microfibers with tunable anhydrous proton conductivity. *Lab on a Chip* **13**, 4549 (2013).

168. F. S. Majedi *et al.*, On-Chip Fabrication of Paclitaxel Loaded Chitosan Nanoparticles for Cancer Therapeutics. *Advanced Functional Materials*, 10.1002/adfm.201301628 (2013).

169. P. M. Valencia *et al.*, Single-Step Assembly of Homogenous Lipid−Polymeric and Lipid−Quantum Dot Nanoparticles Enabled by Microfluidic Rapid Mixing. *ACS Nano* **4**, 1671 (2010).

170. C. He, Y. Hu, L. Yin, C. Tang, C. Yin, Effects of particle size and surface charge on cellular uptake and biodistribution of polymeric nanoparticles. *Biomaterials* **31**, 3657 (2010).

171. N. Kamaly, Z. Xiao, P. M. Valencia, A. F. Radovic-Moreno, O. C. Farokhzad, Targeted polymeric therapeutic nanoparticles: design, development and clinical translation. *Chemical Society Reviews* **41**, 2971 (2012).

172. J. Shi, Z. Xiao, N. Kamaly, O. C. Farokhzad, Self-Assembled Targeted Nanoparticles: Evolution of Technologies and Bench to Bedside Translation. *Accounts of Chemical Research* **44**, 1123 (2011).

173. T. Luhmann, O. Germershaus, J. Groll, L. Meinel, Bone targeting for the treatment of osteoporosis. *Journal of Controlled Release* **161**, 198 (2012).

174. S. I. Thamake, S. L. Raut, Z. Gryczynski, A. P. Ranjan, J. K. Vishwanatha, Alendronate coated poly-lactic-co-glycolic acid (PLGA) nanoparticles for active targeting of metastatic breast cancer. *Biomaterials* **33**, 7164 (2012).

175. R. D. Ross, R. K. Roeder, Binding affinity of surface functionalized gold nanoparticles to hydroxyapatite. *Journal of biomedical materials research Part A* **99**, 58 (2011).

176. R. G. G. Russell, N. B. Watts, F. H. Ebetino, M. J. Rogers, Mechanisms of action of bisphosphonates: similarities and differences and their potential influence on clinical efficacy. *Osteoporos Int* **19**, 733 (2008).

177. S. W. Morton *et al.*, Osteotropic Therapy via Targeted Layer-by-Layer Nanoparticles. *Advanced Healthcare Materials* **3**, 867 (2014).

178. E. Segal *et al.*, Enhanced anti-tumor activity and safety profile of targeted nano-scaled HPMA copolymer-alendronate-TNP-470 conjugate in the treatment of bone malignances. *Biomaterials* **32**, 4450 (2011).

179. A. K. Patri, I. J. Majoros, J. R. Baker, Dendritic polymer macromolecular carriers for drug delivery. *Current opinion in chemical biology* **6**, 466 (2002).

180. L. K. Johnson, C. M. Killian, M. Brookhart, New Pd(Ii)-Based and Ni(Ii)-Based Catalysts for Polymerization of Ethylene and Alpha-Olefins. *J Am Chem Soc* **117**, 6414 (1995).

181. Z. Guan, P. Cotts, E. McCord, S. McLain, Chain walking: A new strategy to control polymer topology. *Science* **283**, 2059 (1999).

182. Z. Guan, Recent Progress of Catalytic Polymerization for Controlling Polymer Topology. *Chemistry–An Asian Journal* **5**, 1058 (2010).

183. Z. Dong, Z. Ye, Hyperbranched polyethylenes by chain walking polymerization: synthesis, properties, functionalization, and applications. *Polym. Chem.*, (2011).

184. X. Zhu, Y. Zhou, D. Yan, Influence of branching architecture on polymer properties. *Journal of Polymer Science Part B: Polymer Physics* **49**, 1277 (2011).

185. G. Sun, Z. Guan, Cascade Chain-Walking Polymerization to Generate Large Dendritic Nanoparticles. *Macromolecules* **43**, 4829 (2010).

186. C. S. Popeney *et al.*, Tandem Coordination, Ring-Opening, Hyperbranched Polymerization for the Synthesis of Water-Soluble Core–Shell Unimolecular Transporters. *ACS Macro Letters* **1**, 564 (2012).

187. H. Gao *et al.*, Synthesis of amphiphilic copolymers with a dendritic polyethylene core and poly (ethylene oxide) arms and their self-assembled nanostructures. *Polym Chem-Uk*, (2013).

188. G. Chen, D. Huynh, P. L. Felgner, Z. Guan, Tandem chain walking polymerization and atom transfer radical polymerization for efficient synthesis of dendritic nanoparticles for bioconjugation. *J Am Chem Soc* **128**, 4298 (2006).

189. G. Chen, P. L. Felgner, Z. Guan, Efficient catalytic synthesis of dendritic polymers having internal fluorescence labels for bioconjugation. *Biomacromolecules* **9**, 1745 (2008).

190. R. Duncan, L. Izzo, Dendrimer biocompatibility and toxicity. *Advanced drug delivery reviews* **57**, 2215 (2005).

191. P. M. Valencia, O. C. Farokhzad, R. Karnik, R. Langer, Microfluidic technologies for accelerating the clinical translation of nanoparticles. *Nature Nanotechnology* **7**, 623 (2012).

192. J. B. Wacker, I. Lignos, V. K. Parashar, M. A. M. Gijs, Controlled synthesis of fluorescent silica nanoparticles inside microfluidic droplets. *Lab on a Chip* **12**, 3111 (2012).

193. S. Haeberle, G. Roth, F. von Stetten, R. Zengerle, Microfluidic lab-on-a-chip platforms: requirements, characteristics and applications. *Chemical Society Reviews* **39**, 1153 (2010).

194. S. Mecking, L. K. Johnson, L. Wang, M. Brookhart, Mechanistic studies of the palladium-catalyzed copolymerization of ethylene and α-olefins with methyl acrylate. *J Am Chem Soc* **120**, 888 (1998).

195. S. M. Moghimi *et al.*, Material properties in complement activation. *Advanced Drug Delivery Reviews* **63**, 1000 (2011).

196. S. M. Moghimi, A. C. Hunter, J. C. Murray, Long-circulating and target-specific nanoparticles: theory to practice. *Pharmacological reviews* **53**, 283 (2001).

197. S. M. Moghimi, Z. S. Farhangrazi, Nanomedicine and the complement paradigm. *Nanomedicine: Nanotechnology, Biology and Medicine*, **9**, 458 (2013).

198. M. B. Pedersen *et al.*, Curvature of Synthetic and Natural Surfaces Is an Important Target Feature in Classical Pathway Complement Activation. *The Journal of Immunology* **184**, 1931 (2010).

199. B. J. C. Janssen, A. Christodoulidou, A. McCarthy, J. D. Lambris, P. Gros, Structure of C3b reveals conformational changes that underlie complement activity. *Nature* **444**, 213 (2006).

200. R. R. Sawant, O. S. Vaze, K. Rockwell, V. P. Torchilin, Palmitoyl ascorbate-modified liposomes as nanoparticle platform for ascorbate-mediated cytotoxicity and paclitaxel co-delivery. *European Journal of Pharmaceutics and Biopharmaceutics* **75**, 321 (2010).

201. Z. Du *et al.*, Paclitaxel-loaded micelles composed of folate-poly(ethylene glycol) and poly(γ-benzyl l-glutamate) diblock copolymer. *Colloids and Surfaces A: Physicochemical and Engineering Aspects* **353**, 140 (2010).

202. K. M. Huh *et al.*, Hydrotropic polymer micelle system for delivery of paclitaxel. *J Control Release* **101**, 59 (2005).

203. Y. Fan, C. Li, H. Cao, F. Li, D. Chen, The intranuclear release of a potential anticancer drug from small nanoparticles that are derived from intracellular dissociation of large nanoparticles. *Biomaterials* **33**, 4220 (2012).

204. N. P. Truong, M. R. Whittaker, C. W. Mak, T. P. Davis, The importance of nanoparticle shape in cancer drug delivery. *Expert opinion on drug delivery* **12**, 129 (2015).

205. E. Blanco, H. Shen, M. Ferrari, Principles of nanoparticle design for overcoming biological barriers to drug delivery. *Nature biotechnology* **33**, 941 (2015).

206. P. Decuzzi, S. Lee, B. Bhushan, M. Ferrari, A theoretical model for the margination of particles within blood vessels. *Annals of biomedical engineering* **33**, 179 (2005).

207. J. Tan, S. Shah, A. Thomas, H. D. Ou-Yang, Y. Liu, The influence of size, shape and vessel geometry on nanoparticle distribution. *Microfluidics and nanofluidics* **14**, 77 (2013).

208. J. A. Kemp, M. S. Shim, C. Y. Heo, Y. J. Kwon, "Combo" nanomedicine: Co-delivery of multi-modal therapeutics for efficient, targeted, and safe cancer therapy. *Advanced drug delivery reviews*, (2015).

209. B. Al-Lazikani, U. Banerji, P. Workman, Combinatorial drug therapy for cancer in the post-genomic era. *Nature biotechnology* **30**, 679 (2012).

210. W. Quispe-Tintaya *et al.*, Nontoxic radioactive Listeriaat is a highly effective therapy against metastatic pancreatic cancer. *Proceedings of the National Academy of Sciences* **110**, 8668 (2013).

211. C. Stigliano, J. Key, M. Ramirez, S. Aryal, P. Decuzzi, Radiolabeled polymeric nanoconstructs loaded with Docetaxel and Curcumin for cancer combinatorial therapy and nuclear imaging. *Advanced Functional Materials* **25**, 3371 (2015).

212. Q. Hu, W. Sun, C. Wang, Z. Gu, Recent advances of cocktail chemotherapy by combination drug delivery systems. *Advanced drug delivery reviews*, (2015).

213. S. Prakash, M. Malhotra, W. Shao, C. Tomaro-Duchesneau, S. Abbasi, Polymeric nanohybrids and functionalized carbon nanotubes as drug delivery carriers for cancer therapy. *Advanced drug delivery reviews* **63**, 1340 (2011).

214. N. Saito *et al.*, Safe clinical use of carbon nanotubes as innovative biomaterials. *Chemical reviews* **114**, 6040 (2014).

215. N. W. S. Kam, M. O'Connell, J. A. Wisdom, H. Dai, Carbon nanotubes as multifunctional biological transporters and near-infrared agents for selective cancer cell destruction. *Proceedings of the National Academy of Sciences of the United States of America* **102**, 11600 (2005).

216. Z. Liu *et al.*, Supramolecular stacking of doxorubicin on carbon nanotubes for in vivo cancer therapy. *Angewandte Chemie International Edition* **48**, 7668 (2009).

217. E. Miyako, S. A. Chechetka, E. Yuba, K. Kono, In Vivo Remote Control of Reactions in Caenorhabditis elegans by Using Supramolecular Nanohybrids of Carbon Nanotubes and Liposomes. *Angewandte Chemie* **127**, 10041 (2015).

218. Y. Qin *et al.*, Near-infrared light remote-controlled intracellular anti-cancer drug delivery using thermo/pH sensitive nanovehicle. *Acta biomaterialia* **17**, 201 (2015).

219. L. Liao *et al.*, A convergent synthetic platform for single-nanoparticle combination cancer therapy: ratiometric loading and controlled release of cisplatin, doxorubicin, and camptothecin. *Journal of the American Chemical Society* **136**, 5896 (2014).

220. L. K. Johnson, C. M. Killian, M. Brookhart, New Pd (II)-and Ni (II)-based catalysts for polymerization of ethylene and. alpha.-olefins. *Journal of the American Chemical Society* **117**, 6414 (1995).

221. Z. Dong, Z. Ye, Hyperbranched polyethylenes by chain walking polymerization: synthesis, properties, functionalization, and applications. *Polymer Chemistry* **3**, 286 (2012).

222. H. Goldansaz *et al.*, Anomalous Rheological Behavior of Dendritic Nanoparticle/Linear Polymer Nanocomposites. *Macromolecules*, (2015).

223. Y. Chen *et al.*, Synthesis and application of polyethylene-based functionalized hyperbranched polymers. *Progress in Polymer Science*, (2015).

224. G. Chen, Z. Guan, Transition metal-catalyzed one-pot synthesis of water-soluble dendritic molecular nanocarriers. *Journal of the American Chemical Society* **126**, 2662 (2004).

225. H. Gao *et al.*, Synthesis, characterization and micellization of amphiphilic polyethylene-b-polyphosphoester block copolymers. *RSC advances* **5**, 49376 (2015).

226. G. Sun, Z. Guan, Cascade Chain-Walking Polymerization to Generate Large Dendritic Nanoparticles. *Macromolecules* **43**, 4829 (2010).

227. M. C. Lukowiak *et al.*, Carbon-based cores with polyglycerol shells–the importance of core flexibility for encapsulation of hydrophobic guests. *Journal of Materials Chemistry B* **3**, 719 (2015).

228. H. Gao *et al.*, Synthesis of amphiphilic copolymers with a dendritic polyethylene core and poly (ethylene oxide) arms and their self-assembled nanostructures. *Polymer Chemistry* **4**, 1107 (2013).

229. L. Xu, Z. Ye, Q. Cui, Z. Gu, Noncovalent Nonspecific Functionalization and Solubilization of Multi-Walled Carbon Nanotubes at High Concentrations with a Hyperbranched Polyethylene. *Macromolecular Chemistry and Physics* **210**, 2194 (2009).

230. K. Petrie *et al.*, Non-covalent/non-specific functionalization of multi-walled carbon nanotubes with a hyperbranched polyethylene and characterization of their dispersion in a polyolefin matrix. *Carbon* **49**, 3378 (2011).

231. A. A. Vasileiou, A. Docoslis, M. Kontopoulou, P. Xiang, Z. Ye, The role of non-covalent interactions and matrix viscosity on the dispersion and properties of LLDPE/MWCNT nanocomposites. *Polymer* **54**, 5230 (2013).

232. L. Xu *et al.*, The Production of High-Concentration Graphene Dispersions in Low-Boiling-Point Organic Solvents by Liquid-Phase Noncovalent Exfoliation of Graphite with a Hyperbranched Polyethylene and the Formation of Graphene/Ethylene Copolymer Composites. *The Journal of Physical Chemistry C*, (2013).

233. K. Arnold, F. Hennrich, R. Krupke, S. Lebedkin, M. Kappes, Length separation studies of single walled carbon nanotube dispersions. *physica status solidi (b)* **243**, 3073 (2006).

234. M. C. Hersam, Progress towards monodisperse single-walled carbon nanotubes. *Nature Nanotechnology* **3**, 387 (2008).

235. H. Gui *et al.*, A facile and low-cost length sorting of single-wall carbon nanotubes by precipitation and applications for thin-film transistors. *Nanoscale* **8**, 3467 (2016).

236. S. D. Ittel, L. K. Johnson, M. Brookhart, Late-metal catalysts for ethylene homo- and copolymerization. *Chemical Reviews* **100**, 1169 (2000).

237. P. C. Hariharan, J. A. Pople, The influence of polarization functions on molecular orbital hydrogenation energies. *Theoretical Chemistry Accounts: Theory, Computation, and Modeling (Theoretica Chimica Acta)* **28**, 213 (1973).

238. C. M. Breneman, K. B. Wiberg, Determining atom-centered monopoles from molecular electrostatic potentials. The need for high sampling density in formamide conformational analysis. *Journal of Computational Chemistry* **11**, 361 (1990).

239. M. Frisch *et al.* (Gaussian, Inc., Wallingford CT, 2009).

240. W. L. Jorgensen, D. S. Maxwell, J. Tirado-Rives, Development and testing of the OPLS all-atom force field on conformational energetics and properties of organic liquids. *J. Am. Chem. Soc* **118**, 11225 (1996).

241. W. L. Jorgensen, J. Tirado-Rives, The OPLS [optimized potentials for liquid simulations] potential functions for proteins, energy minimizations for crystals of cyclic peptides and crambin. *Journal of the American Chemical Society* **110**, 1657 (1988).

242. B. Hess, C. Kutzner, D. van der Spoel, E. Lindahl, GROMACS 4: Algorithms for Highly Efficient, Load-Balanced, and Scalable Molecular Simulation. *Journal of Chemical Theory and Computation* **4**, 435 (2008).

243. D. Van Der Spoel *et al.*, GROMACS: Fast, flexible, and free. *Journal of Computational Chemistry* **26**, 1701 (2005).

244. T. Pakula, D. Vlassopoulos, G. Fytas, J. Roovers, Structure and dynamics of melts of multiarm polymer stars. *Macromolecules* **31**, 8931 (1998).

245. D. Vlassopoulos, G. Fytas, T. Pakula, J. Roovers, Multiarm star polymers dynamics. *Journal of Physics: Condensed Matter* **13**, R855 (2001).

246. F. J. Stadler, V. Karimkhani, Correlations between the characteristic rheological quantities and molecular structure of long-chain branched metallocene catalyzed polyethylenes. *Macromolecules* **44**, 5401 (2011).

247. V. Karimkhani, F. Afshar-Taromi, S. Pourmahdian, F. J. Stadler, Revisiting the long-chain branch formation mechanism in metallocene catalyzed polyethylenes. *Polymer Chemistry* **4**, 3774 (2013).

248. F. S. Majedi *et al.*, Microfluidic assisted self-assembly of chitosan based nanoparticles as drug delivery agents. *Lab on a Chip* **13**, 204 (2013).

249. D. Liu *et al.*, A versatile and robust microfluidic platform toward high throughput synthesis of homogeneous nanoparticles with tunable properties. *Advanced Materials* **27**, 2298 (2015).

250. Q. Feng, J. Sun, X. Jiang, Microfluidics-mediated assembly of functional nanoparticles for cancer-related pharmaceutical applications. *Nanoscale*, (2016).

251. S. Bazban-Shotorbani, E. Dashtimoghadam, A. Karkhaneh, M. M. Hasani-Sadrabadi, K. I. Jacob, Microfluidic Directed Synthesis of Alginate Nanogels with Tunable Pore Size for Efficient Protein Delivery. *Langmuir*, (2016).

252. P. W. Lee *et al.*, Polymer Structure and Conformation Alter the Antigenicity of Virus-like Particle–Polymer Conjugates. *Journal of the American Chemical Society* **139**, 3312 (2017).

253. A. J. Andersen *et al.*, Complement activation by PEG-functionalized multi-walled carbon nanotubes is independent of PEG molecular mass and surface density. *Nanomedicine: Nanotechnology, Biology and Medicine* **9**, 469 (2013).

254. A. J. Andersen *et al.*, Single-walled carbon nanotube surface control of complement recognition and activation. *ACS nano* **7**, 1108 (2013).

255. A. C. Anselmo *et al.*, Elasticity of nanoparticles influences their blood circulation, phagocytosis, endocytosis, and targeting. *ACS nano* **9**, 3169 (2015).

256. J. Key *et al.*, Soft Discoidal Polymeric Nanoconstructs Resist Macrophage Uptake and Enhance Vascular Targeting in Tumors. *ACS nano* **9**, 11628 (2015).

257. W.-C. Huang *et al.*, Engineering Chimeric Receptors to Investigate the Size and Rigidity-Dependent Interaction of PEGylated Nanoparticles with Cells. *ACS nano*, (2016).

258. A. C. Anselmo, S. Mitragotri, Impact of particle elasticity on particle-based drug delivery systems. *Advanced Drug Delivery Reviews*, (2016).

259. Z. Garaiova *et al.*, Cellular uptake of DNA–chitosan nanoparticles: The role of clathrin-and caveolae-mediated pathways. *International journal of biological macromolecules* **51**, 1043 (2012).

260. F. S. Majedi *et al.*, On-Chip Fabrication of Paclitaxel-Loaded Chitosan Nanoparticles for Cancer Therapeutics. *Advanced Functional Materials*, (2013).

261. K. Kostarelos *et al.*, Cellular uptake of functionalized carbon nanotubes is independent of functional group and cell type. *Nature nanotechnology* **2**, 108 (2007).

262. C. Iancu, L. Mocan, Advances in cancer therapy through the use of carbon nanotube-mediated targeted hyperthermia. *Int J Nanomedicine* **6**, 1675 (2011).

263. K. M. Huh *et al.*, Hydrotropic polymer micelle system for delivery of paclitaxel. *Journal of Controlled Release* **101**, 59 (2005).

264. K. M. Huh *et al.*, A new hydrotropic block copolymer micelle system for aqueous solubilization of paclitaxel. *Journal of Controlled Release* **126**, 122 (2008).

265. Z. Du *et al.*, Paclitaxel-loaded micelles composed of folate-poly (ethylene glycol) and poly (γ-benzyl l-glutamate) diblock copolymer. *Colloids and Surfaces A: Physicochemical and Engineering Aspects* **353**, 140 (2010).

266. N. Kol *et al.*, A stiffness switch in human immunodeficiency virus. *Biophysical journal* **92**, 1777 (2007).

267. N. Kol *et al.*, Mechanical properties of murine leukemia virus particles: effect of maturation. *Biophysical journal* **91**, 767 (2006).

268. L. Zhang *et al.*, Microfluidic synthesis of hybrid nanoparticles with controlled lipid layers: understanding flexibility-regulated cell–nanoparticle interaction. *ACS nano* **9**, 9912 (2015).

269. J. Sun *et al.*, Tunable rigidity of (polymeric core)–(lipid shell) nanoparticles for regulated cellular uptake. *Advanced Materials* **27**, 1402 (2015).

270. M. M. Hasani-Sadrabadi *et al.*, Enhanced osteogenic differentiation of stem cells via microfluidics synthesized nanoparticles. *Nanomedicine: Nanotechnology, Biology and Medicine* **11**, 1809 (2015).

271. D. Qin, Y. Xia, G. M. Whitesides, Soft lithography for micro-and nanoscale patterning. *Nature protocols* **5**, 491 (2010).

272. M. A. Azagarsamy, I. A. Marozas, S. Spaans, K. S. Anseth, Photoregulated Hydrazone-Based Hydrogel Formation for Biochemically Patterning 3D Cellular Microenvironments. *ACS Macro Letters* **5**, 19 (2016).

273. P. M. Valencia *et al.*, Effects of ligands with different water solubilities on self-assembly and properties of targeted nanoparticles. *Biomaterials* **32**, 6226 (9//, 2011).

274. M. M. Hasani-Sadrabadi *et al.*, On-chip synthesis of fine-tuned bone-seeking hybrid nanoparticles. *Nanomedicine* **10**, 3431 (2015).

275. C. Wang *et al.*, Suppression of colorectal cancer subcutaneous xenograft and experimental lung metastasis using nanoparticle-mediated drug delivery to tumor neovasculature. *Biomaterials* **35**, 1215 (2014).

276. S. C. Moss, D. J. Lightell, S. O. Marx, A. R. Marks, T. C. Woods, Rapamycin Regulates Endothelial Cell Migration through Regulation of the Cyclin-dependent Kinase Inhibitor p27(Kip1). *The Journal of Biological Chemistry* **285**, 11991 (2010).

277. M. L. Ponce, in *Angiogenesis Protocols: Second Edition*, C. Murray, S. Martin, Eds. (Humana Press, Totowa, NJ, 2009), pp. 183-188.

278. I. Arnaoutova, H. K. Kleinman, In vitro angiogenesis: endothelial cell tube formation on gelled basement membrane extract. *Nature protocols* **5**, 628 (2010).

279. M. D. Ungrin, C. Joshi, A. Nica, C. Bauwens, P. W. Zandstra, Reproducible, ultra high-throughput formation of multicellular organization from single cell suspension-derived human embryonic stem cell aggregates. *PloS one* **3**, e1565 (2008).

280. C. L. Bauwens, M. D. Ungrin, in *Cardiac Tissue Engineering: Methods and Protocols*, M. Radisic, L. D. Black Iii, Eds. (Springer New York, New York, NY, 2014), pp. 15-25.

281. C. Wong *et al.*, Multistage nanoparticle delivery system for deep penetration into tumor tissue. *Proceedings of the National Academy of Sciences* **108**, 2426 (2011).

282. B. Kwak, A. Ozcelikkale, C. S. Shin, K. Park, B. Han, Simulation of complex transport of nanoparticles around a tumor using tumor-microenvironment-on-chip. *Journal of Controlled Release* **194**, 157 (2014).

283. S. Schöttler *et al.*, Protein adsorption is required for stealth effect of poly(ethylene glycol)- and poly(phosphoester)-coated nanocarriers. *Nat Nano* **11**, 372 (2016).

284. S. Palchetti *et al.*, The protein corona of circulating PEGylated liposomes. *Biochimica et Biophysica Acta (BBA) - Biomembranes* **1858**, 189 (2016).

285. S. Tenzer *et al.*, Nanoparticle Size Is a Critical Physicochemical Determinant of the Human Blood Plasma Corona: A Comprehensive Quantitative Proteomic Analysis. *ACS Nano* **5**, 7155 (2011).

286. S. M. Weis, in *Methods in Enzymology*. (Academic Press, 2007), vol. 426, pp. 505-528.

287. E. A. Murphy *et al.*, Nanoparticle-mediated drug delivery to tumor vasculature suppresses metastasis. *Proceedings of the National Academy of Sciences* **105**, 9343 (2008).

288. B. Blouw *et al.*, The invadopodia scaffold protein Tks5 is required for the growth of human breast cancer cells in vitro and in vivo. *PLoS One* **10**, e0121003 (2015).

289. S. Bazban-Shotorbani, E. Dashtimoghadam, A. Karkhaneh, M. M. Hasani-Sadrabadi, K. I. Jacob, Microfluidic directed synthesis of alginate nanogels with tunable pore size for efficient protein delivery. *Langmuir* **32**, 4996 (2016).

290. M. M. Hasani-Sadrabadi *et al.*, Microfluidic manipulation of core/shell nanoparticles for oral delivery of chemotherapeutics: a new treatment approach for colorectal cancer. *Advanced Materials* **28**, 4134 (2016).

291. S. Soleimani *et al.*, Understanding biophysical behaviours of microfluidic-synthesized nanoparticles at nano-biointerface. *Colloids and Surfaces B: Biointerfaces* **145**, 802 (2016).

292. A. Albanese, A. K. Lam, E. A. Sykes, J. V. Rocheleau, W. C. W. Chan, Tumour-on-a-chip provides an optical window into nanoparticle tissue transport. **4**, 2718 (2013).

293. S. N. Bhatia, D. E. Ingber, Microfluidic organs-on-chips. *Nature biotechnology* **32**, 760 (2014).

294. D. Huh *et al.*, Microfabrication of human organs-on-chips. *Nature protocols* **8**, 2135 (2013).

295. D. Huh *et al.*, Reconstituting organ-level lung functions on a chip. *Science* **328**, 1662 (2010).

296. T. M. Göppert, R. H. Müller, Adsorption kinetics of plasma proteins on solid lipid nanoparticles for drug targeting. *International Journal of Pharmaceutics* **302**, 172 (2005).

297. C. D. Walkey, W. C. W. Chan, Understanding and controlling the interaction of nanomaterials with proteins in a physiological environment. *Chemical Society Reviews* **41**, 2780 (2012).

298. M. Mahmoudi *et al.*, Protein−Nanoparticle Interactions: Opportunities and Challenges. *Chemical Reviews* **111**, 5610 (2011).

299. M. C. Vyner, L. Liu, H. D. Sheardown, B. G. Amsden, The effect of elastomer chain flexibility on protein adsorption. *Biomaterials* **34**, 9287 (2013).

300. B. D. Fairbanks *et al.*, A Versatile Synthetic Extracellular Matrix Mimic via Thiol-Norbornene Photopolymerization. *Advanced Materials* **21**, 5005 (2009).

301. N. Kol *et al.*, Mechanical Properties of Murine Leukemia Virus Particles: Effect of Maturation. *Biophysical Journal* **91**, 767 (2006).